

Techniques for Achieving Higher Spatial Resolution

A Thesis Submitted for the Degree of
Doctor of Philosophy

in the Faculty of Science
Bangalore University

by

R. Sridharan



Indian Institute of Astrophysics
Bangalore-560 034. India.

July 2001

To my parents, brothers and sisters.

Declaration

I hereby declare that the matter contained in this thesis is the result of the investigations carried out by me at the Indian Institute of Astrophysics, Bangalore, India, under the supervision of Professor P. Venkatakrisnan. This work has not been submitted to any university or institute for the award of any degree, diploma, associateship or fellowship whatsoever.

In keeping with the general practice of reporting scientific observations, due acknowledgement has been made whenever the work described is based on the findings of other investigators. Any omission which might have occurred by oversight or error in judgement is regretted.

Bangalore - 560 034.

July 2001



R. Sridharan

(Candidate)

Certificate

This is to certify that the thesis entitled 'Techniques for Achieving Higher Spatial Resolution', to be submitted to the Department of Physics, Bangalore University by Mr. R. Sridharan for the award of the degree of Doctor of Philosophy in the faculty of Science, is based on the results of the investigations carried out by him during the last six years, under my supervision and guidance, at the Indian Institute of Astrophysics. This thesis has not been submitted for award of any degree, diploma, associateship, or fellowship whatsoever of any university or institute.

Bangalore - 560 034.

July 2001

P. Venkatakrisnan

(Supervisor)

Acknowledgements

Prof P. Venkatakrishnan has been guiding me patiently to carry out my thesis work for the last six years. His aspiration to carry out outstanding research work has always been a source of inspiration for me. It was a great experience to work with him. I thank him for having given me this opportunity.

I thank the Director, Prof. Ramanath Cowsik for providing me all the necessary facilities to carry out my thesis work. I thank the Chairman, Board of Graduate Studies, Prof. S. S. Hasan, and its present and past members, for their support throughout my stay at IIA.

I thank Prof. M. N. Anandaram, the present Chairman, Department of Physics, Bangalore University, and the previous Chairmen, Prof. M. C. Radhakrishna and Prof. A. R. Hanumanthappa, for their kind support and cooperation in completing the formalities related to the University. I also thank Mr. Krishnamoorthy and all the other members of the Ph.D. section, Central College, Bangalore University, for their co-operation during the last five years.

I thank Prof. Ch. V. Sastry and Dr. R. Ramesh for having given me the opportunity to work with the Gauribidanur Radio Heliograph data in the initial days of my thesis work.

Mr. P. Devendran and H. Hariharan assisted me during observations at Kodaikanal Observatory. I thank them for their help. I also thank, Dr. S. K. Gupta, Mr. P. S. M. Aleem, and Dr. K. Sundara Raman for their kind cooperation during my stay at Kodaikanal.

Mr. P. U. Kamath and Mr. V. K. Subramanian designed the re-imaging unit that was used for the observations at Kodaikanal. M. N. Thimmiah built the instrument. I sincerely thank all of them. I thank Mr. P. K. Mahesh, Mr. Madhava Rao, Mr. Sahayanathan, Mr. Periyamayagam and Mr. J. P. A. Samson for their help at various stages.

I thank Mr. B. Nagaraja Naidu for providing the digital counter that I used for obtaining short exposure images at Kodaikanal.

I thank Mr. A. V. Ananth and Mr. J. S. Nathan for the state of the art computing facilities provided at the computer center. The excellent facilities of the library provided invaluable support for my research work. I thank the librarian Ms. Vagishwari, the assistant librarian Mrs Christina Louis and all the other library staff. I thank Mr. Muralidas and Mr. Sankaranarayanan for their help at various stages.

I thank Prof. B. P. Das for allowing me to make use of the Sun UltraSparc machine (Parity), whose 4 GB RAM was instrumental in saving me a lot of time in some of my protracted calculations.

I thank Prof. Steve Keil and all members of the Sacramento Peak observatory for providing the 'destretching' code.

I thank Dr. William Pence, High Energy Astrophysics Science Archive Research Center, NASA/Goddard Space Flight Center for making the FITSIO software freely available on the World Wide Web and for many clarifications regarding its successful usage. I also thank the anonymous contributors to this package.

I thank Shibu, Sonjay, Ravindra, Paneri, Dal Chand for their help in performing observations at the Udaipur Solar Observatory. I thank all the staff members of USO for their kind cooperation during my stay at USO.

I thank all the fellow students and postdocs of the institute for their cooperation during the period of my thesis work. Special thanks to: Suresh and Raji for helping me with the facilities of the Zero Lab; my bachmates Dharam, Geetha, Rajesh and Suresh for their wonderful company since the course work days; Sankar and Krishnakumar for their help at the various stages of my thesis work; Srikanth and Peyman for many fruitful discussions; Angom Dilip and Rajat Chaudhuri for many things I learnt from them in FORTRAN programming.

I thank Mr. Prabhakara, Mr. Kanakaraj and Mr. Thyagaraja for preparing bound copies of the thesis.

Abstract

This thesis is aimed at developing both hardware and software required for obtaining high resolution images on a regular basis from ground-based telescopes using speckle and interferometric imaging techniques. A program (speckle code) for analysing the speckle data has been developed and used to analyze speckle data obtained from a few solar telescopes.

The first Chapter provides an introduction to the thesis. It starts with an overview of human endeavors to achieve high angular resolution in telescopic observations. It should be mentioned that no serious attempt has been made to present the developments in their chronological order. Another point to be noted is that only technical developments have been highlighted but the scientific achievements that these developments have led to have not been described, basically, to conform to the spirit of the title. These technical developments provide the foundation for the explorations presented in this thesis. The thesis itself finds its place under the the category of image restoration schemes mentioned towards the end of the overview. The next few sections have been devoted to explain the adverse effects of the atmospheric *seeing*, the importance of phases of an object's Fourier transform, and resolution as defined in Astronomy. Questions like *Why is high resolution needed in Solar Physics ?*, *Why should special techniques be developed for ground based observations, while space telescopes have become the order of the day ?*, and *Why speckle and interferometric imaging techniques alone have been addressed in this thesis ?* have been answered in the next few sections.

The second Chapter is concerned with the measurement of the atmospheric coherence diameter -the so-called 'Fried's parameter'. This parameter severely influences the quality of the recorded image in ground based observations; the larger its value, the better is the image quality. Estimation of this parameter is essential in solar speckle imaging. A few methods of estimating this parameter and their applicability to the nature of the data have been explored in this Chapter. The details of the speckle and interferometric imaging observations and the pre-processing methods that are essential for analysing the speckle data and have been adopted in our speckle code have been presented in this Chapter. The details of the back-end instrument developed at the institute for performing speckle observations at Kodaikanal Observatory (KO) have also been described.

In the third Chapter, practical methods used in our speckle code to reconstruct an image from a series of short exposure images have been described. In our speckle code, the Fourier amplitudes of an object are estimated by Labeyrie's speckle interferometry method and the Fourier phases of the object are estimated using Weigelt's speckle masking technique. The reconstructed images of a few sunspot and pore regions, observed with the tunnel telescope of KO show small scale features up to the diffraction limit of the telescope. The identification of these indicates the importance of speckle observations in achieving high spatial resolution. The reconstructed images of two sub-flare regions of the NOAA AR8898, observed with the 15 cm Coude telescope of the Udaipur Solar Observatory indicate that 'frame selection' can be one of the ways of improving the resolution. The high redundancy in the estimated phase of the Fourier transform of the object increases the signal-to-noise ratio of the reconstructions and implies that the reconstruction from a few selected 'good' frames can significantly improve the quality.

The fourth Chapter is concerned with the application of speckle imaging. The speckle imaging technique described in the previous Chapters was used to analyse near-simultaneous filtergrams obtained in the G-band ($\lambda=4305 \text{ \AA}$) and the K line of Ca II ($\lambda=3933 \text{ \AA}$) at a plage region, quiet Sun region and the NOAA AR8923. As the seeing conditions were poor, a reconstruction was obtained from three best images of the sequence of recorded images of each region in the G-band and the K line of Ca II. The G-band bright points (GBPs) were extracted from the corresponding reconstructed images using image segmentation techniques. Then the morphology of the GBPs and the Ca II K network bright points were studied in each region. The prime objective of this study was to see whether this data can offer a clue on the mechanism that leads to the preferential heating at the chromospheric level (network boundaries) while the source, if assumed to be the GBPs, is distributed everywhere. We suggest the possibility of having two classes of GBPs, those present at all locations and those swept by the supergranular horizontal motions to the network boundaries. While the former are perhaps generated continuously and observed at any given time, the latter may cause the preferential heating at the Ca II K network boundaries. The intra-network GBPs could be associated with the intra-network Ca II K bright points, not resolved in the present data.

In the fifth Chapter, the basic principle of the interferometric imaging observations has been described briefly. The possibility of having two kinds of transfer functions in such observations has been indicated. A laboratory experiment performed to understand the details of 'closure phase imaging' has been described. A program was developed to simulate phase screens. Specklegrams and interferograms were generated from the simulated phase screens and used for simulating fringes that could be formed by bright features residing inside pores. These fringes were then compared with those obtained from real observations at KO by placing a non-redundant mask at the re-imaged pupil plane of the telescope. Such observations can be useful, at least to resolve isolated bright points. The problem of "source confusion" can be minimised by restricting the field-of-view to about an arc second.

The last Chapter provides the summary of the thesis work. The speckle code developed by the authors is compared with that developed by others and the advantages are highlighted. This is followed by a brief description of the future plans of the authors.

Scope of the Thesis

The Sun is one among the billions of stars that beautify the space around us. It is so near to us that we can see it in greater detail than any other star. Without the Sun, there would be no earth, no seasons, no climate and no day and night. It is the source of our very existence. An amazing fact is that we have not yet understood it completely! It poses challenging puzzles even after nearly three hundred years of regular observations. This thesis represents yet another attempt to unravel its mysteries. An earnest reader may then wonder, why nothing related to the Sun has appeared in the title! Experience tells us that a real breakthrough in our knowledge on the Sun can occur only through high resolution observations. This thesis is aimed at gaining expertise in such observations. Though the main motivation behind this thesis has been to understand solar phenomena, the methods investigated in it are applicable not only to solar observations but to the broader field of high resolution optical astronomy and hence the title.

The subject matter of this has been divided into six chapters and the focus has been on two high resolution imaging techniques, namely, the **Speckle Imaging** and the **Interferometric Imaging**. The data used in this thesis have been obtained from four different solar telescopes, *viz.* the **Tunnel Telescope of the Kodaikanal Observatory (KO)**, Kodaikanal, India, the **Coude telescope of the Udaipur Solar Observatory (USO)**, Udaipur, India, the **Coude telescope of the Uttar Pradesh State Observatory (UPSO)**, Nainital, India and the **Dunn Solar Telescope of the National Solar Observatory/Sacramento Peak (NSO/SP)**, New Mexico, USA. The back-end instruments needed for the observations at KO were built at the **Indian Institute of Astrophysics (IIA)**, Bangalore. Most of the software required for analysing the data was developed by the author during the last three years.

A major part of this thesis work has been the development of the software (speckle code) to reconstruct an image (of an object) with enhanced contrast from a series of short exposure images. While the Fourier amplitudes of the object are estimated by Labeyrie's innovative speckle interferometry, the Fourier phases are estimated with high redundancy (and hence with improved signal-to-noise ratio of the reconstructions) with Weigelt's speckle masking (triple correlation or bispectrum) technique. The software has been optimised for reconstructing small scale solar features that ride on a bright background or a locally depressed background. The methods developed by various authors to improve the quality of reconstructions have been incorporated into the code. The ability of the code to obtain a 'good' reconstruction from a 'few selected good frames', demonstrated in this thesis via the reconstruction of the speckle images recorded at KO and USO, has made it suitable for reconstructing solar images obtained from large telescopes, where the life times of features are relatively short. Another advantage of the code is that it can also be used to reconstruct images obtained by combining an array of telescopes, which has become the order of the day for achieving high angular resolution. The code can now be used to reconstruct images from existing solar (and stellar) telescopes on a regular basis. Another component of this thesis work is the development of the software required for simulating phase screens and generation of speckelgrams and interferograms from them. The simulated interferograms, again as demonstrated in this thesis, can be used to improve our knowledge of the interferometric image reconstruction of solar features.

Contents

List of Figures	xiv
List of Tables	xvi
List of Symbols	xvii
List of Abbreviations	xx
1 Introduction	1
1.1 High Resolution in Astronomy - An Overview	1
1.2 Atmospheric Turbulence and Seeing	4
1.3 Importance of Phase	5
1.4 Resolution and Fried's Parameter	7
1.5 High Resolution in Solar Physics	10
1.6 Formulation of the Research Problem	13
2 Estimation of Fried's Parameter for the Speckle Data	16
2.1 Methods for Estimation of r_0	17
2.1.1 From Angle-of-arrival Fluctuations	17
2.1.2 Power Spectrum Equalisation Method	21
2.1.3 Spectral Ratio Method	23
2.2 Data	24
2.3 Pre-processing	27

2.4	Estimation of r_0	29
2.4.1	KO Data	29
2.4.2	UPSO Data	30
2.4.3	USO Data	35
2.5	Summary	43
3	Solar Speckle Imaging	45
3.1	Solar Speckle Imaging: Practical Implementation	45
3.1.1	Estimation of the Fourier Amplitudes	46
3.1.2	Estimation of the Fourier Phases	47
3.1.3	Image Reconstruction	51
3.1.4	Validation of the Phase Reconstruction Procedure	52
3.2	Speckle Image Reconstruction of Solar Features	55
3.2.1	KO Data	55
3.2.2	USO Data	63
3.2.3	Discussion	74
3.3	Summary	77
4	On the Morphological Relationship Between G-Band and Ca II K Network Bright Points	79
4.1	Introduction	79
4.2	Observations	81
4.3	Analysis	83
4.4	Results and Discussion	85
4.5	Summary	96

5 Interferometric Imaging	97
5.1 Introduction	97
5.2 Interferometric Imaging using Closure Phase Technique	98
5.3 Interferometric Imaging Systems with Non-zero Transfer Functions . . .	100
5.4 Laboratory Simulation of Interferometric Imaging	101
5.5 Computer Simulations on Interferometric Imaging	105
5.5.1 Generation of Phase Screens	107
5.5.2 Validation of the Simulated Phase Screens	109
5.6 Simulation of Interferometric Imaging of Small Scale Solar Features . .	111
5.6.1 Effect of Finite Bandwidth on the Visibility of the Fringes . . .	111
5.6.2 Simulation of Interferograms	113
5.7 Summary	117
6 Summary and Future Directions	120
6.1 Present Work	120
6.2 Comments on the Speckle Code	123
6.3 Future Directions	125
Appendix:A	127
Appendix:B	139
Bibliography	142

List of Figures

1.1	Importance of Fourier phases.	6
1.2	Definition of resolution.	9
2.1	The Re-imaging unit used at KO.	25
2.2	Mask configuration.	26
2.3	Distribution of r_0 estimated from sequences 1-9 of a sub-flare region. . .	39
2.4	Distribution of r_0 estimated from sequences 10-18 of a sub-flare region. .	40
2.5	Distribution of r_0 estimated from sequences 19-27 of a sub-flare region .	41
2.6	Distribution of r_0 estimated from the 28th sequence of a sub-flare region	42
2.7	Variation of r_0 with time (USO data).	42
3.1	Demonstration of the phase reconstruction procedure.	53
3.2	Two sequences of 16 images of a pore region.	55
3.3	Two sequences of 16 images of a pore region.	57
3.4	A sequence of 18 images; 1-16 observed, 17-average, 18-processed. . . .	58
3.5	A sequence of 18 images; 1-16 observed, 17-average, 18-processed. . . .	58
3.6	Two sequences of 16 images of a pore region.	59
3.7	Two sequences of 36 images of a pore region.	61
3.8	Two sequences of 18 images of a sunspot region.	62
3.9	A portion the NOAA AR8898.	65
3.10	Reconstructed images of sequences 1 to 4 of a sub-flare region.	66
3.11	Reconstructed images of sequences 5 to 8 of a sub-flare region.	67

3.12	Reconstructed images of sequences 9 to 12 of a sub-flare region.	68
3.13	Reconstructed images of sequences 13 to 16 of a sub-flare region.	69
3.14	Reconstructed images of sequences 17 to 20 of a sub-flare region.	70
3.15	Reconstructed images of sequences 21 to 24. of a sub-flare region.	71
3.16	Reconstructed images of sequences 25 to 28 of a sub-flare region.	72
3.17	A sequence of 16 reconstructed images showing filament breakup.	74
3.18	Reconstructed images of a sub-flare region near the edge of a sunspot.	76
3.19	Reconstructed images of a sub-flare region near the edge of a sunspot.	77
3.20	GOES X-ray flux recorded during 7–9 March 2000.	78
4.1	Reconstructed image of a plage region in Ca II K line.	86
4.2	Reconstructed image of a plage region in G-band.	87
4.3	Reconstructed image of a quiet Sun region in Ca II K line.	88
4.4	Reconstructed image of a quiet Sun region in G-band.	89
4.5	Reconstructed image of NOAA AR8923 in Ca II K line.	90
4.6	Reconstructed image of NOAA AR8923 in G-band.	91
4.7	G-band binary map of a plage region overlaid on the G-band image.	92
4.8	G-band binary map of a quiet Sun region overlaid on the G-band image.	93
4.9	G-band binary map of NOAA AR8923 overlaid on the G-band image.	94
5.1	Experimental setup for interferometric imaging.	101
5.2	Fringes obtained in the laboratory experiment.	102
5.3	Contour maps of the images reconstructed from the fringes.	106
5.4	Structure functions of simulated phase screens.	109
5.5	Phase variance over pupils of different sizes in simulated phase screens.	110
5.6	Fringes of a pore region recorded using a NRM at KO.	112
5.7	Simulated fringes of an extended source.	114
5.8	Simulated fringes of an extended source.	116
5.9	Simulated fringes of an extended source.	118

List of Tables

2.1	r_0 estimated from angle-of-arrival fluctuations for 4 by 4 arc sec FOV .	33
2.2	r_0 estimated from angle-of-arrival fluctuations for 8 by 8 arc sec FOV .	34
2.3	r_0 estimated from angle-of-arrival fluctuations for 16 by 16 arc sec FOV	35
2.4	Comparison of r_0 estimated from three different methods.	36
2.5	r_0 estimated from USO data by spectral ratio method	38
3.1	Fourier phase recovery from an image of size 4 by 4 pixels	49
4.1	Characteristics of the observations performed at NSO/SP	82

List of Symbols

Symbol	Description	Page
Chapter 1		
L_0	Outer scale of the turbulence	4
l_0	Inner scale of the turbulence	4
D	Diameter of the telescope	7
$\Delta\theta$	Angular Resolution	8
λ	Wavelength	8
τ	Modulation Transfer Function	8
$f \equiv \mathbf{f} $	Spatial frequency with dimensions (1/length)	8
\mathcal{R}	Resolution defined as integral over the spatial frequencies of ensemble averaged Modulation Transfer Function	8
\mathcal{R}_∞	Resolution obtained with long exposures	9
\mathcal{R}_t	Resolution obtained with short exposures	9
\mathcal{R}_{max}	Limiting resolution	9
$\mathcal{R}/\mathcal{R}_{max}$	Normalised resolution	9
r_0	Fried's parameter	9
R	Focal length	9
Chapter 2		
β_x	Fluctuation in the angle of arrival of light in x direction	17
β_y	Fluctuation in the angle of arrival of light in y direction	17
β^2	Mean square fluctuation in the angle of arrival of light	17
δx	Error in the estimation of the quantity x	
$\langle \dots \rangle$	Ensemble average of the quantity ...	18
a_L	Co-efficient of linear term in the infinite series approximation of the distorted wave-front's phase	18

Δ_C	Error in average phase fluctuations provided by finite series approximation of the distorted wave-front's phase	18
Δ_L	Error in average tilt provided by finite series approximation of the distorted wave-front's phase	18
\mathcal{F}_C	Polynomial representing average phase over aperture (Fried, 1965)	18
\mathcal{F}_L	Polynomial representing average tilt over the aperture (Fried, 1965)	18
$A(D, r_0)$	Ensemble average of a_L	19
$B(x, y)$	Bilinear surface fit for an image with co-efficients $a_0, a_1, a_2,$ and a_3	19
$\alpha \equiv r_0/D$	Modified Fried's parameter	23
$\mathbf{q} \equiv \mathbf{f}/(D/\lambda)$	Normalised spatial frequency	23
A, B	Constants	23
\forall	for all values of	23
$E(\epsilon)$	Ensemble averaged spectral ratio ϵ	23
$f/5$	f -ratio of 5, that is, focal length/diameter = 5	24
$I(m, n)$	Image intensity at the pixel (m, n)	29
\bar{I}	Average intensity	29
C	Contrast	29

Chapter 3

*	Complex conjugate	
$I(\mathbf{f})$	Fourier component of an image at the frequency \mathbf{f}	47
$b(\mathbf{f}_1, \mathbf{f}_2)$	Bispectrum corresponding to the frequencies $(\mathbf{f}_1, \mathbf{f}_2)$	47
$\phi_b(\mathbf{f}_1, \mathbf{f}_2)$	Phase of the average bispectrum at the frequencies $(\mathbf{f}_1, \mathbf{f}_2)$	47
$\phi(\mathbf{f})$	Phase of the Fourier transform of an object at the frequency (\mathbf{f})	47
$\beta(\mathbf{f})$	Error in the phase estimation at the frequency \mathbf{f}	50
$\sigma_{yy}(\mathbf{f})$	Variance of phase perpendicular to the direction of the mean phasor	50
$S(\mathbf{f})$	Mean phasor	50
$M(m, n)$	Number of estimates of phase at the frequency point (m, n)	50

Chapter 5

$\mu(\mathbf{d})$	Complex degree of coherence for the baseline \mathbf{d}	97
α_i	Phase error at i th sub-aperture of an interferometer	99
$\phi_{i,j}$	Phase of μ corresponding to the baseline joining the elements i and j	99
$\phi_{closure}$	Closure phase	99
f_1, f_2, f_3	Focal lengths of lenses L_1, L_2 and L_3 respectively	101
M, N	Number of columns and rows of an array	103

s_x, s_y	Size of pixels in x and y directions	103
dx, dy	Separation between the holes in the mask	103
(x_i, y_i)	Co-ordinates of holes in the mask	103
p_{ij}	Position of peaks in the power spectrum	103
ϕ_{ijk}	Closure phase	104
$A(x, y)$	Distorted wavefront	105
$\phi(x, y)$	2-D phase screen	105
$W_{\phi_0}(\mathbf{f})$	Power spectrum of phase fluctuations	107
$\Phi(f_x, f_y)$	Fourier transform of $\phi(x, y)$	107
L	Length of the phase screen	107
$\Delta\nu$	Bandwidth	111
ν_0	Mean frequency	113
σ_z	Standard deviation of optical path difference	113
ΔP	Path length difference	113
Δl	Coherence length	113
Δr	Sampling in phase screen	113
η	Number of samples per diffraction limit (in the image plane)	113
λ_0	Mean wavelength	113
$i(\mathbf{x})$	2-D image	115
$o(\mathbf{x})$	2-D object	115
$p(\mathbf{x})$	PSF	115
$P(\mathbf{f})$	Fourier transform of the PSF at the frequency \mathbf{f}	115
$O(\mathbf{f})$	Fourier transform of the object at the frequency \mathbf{f}	115

List of Abbreviations

AR	Active Region
ARF	Angle of Arrival Fluctuations
CCD	Charge Coupled Device
DIMM	Differential Image Motion Monitor
DT2861	Data Translation card 2861
EEV	English Electric Valve
ESO	European Southern Observatory
FFT	Fast Fourier Transform
FWHM	Full Width at Half Maximum
GBPs	G band Bright Points
GOES	Geostationary Operational Environmental Satellite
HST	Hubble Space Telescope
IDL	Interactive Data Language
KO	Kodaikanal Observatory
LMSAL	Lockheed Martin Solar Astrophysics Laboratory
MDI	Michelson Doppler Imager
MISMA	Micro Structured Magnetic Atmosphere
MTF	Modulation Transfer Function
NOAA	National Oceanic and Atmospheric Administration
NOAO	National Optical Astronomy Observatory
NRM	Non-Redundant Mask
NSO/SP	National Solar Observatory/Sacramento Peak
OTF	Optical Transfer Function
PSE	Power Spectrum Equalisation
PSF	Point Spread Function
RC	Spearman's Rank Correlation Co-efficient
SEC	Space Environment Center
SOHO	Solar and Heliospheric Observatory
SR	Spectral Ratio
STF	Speckle Transfer Function
SVD	Singular Value Decomposition
TRACE	Transition Region and Coronal Explorer
UPSO	Uttar Pradesh State Observatory
USO	Udaipur Solar Observatory
UT	Universal Time
VLBI	Very Long Baseline Interferometry

Chapter 1

Introduction

1.1 High Resolution in Astronomy - An Overview

From time immemorial, humanity has been striving to unearth the secrets of the heavens. From the Galilean era of modest refractors to the modern era of multi-mirror telescopes and space based interferometers, the focus has been on achieving two things, *viz.* high sensitivity - ability to see faint objects and high angular resolution - ability to see them in greater detail. The invention of the *telescope* by Galileo in 1608, as an aid to the human eye, was a first major step forward in the quest for high resolving power. It was followed by building of telescopes with large apertures. However, at the beginning of the last century, it was realised that the Earth's turbulent atmosphere practically limits the resolution of a ground based telescope to about an arc sec, irrespective of its size.

Then emerged the concept of *interferometry* - making a 'picture' of a distant object from the measurements of the spatial coherence of the light at different points in space as a function of their separation. Michelson (1891) successfully applied this technique to measure the angular diameter of the satellites of Jupiter. In 1921, he introduced a new idea of mimicking a large telescope - collecting the light from a star on two small

mirrors separated enough to resolve the star and reflecting the light into a relatively small telescope. Named as *Michelson's stellar interferometer*, it was the first successful optical interferometer. Michelson and Pease (1921) measured the angular diameters of a few stars with this interferometer. However, mechanical stability, pointing accuracy and atmospheric scintillation prevented the continuous operation of such an instrument at optical wavelengths.

A few decades later, a radio analog of Michelson's stellar interferometer was built by Ryle and Vonberg (1946) to study the radio emissions from the Sun. This was followed by several other radio interferometers with increased baseline lengths. These developments led to the concept of *aperture synthesis* - an art of synthesizing a large telescope using small movable telescopes.

The next major step was the invention of the *intensity interferometer*, first in radio (Hanbury Brown and Twiss, 1954; Jennison and Das Gupta, 1953; 1956) and then in optical (Hanbury Brown and Twiss, 1957) wave bands. An intensity interferometer measures the correlation of fluctuations in the intensity received by two separated telescopes. This is a measure of the modulus of the complex degree of coherence. Tolerance in the mechanical precision and immunity to the atmospheric scintillations are some of the remarkable properties of such an interferometer.

Another breakthrough in the high resolution imaging was the invention of *speckle interferometry* (Labeyrie, 1970). Labeyrie showed that diffraction-limited resolution of celestial objects can be achieved by appropriately averaging sequences of photographs obtained with an exposure time of a few milli-seconds.

Advancement in the technology enabled the practical implementation of *Active and Adaptive Optics* systems in 1980s, though the concept itself was introduced many years ago (Babcock, 1953). These systems compensate for the adverse effect of the Earth's atmosphere on the images in real time. Recent developments (Ellerbroek and Rigaut, 2000; Ragazzoni, Marchetti and Valente, 2000; Beckers, 1989) have demonstrated the capability of these systems to break the barrier of "limited angle imaging".

Space telescopes, like the Hubble Space Telescope (HST) (Peterson and Brandt, 1995; <http://www.stsci.edu/hst/>) and the Solar and Heliospheric Observatory (SOHO) (Fleck, Domingo and Poland, 1995; <http://sohowww.nascom.nasa.gov/>), symbolise another landmark in achieving high resolution.

In recent years, the concept of *interferometric imaging* has gained attention and a number of optical interferometers, both with single and multiple apertures are being built (Armstrong *et al.*, 1995; <http://www.eso.org/projects/vlti>). In a single aperture interferometer, the entrance pupil (or its geometrical image) of the telescope is covered with a mask containing several sub-apertures (Baldwin *et al.*, 1986; Haniff *et al.*, 1987). Each of the sub-apertures can be envisaged as a small telescope. In a multi-aperture interferometer, the light from different small telescopes is combined to make a 'picture' with greater detail.

Another remarkable attempt in achieving high resolution has been the development of the *image restoration schemes*. These schemes ensure high spatial resolution by suitably compensating for the deleterious effects of the turbulent atmosphere on the recorded images. While the deconvolution techniques like Maximum Entropy Method (Frieden, 1972; Ponsonby, 1973; Ables, 1974), CLEAN (Högborn, 1974) and the phase restoration schemes like 'closure phase' (Jennison, 1958) supplement the technological developments in radio interferometry, phase restoration schemes like Knox-Thompson algorithm (1974), Triple-correlation or Bispectrum technique (Weigelt, 1977) supplement the speckle interferometry. Some of the techniques of radio interferometry, for example, the Very Long Baseline Interferometry (VLBI), are being used in optical imaging, too. In recent years, techniques like the *Phase-Diversity* (Gonsalves and Childlaw, 1979; Gonsalves 1982; Paxman and Fienup, 1988) and *Phase-Diversity Speckle imaging* (Seldin and Paxman, 1994; Löfdahl and Scharmer, 1994; Paxman *et al.*, 1996; Paxman, Seldin and Keller, 1999) have been studied and implemented for obtaining high resolution images of extended objects like the Sun.

1.2 Atmospheric Turbulence and Seeing

The Earth's atmosphere is an highly turbulent medium. Heating of the Earth's surface by the solar radiation causes turbulent air motions in the atmosphere. According to the Kolmogorov's theory of fluid turbulence (Kolmogorov, 1941), when the kinetic energy of the air motions at a given length-scale is much larger than the energy dissipated as heat by viscosity of the air at the same scale - a condition indicative of fully developed turbulence - the kinetic energy of large scale motions would be transferred into smaller and smaller scale motions; motions at small scales would be statistically isotropic; at the smallest scales, viscous dissipation would dominate the break-up process.

During day time, large warm packets of air closer to the ground move up due to buoyancy and initiate convection, causing turbulence near the ground (typically, up to one km height from the surface, depending on local orography and strength of the wind). They dissipate their kinetic energy continuously and randomly into smaller and smaller packets of air, each having a unique temperature. These packets are often called *turbulent eddies*. Convection changes with insolation and disappears during night time. However, horizontal circulation of air starts. An important property of the turbulent eddies is that they exist in a variety of length-scales and their distribution is random. There exists an upper limit, L_0 , decided by the process that generates the turbulence and a lower limit, l_0 , decided by the size at which viscous dissipation overtakes the break-up process. Within these limits (often called the 'inertial range'), the energy of an eddy is proportional to the $5/3$ power of its linear size (Kolmogorov, 1941).

Turbulent air motions cause fluctuations (variations) in the density, pressure, temperature and humidity of the air from one point to another. While the local temperature fluctuations (variations) of the air could be of the order of a few hundredth of a degree throughout the atmosphere, fluctuations of a few tenths of a degree or more are typical in the lowest layer of the atmosphere. As the refractive index of the air is highly sensitive to the temperature fluctuations, it varies randomly from one point to

another. Fluctuations in the refractive index induce random optical path lengths to the rays that are normal to the wave-front arriving at the atmosphere from a distant star. Consequently, when the wave-front reaches the entrance pupil of a ground based telescope, it becomes already corrupted in the sense that the surface of constant phase is no longer planar; it has an overall tilt and small scale corrugations on top of it. The r.m.s value of the phase perturbations increases with the size of the wave-front.

The perturbations in the wave-front produce effects similar to optical aberrations in the telescope and thus degrade the image quality. When a very small aperture is used, a small portion of the wave-front is intercepted and the phase of the wave-front is uniform over the aperture. If the amplitudes of the small scale corrugations of the wave-front are much smaller than the wavelength of light, the instantaneous image of a star is sharp and resembles the classical diffraction pattern. But as the wind moves the eddies past the aperture, the tilt of the intercepted wave-front changes. This change in the tilt causes random motion of the star's image at the focal plane. As the aperture size increases, there is a decrease in the sharpness and the amplitude of the motion. When a large aperture is used, the amplitude of the random variation of phase across the intercepted wave-front is larger. This leads to the blurring of the image. The image motion and blurring together are referred to as *atmospheric seeing* or simply *seeing* (Young, 1971; Labeyrie, 1976).

1.3 Importance of Phase

The fact that the phase perturbations in the incident wave-front degrade the image quality can be understood by looking at their relationship with the recorded image. The complex field distribution at the focal (image) plane of a telescope is related to that at the entrance aperture through a Fourier transform relation. The intensity image of a point source recorded at the image plane is the spatial power spectrum (modulus squared Fourier transform) of the complex field distribution at the entrance

aperture. By the autocorrelation theorem (also known as Wiener-Khinchin theorem; see Bracewell, 1986), the inverse Fourier transform of the intensity image is then equivalent to the autocorrelation of the complex field distribution at the entrance aperture. Thus, the presence of any degradation in the phase of the wave-front at the aperture plane would mean degradation of the phases of the autocorrelation function or in the phases of the Fourier transform of the recorded image. We know, from the theory of signal processing, that in the Fourier representation of a signal, phase plays a crucial role of preserving the positional information or the structural details (Oppenheim and Lim, 1981).

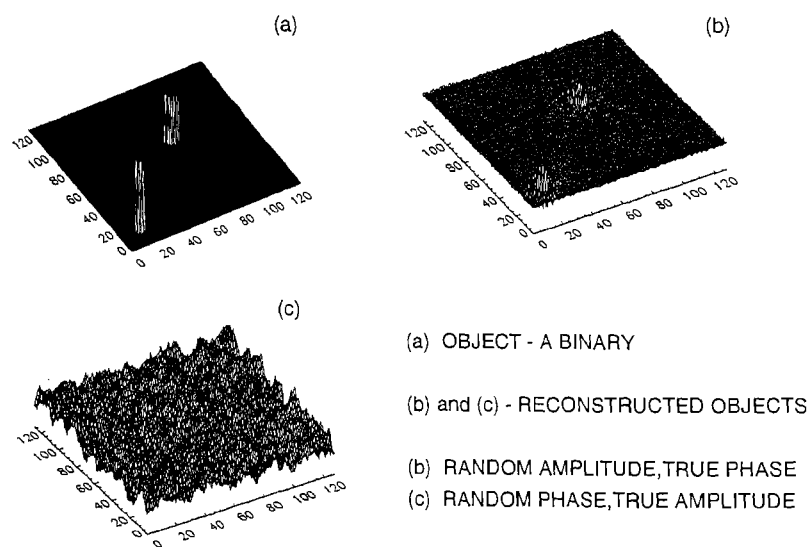


Figure 1.1: (a) Intensity distribution of an ideal binary star. (b) Reconstructed image with random amplitude and true phase. (c) Reconstructed image with random phase and true amplitude.

To highlight this point, consider, for example, a simple astronomical object - a binary star as shown in Figure 1.1 (a). This is an image that would be obtained under ideal conditions. A degraded image can be obtained from this image by corrupting

its Fourier amplitudes and phases and then performing an inverse Fourier transform. Figure 1.1 (b) shows one such image, in which the Fourier amplitudes of the objects have been replaced with random numbers and the Fourier phases have been retained without any modification. Figure 1.1 (c) shows another image, in which the Fourier amplitudes have been retained intact and the Fourier phases have been replaced with random numbers. It should be mentioned that while introducing the modifications, energy conservation should be maintained by multiplying the corrupted quantities with suitable constants. It is clear that when the amplitudes alone are corrupted, the binary nature in the image is recognisable, whereas, when the phases alone are corrupted, the image becomes totally un-recognisable. Thus, the Fourier phase of an image is a very important quantity to identify the structures in it. Thus, the path delay perturbations induced by the atmosphere on the plane wave-front corrupt the phases of the Fourier transform of the image which, in turn, severely degrade the recorded images.

1.4 Resolution and Fried's Parameter

The definition for the angular resolution of an astronomical telescope is based on its ability to separate the images of the two stars of a binary system. In general, for any instrument, a limit, known as Rayleigh's limit, is used to define its resolution. When applied to an optical telescope, this limit implies that in order to declare that the telescope has resolved the two stars, the principal maximum of the diffraction pattern due to one of the stars should fall on the first minimum of the diffraction pattern due to the other star. In the case of a single star, the radius of the first dark ring in the diffraction pattern (Airy pattern) defines the minimum angular separation in the object that can be imaged separately. Quantitatively, the resolution of a telescope with circular aperture of diameter D can be expressed as 1.22 times the ratio of the

observing wavelength to the diameter.

$$\Delta\theta = 1.22\lambda/D. \quad (1.1)$$

As remarked by Fried (1977), the Rayleigh resolution is not an absolute bound and several authors have attempted to develop a more quantitative understanding of what is meant by resolution. For example, Harris (1964) has shown that two point objects separated by less than the Rayleigh limit can be resolved if the signal-to-noise ratio is sufficiently high. Fried himself devised a scale known as resolution scale (Fried, 1977) and prescribed a method to estimate the same from the Optical Transfer Function (OTF) of the system.

In this thesis, we consider the most generally accepted definition of the resolution, namely, the Rayleigh definition. In the presence of atmospheric turbulence, the resolution is drastically impaired. For example, for a 2 m telescope, the theoretical resolution at 5000 Å is about one sixteenth of an arc second. In the presence of atmospheric turbulence, the available resolution is approximately an arc second, thus the resolution is 16 times poorer than that possible theoretically. Surprisingly, as the size of the aperture increases further, there is practically no improvement in the resolution.

For ground based telescopes, it is customary to consider the combination of the turbulent atmosphere in the propagation path and the image forming lens as an image-forming optical system and define the resolution as the integral over the spatial frequencies of the ensemble averaged Modulation Transfer Function (MTF) of the system (Fried, 1966).

$$\mathcal{R} = \int \langle \tau(\mathbf{f}) \rangle d\mathbf{f} \quad (1.2)$$

This is similar to the Strehl ratio, defined as the ratio of the observed intensity image of the star to the maximum possible theoretical intensity. Defining resolution in this way is more generic because it incorporates the effects of exposure times.

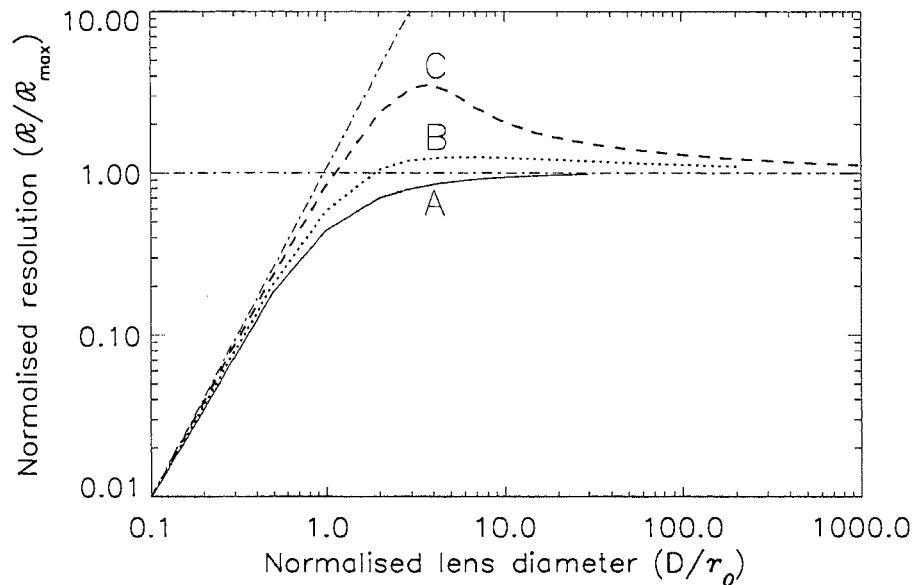


Figure 1.2: Dependence of normalised resolution, $\mathcal{R}/\mathcal{R}_{max}$, on normalised lens diameter, D/r_0 . Solid line (A) - long exposure results, $\mathcal{R}/\mathcal{R}_{max}$. Dotted line (B) - short exposure far field results, $_{ff}\mathcal{R}_0/\mathcal{R}_{max}$, Dashed line (C) - short exposure near field results, $_{nf}\mathcal{R}_0/\mathcal{R}_{max}$, Dash-dot lines indicate asymptotic behaviour ($D/r_0 \rightarrow 0$ and $D/r_0 \rightarrow \infty$); from Fried (1966).

Fried (1966) derived theoretical expressions for average long and short exposure transfer functions based on the statistical theory of the turbulent atmosphere (Rytov approximation; Kolmogorov's hypothesis; see Goodman, 1985; Tatarski, 1961; Tatarski 1968; Brown, 1966, 1967; Fried 1967; Keller, 1969; Ishimaru 1978). Denoting the resolution obtained with long exposure times (typically 1 s) as \mathcal{R}_∞ and that with short exposure times (typically 10 ms) as \mathcal{R}_0 , Fried (1966) showed that significantly better resolution can be obtained with a short exposure than with a long exposure. He also showed that the atmosphere places an upper limit on the resolution that can be obtained with long exposure times. This 'limiting resolution' is given by

$$\mathcal{R}_{max} = \lim_{D \rightarrow \infty} \mathcal{R}_\infty = (\pi/4) (r_0/\lambda R)^2 \quad (1.3)$$

where R is the focal length of the lens forming the image, and r_0 is the diameter of a lens that would give the resolution equal to the \mathcal{R}_{max} in the absence of the atmosphere; r_0 is indeed a crucial parameter in evaluating good observing sites and in determining the quality of the degraded image and is aptly called ‘Fried’s parameter’. There are many ways of interpreting this parameter: it is a characteristic scale of atmospheric turbulence over which the r.m.s. phase fluctuations in the wave-front is 1 radian. A lens of diameter r_0 is capable of achieving a 30% Strehl definition and an angular resolution of the order of λ/r_0 (Fried, 1965); it is the coherent length of the complex amplitude of the perturbed wave-front (Ricort and Aime, 1979); it is the coherence diameter of the atmosphere (Goodman, 1985).

Fried normalised the resolutions obtained with long and short exposure transfer functions by dividing them by the limiting resolution. Figure 1.2 shows the normalised resolution $\mathcal{R}/\mathcal{R}_{max}$ as a function of normalised lens diameter D/r_0 (Fried, 1966). For $D/r_0 \ll 1$, the resolution increases as square of D/r_0 and for $D/r_0 \gg 1$, the resolution reaches an asymptotic value of \mathcal{R}_{max} . The dash-dot lines indicate the asymptotic behaviour. An interesting point to note is that these the two asymptotes intersect at $D = r_0$ and this forms the basis of the definition of r_0 . In conventional imaging, exposure times are more than 1 s (for faint extra-galactic sources, it can be as high as an hour) and thus an image is averaged over several states of the atmosphere, leading to a poorer resolution.

1.5 High Resolution in Solar Physics

High angular resolution has always been necessary for solar observations. The Sun, being the nearest star, is the sole “laboratory” where robust “experiments” can be performed and their results interpreted to understand physical processes that occur in it and in other stars. Though the Sun has been observed now for more than two centuries, it still poses many interesting puzzles. The chaotic granulation, the formation

and evolution of sunspots, pores, umbral dots and penumbral grains are some of the photospheric features that require high resolution observations. At the chromosphere, the structure is dictated by the magnetic field and morphological features like spicules, fibrils, filaments and prominences are of importance. The following is a brief description of some of the problems that forces a solar physicist to look for high angular resolution images.

Granulation: The solar surface observed in white light (either from ground based telescopes at very good sites or from a space telescope) or in a narrow band continuum, outside the active regions, shows a cellular pattern of bright hexagonal structures of about an arc second in size separated by dark lanes. A widely accepted fact is that granules are manifestations of the convective transport of energy from sub-photospheric layers to the photosphere. However, this picture has undergone a vast modification in recent years. While it is believed that large granules are certainly due to convective phenomena, the smaller ones, whose number increases steeply down to the diffraction limit of the modern telescopes, possibly originate from the fragmentation of large ones due to small-scale turbulent flows. Three dimensional numerical models and the high resolution simulations of convection (Stein and Nordlund, 1998) predict scale sizes that are less than the diffraction limit of the existing telescopes.

Thin Flux Tubes: Small (~ 200 km) individual bright patches, observed near the edges of the solar images in white light and near the disk center in certain spectral lines are called *faculae*. The extra brightness of these features has been attributed to the presence of thin flux tubes of high field strength (1 to 2 kG), and small (300-400 km (Stenflo, 1973)) or even smaller cross section (Venkatakrisnan 1986; Solanki *et al.*, 1996). In the quiet region of the photosphere, there is a network (to be distinguished from the classical chromospheric network pattern which is of ~ 30000 km in size) of bright points of size < 0.5 arc sec and co-spatial with the inter-granular lanes. These bright points have been associated with the magnetic fields. Studies of interaction of these bright points with the granules (Roudier *et al.*, 1994) indicate that 15 to 20% of

them elongate, when they are ‘squeezed’ by expanding granules, by a factor of 9 with a simultaneous increase in their brightness by a factor of 1.25 relative to the average photosphere. This is against the predictions of the theoretical models of Knölker and Schüssler (1988), that the magnetic elements larger than 500 km (> 0.7 arc sec) should appear dark. High resolution magnetographic observations indicate that the transition from bright to dark can occur even at smaller scales (300 km, ~ 0.4 arc sec). Muller *et al.*, (1994) suggest that during elongation, some mechanical energy should contribute to the heating process. In a recent observation, using high resolution magnetograms and filtergrams, Muller *et al.*, (2000) showed that the magnetic element present in the network becomes bright and forms a bright point when it is compressed by the surrounding granules as they converge. Obviously, there is further need to increase the angular size, specifically to fix the size and understand the dynamics of the smallest flux tubes.

Micro Structured Magnetic Atmosphere (MISMA): Recently Sánchez Almeida *et al.*, (1996) have inferred from the asymmetry in the Stokes V profile that the photospheric magnetic field contains structures that are finer (of size ~ 1 -20 km) those known so far (Sánchez Almeida, 1998). For the magnetic flux to be conserved in the penumbra, the vertical gradient of the vertical magnetic field has to be perfectly balanced by the horizontal gradients of the horizontal components. While the vertical gradient is evaluated by reproducing the observed asymmetric Stokes profiles, the horizontal gradients are evaluated from the pixel to pixel variation of the measured magnetic fields. It is found that these two independent estimates disagree by up to two orders of magnitude (Sánchez Almeida, 1998). The inconsistency is explained by invoking the concept that there might be unresolved structures within the resolution element and that they might be of opposite polarity so that in a volume average, the net field is underestimated. The best resolution available today is much less than that needed to resolve these micro structures.

Observations of Flares: Sudden intense release of energy from some specific regions,

where there is a (sudden) change in magnetic field is called a solar flare. The change in the magnetic field is usually caused by the emergence of new flux. During a flare, enormous amount of energetic particles are released (electrons with 10 MeV and nucleons with several hundreds of MeV). The mechanism for the onset of a flare is not yet completely understood. Moreover, due to its adverse effect on satellite communication systems, flare prediction is an important issue in space weather forecast. High spatial and temporal resolution is necessary for a detailed study of the evolution of flares. Moreover, statistics of white light flares (Foukal, 1990; Xuan *et al.*, 1998; Sylvester and Sylvester, 2000) and the tiny flares (nanoflares) that could occur at H_α may shed more light on our understanding of both the flaring events and the associated active regions.

Coronal heating: One of the unsolved mysteries in the last six decades is the million degree temperature structure of the solar corona. Recent SOHO/MDI results (Schrijver *et al.*, 1998) have shown the importance of flux cancellation events at small-scales for coronal heating. The observations with Transition Region and Coronal Explorer (TRACE) have shown fine scale magnetic structures at coronal heights (<http://www.lmsal.com/TRACE/POD/TRACEpod.html>). The sizes of these fine structures, when extrapolated to the photosphere would amount to the sizes of a few kilometers. Thus high resolution simultaneous observations of the solar corona and the photosphere may shed light on both the heating mechanisms and their possible origin at the photospheric levels.

1.6 Formulation of the Research Problem

As atmospheric turbulence limits the performance of a ground based telescope, it is quite natural to think of telescopes that can be operated from the space. Several space telescopes have already been launched and the amount of information obtained from them is really remarkable. However, space telescopes have associated problems: weight and volume constraints prevent even medium sized telescopes; telemetry bot-

tlenecks prevent fine sampling; back-end instruments do not get updated in tune with the advancement in state-of-art technology; the lifetime is less and cost high; Pre-determined, fixed, observing schedules prohibit unforeseen, quick investigations (<http://www.sunspot.noao.edu>; <http://www.uso.ernet.in>). In order to avoid all these problems, one is forced to develop ground-based techniques that are immune to the atmospheric turbulence.

Several methods have been invented and used to obtain diffraction limited images from the ground. In this thesis, we have tried to develop techniques that will help us obtain high resolution images of small scale solar features. The aim is to understand the technical details of high resolution imaging systems and provide a platform that will help us in obtaining high resolution images on a regular basis.

We start with the simplest and well established technique, namely the speckle imaging. We wish to develop our own hardware and software facilities for obtaining and analysing the data respectively. In the course of the development of the technique, we try to address some of the technical problems. One of the major problems in speckle imaging is the calibration of the Fourier amplitudes. Knowledge of Fried's parameter is essential for calibrating the Fourier amplitudes in solar speckle imaging. We explore a few methods to obtain reliable values of Fried's parameter and their applicability to different real data sets.

Then we move on to another high resolution technique - interferometric imaging. Here again, the aim is to understand the technical details and develop the required facilities. We also try to establish a tool that will help us in simulating the real data as closely as possible, and use it to improve our understanding of the techniques.

It may be in order to state the reason for studying these two techniques alone in this thesis. Labeyrie's Speckle Interferometry is one of the greatest and marvelous achievements of modern high resolution imaging techniques. Speckle Imaging has been well established for single apertures. The results are comparatively insensitive to telescope figuring errors, provided the atmosphere introduces worse aberrations (Bates, 1982).

Even anisoplanatism is not a serious problem, at least in the stellar imaging, as partial lack of isoplanatism merely reduces the contrast. It needs relatively simpler software and hardware facilities than the other (Phase Diversity and Phase Diversity Speckle Imaging, Adaptive Optics) techniques and thus can form the first step towards the development of ground based high resolution imaging facilities.

The lesson learnt from radio interferometry shows that ultrahigh resolution can be obtained from only an optical analog of Very Long Baseline Interferometry. A simple optical interferometric imaging system can be obtained by replacing the aperture of a single telescope with a non-redundant mask. Radio interferometric methods can be used to reconstruct the images. The absence of certain spatial frequency information can lead to the loss in the dynamic range in the reconstructed images - more so for extended sources like the Sun. An array of telescopes can be cleverly chosen with an optimum value of diameter and the separation between the telescopes so as to record information at all the spatial frequencies of an equivalent monolithic telescope. The bispectrum technique can then be extended to process speckle interferograms (Pehlemann, E. and von der Lühe, 1989, Reinheimer and Weigelt, 1987).

Chapter 2

Estimation of Fried's Parameter for the Speckle Data

In general, the transfer function of an instantaneous image is an inseparable combination of the transfer function of the atmosphere and that of the telescope (Ricort and Aime, 1979). However, in the case of a long exposure image, the transfer function can be written as the product of the transfer function of the atmosphere and that of the telescope (Rodier, 1981). Hence, *if r_0 is known*, a long exposure image can be deconvolved (using the theoretical expression for the long exposure transfer function and linear filters like optimal and Wiener filtering; see Press *et al.*, 1993; Gonzalez and Wintz, 1977) and the resulting image can be subjected to scientific study.

As the degradation produced by the atmosphere varies both with space (direction) and time, in stellar speckle interferometry the PSF is usually obtained by observing a point object in the direction close to the extended object, immediately before or after recording its image. An ensemble average of the power spectrum of the PSF (known as Speckle Transfer Function (STF)) is estimated from the recorded data and then used to compensate for the attenuation of the Fourier amplitudes of the object. Due to ubiquitous solar light, it is impractical to locate a point object in the sky during day-time

observations. Consequently, in solar speckle interferometry, the Fourier amplitudes of the object are compensated using a theoretical transfer function, derived first by Korff (1973). *Again, knowledge of r_0 is essential to estimate the theoretical STF.*

Several methods have been reported in the literature for estimating this parameter from solar images (Brandt, 1969, 1970; Aime *et al.*, 1978; Roddier, 1981; von der L uhe, 1984a; Seykora, 1993). We briefly describe three of these methods in Section 2.1. In Section 2.2, we present the details of our speckle data. In Section 2.3, we describe the various preprocessing methods. In the last section, we present the details of the estimation of r_0 using one of the aforementioned methods depending upon the nature of our speckle data.

2.1 Methods for Estimation of r_0

2.1.1 From Angle-of-arrival Fluctuations

Fried (1965) expanded the phase of the wave-front over a circular aperture (for example, at the entrance pupil of a telescope) in terms of a series of orthonormal polynomials, each representing a specific geometrical shape and found that the coefficient of the linear term is much larger than that of the spherical and quadratic terms for a given r_0 and diameter D of a telescope. He concluded that the random tilting of the wave-front is the major distortion. The random tilting of the wave-front from its average position causes fluctuations in the angle-of-arrival of the light rays (assumed to be normal to the surface of the wave-front). If β_x and β_y denote the fluctuations in the angle-of-arrival in x and y directions respectively, then the resultant fluctuation $\langle \beta^2 \rangle$ is given by (Fried, 1975)

$$\langle \beta^2 \rangle \equiv \langle \beta_x^2 \rangle + \langle \beta_y^2 \rangle = 0.357\lambda^2 r_0^{-5/3} D^{-1/3}. \quad (2.1)$$

From Equation 2.1, it is clear that:

1. For a given r_0 (i.e. for given seeing conditions), the mean square fluctuation in the angle-of-arrival of the light rays decreases as the diameter of the telescope increases; that is, for large telescopes, fluctuations are negligible.
2. For a given D , the mean square fluctuation in the angle-of-arrival of the light rays decreases as r_0 increases; i.e., the image motion is small when the seeing is good.

The fluctuations in the angle-of-arrival of the light rays cause image motion at the focal plane of a telescope. The image of a point source obtained using small and medium sized telescopes moves randomly in the focal plane and the magnitude of the displacement depends on the seeing conditions. By carefully measuring the random displacement of the centroid of the image, the mean square fluctuation in the angle-of-arrival and r_0 can be estimated (Equation 2.1).

Error estimation: The error $\delta\beta$ in the measurement of β is approximately equal to the error $\delta\theta$ in the measurement of the displacement. The error δr_0 in the estimation of r_0 is given by $\delta r_0 = 1.2 r_0 \delta\theta/\beta$. Thus, δr_0 is directly proportional to the error or accuracy in the measurement of the displacement. In order to achieve higher accuracy in the measurement of the displacements, higher spatial sampling is necessary.

Application to Images of Extended Sources: When applied to images of extended sources, it is found that only high frequency components of the image contribute substantially to the image motion. This can be proved in the following way: The fluctuation in the angle-of-arrival can be evaluated using an equation of the form

$$\begin{aligned} \langle (a_L)^2 \rangle &= (\pi D^2/4)(\Delta_C - \Delta_L) \\ &= (\pi D^2/4) \frac{1}{R^2} \int_0^D r dr \left[\mathcal{F}_C(r, D) - \mathcal{F}_L(r, D) \right] \mathcal{D}(r), \end{aligned} \quad (2.2)$$

where the symbols have same meaning as in Fried's paper (1965), except that the Gothic font style of the symbols have been replaced by Calligraphic font style. Substituting

the functions from Equations. (5.6a) and (5.6b) of that paper, we obtain

$$\left\langle (a_L)^2 \right\rangle = \int_0^D \mathcal{F}(r) dr = 0.883(\pi D^2/4) / (r_0/D)^{5/3} \equiv A(D, r_0), \quad (\text{say}). \quad (2.3)$$

Separating the integral representing $\left\langle (a_L)^2 \right\rangle$ into two parts, first with limits 0 to $D/2$ and the second with limits $D/2$ to D , we find

$$\begin{aligned} \left\langle (a_L)^2 \right\rangle &= \int_0^{D/2} \mathcal{F}(r) dr + \int_{D/2}^D \mathcal{F}(r) dr \\ &= A(D/2, r_0) + \left[A(D, r_0) - A(D/2, r_0) \right] \\ &= A(D, r_0) / 2^{11/3} + A(D, r_0)(2^{11/3} - 1) / 2^{11/3}. \end{aligned} \quad (2.4)$$

The ratio of the second part to the first part of the this equation is ≈ 11.699 . *Calling the spatial frequency components less than $D/2\lambda$ as 'low' spatial frequency components and the rest as 'high' spatial frequency components, we conclude that 'high' frequency components contribute more to the image motion than the 'low' frequency components.*

The relative shift of an image with respect to a reference image can be estimated using a cross-correlation technique (von der Lühe, 1983) in terms of pixel/sub-pixel units and the variance can be estimated in arc seconds. The cross-correlation is highly sensitive to the low frequency components. This is due to the fact that the strength of the low frequency components is higher than that of the high frequency components in the Fourier domain. Thus image motion estimated using cross-correlation technique would mainly be determined by low frequency components. As the contribution of the low frequency components to the image motion is relatively small, any attempt to estimate the image r.m.s. motion (using cross-correlation technique) without removing low frequency components, would lead to a small value for the variance and consequently a large value for r_0 . The low frequency components can be removed either by fitting and subtracting a surface of the form $B(x, y) = a_0 + a_1 \cdot x + a_2 \cdot y + a_3 \cdot xy$ from the image or by a Fourier high-pass filter. It should be noted that Smithson and Tarbell (1977) and von der Lühe (1983) have pointed out the need for subtracting a bi-linear fit from the data to avoid the shift in the peak of the auto-correlation function due

to the presence of linear trends. We find that such a procedure always essential while estimating r_0 from the image motion.

Limitations of the method: Since the variance of the image motion reduces drastically with increase in the size of the aperture, it becomes difficult to estimate it accurately. Moreover, blurring becomes a major component of the seeing for large apertures. Thus estimating the Fried's parameter using image motion may not be suitable for relatively large ($D \gg r_0$) telescopes. However, it can be used while observing with small and medium size telescopes.

This method demands high spatial sampling. For example, to estimate r_0 with an accuracy of 10%, given $r_0 = 5$ cm, $\lambda = 6563$ Å, and $D = 30$ cm, image motion has to be measured with an accuracy of 0.1 arc sec. The accuracy is limited by the spatial sampling of the image. The accuracy can be improved by a factor of two using an interpolation algorithm (Niblack, 1986) for determining the peak of the cross-correlation function. This would imply that the sampling must be approximately 3 pixels per diffraction limit. For $D = 0.15$ with other parameters the same as given above and again assuming an accuracy of half-a-pixel, the spatial sampling needed would be nearly 5 pixels per diffraction limit. For small telescopes, this would mean magnification of the image at least by a factor of 3. When filters with bandwidths of 0.5 to 1 Å are used, the light level would be decreased drastically.

The motion of the image at the focal plane is equivalent to the change in the tilt of the isophase surface of the wave-front at the aperture plane. The change in the tilt occurs within a duration of a few milliseconds (typically 10 ms). To measure the consecutive positions of the image exactly, the exposure time for each of the recorded image of a sequence should be less than or of the order of 10 ms. Thus, for faint stars, light level becomes a serious problem. Moreover, the seeing conditions do not remain constant for a long time and a large number of frames have to be recorded in a short (\sim one minute for solar observations (von der Lühe, 1993)) duration to achieve

statistically significant results. Thus, *the need for short exposure times to freeze the atmosphere and the the need for high frame rate are some of the constraints on this method.*

It has been mentioned in the literature that one of the major drawbacks of this method is that the image motion due to the atmosphere cannot be distinguished from that due to improper tracking and vibrations of the telescope. In other words, this method is highly susceptible to tracking errors and can lead to incorrect estimation of the image motion due to the atmosphere. However, by spectral decomposition of the image motion, as seen above, one can indeed distinguish between the two. An alternate scheme that is insensitive to the tracking errors, popularly known as DIMM, has been developed by Fried (1975) and others (Sarazin and Roddier, 1990). It consists of two small apertures mounted on a single tracking system, separated by some distance. r_0 is estimated from the mean square value of the difference in the angle-of-arrival fluctuations.

2.1.2 Power Spectrum Equalisation Method

In this method (Castleman, K. R., 1979; Stockham *et al.*, 1975; Huang *et al.*, 1971; Andrews and Hunt, 1977), first the degraded image is segmented into square regions that are large compared to the extent of the degrading point spread function. For each segment, the power spectrum is estimated and the logarithm of power spectra are added together and an average (i.e., geometric mean) power spectrum is obtained. If the scene under consideration is complex enough, the signal components tend to average out in the log power spectrum. The degrading transfer function does not get averaged out as it is constant throughout the region (as long as the region is smaller than an isoplanatic patch). In the absence of noise, the average power spectrum, approximately converges to the logarithm of the squared magnitude of the degrading transfer function. An important assumption in this method is that the object and

the noise power spectrum are stationary. Though the atmospheric turbulence is not strictly stationary, it is believed to be locally homogeneous and isotropic and hence this method can be applied to long-exposure images.

Implementation of the method: We implemented the following procedure to obtain the Full Width at Half Maximum (FWHM) of the degrading PSF from a single long exposure image.

- Step 1 : Divide the image into a number of segments, each of half the size of the original segment.
- Step 2 : Multiply the segments by a 100% Hanning window. This is basically to reduce the 'leakage error' (Bracewell, 1986).
- Step 3 : Estimate the power spectrum of these segments.
- Step 4 : Estimate the noise as the standard deviation of the power spectrum values of those pixels, that are beyond the diffraction limit.
- Step 5 : Subtract the estimated noise from the power spectrum. Replace any small negative values of the order of 10^{-5} by zeros.
- Step 6 : Find the average log power spectrum of all the segments.
- Step 7 : Find the square-root of the average (ie., geometric mean) power spectrum of the images and divide it by the telescopes transfer function.
- Step 8 : Find the inverse Fourier transform of the resulting function to obtain the PSF.
- Step 9 : Fit 1-D Gaussian to the cross-sections of the PSF (along x and y directions) and estimate the FWHM. The average value of the FWHM is converted into radians and then r_0 is estimated as λ/FWHM

Error Estimation: If $\delta\theta$ is the error in the estimation of the FWHM corresponding to an error of δr_0 in r_0 , then the error δr_0 in the estimation of r_0 is $\delta r_0 = r_0^2 \delta\theta / \lambda = r_0 \delta\theta / (\lambda / r_0)$. $\delta\theta$ is decided by the spatial sampling in the image. Again, we find that high spatial sampling reduces the error involved in the determination of r_0 . However, for a given spatial sampling, error will be less for bad seeing conditions. In other words, higher the r_0 , higher will be the error, for a given spatial sampling.

2.1.3 Spectral Ratio Method

In this method (von der Lühe, 1984a), the ratio ϵ of the squared modulus of the average Fourier transform of an image to the ensemble average of its modulus squared Fourier transform is used as a diagnostic of the seeing conditions at the time of observations. It is called ‘spectral ratio’ and is a function of the telescope and the seeing conditions alone. If the object under consideration contains structures beyond $\mathbf{q} = \alpha$, where $\mathbf{q} \equiv \mathbf{f}/(D/\lambda)$ is the normalised spatial frequency, \mathbf{f} is the spatial frequency and $\alpha \equiv r_0/D$ is the modified Fried’s parameter, then ϵ steeply decreases beyond this limit. When the ensemble average of ϵ is expressed as a function of α and \mathbf{q} , isocontour lines satisfy the relation,

$$\alpha = A \cdot q^B, \quad \forall \alpha \leq 0.3 \quad (2.5)$$

where A and B are constants. While applying this method to real data, first the theoretical value of the spectral ratio is estimated and constants A and B are determined for various values of ϵ . A log-log plot of $E(\epsilon(\mathbf{q}))$ vs. \mathbf{q} is then obtained for the observed data and the ratio obtained from theoretical models is overplotted. The normalised frequency \mathbf{q} at which the slopes of the theoretical and observed spectral ratios match closely is determined and the corresponding spectral ratio is identified. Then the constants A and B corresponding to the identified spectral ratio are inserted in Equation 2.5 and α and r_0 are determined. The following two conditions should be met for the successful application of this method: (1) The total duration of observation

should be short enough to justify ergodicity hypothesis, (2) The total number of images recorded should be large enough to ensure that the arithmetic average is equal to the ensemble average.

Error Estimation: If δA , δB and $\delta \mathbf{q}$ are the errors in the measurement of A , B and \mathbf{q} respectively, then the most probable error δr_0 (Bevington and Robinson, 1992) in the measurement of r_0 is $\delta r_0 = r_0 [(\delta A/A)^2 + (\delta \mathbf{q}/\mathbf{q})^2 + (\delta B \log \mathbf{q})^2]^{1/2}$. Thus, the accuracy of the result depends on the accuracy of the measurements of $A(\epsilon)$ and $B(\epsilon)$, \mathbf{q} and $|\mathbf{q}|$. $\delta \mathbf{q}$ can be assumed to be equal to the smallest spacing in the Fourier domain expressed in normalised spatial frequency units. If we assume that A and B are measured with high accuracy such that $\delta A = 0$ and $\delta B = 0$, then the percentage error in r_0 is proportional to the percentage error in \mathbf{q} . As $|\mathbf{q}|$ is limited to the range 0.2 to 0.3 (von der Lühe, 1984a), the accuracy of the estimation increases when $|\delta \mathbf{q}|$ is small. In other words, better accuracy can be obtained when this method is used for large ($D \gg r_0$). Even when δB is non-zero, error in r_0 is less when $|\mathbf{q}|$ is small as implied by the third term in $(\delta r_0)^2$. Unlike the methods described earlier, this method does not demand very high spatial sampling.

2.2 Data

Kodaikanal Observatory Data: Speckle and interferometric imaging observations were performed on 2nd, 3rd and 4th August 1998 between 1 and 5:30 UT, with the 38 cm tunnel telescope of the Kodaikanal Observatory (KO) (Bappu, 1967) using a re-imaging unit shown in Figure 2.1. The pupil plane was re-imaged using a 300 mm $f/5$ collimator. A 5 mm aperture and a filter with 160 Å bandpass, centered at 6520 Å, were placed in the diverging beam close to the collimator. A non-redundant mask (NRM, Figure 2.2) containing seven identical holes, each of diameter 300 micron was placed in the collimated beam. 1 mm on the mask plane corresponded to 12 mm on

the original pupil plane. The collimated beam was focused on to the EEVTM camera P46582 consisting of 578 by 576 pixels of size 15 by 22.5 micron. The images were acquired using a DT2861 frame grabber card which also re-sampled each row of the image into 512 pixels. Only the central 128 by 64 pixels were activated using the hardware windowing capability of the frame grabber card and used to record the image of a pinhole of 1.5 mm diameter. This resulted in a circular field-of-view of about 8.25 arc sec in size, with 0.0931 arc sec per pixel along a row and 0.12375 arc sec per pixel along a column. The theoretical resolution limit of the telescope is 0.43 arc sec at 6520 Å. Several sets of images of a few sunspots and pores were recorded. Each set

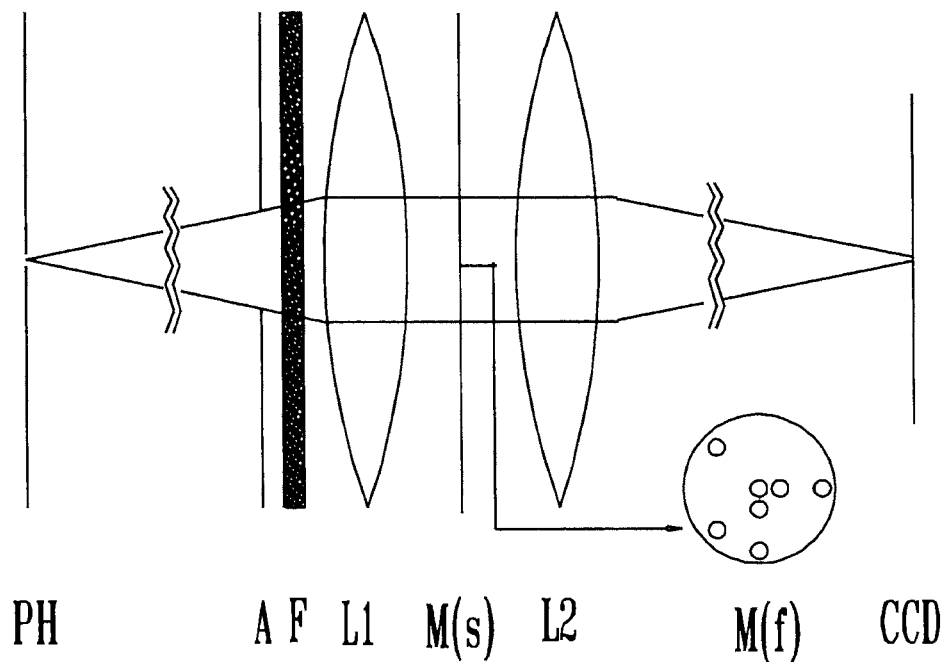


Figure 2.1: The Re-imaging unit consists of: pinhole PH , which selects a portion of the Sun's image; Aperture A of 5 mm diameter; H_{α} filter F ; Collimating lens $L1$; side view of the mask $M(s)$; face on view of the mask $M(f)$; camera lens $L2$; Charge Coupled Device (CCD).

consisted of four sequences separated by about 17 s. After the first two sequences, the mask was removed facilitating speckle imaging of the same region for the remaining two

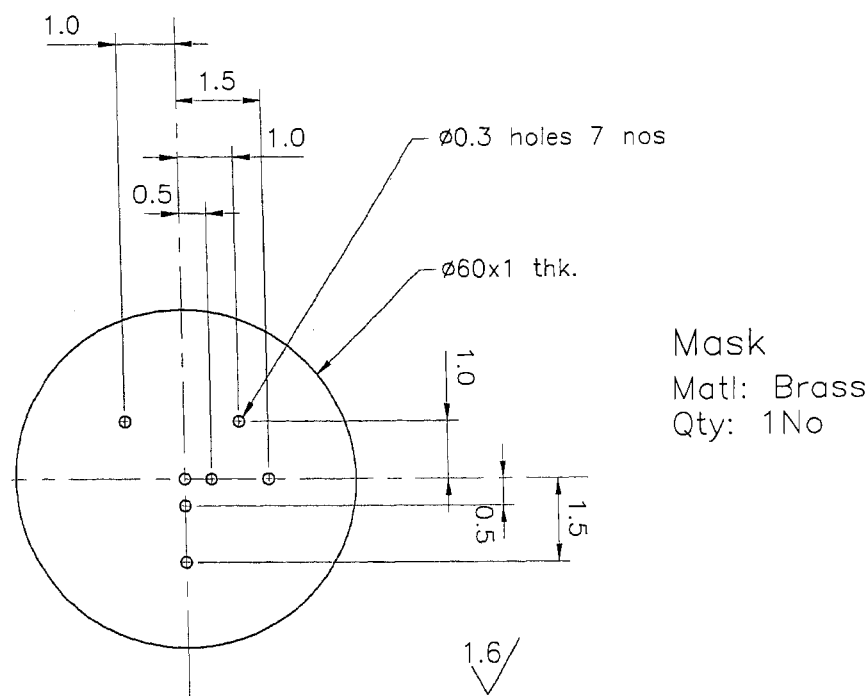


Figure 2.2: Mask configuration.

sequences. Each subset consisted of sixteen frames (the maximum number of buffers available in the frame grabber card) with an exposure time of 9 ms and 1 ms each for interferometric and speckle imaging respectively. The interval between the consecutive frames in a subset was about 88 ms. The observations were accompanied by regular dark-current and flat-field (defocused quiet regions) images.

Uttar Pradesh State Observatory Data: Four sequences of images of an isolated sunspot and three sequences of images of a spot pair were recorded on on 2nd June 1999 between 1:17 and 3:20 UT with the 15 cm Coude telescope of Uttar Pradesh State Observatory (Verma, 1999). The primary image was magnified using a Barlow lens. A Halle- H_{α} filter with 0.5 \AA bandwidth was placed near the focus. A 12 bit EEV37 camera consisting of 512 by 512 pixels of size 15 micron, cooled by a liquid circulatory unit,

was used to record 1000 frames per sequence at the rate of ~ 40 frames per second with an exposure time of 7 ms per frame. The recorded field-of-view was 65 by 65 arc sec in size with 0.65 arc sec per pixel. Five dark current and 100 flat-field (twilight sky) frames were recorded. The theoretical resolution limit of the telescope is 1.1 arc sec at 6563 Å.

Udaipur Solar Observatory Data: Sixteen sequences of images of a sub-flare region and twenty eight sequences of images of another sub-flare region, both belonging to the NOAA AR8898 were recorded on 9th March 2000 between 5:30 and 7:00 UT with the 13.5 cm Coude telescope of Udaipur Solar Observatory (Ambasta, 1999). The selected region of the primary image was re-imaged using a combination of two lenses. A Halle- H_{α} filter with 1 Å bandwidth was placed between the two lenses. The 8 bit Photometric CCD camera consisting of 768 by 493 pixels of size 11 by 13 micron was used to record 100 frames per sequence at the rate of 1.2 frames per second with an exposure time of 20 ms per frame. The recorded field-of-view was 57.6 by 67.8 arc sec with 0.45 arc sec per pixel along a row and 0.53 arc sec per pixel along a column. The theoretical resolution limit of the telescope is 1.22 arc sec at 6563 Å.

2.3 Pre-processing

Dark and Flat-field Corrections: Average dark and flat-field images are obtained from the recorded series of dark and flat-field images. The images of the object are corrected using the standard procedure (McLean, 1989). When the flat-field images contain artifacts due to dust specks, the procedure described by von der Lühe (1993) is adopted to minimise their effect. However, it should be noted that Equation 4 of that paper is erroneous and should be modified to

$$\bar{f}(x) = \frac{a(x)}{\bar{a}(x)}[f(x) - d(x)] + d(x) \quad (2.6)$$

where the symbols have the same meaning as mentioned in that paper.

Registration: In general, a sequence of images obtained from a ground based telescope will have motion due to atmosphere as well as imperfect tracking. While the former has relatively higher contribution from high spatial frequency components (Sec 2.1.1, Page 17, 19) the latter has uniform contribution from low and high frequency components and is coherent over the entire field-of-view. The images of the sequence can be aligned using cross-correlation technique (von der Lühe, 1983). When used to align the images that contain a large number of isoplanatic patches, this technique would detect only the coherent motion of the entire-field of view. This fact is used to align the images to account for tracking errors alone. To detect the image motion due to atmosphere, the images have to be segmented into several isoplanatic patches and a bi-linear least square surface has to be subtracted from each of segments. The cross-correlation gives the amount of shift needed to align a given image with a reference image with pixel accuracy. However, the accuracy can be improved by a factor of two using an interpolation method (Niblack, 1986). The necessary shifts are incorporated by multiplying the Fourier transform of the image by a phase factor $\exp(2\pi j(k_x x/m + k_y y/n))$, where m and n are the number of pixels along a row and column of the image respectively and x and y are the required shifts in the corresponding directions. Functions `f_ccorr.pro` and `sushift.pro` written in IDL for these purposes have been included in Appendix:A.

De-stretching: When the field-of-view of the recorded image is much larger than the size of the isoplanatic patch, different portions of the image move differently and hence the image gets distorted. The process of removing the effects of anisoplanatic image motions from a time series of images is called *de-stretching* (November, 1986; Topka, Tarbell and Title, 1986). For de-stretching our images, we used the software package developed by the scientific staff of Sacramento Peak Observatory. The package was provided by Prof. Steve Keil (Keil, 2000) of the observatory.

Frame Selection: Most often it is convenient to select the best images from a series of images for further analysis (reference image in de-stretching, for example). A few bad images of a series of images recorded during moderate seeing conditions can significantly alter the gain obtained from a few best images. We characterised each image by its contrast (or sharpness) and identified the image having the highest contrast as the best image of the series. The contrast is estimated as the ratio of the sum of mean square intensity gradient in x and y directions and the mean intensity squared (Scharmer, 2000).

$$C = \sum_{m,n} ((I(m+d, n) - I(m, n))^2 + (I(m, n+d) - I(m, n))^2) / (\bar{I})^2, \quad (2.7)$$

where d can be selected as the number of pixels within the diffraction limit or a pixel more than that.

Frame Segmentation: The step after pre-processing and de-stretching a sequence of images is to divide each image into several overlapping segments that are smaller than the typical size of the isoplanatic patch. We followed the procedure described by von der Lühe (1993). We repeat the segmentation process for all the images of a sequence and form a ‘sub-image sequence’ with the corresponding segments of the sequence. We estimate r_0 for each sub-image sequence.

2.4 Estimation of r_0

2.4.1 KO Data

As mentioned earlier, the frame grabber re-sampled the image along a row. Moreover, the video input supplied by the camera was ac-coupled and dc-restored. Thus, there was no one-to-one correspondence between the pixels in the CCD and the digitised images. Because of these reasons, we could not do meaningful flat-field corrections.

However, while analysing the speckle data, we selected only those small scale features that were away from the location of dust specks in the flat-field images. We used the frame to frame motion of the features as an indicator of their solar origin. We selected rectangular windows, centered at the feature of interest from the recorded images and re-sampled them to have identical plate scale along the rows and columns. We de-stretched the images when the selected field-of-view exceeded 4 arc sec. We estimated r_0 using spectral ratio method for a few data sets. For two sub-sets (consisting of 16 images) of a pore region, (comprising 4 overlapping segments, each of ~ 3 arc sec) the average value was found to be 9 ± 3 cm. For two sub-sets (consisting of 16 images) of a sunspot region, (comprising 4 overlapping segments, each of ~ 3 arc sec) the average value was found to be 7 ± 3 cm. The huge error bars could be due to estimating r_0 from just 16 frames. Moreover, in the absence of flat-field images, noise could not be estimated reliably. In a few cases, the observed spectral ratio was found to be close to unity till the diffraction limit.

2.4.2 UPSO Data

The images of the three sequences of a sunspot and four sequences of a spot pair were pre-processed using the procedure described in the previous section. The registered, rescaled images had 128 pixels in either directions with a field-of-view of 62.4 arc sec square.

Estimation of r_0 from angle-of-arrival fluctuations: The registered images were divided into a number of overlapping segments as explained earlier and r_0 was estimated for each segment, using all the corresponding segments of the sequence of (~ 920) images as explained in Section 2.1.1 (Page 17). A bilinear least square surface was fitted to each segment and subtracted from it before estimating cross-correlation. Three different sizes of the segments were considered, namely 8 by 8 pixels corresponding to

3.9 arc sec square (leading to a total of 961 segments), 16 by 16 pixels corresponding to 7.8 arc sec square (225 segments), and 32 by 32 pixels corresponding to 15.6 arc sec square (49 segments). Tables 2.1, 2.2 and 2.3 show, respectively, the estimated values of r_0 along with error bars for the three different segment sizes for a sequence of the spot pair. It was found that the smaller the segment size, the larger the errors in the estimation. For segments of size 8 by 8 pixels, the average value was 11.7 ± 5.2 cm; for segments of size 16 by 16 pixels, the average value was 5.8 ± 1.5 cm; and for segments of size 32 by 32 pixels, the average value was 8 ± 7 cm. This is understandable, because for smaller segments the number of pixels in a segment are less, the signal-to-noise ratio is poor and hence the correlation breaks down. Fourier transforms may not give correct results when the array size is very small. Also it was found that, for the segment size of 32 by 32 pixels, 17 out of 49 segments (Table 2.3) have relatively large error bars. A more careful inspection revealed that location of these segments correspond either to the edges of the field-of-view or to edges of the sunspot. Errors can occur in the former case because of the change of scene near the edges after registration. In the case of sunspots, errors can occur if the segment does not cover them completely. However, the errors are relatively large for the segments near the edges of the field-of-view. Neglecting these 17 segments while estimating the average gives a value of 3 ± 0.4 cm. For larger segments, anisoplanatic effects may dominate. However this does not appear to be a serious problem, as more than 75% of the estimates have low error bars in this case (the remaining 25% correspond to the edges of the field-of-view or of the sunspots). Thus, the optimum size was found to be 32 pixels; it allows us to estimate r_0 for a majority of the segments with about 25% accuracy.

The procedure was repeated for a few more sequences and the trend was found to be similar. Thus, we concluded that the average value of r_0 for the sequences is 3.7 ± 0.7 cm. The images have been recorded at a fast rate and the time interval between the images is ~ 25 ms. Thus each recorded image corresponds to one particular state of the atmosphere. Therefore, these images are well suited for estimating r_0 from angle-of-

arrival fluctuations. As mentioned in Section 2.1.1, higher sampling would improve the accuracy of the estimated values.

Power-spectrum equalisation method: An average image was obtained by adding all the images of the registered, de-stretched sub-image sequence and r_0 was estimated along with error bars using the procedure explained in the Section 2.1.2. Three different segment sizes were considered. It was found that the spatial variation of r_0 was very less (standard deviation $\sim 10^{-5}$), indicating that r_0 was more or less same for the entire field of view. The error bars were found to be small for the segment size of 32 by 32 pixels. Thus the trend is similar to that obtained from angle of arrival fluctuations - namely, the error is less when r_0 is estimated for a segment of size 32 by 32 pixels. As the size of the image should be larger than the degrading PSF, segments of size 8 by 8 pixels were not considered. For the sequence, for which r_0 values estimated from angle-of-arrival fluctuations have been presented in Tables 2.2 and 2.3, this method gives an average value of 8.5 ± 2.6 cm and 3.12 ± 0.17 cm respectively. The values were similar for the other sequences too. As the error bars are less for segments of 32 by 32 pixels we conclude that the average value of r_0 is 3 ± 0.17 cm for all the observed sequences.

Spectral ratio method: We estimated r_0 using the spectral ratio method for all the registered, de-stretched image sequences. We restricted the analysis to only segments of size 16 by 16 pixels (7.8 arc sec square). For each sequence, the images were divided into 225 overlapping segments and r_0 was estimated for all the segments. For all the sequences, the average value of r_0 was found to be 3.26 ± 0.57 cm.

Table 2.4 shows average values of r_0 estimated using all the three methods for all the sequences.

S	r_0 (cm)	S	r_0 (cm)	S	r_0 (cm)	S	r_0 (cm)	S	r_0 (cm)	S	r_0 (cm)	S	r_0 (cm)	S	r_0 (cm)	S	r_0 (cm)	S	r_0 (cm)	S	r_0 (cm)
1	11.615.1	101	10.424.2	201	11.725.1	301	11.625.1	401	10.514.2	501	11.314.8	601	13.315.5	701	10.013.9	801	12.015.4	901	11.114.7		
2	11.615.0	102	11.625.1	202	10.944.5	302	9.501.5	402	11.414.9	502	14.317.4	602	11.515.0	702	11.915.3	802	11.815.2	902	11.114.7		
3	12.115.5	103	11.515.0	203	12.515.8	303	11.715.1	403	10.714.3	503	11.014.6	603	12.215.6	703	12.315.6	803	13.016.2	903	11.414.9		
4	12.515.8	104	11.014.6	204	11.615.1	304	11.414.9	404	11.414.9	504	10.914.5	604	10.114.3	704	12.915.9	804	11.515.0	904	12.915.9		
5	12.816.1	105	11.815.2	205	12.816.0	305	13.216.4	405	10.714.4	505	9.601.3	605	11.114.6	705	12.816.0	805	12.015.4	905	11.715.1		
6	12.716.0	106	10.914.5	206	11.014.6	306	11.815.2	406	13.116.4	506	12.215.6	606	11.214.8	706	11.515.0	806	11.815.2	906	10.714.4		
7	13.917.3	107	11.214.8	207	11.615.1	307	11.314.8	407	11.114.7	507	12.315.6	607	11.615.0	707	11.114.7	807	11.214.8	907	12.115.5		
8	14.117.2	108	11.314.8	208	10.714.4	308	12.214.7	408	11.114.7	508	12.515.8	608	11.815.2	708	12.415.7	808	12.115.4	908	11.144.7		
9	14.717.8	109	12.716.0	209	12.315.6	309	13.516.7	409	11.715.2	509	10.214.0	609	10.414.2	709	11.114.7	809	12.015.3	909	12.615.0		
10	10.514.2	110	11.815.3	210	11.014.6	310	12.115.4	410	13.616.7	510	10.814.4	610	12.415.7	710	10.914.5	810	13.917.0	910	13.116.4		
11	14.217.3	111	11.144.7	211	12.015.4	311	13.316.5	411	11.214.8	511	11.214.8	611	11.114.7	711	11.615.1	811	14.217.3	911	12.015.4		
12	14.017.1	112	12.015.4	212	11.815.2	312	12.515.8	412	12.215.6	512	11.114.7	612	11.615.1	712	10.414.2	812	11.515.0	912	10.314.1		
13	14.517.6	113	12.615.4	213	12.916.1	313	11.715.1	413	11.214.8	513	10.514.2	613	11.615.1	713	11.715.2	813	12.916.1	913	10.814.4		
14	13.216.4	114	11.314.8	214	12.916.2	314	12.115.4	414	12.415.7	514	12.215.5	614	10.214.0	714	13.716.9	814	11.114.7	914	13.516.7		
15	12.315.6	115	12.015.4	215	12.015.4	315	11.615.1	415	11.014.6	515	14.017.2	615	10.914.5	715	14.217.4	815	11.515.0	915	12.015.4		
16	11.915.3	116	11.214.8	216	13.716.8	316	11.214.7	416	12.215.5	516	12.415.7	616	11.214.8	716	12.315.6	816	12.816.0	916	11.114.7		
17	11.615.0	117	11.515.0	217	12.516.7	317	11.014.6	417	11.014.6	517	10.714.4	617	10.914.5	717	12.615.9	817	12.516.8	917	11.314.8		
18	11.815.2	118	10.114.3	218	11.314.8	318	12.615.9	418	11.915.3	518	9.901.3	618	10.414.2	718	10.414.2	818	12.115.5	918	14.017.2		
19	12.916.2	119	12.115.5	219	12.015.4	319	11.114.6	419	12.015.4	519	9.901.3	619	10.614.3	719	10.814.4	819	10.214.0	919	11.615.0		
20	11.915.3	120	11.815.2	220	11.214.7	320	12.516.8	420	11.214.8	520	9.901.3	620	11.214.8	720	12.415.7	820	10.514.2	920	11.114.7		
21	12.315.6	121	11.915.3	221	12.215.6	321	11.414.9	421	12.115.4	521	13.416.6	621	11.615.0	721	9.901.3	821	11.214.7	921	10.614.3		
22	11.715.1	122	13.016.2	222	12.215.5	322	11.114.7	422	11.515.0	522	10.314.0	622	11.815.2	722	11.814.6	822	11.715.1	922	12.615.9		
23	12.515.8	123	11.214.7	223	12.115.5	323	10.114.3	423	11.414.9	523	13.316.5	623	12.015.4	723	9.901.3	823	11.114.6	923	12.315.6		
24	10.714.4	124	11.214.7	224	10.514.2	324	10.614.3	424	9.901.3	524	10.013.8	624	11.114.7	724	13.816.9	824	9.901.3	924	11.314.8		
25	12.315.6	125	10.914.5	225	12.415.7	325	11.815.2	425	12.015.4	525	11.715.1	625	12.215.6	725	11.515.0	825	10.214.0	925	11.715.1		
26	12.615.9	126	11.414.9	226	12.716.0	326	12.115.7	426	11.815.2	526	12.315.7	626	14.017.1	726	9.901.3	826	11.414.9	926	12.215.6		
27	11.915.3	127	10.614.3	227	11.915.3	327	11.715.1	427	13.116.3	527	11.815.2	627	11.314.8	727	13.216.4	827	12.415.7	927	11.815.2		
28	13.716.8	128	10.814.4	228	11.515.0	328	10.914.5	428	12.716.0	528	13.216.4	628	13.216.4	728	12.415.7	828	12.516.8	928	11.214.8		
29	11.815.2	129	11.815.2	229	12.115.5	329	12.716.0	429	9.901.3	529	10.714.4	629	9.701.4	729	12.315.5	829	13.816.8	929	12.415.7		
30	11.815.2	130	11.515.0	230	12.015.4	330	12.516.8	430	11.615.1	530	13.614.8	630	10.314.0	730	11.915.3	830	11.715.2	930	11.715.2		
31	12.615.9	131	11.414.9	231	11.314.8	331	11.815.2	431	11.615.1	531	13.316.5	631	11.615.0	731	10.314.0	831	10.914.5	931	10.914.5		
32	11.915.3	132	11.314.8	232	11.815.2	332	9.901.3	432	12.115.5	532	14.017.2	632	12.015.4	732	12.816.1	832	12.716.0	932	11.615.0		
33	10.614.3	133	11.715.1	233	11.715.1	333	12.716.0	433	14.017.2	533	12.015.4	633	11.515.0	733	13.614.8	833	12.415.7	933	12.415.7		
34	11.314.8	134	11.515.0	234	11.014.6	334	12.716.0	434	11.915.3	534	13.817.0	634	10.214.0	734	10.013.8	834	11.815.2	934	13.917.0		
35	12.916.2	135	12.515.8	235	11.615.1	335	14.717.8	435	13.516.7	535	12.715.9	635	13.416.6	735	12.816.9	835	12.015.4	935	12.215.6		
36	12.115.5	136	11.815.2	236	12.215.5	336	10.114.3	436	11.114.7	536	11.114.6	636	10.914.5	736	13.917.0	836	11.615.1	936	10.514.2		
37	11.715.2	137	11.615.1	237	10.714.4	337	11.114.6	437	11.715.1	537	11.815.2	637	12.115.5	737	12.816.0	837	11.414.9	937	10.714.4		
38	11.014.6	138	11.715.2	238	11.615.0	338	13.416.6	438	11.214.8	538	9.901.3	638	10.214.0	738	11.815.2	838	11.715.1	938	10.214.0		
39	10.614.3	139	11.314.8	239	11.915.3	339	11.815.2	439	12.716.0	539	10.013.8	639	9.901.3	739	12.215.6	839	11.214.8	939	12.415.7		
40	12.916.2	140	11.114.6	240	11.414.9	340	12.215.5	440	11.715.2	540	11.314.8	640	11.214.7	740	12.115.5	840	12.415.7	940	13.116.3		
41	12.315.6	141	11.815.2	241	11.515.0	341	12.516.8	441	13.316.5	541	11.114.6	641	10.714.4	741	11.615.0	841	11.615.0	941	12.415.7		
42	11.414.9	142	13.416.6	242	10.814.4	342	12.315.7	442	11.014.6	542	13.614.8	642	10.314.0	742	12.916.1	842	12.615.9	942	14.017.2		
43	11.314.8	143	11.314.8	243	11.314.8	343	14.017.1	443	11.214.7	543	10.401.3	643	12.015.4	743	11.815.2	843	11.314.8	943	13.416.6		
44	11.815.2	144	11.615.1	244	11.414.9	344	11.514.9	444	8.801.3	544	11.715.1	644	13.416.6	744	10.814.4	844	11.615.0	944	12.115.5		
45	12.716.0	145	12.716.0	245	11.515.0	345	12.615.9	445	10.514.2	545	11.815.2	645	11.014.6	745	13.614.8	845	11.515.0	945	10.814.4		
46	11.514.9	146	13.516.7	246	11.414.9	346	13.016.2	446	11.014.6	546	10.814.4	646	10.614.3	746	16.718.0	846	11.715.2	946	12.816.0		
47	12.615.9	147	11.915.3	247	11.414.9	347	11.815.2	447	12.516.8	547	11.815.3	647	10.214.0	747	10.714.4	847	11.414.9	947	11.815.2		
48	11.615.1	148	13.116.3	248	14.217.3	348	10.714.4	448	10.514.2	548	9.901.3	648	10.814.4	748	10.314.0	848	11.114.7	948	13.614.8		
49	11.815.2	149	12.015.4	249	12.115.5	349	9.901.3	449	13.614.8	549	10.214.0	649	11.414.9	749	10.514.2	849	13.716.9	949	11.515.0		
50	11.414.9	150	11.514.9	250	11.815.2	350	13.116.3	450	10.614.3	550	10.414.2	650	9.701.4	750	13.516.6	850	11.314.8	950	10.914.5		
51	11.615.0	151	11.314.8	251	11.114.7	351	11.915.3	451	13.016.2	551	8.401.2	651	11.815.2	751	10.814.4	851	11.114.6	951	12.615.9		
52	11.314.8	152	11.514.9	252	10.814.4	352	12.115.4	452	10.214.0	552	10.214.0	652	10.814.4	752	11.615.1	852	11.615.1	952	12.816.0		
53	12.816.0	153	11.915.3	253	11.615.1	353	13.316.5	453	11.114.6	553	11.014.6	653	12.516.8	753	10.414.2	853	10.914.5	953	11.314.8		
54	11.715.1	154	13.917.0	254	13.416.6	354	11.915.3	454	8.901.2	554	12.115.5	654	11.414.9	754	10.814.4	854	11.515.0	954	10.814.4		
55	11.815.3	155	12.015.4	255	11.414.9	355	11.414.9	455	11.515.0	555	14.117.3	655	11.515.0	755	11.715.1	855	11.114.7	955	10.614.3		
56	11.214.7	156	11.014.6	256	13.016.2	356	11.014.6	456	12.015.4	556	11.515.0	656	11.214.8	756	13.416.6	856	12.215.5	956	10.714.4		
57	12.215.5	157	11.314.8	257	10.																

S	r_0 (cm)	S	r_0 (cm)	S	r_0 (cm)	S	r_0 (cm)	S	r_0 (cm)
1	5.70±1.4	46	5.60±1.3	91	8.10±2.6	136	6.20±1.6	181	4.40±.90
2	5.60±1.3	47	5.40±1.3	92	9.10±3.2	137	10.3±4.1	182	5.80±1.4
3	5.90±1.5	48	6.10±1.5	93	5.50±1.3	138	7.00±2.0	183	5.00±1.1
4	6.00±1.5	49	5.40±1.2	94	4.80±1.0	139	5.30±1.2	184	6.20±1.6
5	5.60±1.3	50	6.00±1.5	95	5.30±1.2	140	5.00±1.1	185	5.10±1.1
6	5.20±1.2	51	5.50±1.3	96	6.30±1.7	141	5.70±1.4	186	6.40±1.7
7	6.90±1.9	52	5.70±1.4	97	5.40±1.3	142	5.40±1.2	187	4.90±1.0
8	5.30±1.2	53	10.4±4.2	98	6.00±1.5	143	6.20±1.6	188	5.60±1.3
9	6.40±1.7	54	6.10±1.5	99	6.70±1.9	144	6.20±1.6	189	5.30±1.2
10	5.60±1.3	55	5.30±1.2	100	7.60±2.3	145	7.20±2.1	190	4.40±.90
11	5.60±1.3	56	7.60±2.3	101	7.90±2.5	146	6.70±1.9	191	4.70±1.0
12	5.00±1.1	57	5.60±1.3	102	11.9±5.3	147	5.70±1.4	192	4.60±.90
13	5.30±1.2	58	5.40±1.2	103	6.10±1.6	148	6.30±1.7	193	6.90±1.9
14	6.40±1.7	59	5.10±1.1	104	5.80±1.4	149	6.80±1.9	194	5.70±1.4
15	6.10±1.6	60	7.50±2.3	105	5.60±1.3	150	7.90±2.5	195	7.00±2.0
16	6.50±1.7	61	6.70±1.9	106	6.50±1.7	151	6.70±1.9	196	5.40±1.2
17	5.50±1.3	62	5.10±1.1	107	5.50±1.3	152	6.60±1.8	197	6.40±1.7
18	7.20±2.1	63	5.90±1.4	108	4.90±1.0	153	5.80±1.4	198	5.80±1.4
19	6.20±1.6	64	6.50±1.7	109	5.10±1.1	154	4.80±1.0	199	3.90±.70
20	4.20±.80	65	5.70±1.4	110	5.20±1.1	155	4.90±1.0	200	4.40±.80
21	5.80±1.4	66	5.40±1.2	111	5.30±1.2	156	4.90±1.0	201	4.80±1.0
22	5.10±1.1	67	5.30±1.2	112	6.60±1.8	157	4.60±.90	202	3.90±.70
23	6.40±1.7	68	5.80±1.4	113	6.90±2.0	158	4.90±1.0	203	4.20±.80
24	5.30±1.2	69	5.60±1.3	114	5.10±1.1	159	4.90±1.0	204	4.00±.70
25	5.20±1.2	70	5.60±1.3	115	4.90±1.0	160	5.70±1.4	205	4.50±.90
26	4.40±.90	71	5.00±1.1	116	5.70±1.4	161	12.3±5.6	206	4.70±1.0
27	5.30±1.2	72	5.10±1.1	117	5.90±1.5	162	4.90±1.0	207	4.50±.90
28	4.70±1.0	73	5.30±1.2	118	7.30±2.2	163	6.30±1.7	208	5.90±1.5
29	4.80±1.0	74	5.40±1.2	119	9.90±3.8	164	6.00±1.5	209	5.40±1.2
30	4.00±.70	75	5.70±1.4	120	6.70±1.9	165	6.60±1.8	210	6.40±1.7
31	5.30±1.2	76	7.80±2.4	121	9.40±3.4	166	6.40±1.7	211	5.60±1.3
32	4.80±1.0	77	5.50±1.3	122	6.60±1.8	167	5.10±1.1	212	5.80±1.4
33	5.60±1.3	78	6.00±1.5	123	5.00±1.1	168	5.90±1.5	213	5.80±1.4
34	4.90±1.1	79	5.50±1.3	124	4.10±.70	169	5.10±1.1	214	4.30±.80
35	5.40±1.2	80	5.30±1.2	125	4.80±1.0	170	5.30±1.2	215	4.80±1.0
36	5.40±1.2	81	5.20±1.2	126	4.90±1.0	171	6.50±1.7	216	4.10±.70
37	5.70±1.4	82	4.50±.90	127	5.80±1.4	172	4.70±1.0	217	4.40±.90
38	6.10±1.6	83	5.30±1.2	128	5.30±1.2	173	3.60±.60	218	4.80±1.0
39	5.90±1.5	84	7.80±2.4	129	5.40±1.3	174	4.80±1.0	219	6.00±1.5
40	4.70±1.0	85	4.80±1.0	130	6.00±1.5	175	4.60±.90	220	5.30±1.2
41	5.70±1.4	86	4.90±1.0	131	4.10±.80	176	4.80±1.0	221	4.60±.90
42	5.50±1.3	87	7.10±2.1	132	5.10±1.1	177	9.30±3.4	222	5.00±1.1
43	6.30±1.7	88	5.20±1.1	133	8.70±3.0	178	5.10±1.1	223	5.40±1.3
44	6.00±1.5	89	5.10±1.1	134	15.7±8.9	179	9.70±3.6	224	4.30±.80
45	6.30±1.7	90	7.20±2.1	135	6.30±1.7	180	7.10±2.1	225	4.40±.80

Table 2.2: r_0 estimated from angle-of-arrival fluctuations, for a sequence of images of a spot pair with a segment size of 16 by 16 pixels (~ 8 arc sec). S is the segment number and r_0 is the corresponding Fried's parameter.

S	r_0 (cm)								
1	3.700±.6000	11	22.50±17.10	21	4.200±.8000	31	2.600±.3000	41	12.50±5.800
2	3.100±.4000	12	2.700±.4000	22	9.000±3.200	32	4.400±.9000	42	86.70±202.0
3	3.700±.6000	13	11.20±4.700	23	5.700±1.400	33	6.200±1.600	43	1.800±.2000
4	1.900±.2000	14	7.000±2.000	24	4.100±.8000	34	4.000±.7000	44	2.700±.4000
5	4.100±.7000	15	42.20±54.00	25	2.500±.3000	35	6.000±1.500	45	2.200±.2000
6	9.200±3.300	16	5.500±1.300	26	3.000±.4000	36	1.900±.2000	46	2.100±.2000
7	4.000±.7000	17	4.100±.8000	27	13.40±6.600	37	3.200±.5000	47	2.800±.4000
8	2.300±.3000	18	2.900±.4000	28	33.70±35.80	38	2.100±.2000	48	3.700±.6000
9	3.800±.6000	19	3.400±.5000	29	3.300±.5000	39	2.100±.2000	49	3.700±.6000
10	6.500±1.700	20	16.40±9.500	30	3.000±.4000	40	2.200±.2000		

Table 2.3: r_0 estimated from angle-of-arrival fluctuations, for a sequence of images of a spot pair with a segment size of 32 by 32 pixels (~ 16 arc sec). S is segment number and r_0 is the corresponding Fried's parameter.

2.4.3 USO Data

All the 28 sequences of images of a sub-flare region were subjected to dark and flat-field corrections and then registered using the procedure described earlier. The size of images in the registered sequences varied from one sequence to the other, with a typical size of 36 by 63.6 arc sec. A comparison of this size with the initial size 57.6 by 67.8 arc sec of the recorded images implies significant tracking errors. For each sequence, a square window of size 36 arc sec was selected from the registered images and then re-sampled to have 128 pixels in either direction. As the tracking of the telescope was poor, it was meaningless to estimate Fried's parameter from the angle-of-arrival fluctuations. The power spectrum equalisation method produced unrealistic values of r_0 . This could be due to the fact that the number of images averaged (~ 90) were not sufficient.

We estimated r_0 using spectral ratio method. First, we estimated the theoretical spectral ratios using the speckle transfer functions and short exposure transfer functions for various values of D/r_0 , with r_0 ranging from 2 to 10 cm in steps of 0.1 cm for an array size of 32 by 32 pixels. We estimated the constants A and B (Equation 2.5) for various values of spectral ratios ranging from 0.2 to 0.9 in steps of 0.001. Then

Seq.	ARF (cm)	PSE (cm)	SR (cm)	C	RC	Remarks
1.	3.98±0.73	3.12±0.17	3.11±0.88	0.37	0.54	single sunspot
2.	3.93±0.74	3.12±0.17	2.98±0.79	0.34	0.36	single sunspot
3.	4.11±0.80	3.12±0.17	3.05±0.83	0.34	0.43	single sunspot
4.	3.55±0.62	3.12±0.17	3.11±0.88	0.32	0.44	single sunspot
5.	3.21±0.51	3.12±0.17	2.83±0.71	0.53	0.63	spot pair
6.	3.42±0.58	3.12±0.17	2.86±0.71	0.53	0.61	spot pair
7.	3.60±0.64	3.12±0.17	2.87±0.71	0.48	0.52	spot pair

Table 2.4: Comparison of average value of r_0 estimated from three different methods for all the sequences. ARF - From angle-of-arrival fluctuations; PSE - Power spectrum equalisation method; SR- Spectral ratio method. Estimates with error bars more than 25% were neglected while determining the average from angle-of-arrival fluctuations method. C is the correlation coefficient of average contrast of the segments and the corresponding r_0 estimated from spectral ratio method and RC is the corresponding Spearman's rank correlation coefficient. The significance of rank correlation was less than 10^{-8} .

we divided the images into segments of size 32 by 32 pixels (9 arc sec) and estimated the spectral ratios for each of the segments. By comparing the the slopes of the observed spectral ratios with the theoretical ratios in a log-log plot of spectral ratio ϵ vs. normalised spatial frequency \mathbf{q} , in the frequency range of 0.1 to 0.4, we estimated the spectral ratio. Then using the corresponding constants A and B , we inferred r_0 . We also estimated the error as described in Section 2.1 (Page 24). We repeated the procedure for all the 28 sequences of images.

Spatial and Temporal variation of r_0 : Figures 2.3 to 2.6 show the spatial distribution of r_0 estimated for all the 28 sequences. For each sequence, we obtained the average value r_0 over the field-of-view (average of r_0 values of all the segments). Figure 2.7 shows the variation of r_0 with time. The time-interval between consecutive sequences was not uniform but varied between 30 seconds to 1 minute. The duration of acquisition of a sequence was ~ 82 seconds. Consequently, the time interval is not uniform in the plot. An approximate value of 112 seconds ($82 + 30$ s) has been assumed as an interval between the consecutive estimates. It indicates the variation of r_0 over an hour duration. Table 2.5 gives the average (spatial average) value of r_0 for each of the sequences. The linear and Spearman's rank correlation coefficient of the estimated r_0 values with the average contrast of the segments are also tabulated. We find that in most of the cases, the correlation is significant indicating the fact that higher contrast values correspond to higher r_0 . There are a few sequences where the significance of the rank correlation is more than 0.1.

We estimated r_0 corresponding to 16 sequences of another sub-flare region in a similar manner. The average value was found to be 3.5 ± 0.8 cm.

Criticism on Various Methods of Estimating r_0 : The method of estimation of r_0 from angle-of-arrival fluctuations demands high spatial and temporal sampling. Image motion caused by improper tracking is coherent over the entire field of view and can be estimated from the low frequency components of the image using cross-correlation technique. However, the results are not accurate for the regions near the edges of the field of view. Moreover, this method is sensitive to the scene (sunspots, for example) under consideration. Power spectrum equalisation method seems to be a more powerful method provided the assumptions of stationarity is valid and the size of the processing image is much larger than the degrading PSF, because, it does not involve any theoretical calculations and the results are obtained through observed data only. But it demands high spatial sampling. Spectral ratio method seems to be the most widely ap-

Seq.	$r_0(\text{cm})$	C	RC	S	Seq.	$r_0(\text{cm})$	C	RC	S
1	3.37 ± 0.59	0.42	0.38	7×10^{-3}	15	3.35 ± 0.56	0.45	0.46	8×10^{-4}
2	3.47 ± 0.60	0.22	0.21	1×10^{-1}	16	3.04 ± 0.49	0.66	0.77	1×10^{-11}
3	3.52 ± 0.60	0.29	0.32	2×10^{-2}	17	3.10 ± 0.52	0.55	0.59	6×10^{-6}
4	3.42 ± 0.58	0.49	0.52	1×10^{-4}	18	3.11 ± 0.55	0.63	0.69	3×10^{-8}
5	3.03 ± 0.51	0.47	0.68	5×10^{-8}	19	3.02 ± 0.53	0.68	0.73	1×10^{-9}
6	3.20 ± 0.56	0.56	0.72	6×10^{-9}	20	3.24 ± 0.54	0.42	0.43	1×10^{-3}
7	3.18 ± 0.53	0.68	0.71	1×10^{-8}	21	3.08 ± 0.54	0.50	0.47	5×10^{-4}
8	3.41 ± 0.57	0.45	0.45	1×10^{-3}	22	3.32 ± 0.55	-0.10	-0.02	9×10^{-1}
9	3.34 ± 0.57	0.66	0.68	5×10^{-8}	23	3.22 ± 0.56	0.47	0.54	5×10^{-5}
10	3.25 ± 0.56	0.31	0.55	4×10^{-4}	24	3.46 ± 0.61	0.09	0.01	9×10^{-1}
11	3.52 ± 0.58	0.27	0.18	2×10^{-1}	25	3.42 ± 0.57	0.30	0.29	4×10^{-2}
12	3.29 ± 0.57	0.31	0.42	2×10^{-3}	26	3.10 ± 0.53	0.67	0.63	1×10^{-6}
13	3.17 ± 0.54	0.58	0.57	1×10^{-5}	27	3.42 ± 0.56	0.30	0.29	3×10^{-2}
14	2.83 ± 0.53	0.56	0.63	2×10^{-5}	28	3.39 ± 0.60	0.47	0.44	1×10^{-3}

Table 2.5: r_0 estimated by spectral ratio method for all the 28 sequences. Linear and Spearman's rank correlation coefficients (C and RC respectively) of the estimated r_0 with the average contrast of the segments for all the sequences are given. S denotes the significance of the rank correlation.

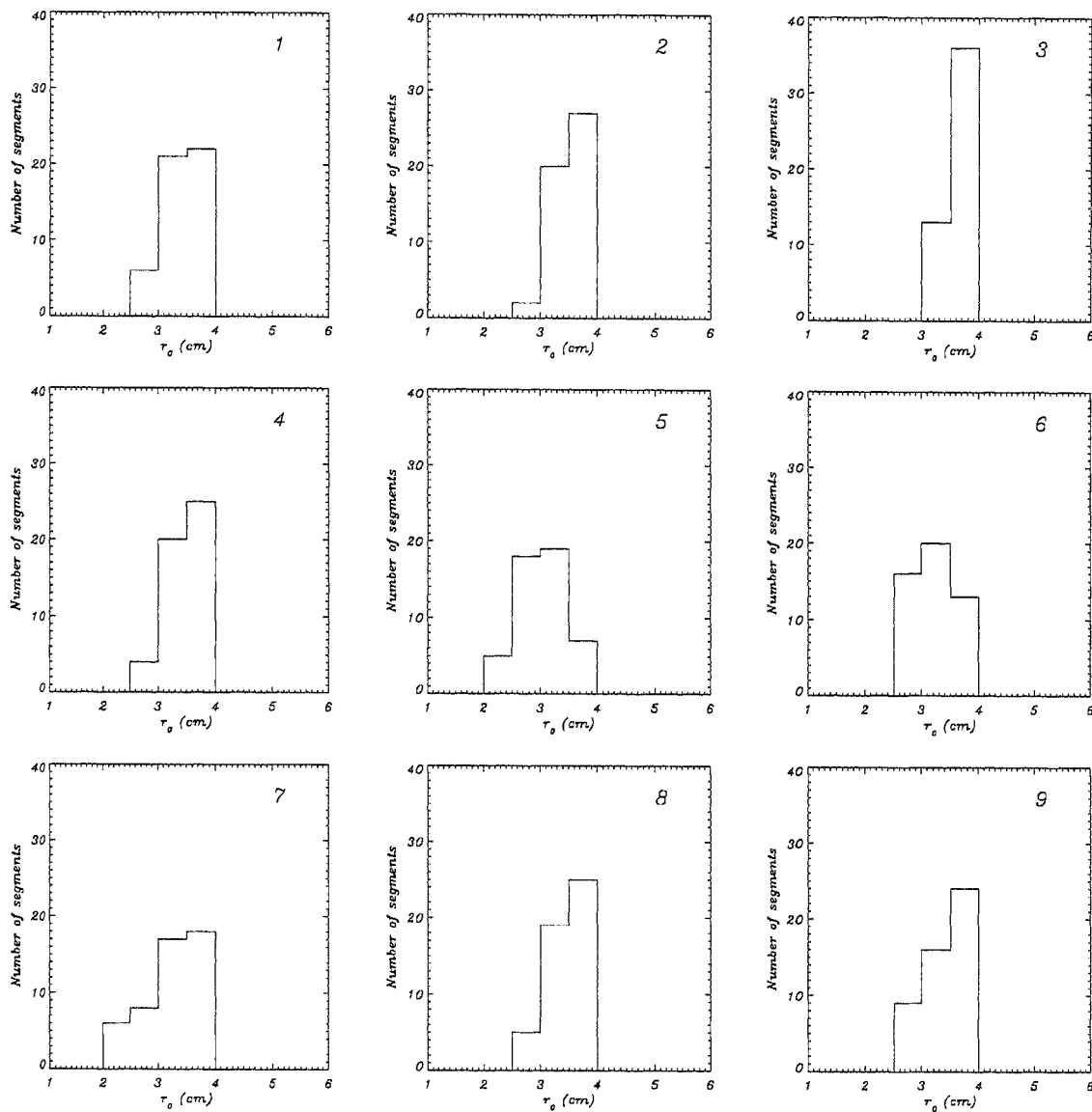


Figure 2.3: Spatial distribution of r_0 estimated using spectral ratio method for sequences 1-9 of a sub-flare region. The segment size was 32 pixels square (9 arc sec). The number of segments is 49 in each sequence. The bin-size is 0.5 cm.

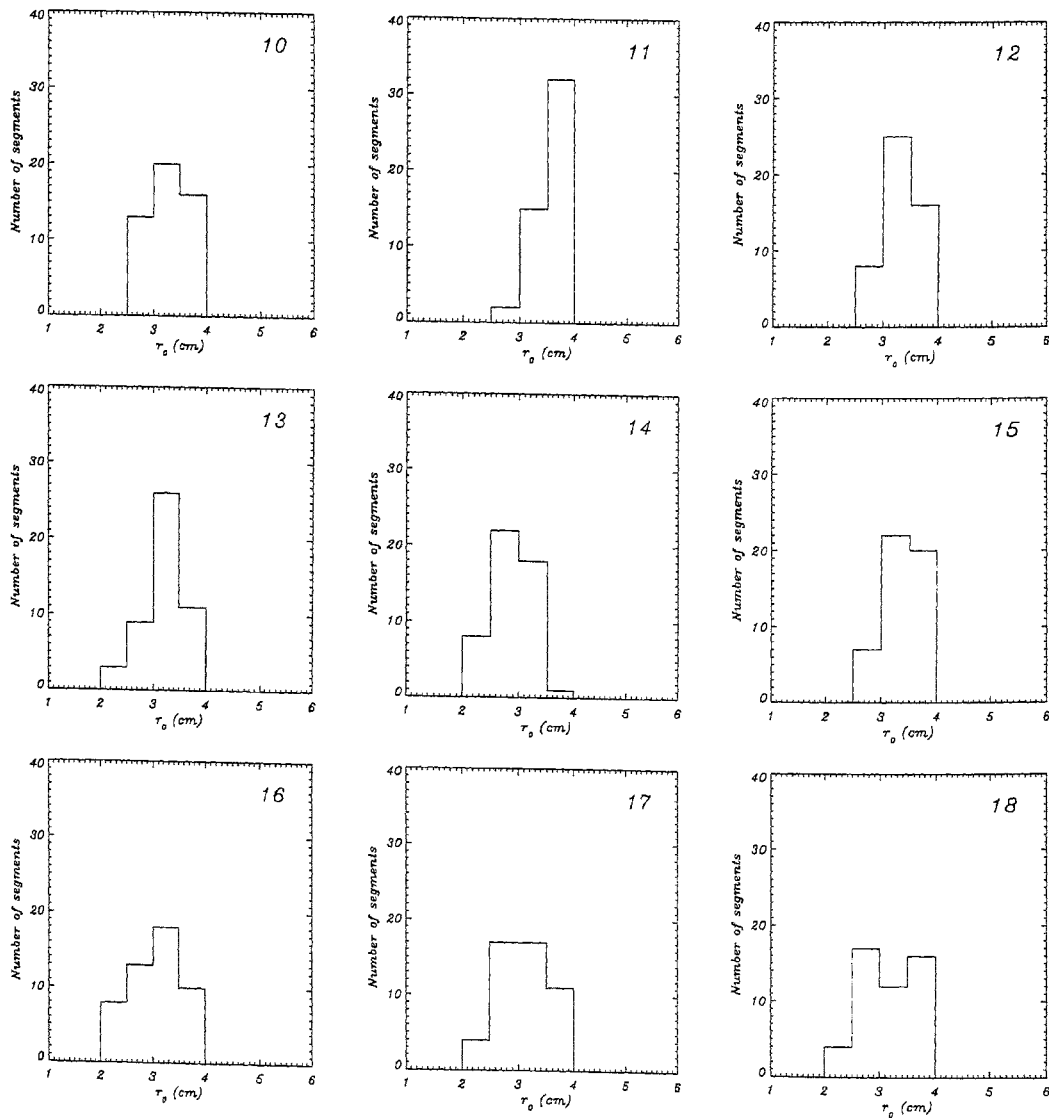


Figure 2.4: Spatial distribution of r_0 estimated using spectral ratio method for sequences 10-18 of a sub-flare region. The segment size was 32 pixels square (9 arc sec). The number of segments is 49 in each sequence. The bin-size is 0.5 cm.

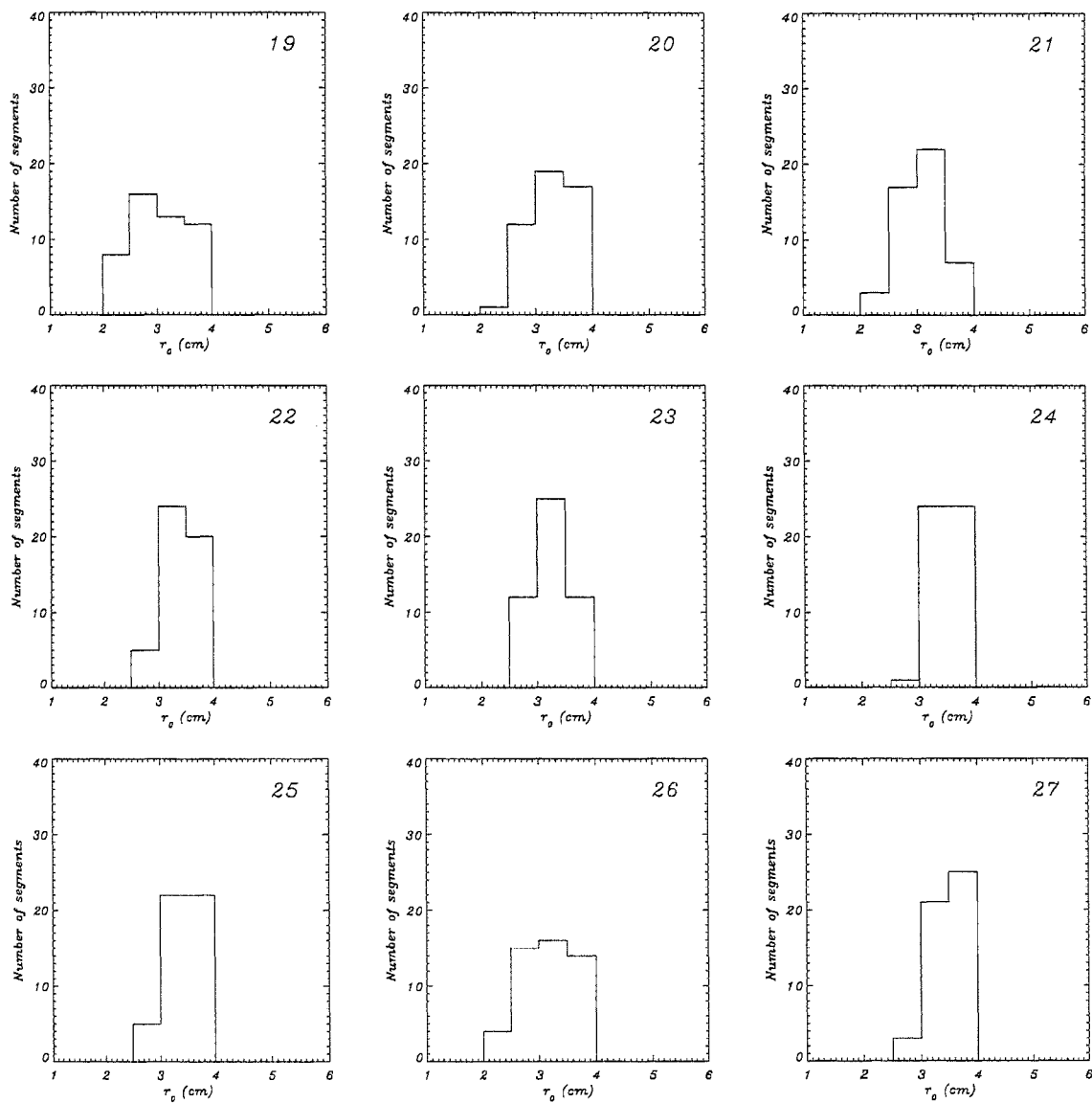


Figure 2.5: Spatial distribution of r_0 estimated using spectral ratio method for sequences 19-27 of a sub-flare region. The segment size was 32 square pixels (9 arc sec). The number of segments is 49 in each sequence. The bin-size is 0.5 cm.

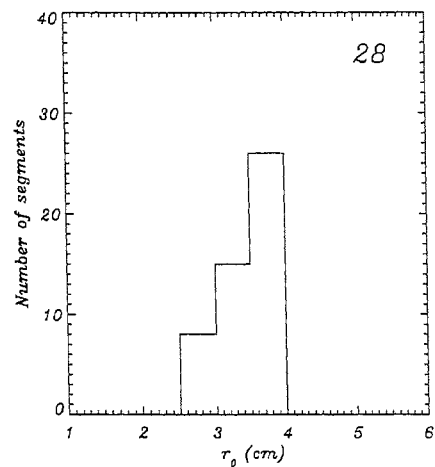


Figure 2.6: Spatial distribution of r_0 estimated using spectral ratio method for the 28th sequence of a sub-flare region. The segment size was 32 square pixels (9 arc sec). The number of segments is 49 in each sequence. The bin-size is 0.5 cm.

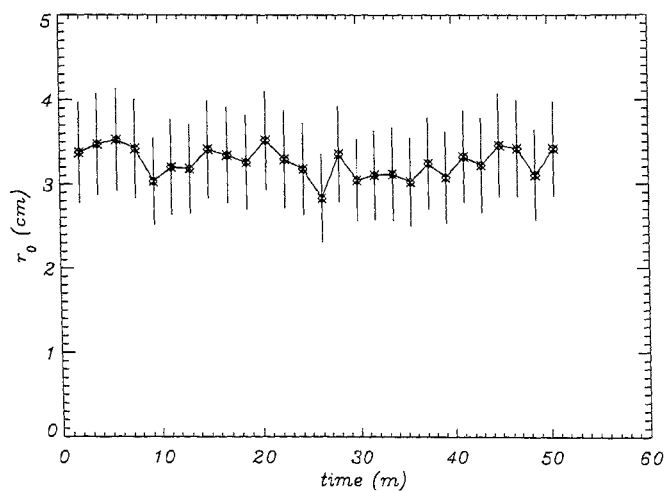


Figure 2.7: Variation of average (spatial) r_0 with time. As the time interval between the sequences was not uniform, an approximate value of 112 seconds has been assumed to be the interval between the sequences.

plicable method and is well suited for speckle observations, as r_0 is estimated from the data itself. It does not require very high spatial sampling; it is independent of the scene under consideration. However, this involves visual comparison of the observed profiles of the spectral ratio ($\epsilon(\mathbf{q})$) with those obtained from theoretical model. While the theoretical STF (Korff, 1973) itself has associated uncertainty due to finite bandwidth, its numerical evaluation is highly time consuming for large array sizes. Aime *et al.*, (1978) have prescribed a method to estimate r_0 from a series of observations based on the distinct behavior of the (STF) at low and high spatial frequencies. The method seems to fail when the differences of the r_0 values of two independent observations are small or the life time of small scale features is smaller than time interval between two independent observations. Seykora (1993) has proposed a method of estimating r_0 from scintillation measurements. This method can be applied only to extended objects; that is, over a large field of view. It is suitable for measuring the atmospheric seeing at different heights. Krishnakumar and Venkatakrishnan (1997; also Krishnakumar, 1998) have proposed a method to estimate r_0 through a parametric search method. This method works well for stellar images, but needs modification before it can be applied to solar images.

2.5 Summary

In this Chapter, we have described the details of speckle imaging observations performed at KO, UPSO and USO. We have described the methods of pre-processing that we adopted for analysing the speckle data. We have explored the possibility of estimating r_0 from three different methods. We have used some of these methods to estimate r_0 for our speckle data. We found that in all these methods, the estimated value of r_0 has an error of 25%. While estimating r_0 from the fluctuations in the angle of arrival of the light, we found that high frequency components contribute more to the image motion than the low frequency components. The spectral ratio method seems to be

the most suitable method for speckle data. The average value of r_0 at USO and UPSO was $\sim 3 \pm .7$ cm on days when these observations were performed. A small spatial variation of r_0 over the field-of-view of ~ 60 arc sec implies a large isoplanatic patch size (assuming a single turbulent layer model) which in turn indicates that most of the degradation is caused close to the telescope (ground turbulence). At KO, the values of r_0 ranging from 6–10 cm were observed on the three days of observations described earlier in this Chapter.

Chapter 3

Solar Speckle Imaging

3.1 Solar Speckle Imaging: Practical Implementation

Speckle imaging of small scale solar features needs careful processing methods. The Sun as a whole being an extended source does not produce speckles. Only the small scale solar features riding on a bright background produce speckles. Consequently, these features appear to have very low contrast and observing them becomes a difficult task. We have developed software (hereafter referred to as the speckle code) for reconstructing such small scale features using specklegrams. We estimate the amplitudes and the phases of the Fourier transform of the object using speckle interferometry (Labeyrie, 1970) and bispectrum techniques (Weigelt, 1977; Lohmann, Weigelt and Wirtzner, 1983) respectively. We make use of the fact that the phase of the average bispectrum of the images is equal to the phase of the bispectrum of the object. We estimate the phases of the Fourier transform of the object from its bispectrum using a recursive relation. In Section 2.3, we have described the various pre-processing steps, frame selection and segmentation that we followed while reconstructing small scale so-

lar features from the observed speckle data. The field-of-view is restricted to a few arc seconds (~ 8 arc sec square) basically to reduce the effect of anisoplanatism (Harvey and Breckinridge, 1973; Wang, 1975; Breckinridge and McAllister, 1976; Nisenson and Stachnik, 1978; Pollaine, Buffington and Cranford, 1979; Fried, 1979; Roddier, 1981; Roddier, Gilli and Vernin, 1982; von der Lühe, 1984b; von der Lühe, 1993) on the reconstructed images. In what follows, this restricted piece of the recorded image is called a sub-image. A time sequence of the same region is called a sub-image sequence. In the following sections, we describe the procedure for reconstructing a sub-image from the corresponding sub-image sequence.

3.1.1 Estimation of the Fourier Amplitudes

- a:* The first step is the estimation of r_0 for the sub-image sequence using any one of the methods described in Chapter 2. When spectral ratio method is used, first the theoretical speckle transfer function (Korff, 1973) and the short and long exposure transfer functions are estimated¹ for various values of D/r_0 , varying r_0 in steps of 0.1 cm and then used to estimate theoretical spectral ratios.
- b:* The second step is the estimation of the ensemble average power spectrum of the images and subtraction of the deterministic noise power spectrum from it. The noise power spectrum is estimated from the flat-field images (von der Lühe, 1993). The following procedure is adopted prior to the estimation of both the signal and noise power spectrum to improve the accuracy of the estimates: Each image of the sequence is divided by its average value to remove the effect of frame-to-frame variation of the sky brightness; a bi-linear least square surface is fitted to each of the images and subtracted from it; the average values and the fitted surfaces are preserved separately; Each image is multiplied by an optimum apodisation window (Keller, 1999; see Appendix:B) that not only reduces the

¹A FORTRAN 77 program written for this purpose is included in Appendix:A

leakage error (Bracewell, 1986) but also reduces the distortion that occurs in the phase estimates when a 20% Hanning window is used. When reliable estimates of the noise power spectrum are not available (because of the absence of proper flat-field images), the standard deviation of the average power spectrum of the image beyond the diffraction limit is subtracted from the average power spectrum and the resultant power spectrum is considered equivalent to that of the noise corrected power spectrum. A noise filter is constructed by dividing the noise-corrected power spectrum of the image by the average power spectrum (Brault and White, 1971) and smoothed by three pixels.

- c: The average power spectrum is divided by the Speckle Transfer Function (STF) corresponding to the estimated value of r_0 . The division is restricted only to those frequencies for which the STF is greater than 10^{-3} . The resulting power spectrum is multiplied by the smoothed noise filter. The Fourier amplitudes of the object are obtained by taking square root of the compensated average power spectrum of the images.

3.1.2 Estimation of the Fourier Phases

We estimate the ensemble average of the bispectrum of the images. If $I(\mathbf{f})$ is the Fourier component of the image at the frequency \mathbf{f} , then the bispectrum corresponding to the frequencies $\mathbf{f1}$ and $\mathbf{f2}$ is defined as

$$b(\mathbf{f1}, \mathbf{f2}) = I(\mathbf{f1})I(\mathbf{f2})I^*(\mathbf{f1} + \mathbf{f2}), \quad (3.1)$$

where '*' denotes complex conjugate. The phase of the average bispectrum $\phi_b(\mathbf{f1}, \mathbf{f2})$ is given by

$$\phi_b(\mathbf{f1}, \mathbf{f2}) = \phi(\mathbf{f1}) + \phi(\mathbf{f2}) - \phi(\mathbf{f1} + \mathbf{f2}), \quad (3.2)$$

where $\phi(\mathbf{f})$ denotes the phase of the object's Fourier transform at \mathbf{f} (Lohmann, Weigelt and Wirnitzer, 1983). Equation (3.2) gives a recursive relation for estimating the phase

of the object's Fourier transform at the frequency $\mathbf{f1} + \mathbf{f2}$. If $\phi(\mathbf{f1})$ and $\phi(\mathbf{f2})$ are known, $\phi(\mathbf{f1} + \mathbf{f2})$ can be calculated using the average bispectrum as

$$\phi(\mathbf{f1} + \mathbf{f2}) = \phi(\mathbf{f1}) + \phi(\mathbf{f2}) - \phi_b(\mathbf{f1}, \mathbf{f2}), \quad (3.3)$$

The phase at any point in the Fourier plane can be estimated as an average value of the estimates obtained by integrating along different paths.

The bispectrum phases are of mod 2π . Therefore, the recursive reconstruction in Equation (3.3) may lead to π phase mismatches between the computed phase values along different paths to the same point in the frequency space. Another way of computing the argument of the term $e^{i\phi(\mathbf{f1}+\mathbf{f2})}$ is given by

$$e^{i\phi(\mathbf{f1}+\mathbf{f2})} = e^{i[\phi(\mathbf{f1})+\phi(\mathbf{f2})-\phi_b(\mathbf{f1},\mathbf{f2})]}. \quad (3.4)$$

In other words, the average bispectrum values are divided by their absolute values to obtain unit amplitude phasors. The phase values obtained using the unit amplitude phasor recursive reconstructor are insensitive to π ambiguities. Since the bispectrum is a four dimensional function, it is difficult to represent it in a three dimensional coordinate system. We calculate the bispectrum and store them in an 1-D array and use them later to calculate the phase by keeping track of its component frequencies. An algorithm used to estimate the phase of the object's Fourier transform of an image of size 4 by 4 pixels is given in Table 3.1. The entries in column 1 of the Table are the bispectrum values for a 4 by 4 array for the lower half (and extreme left in the upper half) of the Fourier plane. The remaining values are determined using the hermitian symmetry property. The phase values are estimated as given in column 2 of the Table. Assuming

$$\phi(0,0) = 0, \quad \phi(\pm 1,0) = 0, \quad \text{and} \quad \phi(0,\pm 1) = 0$$

as *initial conditions*, the phase values are estimated by unitary amplitude method. *However, in practice, these values are obtained from the average short exposure image so that the object's position information is preserved.* Again the phase values given in

bispectrum values	Fourier phases
$b((-1,0),(0,0)) = I(-1,0) I(0,0) I^*(-1,0)$	$\phi(-1,0) = \phi(-1,0) + \phi(0,0) - \phi_b((-1,0),(0,0))$
$b((1,0),(0,0)) = I(1,0) I(0,0) I^*(1,0)$	$\phi(1,0) = \phi(1,0) + \phi(0,0) - \phi_b((1,0),(0,0))$
$b((-1,0),(-1,0)) = I(-1,0) I(-1,0) I^*(-2,0)$	$\phi(-2,0) = \phi(-1,0) + \phi(-1,0) - \phi_b((-1,0),(-1,0))$
$b((0,0),(0,-1)) = I(0,0) I(0,-1) I^*(0,-1)$	$\phi(0,-1) = \phi(0,0) + \phi(0,-1) - \phi_b((0,0),(0,-1))$
$b((0,-1),(0,-1)) = I(0,-1) I(0,-1) I^*(0,-2)$	$\phi(0,-2) = \phi(0,-1) + \phi(0,-1) - \phi_b((0,-1),(0,-1))$
$b((0,-1),(-1,0)) = I(0,-1) I(-1,0) I^*(-1,-1)$	$\phi(-1,-1) = \phi(0,-1) + \phi(-1,0) - \phi_b((0,-1),(-1,0))$
$b((0,-1),(1,0)) = I(0,-1) I(1,0) I^*(1,-1)$	$\phi(1,-1) = \phi(0,-1) + \phi(1,0) - \phi_b((0,-1),(1,0))$
$b((0,-1),(-2,0)) = I(0,-1) I(-2,0) I^*(-2,-1)$	$\phi(-2,-1) = \phi(0,-1) + \phi(-2,0) - \phi_b((0,-1),(-2,0))$
$b((-1,0),(-1,-1)) = I(-1,0) I(-1,-1) I^*(-2,-1)$	$\phi(-2,-1) = \phi(-1,0) + \phi(-1,-1) - \phi_b((-1,0),(-1,-1))$
$b((0,-1),(-1,-1)) = I(0,-1) I(-1,-1) I^*(-1,-2)$	$\phi(-1,-2) = \phi(0,-1) + \phi(-1,-1) - \phi_b((0,-1),(-1,-1))$
$b((0,-2),(-1,0)) = I(0,-2) I(-1,0) I^*(-1,-2)$	$\phi(-1,-2) = \phi(0,-2) + \phi(-1,0) - \phi_b((0,-2),(-1,0))$
$b((0,-1),(1,-1)) = I(0,-1) I(1,-1) I^*(1,-2)$	$\phi(1,-2) = \phi(0,-1) + \phi(1,-1) - \phi_b((0,-1),(1,-1))$
$b((0,-2),(1,0)) = I(0,-2) I(1,0) I^*(1,-2)$	$\phi(1,-2) = \phi(0,-2) + \phi(1,0) - \phi_b((0,-2),(1,0))$
$b((0,-1),(-2,-1)) = I(0,-1) I(-2,-1) I^*(-2,-2)$	$\phi(-2,-2) = \phi(0,-1) + \phi(-2,-1) - \phi_b((0,-1),(-2,-1))$
$b((0,-2),(-2,0)) = I(0,-2) I(-2,0) I^*(-2,-2)$	$\phi(-2,-2) = \phi(0,-2) + \phi(-2,0) - \phi_b((0,-2),(-2,0))$
$b((-1,0),(-1,-2)) = I(-1,0) I(-1,-2) I^*(-2,-2)$	$\phi(-2,-2) = \phi(-1,0) + \phi(-1,-2) - \phi_b((-1,0),(-1,-2))$
$b((-1,-1),(-1,-1)) = I(-1,-1) I(-1,-1) I^*(-2,-2)$	$\phi(-2,-2) = \phi(-1,-1) + \phi(-1,-1) - \phi_b((-1,-1),(-1,-1))$
$b((0,1),(-2,0)) = I(0,1) I(-2,0) I^*(-2,1)$	$\phi(-2,1) = \phi(0,1) + \phi(-2,0) - \phi_b((0,1),(-2,0))$
$b((-1,0),(-1,1)) = I(-1,0) I(-1,1) I^*(-2,1)$	$\phi(-2,1) = \phi(-1,0) + \phi(-1,1) - \phi_b((-1,0),(-1,1))$

Table 3.1: Estimation of the phase of object's Fourier transform from its image of size 4 by 4 pixels

the Table are only for the lower half (and extreme left in the upper half) of the Fourier plane. Using the hermitian symmetry, the phase values at the upper half plane are determined.

Noise filter for phase estimation. The estimated phases are further improved using the noise filter developed by de Boer (1996): the phase consistency function is used to provide less weight to the phasors with lower signal to noise ratio. For each phase estimate at a given point in the frequency space, a correlation function is defined and the estimates that differ significantly from their counterparts are eliminated.

Error estimation: With the implementation of the noise filter and the correlation function, the number of estimates of phases for a given frequency is slightly reduced. Denoting $M(m, n)$ as the resulting number of estimates, we obtain the mean value of these $M(m, n)$ phasors as the phasor of the object's Fourier transform. Following Buscher (1988), we define phase error of object's phase as

$$\beta(\mathbf{f}) = \frac{\sigma_{yy}(\mathbf{f})}{M|\langle S(\mathbf{f}) \rangle|} \quad (3.5)$$

where $\sigma_{yy}^2(\mathbf{f})$ is the variance of the phase perpendicular to the direction of the mean $\langle S(\mathbf{f}) \rangle$. We estimate an azimuthal average of these phase errors and obtain a plot of phase errors vs normalised spatial frequency. It is found that at low frequencies, the phase error is less. It increases and reaches a value of about 0.4 radians at intermediate frequencies and then decreases at higher frequencies. The reason for the decrease is that at high frequencies the estimated phase is an average of a large number of independent estimates. Moreover, Equation (3.5) is valid only when the number of estimates are large and cannot be used for estimating the errors at low frequencies, where the number of estimates are relatively lower.

3.1.3 Image Reconstruction

The final image is reconstructed by performing an inverse Fourier transform of a complex array, obtained by multiplying the calibrated amplitudes with the corresponding phase values. The reconstructed image is then divided by the ‘optimised apodisation window’ described earlier. As the apodisation window falls off to zero at the edges, division cannot be performed at the edges. This results in loss of data near the edges (at most at two columns and rows near the edges) of the reconstructed images. The average of all the bi-linear surface fits which were preserved separately is then added to the final image. It is then multiplied by the average of all the average intensities that were preserved separately to obtain the reconstructed sub-image. Finally, all the reconstructed sub-images are mosaicked using the following procedure: Two arrays o and b are defined with their sizes equal to that of the original image from which the sub-images were extracted; Initially all the elements of these arrays are set to zero; Each reconstructed sub-image is multiplied by a 100% Hanning function and added to the array o at the same location of the image from which it was extracted initially; The Hanning function is added to the array b at the corresponding location; Finally the array o is divided by the array b to yield the final reconstructed image. Again, there is data loss at the edges of the final reconstructed image due to division by zero. We have written a program in FORTRAN 77 that incorporates all the procedures described above. It requires three inputs, *viz.*

- a data cube (a sequence of 2-D images) containing registered, de-stretched images.
- a data cube containing flat-field images.
- r_0 values for all the segments of the images.

The program produces the final reconstructed image that has field-of-view slightly lesser than the input images. It takes about 10 minutes to reconstruct an image from

a series of 90 images of size 128 by 128 square pixels, and requires a RAM size of ~ 100 MB.

3.1.4 Validation of the Phase Reconstruction

Procedure

In this section, we first demonstrate (using our software) how the triple correlation of an 1-D object can be obtained in the image plane through cross-correlation (It should be noted that the triple correlation of a binary system has been obtained by Lohmann, Weigelt and Wirtitzer (1983) and Karbelkar (1989)). Then we validate our phase reconstruction procedure by estimating the Fourier phases from the bispectrum of the object and reconstructing the object. Figure 3.1(a) shows an ideal object intensity distribution in 1-D. Figure 3.1(b) shows the triple correlation of this object, which is a 2-D image. It was obtained by performing the correlation in the image plane. Figure 3.1(c) shows the Fourier transform of the triple correlation obtained in 3.1(b). We estimated the bispectrum from the Fourier transform of the object (that is, Fourier transform of 3.1(a)) using a 1-D version of our speckle code. We estimated the Fourier phases of the object from the bispectrum. We assumed unit amplitude phasor ($\exp(j 2 \pi)$) for the phases at the smallest spatial frequencies. We estimated the Fourier amplitude from the square root of the power spectrum of the object shown in Figure 3.1(a). Finally, we reconstructed the 1-D image from the estimated Fourier amplitudes and phases.

Figure 3.1(d) (dotted line) shows the reconstructed image. It does not match exactly with the original object. The entire image is shifted towards right side by a few pixels. This is because of using unit amplitude phasors for the smallest frequency. The solid line shows the reconstructed image when the unit amplitude phasors are replaced by those obtained from the smallest frequency component of the Fourier transform of the object. It matches exactly with the original object intensity distribution. A computer program (`1dbpm.pro`) written in IDL, that produces the Figure 3.1(a)-(d) has been

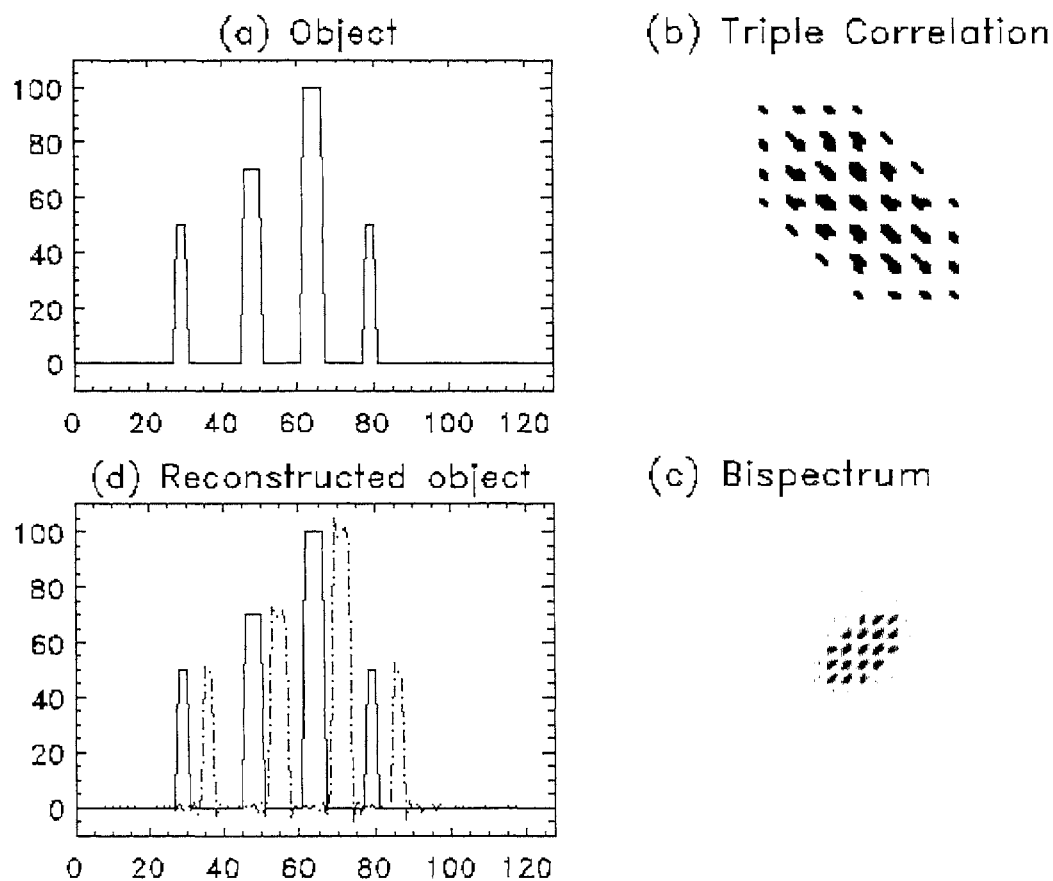


Figure 3.1: Demonstration of the phase reconstruction procedure: (a) An ideal 1-D object intensity distribution; (b) Triple correlation of the object; (c) Fourier transform of triple correlation (b); (d) Image reconstructed using our phase reconstruction algorithm. The dotted line is the reconstruction obtained assuming that the object phase is zero at the lowest spatial frequencies. In such cases, the absolute position information is lost (note the shift in the position with respect to the continuous line). The continuous line represents the reconstruction in which true object phases have been used at the smallest spatial frequencies. In practice, the corresponding phases of an equivalent long exposure image are used.

included in Appendix:A

We arrive at two conclusions from this exercise. First, our phase reconstruction procedure produces exact Fourier phases with minimum errors. The source of this error lies in the assumption that at the smallest spatial frequencies ($f = \pm 1$), the Fourier phase of the object is zero. Obviously, this will lead to loss of absolute position information and hence there is a shift in the reconstructed image. Once we replace the unit amplitude phasors by those of the object's Fourier transform for the smallest frequencies, the reconstructed image matches exactly with the original object, again validating our phase reconstruction procedure.

Second, assuming the Fourier phases of the object as zero at the smallest spatial frequencies not only leads to the loss of the absolute position information, but also affects the photometry of the reconstructed images. This is obvious from the dotted line. In practice, we estimate the phases of the smallest Fourier component from the average short exposure image. Thus, the accuracy in the position of various features in the reconstructed image depends on the accuracy with which the phase of the smallest Fourier component is estimated from the average short exposure image. Normally, in stellar speckle imaging and in radio astronomy, the phases of the smallest Fourier components are obtained from the long exposure image. The idea is that in the case of long exposures, the images move uniformly about the mean position and hence the exact position information (and hence the phase information at the smallest frequency) is preserved. However, in solar speckle imaging, the average short exposure image is obtained after correcting for the image motion (tilt component of the wave-front distortion) and hence absolute position information is preserved. Moreover, the images are de-stretched before processing and thus the absolute position information is expected to be preserved.

In this example, we have assumed that the Fourier amplitudes are determined exactly. Thus, the described example accounts for the validation of the phase reconstruction procedure. Also, we have included noise filters in the real 2-D version of the

speckle code, which is expected to improve the quality of the reconstructions.

3.2 Speckle Image Reconstruction of Solar Features

3.2.1 KO Data

The speckle images obtained from KO (Section 2.2, Page 24, 29) were reconstructed using our speckle code. The following is the summary of our main results.

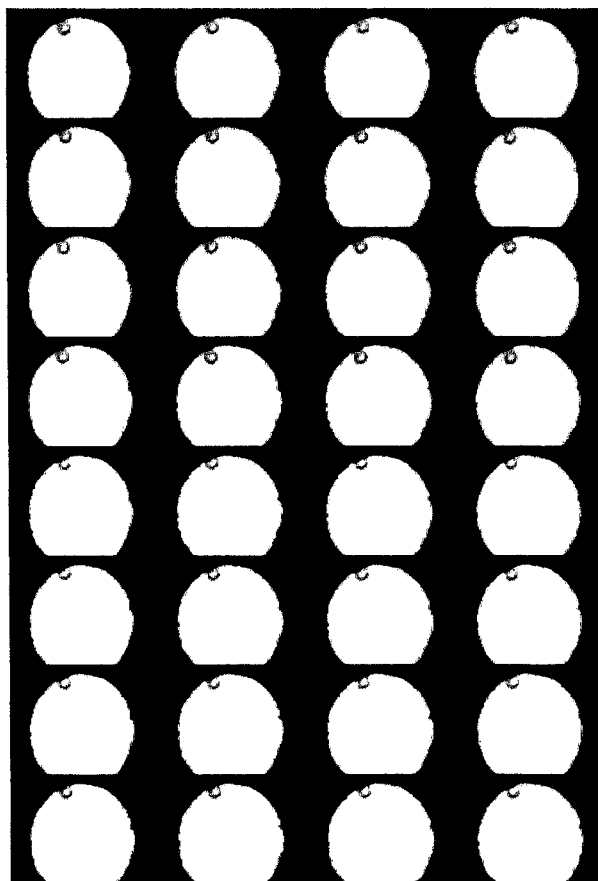


Figure 3.2: Two sequences of 16 images of a pore region. Each image covers a field-of-view of ~ 8.25 arc sec. The pore is seen in the top left sector near the edge of the field-of-view and contains a bright feature.

Feature 1: Figure 3.2 shows two typical sequences of 16 speckle images recorded on 3rd August 1998 around 1:45 UT. Each image is of 128 by 96 pixels. The circular white disc is the image of the pinhole (a portion of the Sun's image). The images were recorded using the 'hardware window' option of the frame-grabber. The image of the pinhole was not centered at the center of the window and hence a few rows of data near the bottom of the window have been lost. Thus, the complete circular image of the pinhole is not seen.

The pinhole covers a field-of-view of 8.25 arc sec. The first 16 images were recorded in succession at the rate of 11 frames per second, the next 16 images were recorded at the same rate after an interval of 17 seconds. The reason for displaying these images is the following: In each image, in the top left sector near the edge of the field-of-view, there is a pore and inside it there is a bright feature. The size of the pore is approximately 1.11 arc sec and the size of the bright feature within the pore is approximately 0.65 arc sec. The position of the pore is shifted slightly in the second sequence of 16 images (starting from 5th row) indicating that it is of solar nature and not due to dust. As the feature was near the edge, we could not process and reconstruct it.

Feature 2: Figure 3.3 shows another example of the presence of bright features inside the pores. It was observed on 4th August 1998 around 4:45 UT. The first four rows represent the first sequence of sixteen images. The image has been displayed on logarithmic scale in order to highlight the presence of the bright feature inside the pore. The region of pore has been encircled to highlight its presence. The feature keeps moving within the field-of-view, indicating its solar origin. Below the encircled region, there is a black spot (pore), which also keeps moving across the field-of-view. At the edge of this black spot, there is a very small bright feature (visible in images 13, 14, 15 and 16, fourth row from the top). The next 4 rows represent the second sequence of sixteen images.

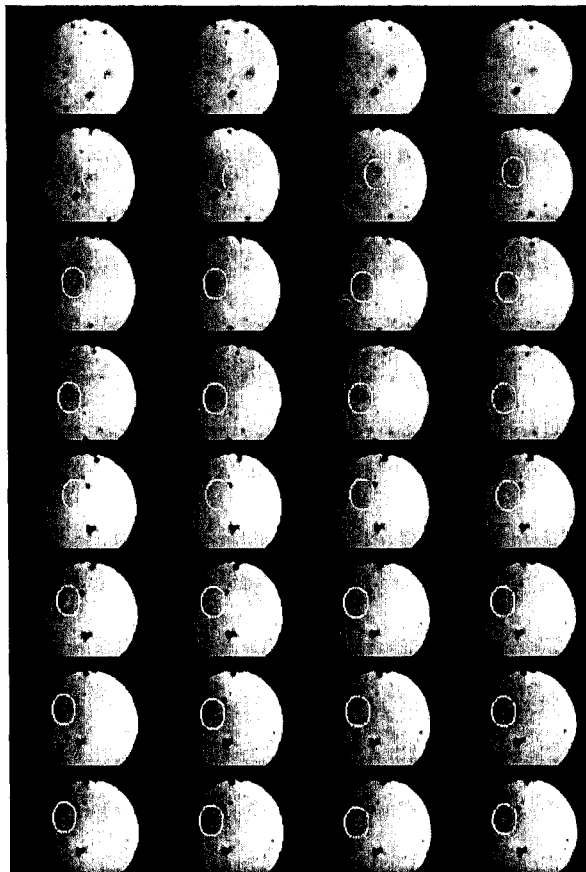


Figure 3.3: Two sequences of 16 images of a pore region. Each image covers a field-of-view of ~ 8.25 arc sec. The encircled region highlights a bright feature inside the pore.

Feature 2(a): Figure 3.4 shows a sequence of 18 images of size 2.16 arc sec square, containing the pore (and the bright feature). The first sixteen of these images represent a zoomed in version of the highlighted region of the the first sequence of 16 images in Figure 3.3. The seventeenth image is the average of the preceding 16 images. The eighteenth image is the reconstruction without amplitude calibration. The size of the pore is 0.7 arc sec and the size of the bright feature within it is ~ 0.3 arc sec.

Feature 2(b): Figure 3.5 shows a sequence of 18 images of size 1.49 arc sec square, containing the bright feature. The first sixteen of these images represent a zoomed in

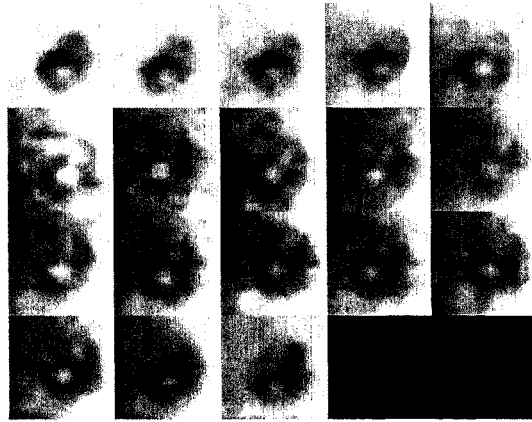


Figure 3.4: A sequence of 18 images; the first 16 represent a zoomed in version of the highlighted region of the first sequence of 16 images in Figure 3.3. The 17th image is the average of the preceding 16 images. The 18th image is the reconstruction without amplitude amplification. Each image is of size 2.16 by 2.16 arc sec.

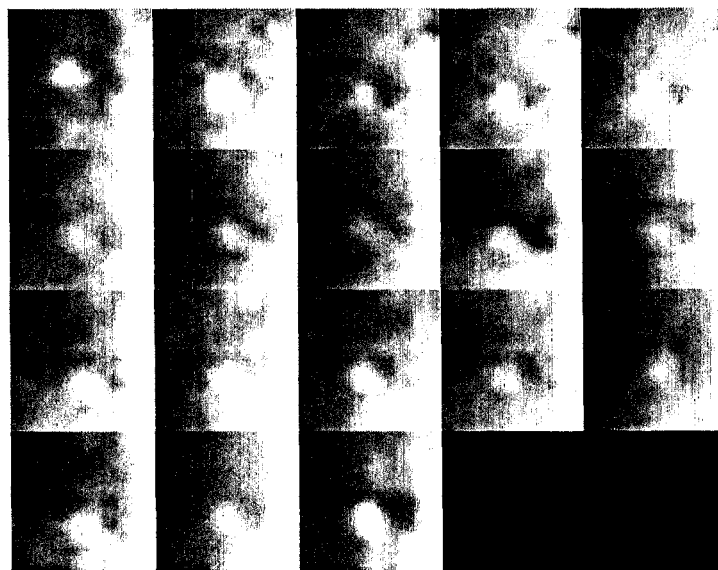


Figure 3.5: A sequence of 18 images; the first 16 represent a zoomed in version of the highlighted region of the second sequence of 16 images in Figure 3.3. The 17th image is the average of the preceding 16 images. The 18th image is the reconstruction without amplitude amplification. Each image is of size 1.49 by 1.49 arc sec.

version of the highlighted region of the second sequence of 16 images shown in Figure 3.3. The seventeenth image is the average of the preceding 16 extracted images. The eighteenth image is the reconstruction without amplitude calibration. The size of the bright feature is ~ 0.3 arc sec.

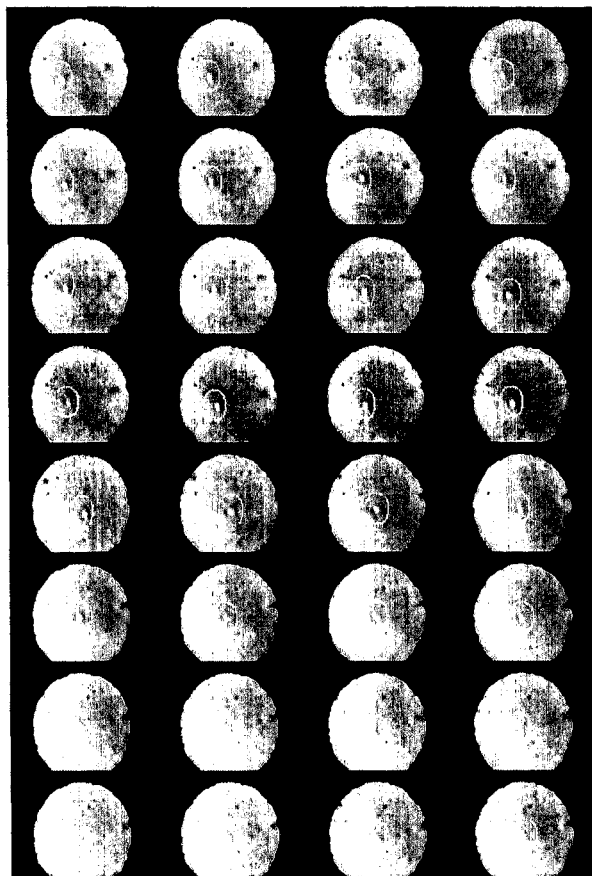


Figure 3.6: Two sequences of 16 images of a pore region. Each image covers a field-of-view of ~ 8.25 arc sec. The encircled region highlights a bright feature inside the pore.

Feature 3: Figure 3.6 shows a another sequence of images recorded on 3rd August 1998 around 1:55 UT. The images have been displayed on logarithmic scale to enhance the visibility. There is a small bright feature of size ~ 0.43 arc sec in all the 32 frames (two sequences). The spatial location of the feature is shifted from frame to frame.

Figure 3.7 shows a sequence of images of size 4.3 by 4.3 arc sec extracted from the Figure 3.6. The first 16 images (starting from top left) show the raw images corresponding to the first sequence. The seventeenth image is an average of all the preceding 16 images. Due to the motion of the feature from frame to frame, it is faintly visible in the average image. It indicates that the feature is riding on a huge background. The contrast of this feature (defined as $(I_f - I_{bg})/I_{bg}$, where I_f and I_{bg} are the intensities of the feature and the surrounding background respectively) varies from frame to frame with a minimum value of 8.9% and a maximum value of 11.6%. The average contrast is $\sim 10\%$. The eighteenth image (second row, last column) is the reconstructed image. The image was divided into four overlapping segments and then reconstructed using our speckle code. Fried's parameter was estimated using spectral ratio method for all the four segments. The contrast of the feature is enhanced in the reconstruction; it appears sharp. Moreover, it implies that the triple correlation technique is insensitive to the image motion; that is, even in the presence of small scale image motion, the phase reconstruction procedure brings out the presence of features. This is an advantage of the triple correlation technique over the Knox-Thompson algorithm. The next 16 images (starting from third row) represent the de-stretched images. The 35th image (fourth row, last but one column) shows the average of de-stretched images. The bright feature is clearly identified in the average de-stretched image. On the one hand, it shows the importance of de-stretching and on the other hand, it implies the correctness of the de-stretching code. The 36th image (fourth row, last column) shows the reconstruction from the de-stretched images. A dust speck, present near the lower right side of the features appears to be removed in the reconstructed images. This is another advantage of the triple correlation technique: the reconstruction is insensitive to instrumental aberrations. The next four rows represent similar images of the second sequence. The average contrast of the bright feature in the raw images of this subset is $\sim 13\%$.

The high frequency components are enhanced in the reconstructed images. They can be suppressed by restricting the amplitude amplification to only those regions

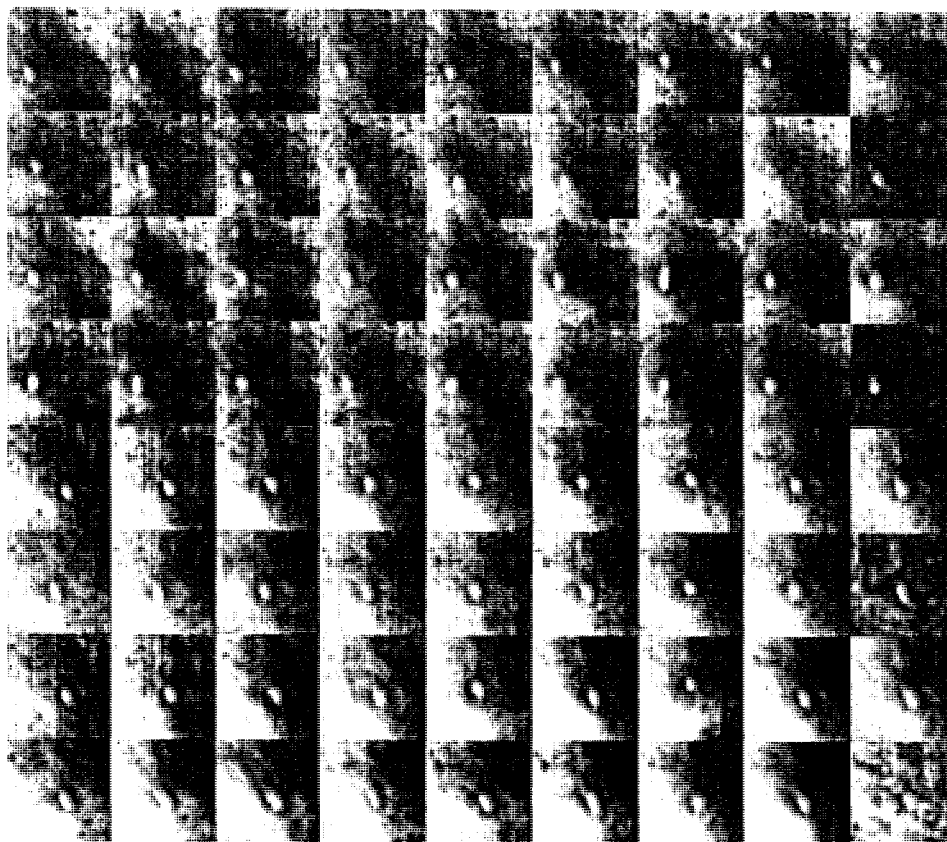


Figure 3.7: Two sequences of 36 images separated by 17 s; In each sequence, the first 16 represent a zoomed in version of the highlighted region of the first sequence of 16 images in Figure 3.6. The 17th image is the average of the preceding 16 images. The 18th image is the reconstruction. The next 18 represent the same images after de-stretching. Each image is of size 4.3 by 4.3 arc sec.

where the STF is greater than 0.1. In the reconstructions presented here, a value of 0.005 was used.

The feature has been observed for about 20 seconds in speckle images. This is the lower limit for its lifetime.

Feature 4: Figure 3.8 represents two sequences of images of a sunspot region. These images have been extracted from a recorded sequence of images and resized to 4.3 arc sec square. These images were recorded on 3rd August, 1998 around 2:00 UT. There is

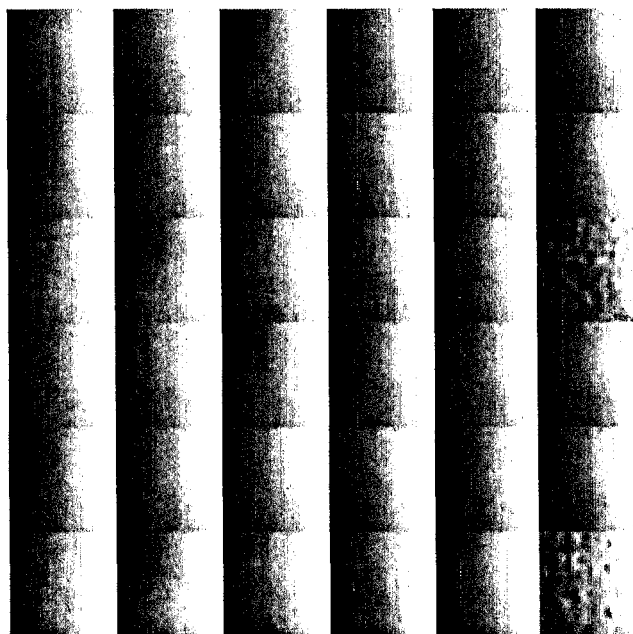


Figure 3.8: Two sequences of 18 images separated by 17 s; In each sequence, the first 16 represent a zoomed in version of a sunspot region. The 17th image is the average of the preceding 16 images. The 18th image is the reconstruction. Each image is of size 4.3 by 4.3 arc sec.

a gradient in the intensity values of the images. The intensity of the image increases gradually from left to right. This is a typical feature of any sunspot region near the limb. The first 16 images are pre-processed images. The 17th image (third row, last but one column) is an average of the preceding sixteen images. The 18th image (third

row, last column) is the reconstruction from the first 16 images. The images were divided into 4 overlapping segments and reconstructed using the speckle code. Fried's parameter estimated from spectral ratio technique was used in the reconstruction. High spatial frequency components have been enhanced in the reconstruction. The Fourier amplitudes were amplified only when the STF has value greater than 0.05. The processed images are featureless, whereas the reconstruction shows the presence of a small bright feature near the top right. The images in the next three rows (sixteen of them) are pre-processed images obtained from the next sequence of 16 images. The last two images are the average and reconstructed images respectively.

3.2.2 USO Data

In Section 2.2, (Page 27, 35) we described the details of the speckle observations at USO. Figure 3.9 shows a portion of the NOAA AR8898 recorded by us on 9th March 2000 around 5:30 UT. It was located at S13W20; at the Carrington longitude of 199, covering an area of 550 millionths of the solar hemisphere. It was visible on the solar disk between 2nd and 15th March 2000.

First, we recorded 16 sequences of images of size 57.6 by 67.8 arc sec centered at the bright region (centered at (65,44) in Figure 3.9, ~ 45 arc sec away from the beta type spot region that is present in the lower right corner). Then we recorded 28 sequences of images of the spot region.

As the tracking was poor, the effective size of the image available for reconstruction was nearly half the original size. We carried out two kinds of studies.

Case 1: Image Reconstruction:

We estimated r_0 for all the registered, de-stretched image sequences of the sunspot region and reconstructed the images using our speckle code. Having reconstructed the images of all the 28 sequences, we posed the following questions:

- How does the image reconstructed from 5 best frames compare with that reconstructed from all the frames?
- How does the image reconstructed from the 5 worst frames compare with that reconstructed from all the frames?
- How does the reconstruction (5 best frame, the 5 worst frames, all the frames) compare with that obtained as a collage of best isoplanatic patches, each patch compensated by telescope transfer function?

For each sequence, we selected the best segments using our frame selection method (Equation (2.7), page 29). We then generated a mosaic of the best isoplanatic patches. Figures 3.10 to 3.16 show the reconstructed images of all the 28 sequences. The first column corresponds to the speckle reconstruction from 5 best frames. The second column corresponds to the speckle reconstruction from the 5 worst frames. The third column corresponds to the speckle reconstruction from all the available frames of the sequence. The fourth column corresponds to the reconstruction obtained as a collage of the best isoplanatic patches.

The reconstructed images clearly show enhancement in the contrast. In a majority of the sequences, a good reconstruction has been possible with five best frames. This indicates that the bispectrum technique can provide good reconstructions even from a few good frames. This is basically due to the large number of estimates of the Fourier phases of the object (Pehlemann and von der Lühe, 1989). Though the reconstruction from all frames of any sequence is not as good as that from the 5 good frames, it is better than the image obtained as a collage of the best isoplanatic patches. The reconstruction from the 5 worst frames is comparable to that from all the frames. Thus, we conclude that the selection of the best frames significantly improves the quality of the reconstructions. The reconstructed image of the 14th sequence is entirely different from the rest because the sunspot region moved several arc sec away from the field-

of-view due to poor tracking. A few reconstructions do not show enhancement in the contrast (for example, sequences 17 to 20 and 22, 24 and 26). This could be due to the transient worsening of the sky conditions during the observations (heavy winds were present). A few reconstructions have high frequency fringes (artifacts) near the edges. This is due to the loss of field-of-view while de-stretching.

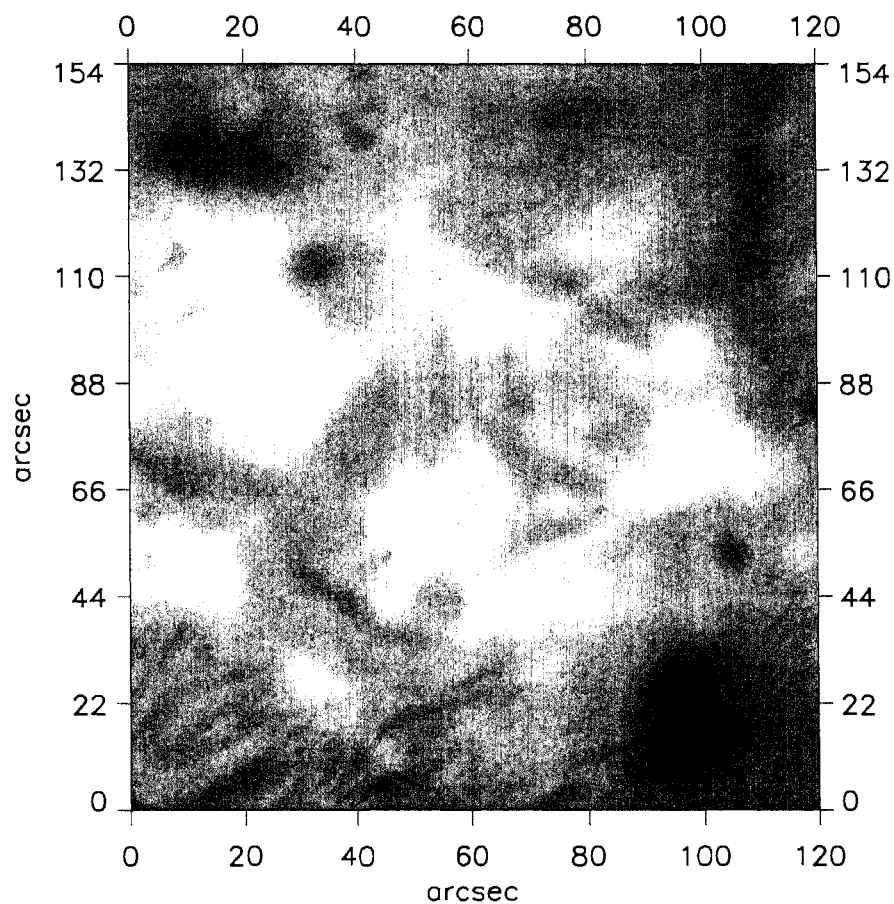


Figure 3.9: A portion the NOAA AR8898 recorded around 5:30 UT at the beginning of the observations. 16 sequences of images, each containing 100 images of size 57 by 67 arc sec centered at the bright region (65,44) were first recorded. It was followed by another similar sequence of 28 images centered at the sunspot (lower right).

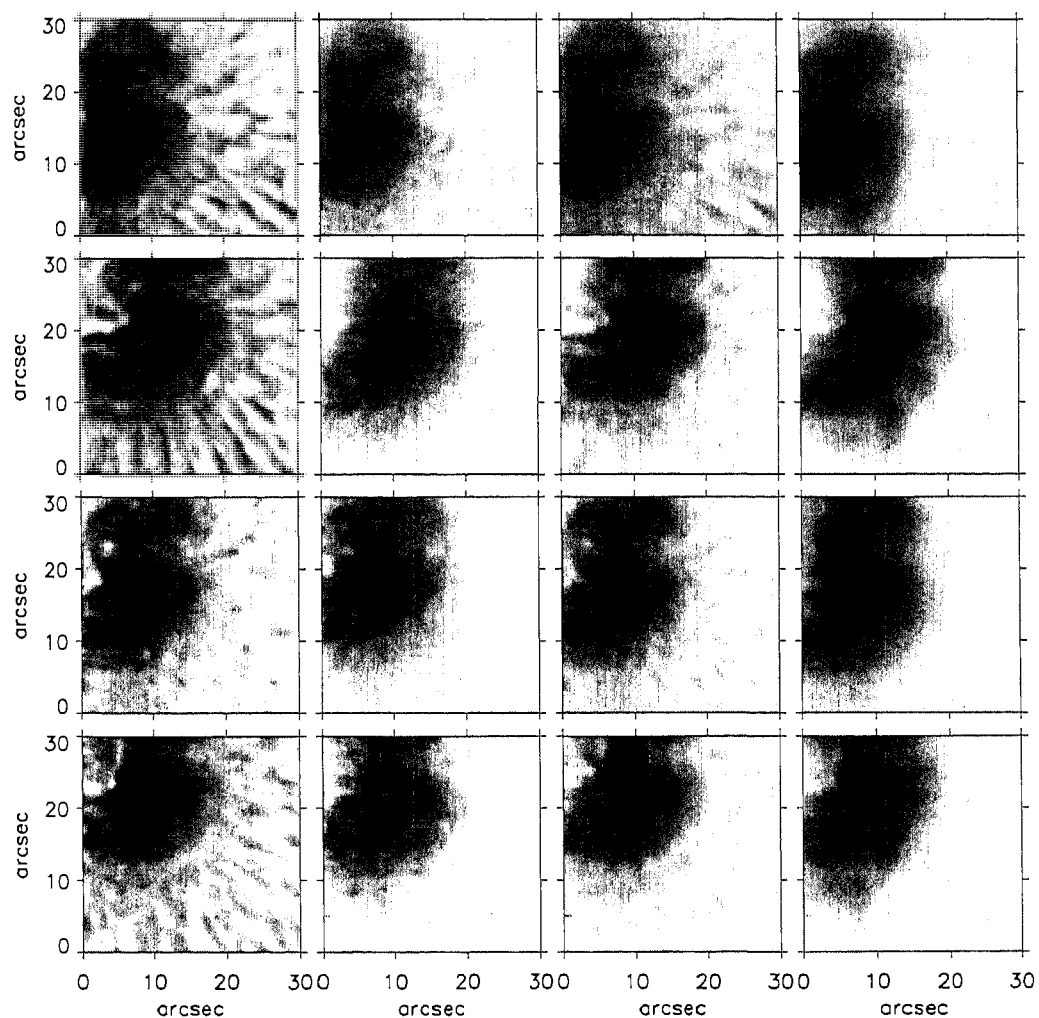


Figure 3.10: Reconstructed images of sequences 1 to 4 (row-wise). The first column is the reconstruction from 5 best frames. The second column is the reconstruction from the 5 worst frames. The third column is the reconstruction from all the frames (~ 90). The fourth column is the collage of best segments, each corrected for the transfer function of the telescope.

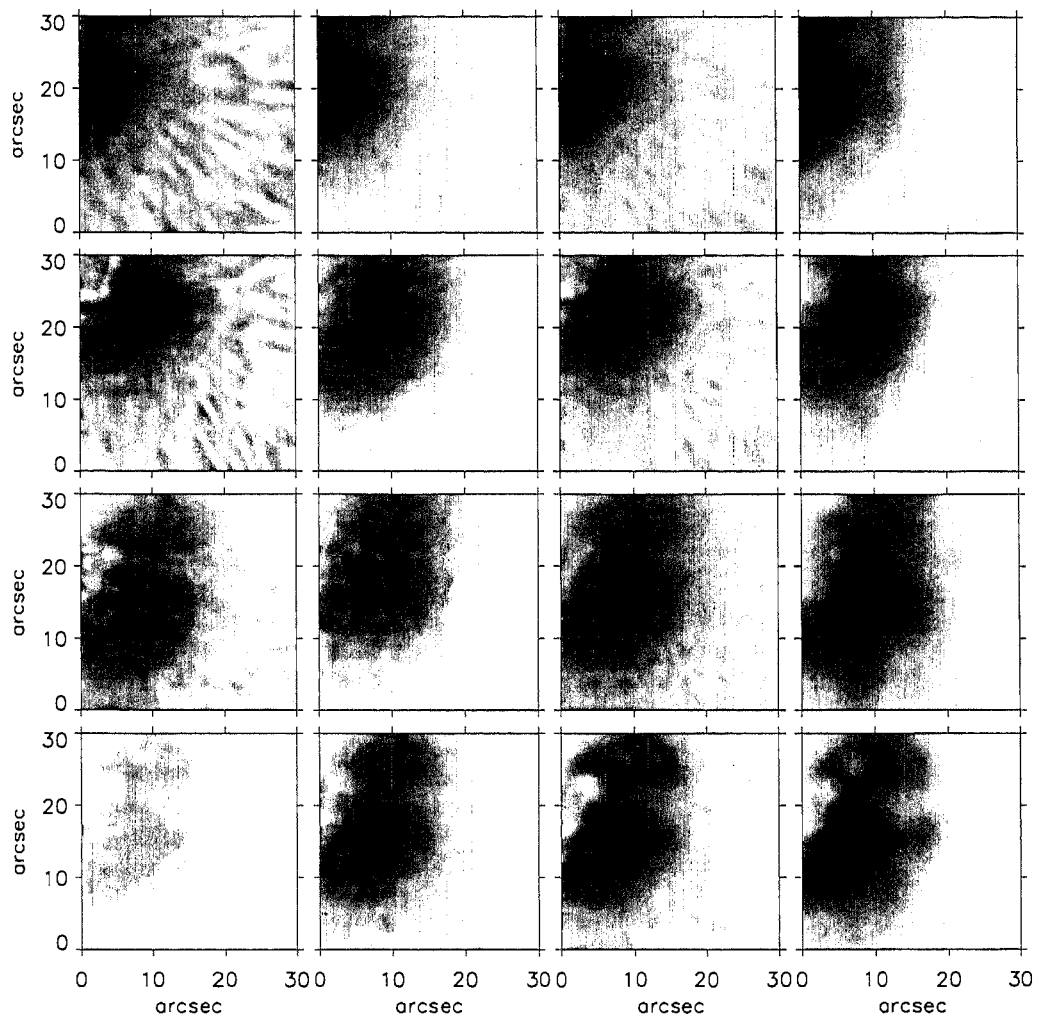


Figure 3.11: Reconstructed images of sequences 5 to 8. (row-wise). The first column is the reconstruction from 5 best frames. The second column is the reconstruction from the 5 worst frames. The third column is the reconstruction from all the frames (~ 90). The fourth column is the collage of best segments, each corrected for the transfer function of the telescope.

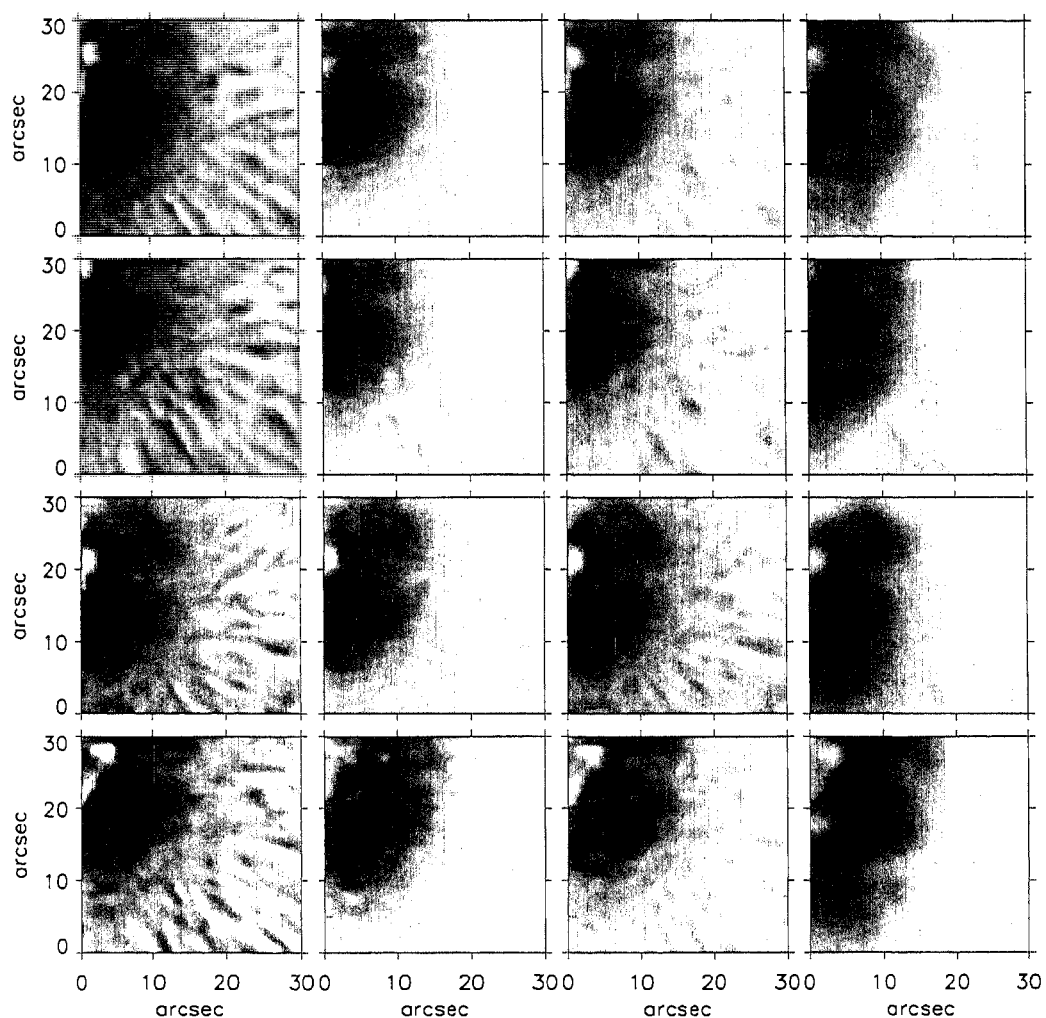


Figure 3.12: Reconstructed images of sequences 9 to 12. (row-wise). The first column is the reconstruction from 5 best frames. The second column is the reconstruction from the 5 worst frames. The third column is the reconstruction from all the frames (~ 90). The fourth column is the collage of best segments, each corrected for the transfer function of the telescope.

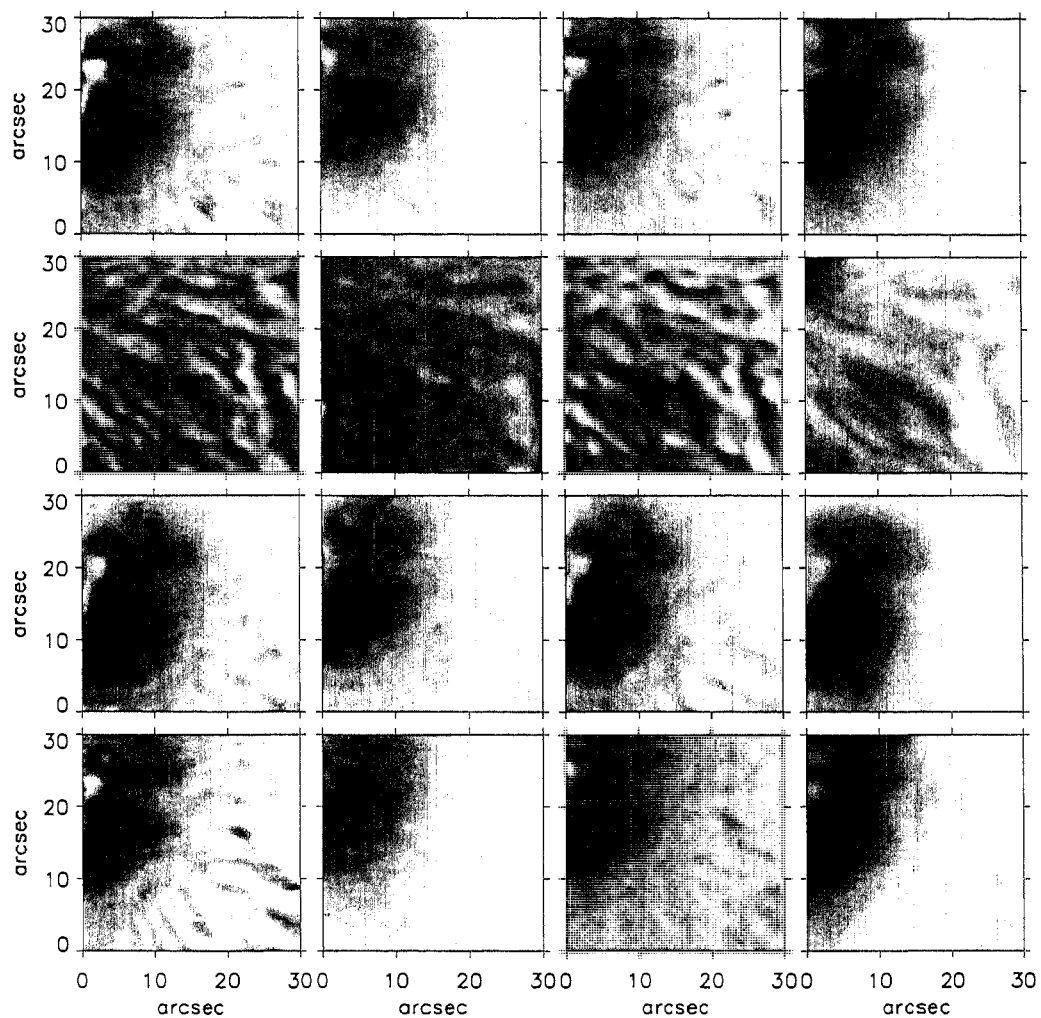


Figure 3.13: Reconstructed images of sequences 13 to 16. (row-wise). The first column is the reconstruction from 5 best frames. The second column is the reconstruction from the 5 worst frames. The third column is the reconstruction from all the frames (~ 90). The fourth column is the collage of best segments, each corrected for the transfer function of the telescope.

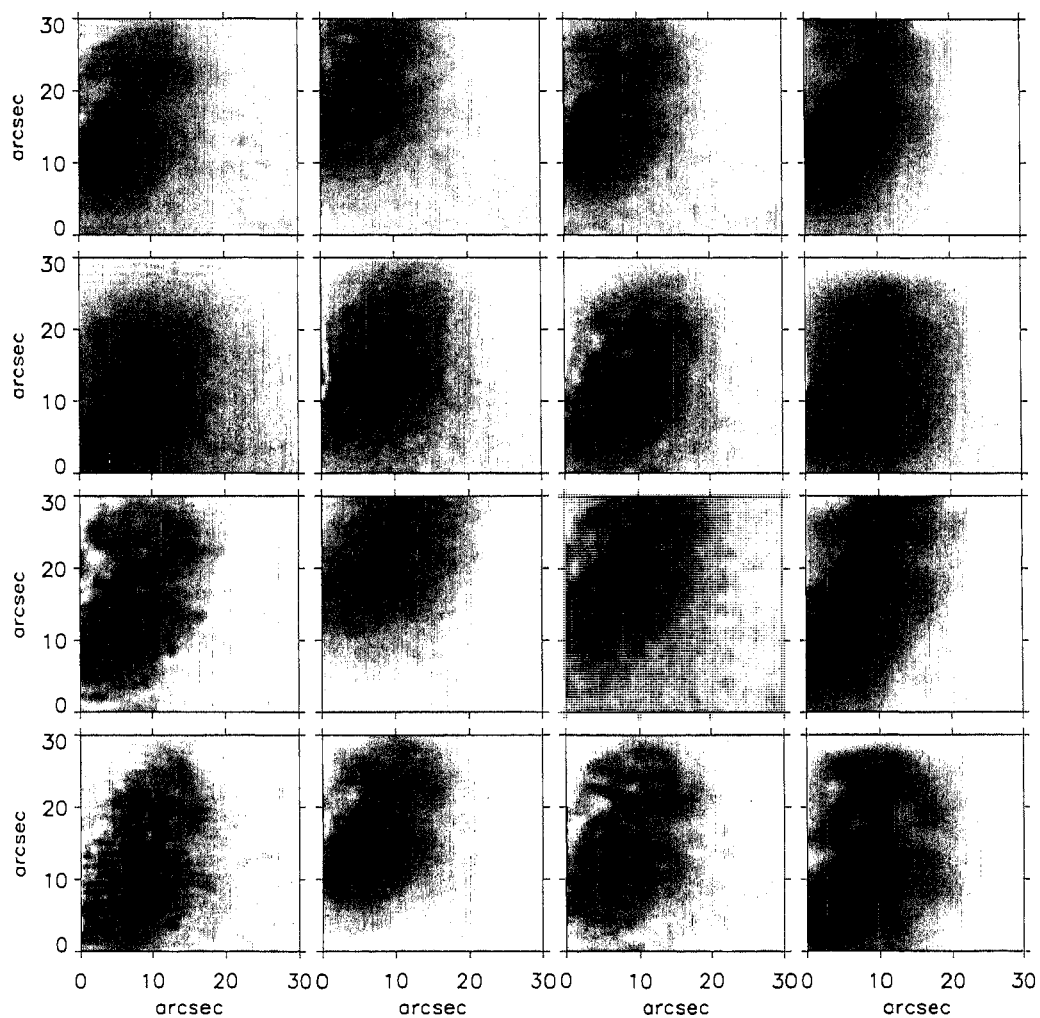


Figure 3.14: Reconstructed images of sequences 17 to 20. (row-wise). The first column is the reconstruction from 5 best frames. The second column is the reconstruction from the 5 worst frames. The third column is the reconstruction from all the frames (~ 90). Fourth column is the collage of best segments, each corrected for the transfer function of the telescope.

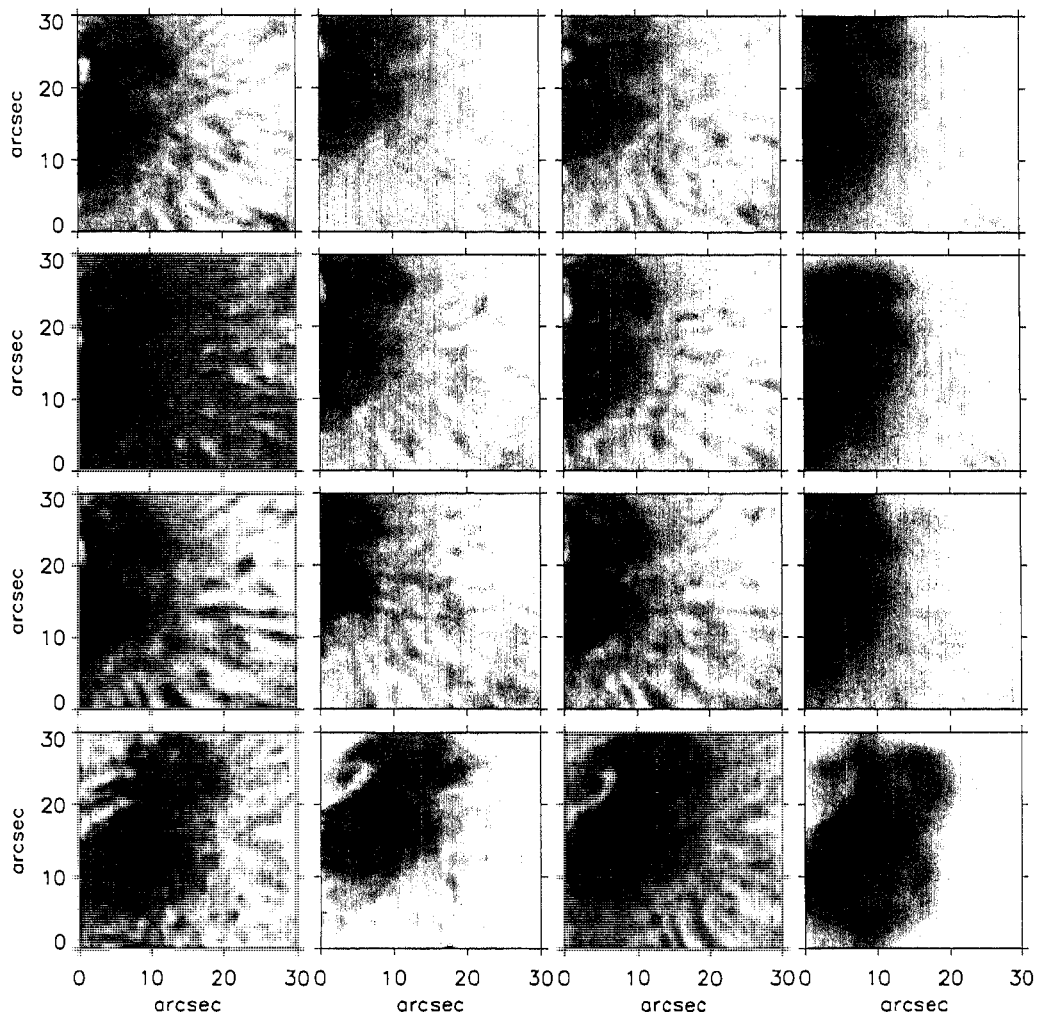


Figure 3.15: Reconstructed images of sequences 21 to 24. (row-wise). The first column is the reconstruction from 5 best frames. The second column is the reconstruction from the 5 worst frames. The third column is the reconstruction from all the frames (~ 90). Fourth column is the collage of best segments, each corrected for the transfer function of the telescope.

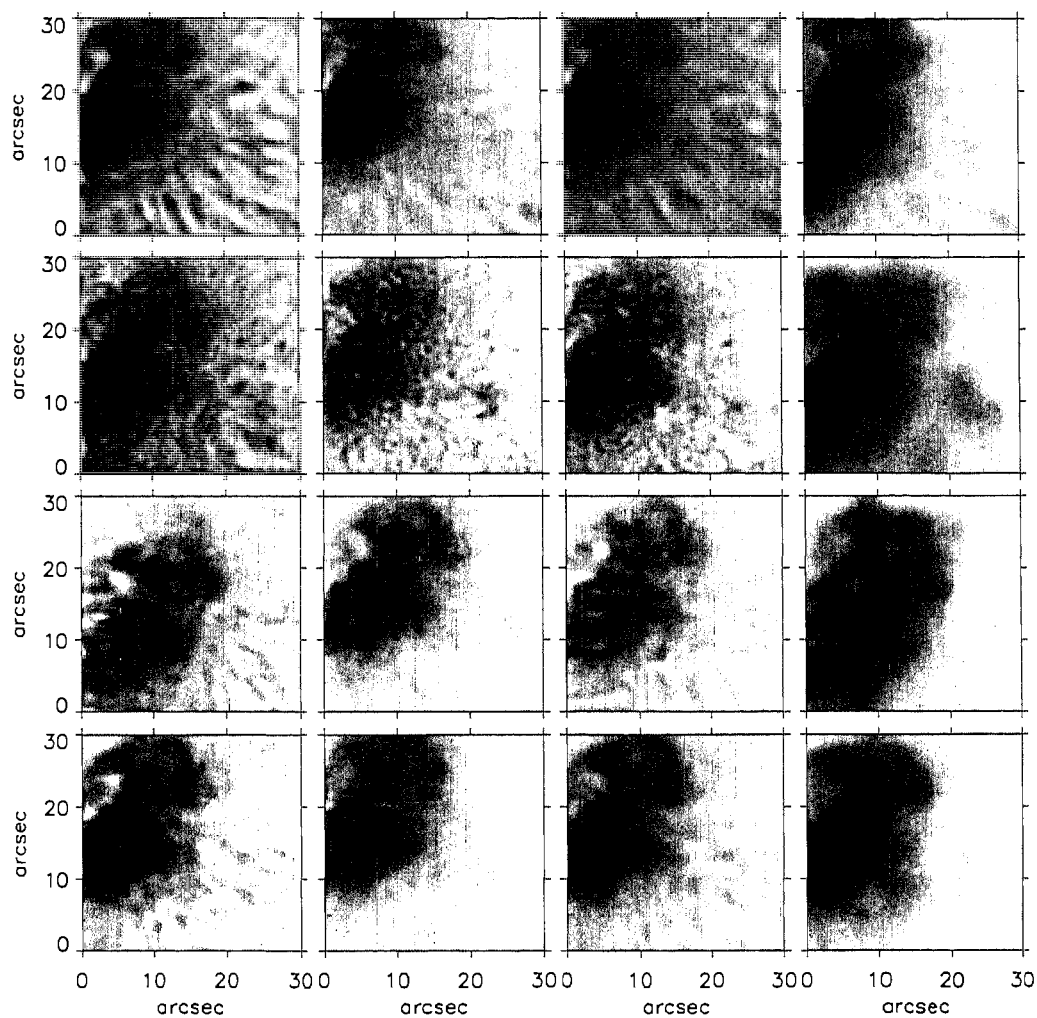


Figure 3.16: Reconstructed images of sequences 25 to 28. (row-wise). The first column is the reconstruction from 5 best frames. The second column is the reconstruction from the 5 worst frames. The third column is the reconstruction from all the frames (~ 90). Fourth column is the collage of best segments, each corrected for the transfer function of the telescope.

Case II: Speckle Image Reconstruction of sub-flare regions:

Filament break-up before a sub-flare: We selected the first 32 frames of each sequence (to reduce the influence of the tracking errors) and reconstructed 16 images using our speckle code. Figure 3.17 shows the reconstructed images. The time interval between consecutive images is approximately 112 seconds. A filament is seen to break up into several pieces during a period of ~ 30 minutes. It is known (Zirin, 1989) that filaments breakup with considerable twisting and turbulence at the start of a flare. However, one requires good sky conditions to observe such events. In the present case, we could observe this event even with relatively moderate seeing conditions only because of the speckle technique. Thus the regular use of the speckle technique will enable us to collect more details about such events.

Sub-flare near the edge of the sunspot: We selected the first 32 frames of each sequence (to reduce the influence of the tracking errors) and reconstructed 28 images using our speckle code. Figures 3.18 and 3.19 show the reconstruction of the 28 sequences (spanning an hour's duration). While the first two reconstructions show a sub-flare kernel (brightening) near the edge of the lower sunspot, the rest show two bright kernels. The two kernels later expand into a 'ribbon' connecting the original kernels. (seen in the reconstruction from 8th sequence and faintly visible in reconstruction from 7th sequence). The length of the ribbon is ~ 8 arc sec. As the time interval between two consecutive reconstructions is approximately 112 s, the elongation speed of the ribbon is ≥ 50 km/s . This is compatible with the values reported by Zirin (1989). The area of the region containing the two kernels is ~ 38 arc sec square. Thus it can be classified as a sub-flare. Occasionally, the kernel near the lower left appears to have two distinct bright components (reconstruction from sequences 9 and 10). There is brightening near the top left corner of the reconstructed images. This brightening occurs in the location of the filament break-up described earlier. In almost all the

reconstructions, small scale brightenings are seen inside the sunspot.

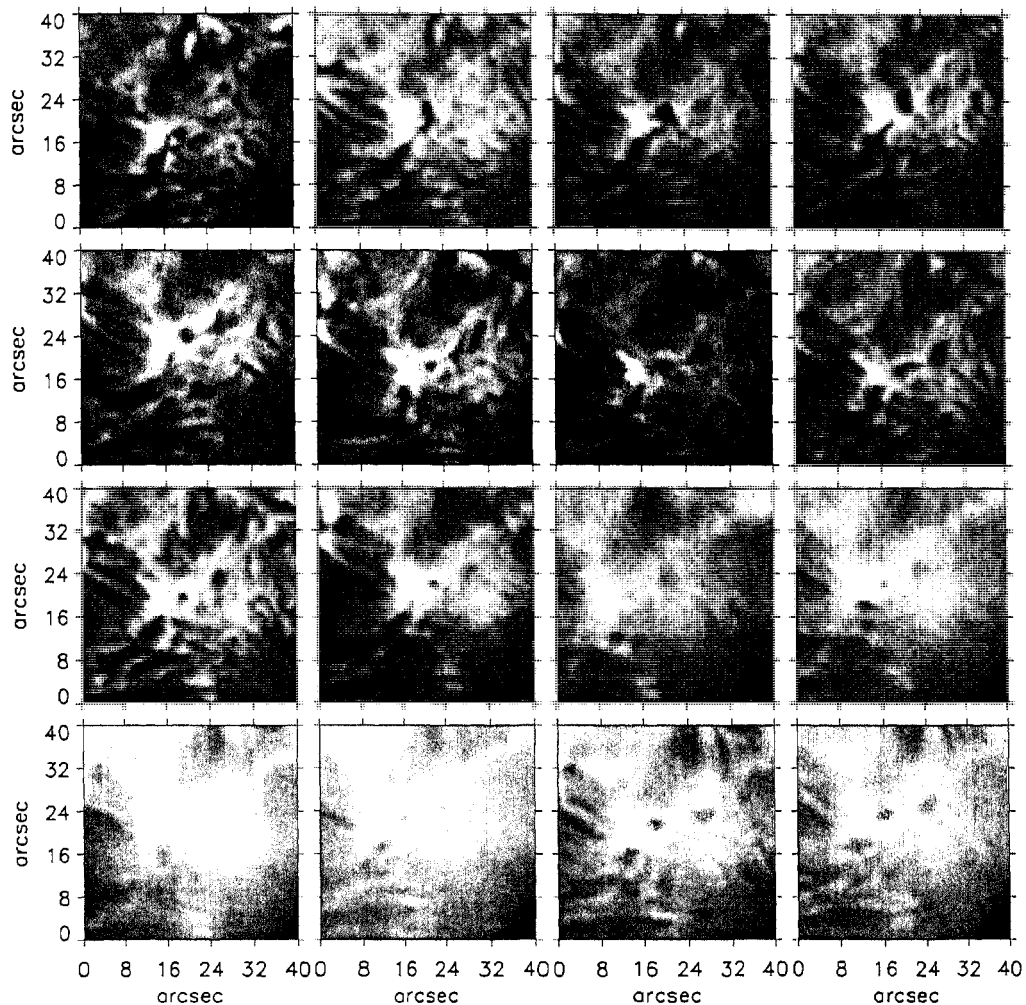


Figure 3.17: 16 consecutive reconstructed images of a sequence of sub-flare region. The filament break-up is clearly seen. A sub-flare erupted at this region a few minutes later.

3.2.3 Discussion

The images reconstructed from KO data contain features that are at the diffraction limit of the telescope. The enhancement in contrast of the reconstructed images is evident. High frequency artifacts appear even after multiplying the raw reconstruc-

tion with a Hanning function to smooth the object power spectrum before amplitude compensation. This could be due to the improper estimation of the noise power spectrum. We have observed the presence of bright features inside pores with a filter of 160 Å bandwidth centered at 6520 Å. Such small scale brightenings have been reported by Denker (1998).

We observed two sub-flare regions of AR8898 at USO. We observed the breaking up of a filament around 5:50 UT (we started our observations around 5:30 UT). Two small X-ray flares have been recorded by GOES at 6:11 UT and 07:22 UT (Figure 3.20) respectively. But the spatial locations of these X-ray flares is not known. we observed a sub-flare at the edge of the sunspot present in the region. At the same time there was an increase in the brightness near the location of the filament (seen as brightening in upper left corner of our reconstructions). We also found that three optical flares of class 3-4 have been observed on the same day at 14:57 UT, 15:02 UT, 15:08 UT respectively in the Active Region 8898. (<http://www.sec.noaa.gov/Data/solar.html/\#reports>). From the Kitt Peak magnetograms (recorded at 14:58 UT, on the same day), we see a polarity inversion line at the same location. Thus, the sub-flares that we observed preceded the onset of major flares in the region.

A few comments on the reconstruction of the images of the sub-flare region (sunspot region) are in order. All these images have been reconstructed with 32 frames (case II). In most of the cases, there is an increase in the contrast both inside and outside the sunspot region. Inside the sunspot, we see small scale brightenings, which, can be identified with the chromospheric umbral dots (Kitai, 1986). We measured the size of the dots in a few cases using a similar procedure described by Denker (1998) and obtained a value of ~ 2 arc sec. It is interesting to note the presence of such chromospheric dots, particularly during the occurrence of flares.

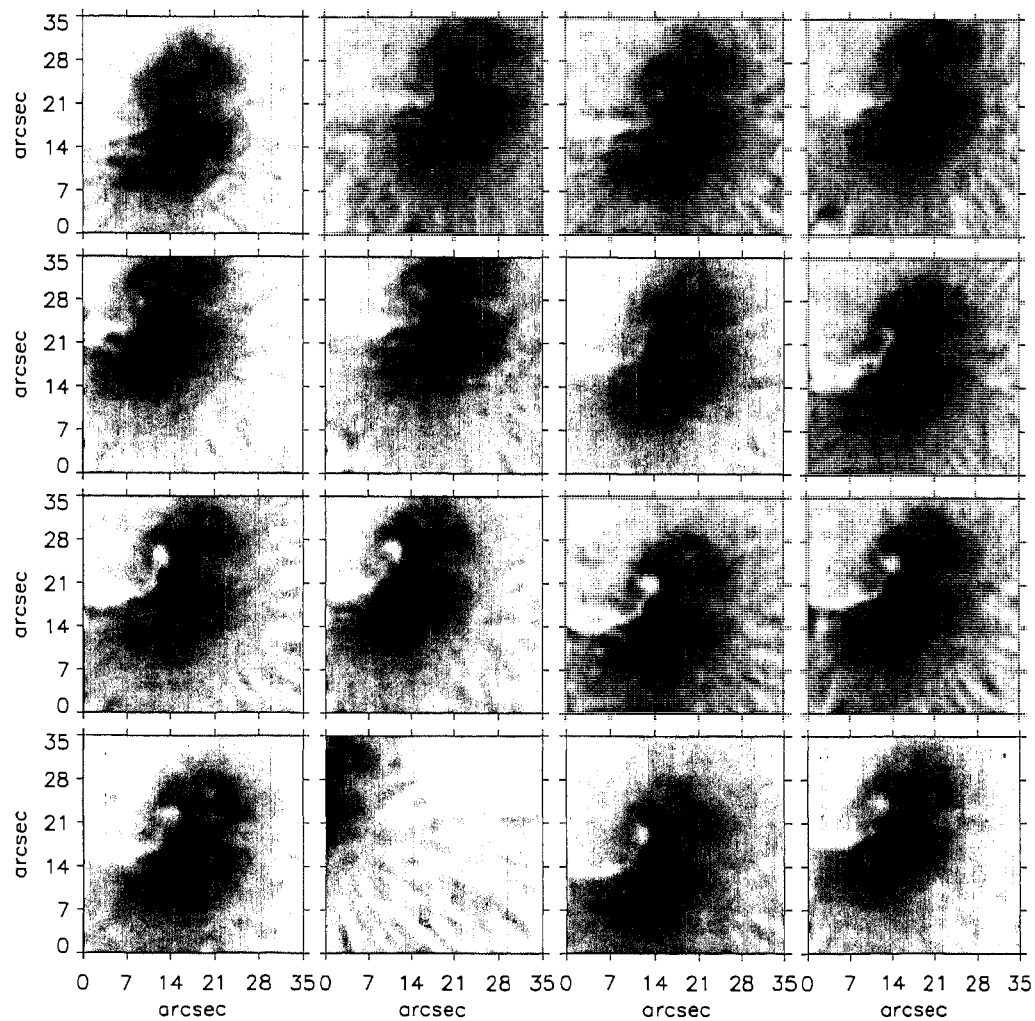


Figure 3.18: First 16 (out of 28) consecutive reconstructed images of a sequence of sub-flare region near the edge of a sunspot. The images have been reconstructed from 32 frames.

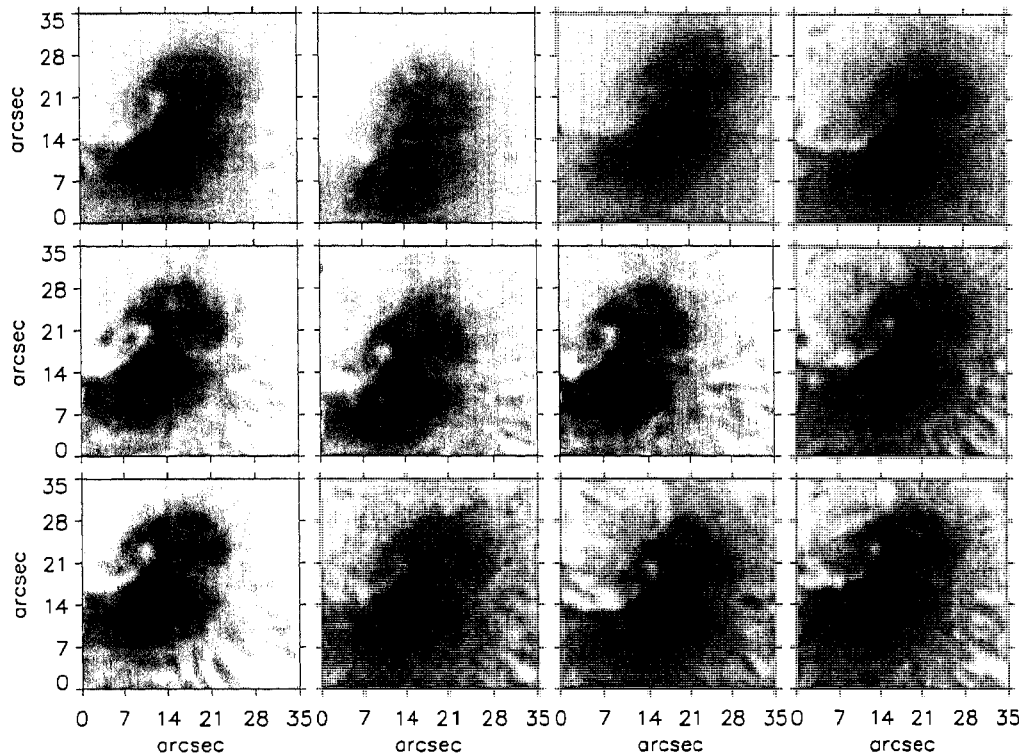


Figure 3.19: Last 12 (out of 28) consecutive reconstructed images of a sequence of sub-flare region near the edge of a sunspot. The images have been reconstructed from 32 frames

3.3 Summary

In this Chapter, we first described the practical methods adopted for analyzing speckle data. Then we presented the details of our speckle code and validated it (particularly phase reconstruction procedure) with an example. We used our speckle code to reconstruct small scale solar features. In our speckle observations at KO, we found tiny small scale brightenings inside pores. Observations of these features have been possible only because of the short exposure nature of the speckle observations. We have presented the speckle reconstruction of two sub-flare regions of NOAA AR8898. We found the breaking up of a small filament. We also found presence of chromospheric umbral dots

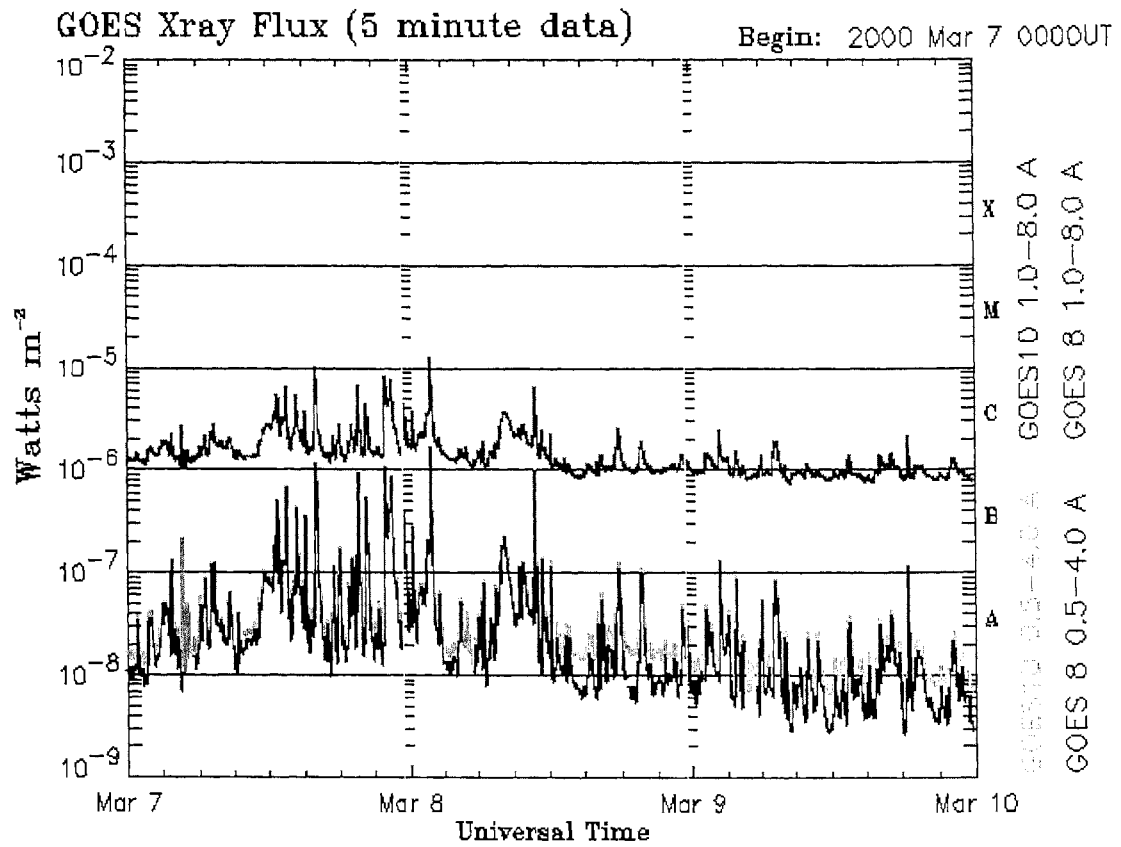


Figure 3.20: GOES X-ray flux recorded during 7–9 March 2000. The two flare-events that coincided with our observations have been marked. (Courtesy: NOAA/SEC, Boulder, CO, USA).

inside the sunspot from our speckle reconstructions. Our speckle reconstructions show enhancement in the contrast, even with a few good frames. The high redundancy of phase information increases the signal-to-noise of the reconstructions (Pehlemann and von der Lühe, 1989). The typical life-times of small scale solar features is ~ 30 seconds (von der Lühe and Zirker, 1988). Thus ability to reconstruct an image from a small number of frames (speckle images) is essential while observing with large telescopes and our speckle code meets that requirement.

Chapter 4

On the Morphological Relationship Between G-Band and Ca II K Network Bright Points

4.1 Introduction

The solar surface exhibits very high contrast bright points of size ~ 0.2 arc sec in short exposure filtergrams obtained with an interference filter of ~ 10 Å passband centered at 4305 Å from the best sites under good seeing conditions (Berger *et al.*, 1995; Kitai and Muller, 1984; Muller and Roudier, 1984; Muller, 1985). This wavelength region of the solar spectrum was originally designated by the letter ‘G’ by Fraunhofer and is currently known as ‘G-band’. It is densely populated with absorption lines of the CH radical and a few elements. It is formed in the upper photosphere (Zirin, 1989). It is observed (Berger and Title, 1996) that the bright points occur without exception on the sites of isolated magnetic flux concentrations. It is believed that (Title *et al.*, 1992; Keller, 1992; Yi and Engvold, 1993; Berger *et al.*, 1995) the observed bright points can be associated with ‘thin flux tubes’ (Spruit, 1976) which have become a standard

theoretical model for the small scale magnetic flux in the solar photosphere. Berger and Title (2001) have investigated the relationship between the the bright points of the G-band and the photospheric magnetic field, using co-temporal observations at G-band, Ca II λ 3933 K line, Fe I 6302 Å magnetograms and 6563 Å H α and identified a class of G-band bright points that appear on the edges of bright, rapidly expanding granules and are non-magnetic (at the flux limit). Recently, Steiner, Hauschildt and Bruls (2001) compared the theoretical G-band spectrum, computed on the basis of a realistic atmosphere for a magnetic flux tube with that from the quiet Sun surroundings and found that the former has significantly high intensity throughout the spectrum because it is hotter than the quiet Sun and the difference is more pronounced within the range of CH band lines. They attributed the enhanced contrast in the G-band to the reduction in the abundance of the CH radicals through dissociation in the deep photospheric layers of the hotter flux-tube atmospheres compared to the quiet Sun surroundings; this process weakens the CH lines within the flux tube and allows more of the continuum to shine through the thinned forest of CH lines.

The lower ($h < 1500$ km) and middle ($1500 \leq h \leq 2250$ km) chromosphere of the Sun reveals a conspicuously bright network of cells of size ~ 33000 km when observed in the K line of Ca II (Title, 1966; Foukal, 1990). The walls of the cells are outlined by bright flocculi. The cells are well defined except for occasional gaps in the cell boundaries and are present everywhere in the disk. The cellular pattern is lost near the limb but bright flocculi survive. Near the active region, the cell is completely filled with bright material and the cell forms the part of chromospheric faculae. It is found that the chromospheric network is closely associated with the photospheric network which in turn is highly associated with the distribution of the longitudinal magnetic fields at the photosphere (Chapman and Sheeley, 1968). The origin of the chromospheric network lies in supergranulation, a cellular pattern of horizontal motions in the upper photosphere covering most of the quiet Sun. The supergranulation is closely related to both the chromospheric and the photospheric networks. It is believed

that the horizontal currents associated with each supergranule sweep the magnetic fields to its boundaries and these magnetic fields cause excess heating, which, in turn causes the bright chromospheric network (Bray and Loughhead, 1974). It is also known that supergranular flows do not always fill the cell, as evidenced by incomplete cell boundaries.

The Network Bright Points (NBPs) of the photosphere (Stenflo and Harvey, 1985; Muller, 1985) have been identified to exhibit high contrast in violet band head of CN radical (Chapman, 1970) and in the G-band (Muller, 1985). It is also known that the NBPs are closely associated with the coarser calcium network bright points (Chapman and Sheeley, 1968; Muller, 1985). However, it is puzzling to note that while the G-band bright points are distributed all over the disk (Berger *et. al*, 1995; Muller, 1985), the chromospheric network bright points are preferentially present along the boundaries of the network cells. In this Chapter, we try to address the following question: What is the physical phenomenon that dictates the preferential heating at the chromospheric levels, though the sources from below - if assumed to be the G-band bright points - are distributed all over the disk? To find an answer to this question, we performed near-simultaneous observations at the G-band and the K line of Ca II at three different regions of the solar surface. In the following Sections, we describe the details of our observations and analyses, and discuss the results in the light of the aforementioned question.

4.2 Observations

A quiet Sun region, a plage region and the NOAA AR8923 were observed near simultaneously at the K line of Ca II ($\lambda = 3933 \text{ \AA}$) and at the G-band of CH radical ($\lambda = 4305 \text{ \AA}$) on 24th, 25th and 26th March 2000 respectively, using the 76 cm Dunn Solar Telescope of the Sacramento Peak Observatory (Evans, 1967), Sunspot, New Mexico, USA. The selected region of the primary image was collimated using a telecentric lens

Series	Date (ddmmyy)	Time UT	$\Delta t(\text{ms})$		θ	M		Remarks
			G-band	Ca II K		G-band	Ca II K	
A	24.03.00	15:28:41	50	50	269.383	150	150	QR
B	24.03.00	15:36:48	50	50	269.278	300	300	QR
C	25.03.00	14:57:40	70	70	170.527	300	300	RAR
D	25.03.00	15:12:53	70	70	171.652	300	300	RAR
E	25.03.00	15:28:17	70	70	172.836	300	300	RAR
F	25.03.00	15:43:35	70	70	173.973	300	300	RAR
G	26.03.00	14:42:26	70	50	181.131	300	300	AR8923
H	26.03.00	15:01:17	70	50	181.584	50	50	AR8923
J	26.03.00	15:04:08	70	50	181.650	50	50	AR8923
K	26.03.00	15:06:43	70	50	181.700	50	50	AR8923
L	26.03.00	15:09:14	70	50	181.765	50	50	AR8923
M	26.03.00	15:12:00	70	50	181.831	50	50	AR8923
N	26.03.00	15:14:45	70	50	181.897	50	50	AR8923
O	26.03.00	15:19:05	70	50	181.997	50	50	AR8923
P	26.03.00	15:21:42	70	50	182.062	50	50	AR8923
Q	26.03.00	15:24:14	70	50	182.125	50	50	AR8923
R	26.03.00	15:26:55	70	50	182.190	50	50	AR8923
S	26.03.00	15:29:39	70	50	182.256	50	50	AR8923
T	26.03.00	15:32:25	70	50	182.322	50	50	AR8923

Table 4.1: Characteristics of observations performed at Sacramento Peak. Observations were performed at $\lambda = 430.5 \pm 0.5$ (G-band) and $\lambda = 393.3 \pm 0.15$ (Ca II K) near-simultaneously. First column represents different series of data recorded. Second and third columns represent the date and Universal Time of the observations. Δt is the exposure time. θ is the heliocentric position angle of the observed region. M is the number of frames recorded per series. Plate scale for G-band data is 0.07396 arc sec per pixel and for Ca II K data is 0.09343 arc sec per pixel. QR - Quiet Region, RAR - Remnant Active Region (Plage Region), AR8923 - NOAA Active Region 8923.

of focal length 1500 mm. Another telecentric lens of focal length 1553 mm formed the final image, with a plate scale of 3.89 arc sec per mm. A 50/50 cube beam splitter was placed in the path of the beam immediately after the image forming lens. A G-band filter with 10 Å passband was placed in one beam and a Ca II K filter with 3 Å FWHM was placed in the other. The 16 bit Pixel Vision camera consisting of 512 by 512 square pixels of size 24 micron was used to record a few sequences of images at the K line of Ca II at the rate of one frame per 2.7 s. The 10 bit Thompson camera consisting of 640 by 640 square pixels of size 19 micron was used to record a few sequences of images in the G-band at the rate of one frame per 2.7 s. The field-of-view was 47.8354 by 47.8354 arc sec with 0.09343 arc sec per pixel for the images recorded in the K line and 47.3371 by 47.3371 arc sec with 0.07396 arc sec per pixel for the images recorded in the G-band. The theoretical resolution of the telescope was 0.13 arc sec at the K line of Ca II and 0.14 arc sec at the G-band. Table 4.1 indicates finer details of the observations.

4.3 Analysis

Since the exposure time was more than 20 ms, the recorded G-band bright points were smeared in most of the frames. The images were recorded with at the rate of 2.7 s per frame. Assuming the value of sound speed as 10 km per second, the life time of the features is ~ 10 s. Thus, we could not use more than 3 consecutive frames for speckle reconstructions. Moreover, because of poor seeing conditions, the images were completely blurred on many occasions. Thus, we could not perform analysis of long time sequences. Instead, we selected three consecutive best images using our frame selection method (Section 2.7, Page 29) and obtained a speckle reconstruction for each region (AR8923, plage and quiet Sun regions). Figures 4.1 and 4.2 represent the reconstructed images of a plage region in Ca II K line and G-band respectively. Figures 4.3 and 4.4 represent the reconstructed images of a quiet Sun region in Ca II K

and G-band respectively. Figures 4.5 and 4.6 represent the reconstructed images of the AR8923 in Ca II K and G-band respectively. The images recorded in G-band were rotated, re-sampled and shifted (using `sushift.pro` mentioned in Chapter 3) to match the Ca II K images. The required amount of shifts were estimated up to half a pixel accuracy by cross-correlating the US Air Force target pattern recorded at Ca II K line and G-band.

In the absence of continuum images, we adopted the following procedure to extract the G-band bright points from the reconstructed images

- We used a ‘blob finding’ algorithm (Tomaita, 1990; Berger *et al.*, 1995) to extract bright blobs from the reconstructed image
- We then performed an un-sharp masking to sharpen the edges of the blobs.
- We then obtained a binary image by setting the intensity values of all the pixels above a ‘hard’ threshold to unity and the rest to zero. We selected the threshold using the following criteria: We obtained an histogram of the un-sharp masked image and empirically selected a value (1.25 for plage region, 0.4 for quiet Sun region, and 0.5 for the AR8923) at the right side of the peak. We found the average intensity of all the pixels having value greater than the selected value minus one standard deviation as the threshold value.
- We then ‘opened’ (Haralick, Sternberg and Zhuang, 1987) one copy of the binary image using dilation and erosion processing with 5 pixel kernel to reduce the large residual granulation noise. We subjected another copy of the binary image to a median filter to reduce the noise due to isolated peaks (salt and pepper noise).
- Finally we created a binary bright point map by performing a Boolean ‘OR’ operation of the two copies of the binary images. Figures 4.7, 4.8 and 4.9 show the binary bright point maps of the plage region, quiet Sun region and the AR8923 overlaid on the corresponding G-band images.

4.4 Results and Discussion

In what follows, we present a detailed comparison of the processed image of Ca II K and the G-band image for the three different regions. We refer to the features in the Figures by their co-ordinates. For example, [0,0] represents lower left corner of the image; [45,45] represents upper right corner of the image. A feature covering more than a single point in the image is represented by the coordinates of its lower left corner and the upper right corner. We use the term GBP to denote G-band bright points. The Ca II K images (Figures 4.1, 4.3, and 4.5) printed on tracing sheets, have been placed on top of the binary bright point maps overlaid on the corresponding G-band images (Figures 4.7, 4.8 and 4.9), to help the readers to clearly see the points mentioned below.

Plage region (Figure 4.1 and 4.2):

1. At the outset, we find a striking correlation between the large scale distribution of the GBPs and the bright network of the Ca II K line.
2. The GBPs seem to be shifted horizontally by 0.5 arc sec with respect to the Ca II K network bright points. Since we have aligned the images as accurately as possible, we can not attribute this offset (~ 5 pixels) to alignment errors. However, as mentioned in Section 4.2, the field-of-view of the G-band images is less than that of Ca II K images by 0.5 arc sec. This could perhaps be the reason for the spatial mismatch. At the same time, we also find a GBP aligned with an isolated brightening in Ca II K image ([1,3] in Ca II K image). This implies that the error due to the difference in the field-of-view is distributed throughout the image.
3. In a majority of the cases, for a brightening in Ca II K image, there is an associated GBP.
4. There are a few brightenings in Ca II K images, for which there are no associated GBPs. For example, brightenings in Ca II K images at [9,35], [10,37], [15,37], [4.5,13; 6.5,13] do not have associated GBPs that can be clearly identified.

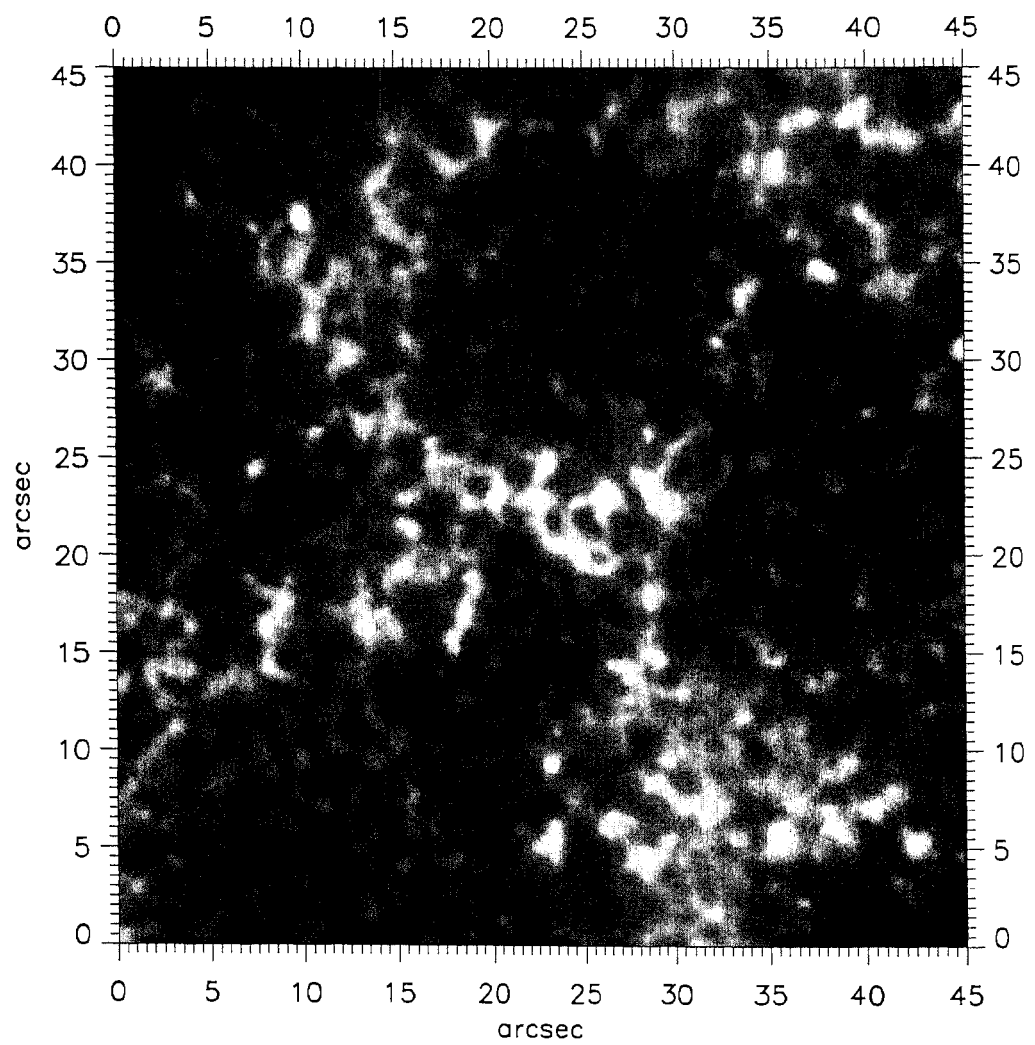


Figure 4.1: Image reconstructed from three best frames of a plage region in Ca II K line.

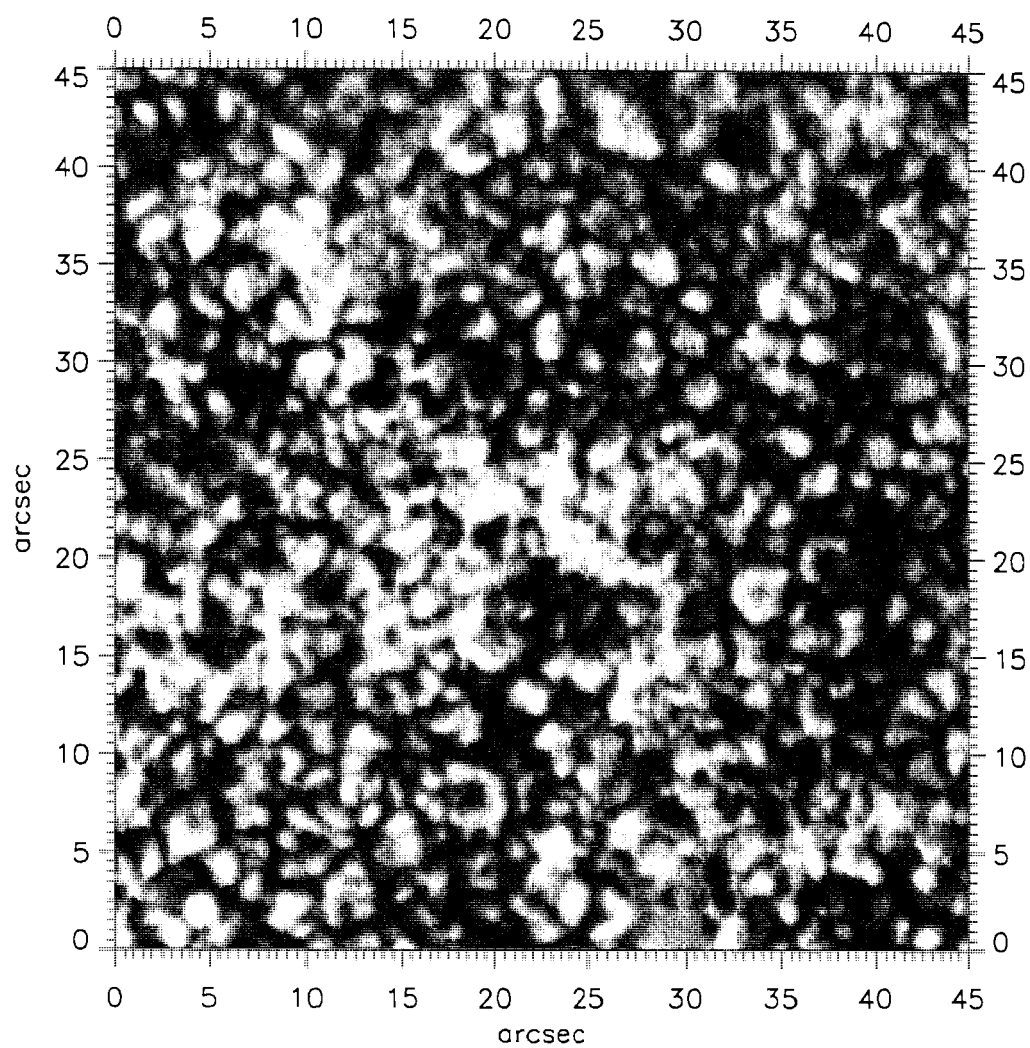


Figure 4.2: Image reconstructed from three best frames of a plage region in G-band.

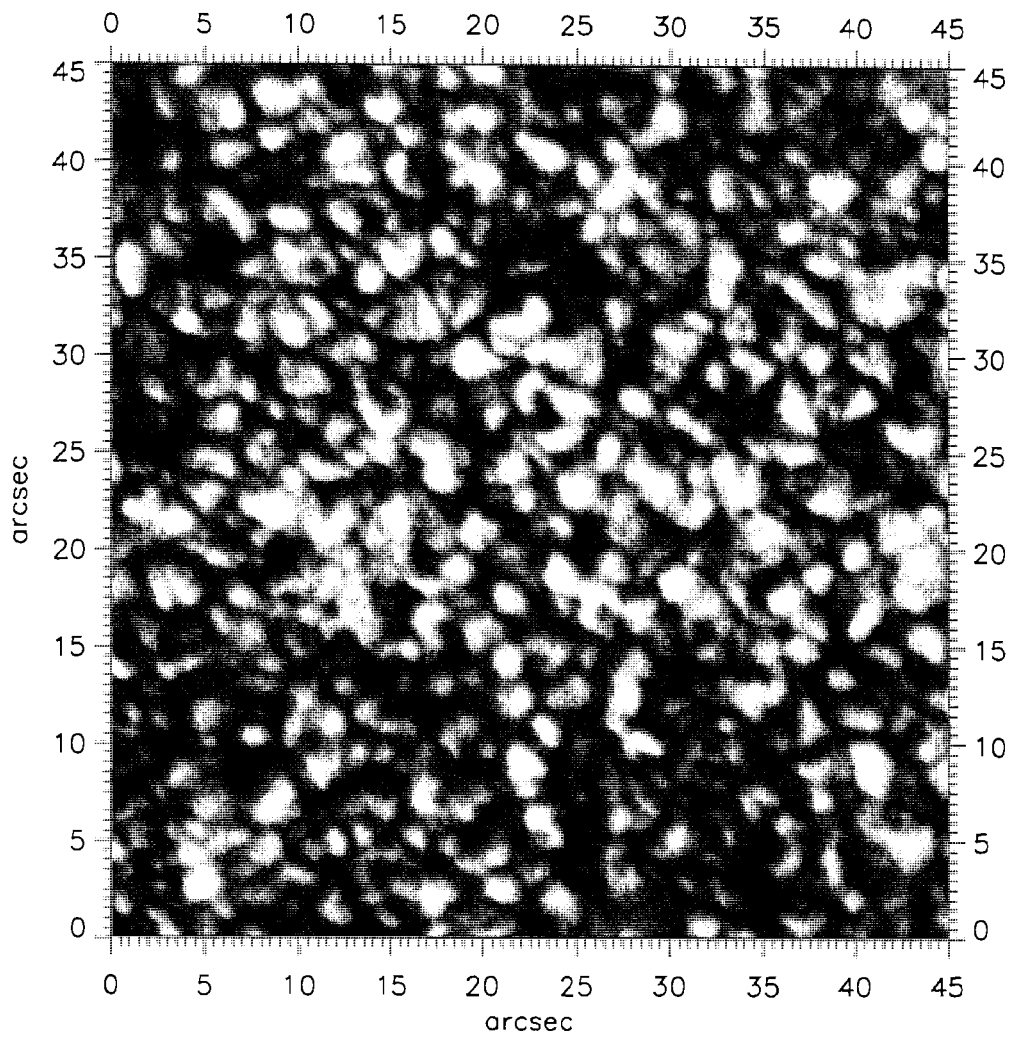


Figure 4.4: Image reconstructed from three best frames of a quiet Sun region in G-band.

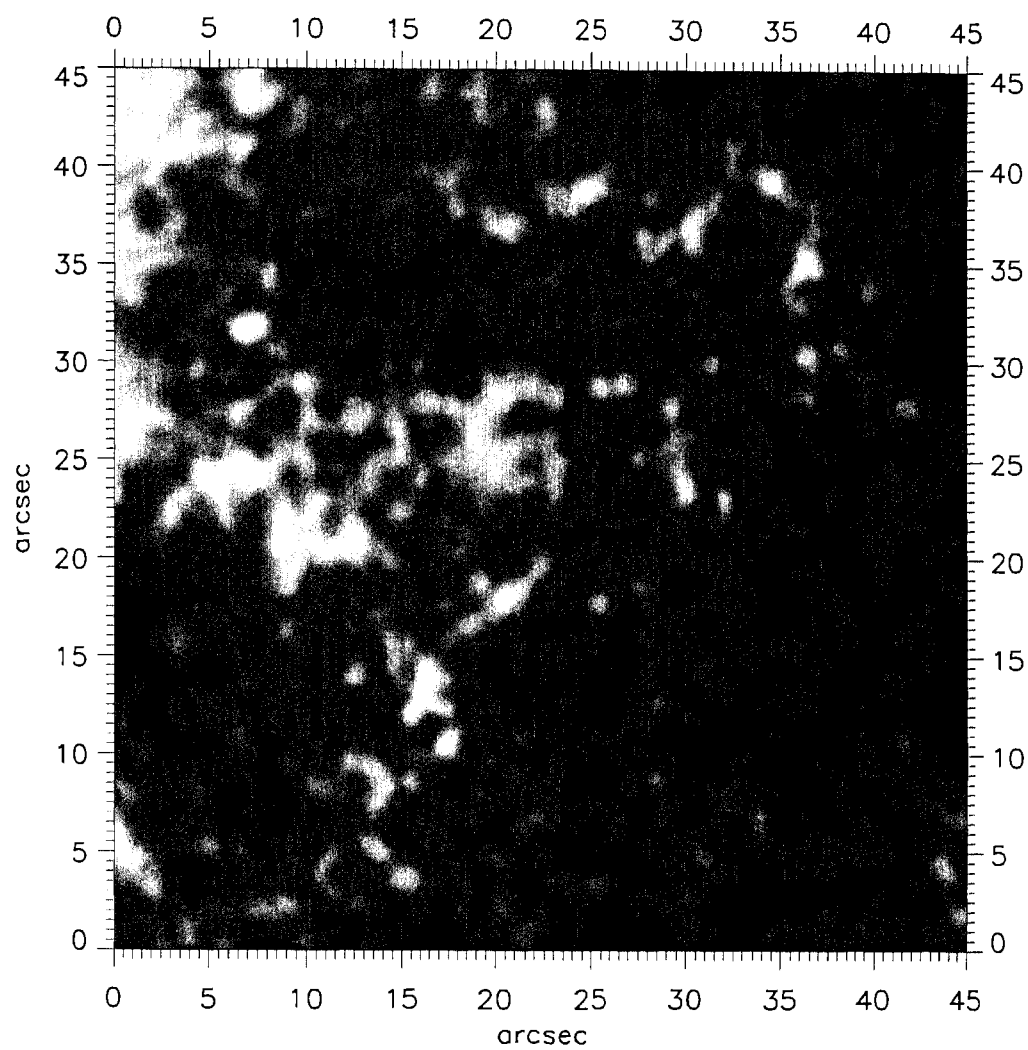


Figure 4.5: Image reconstructed from three best frames of NOAA AR8923 in Ca II K line.

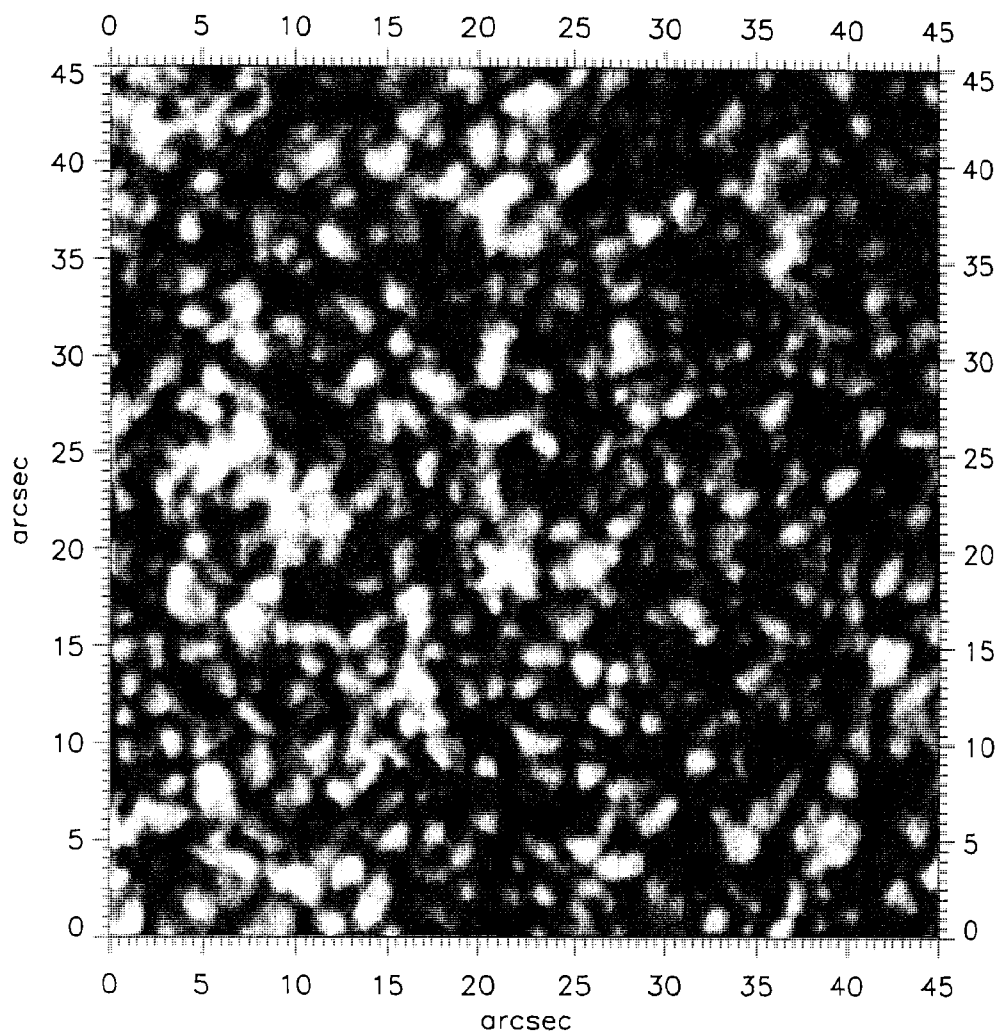


Figure 4.6: Image reconstructed from three best frames of NOAA AR8923 in G-band.

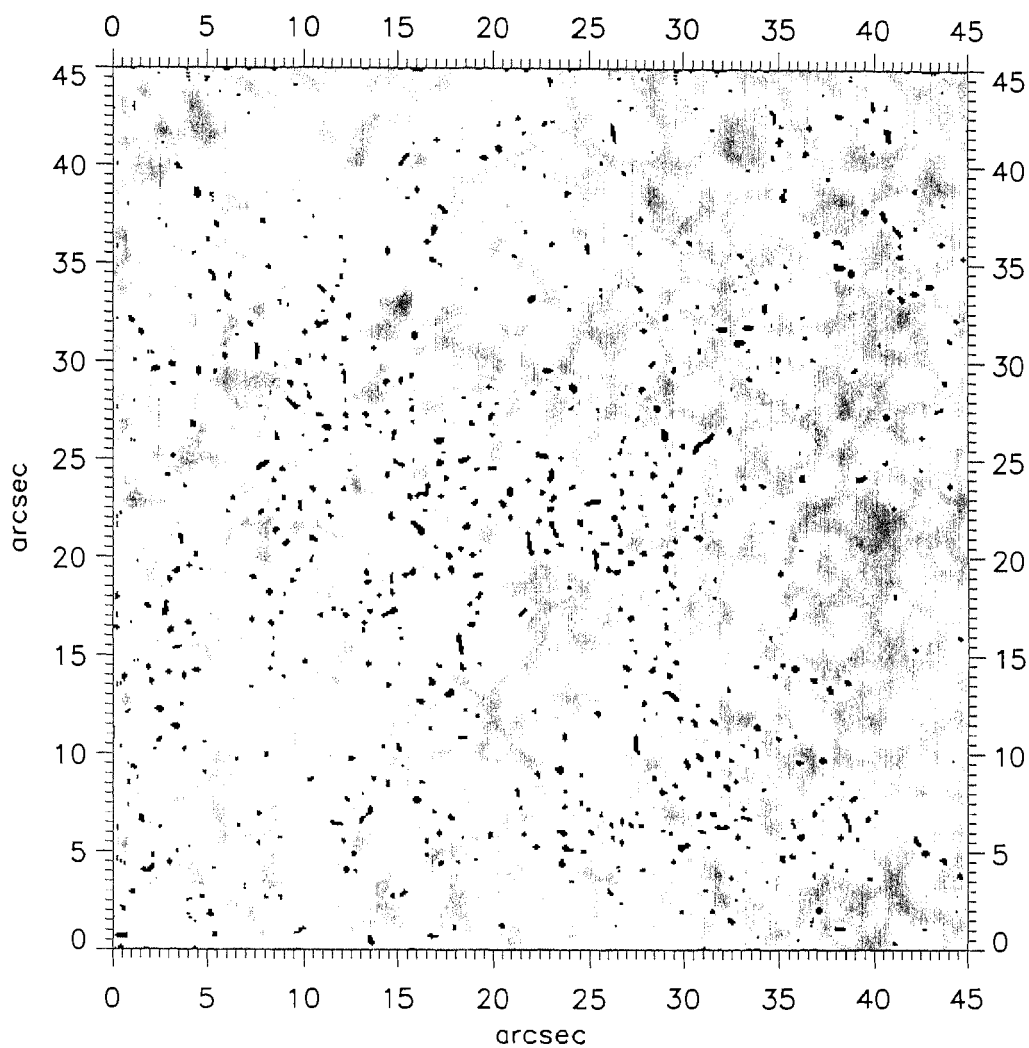


Figure 4.7: G-band binary map of a plage region overlaid on the corresponding reconstructed G-band image.

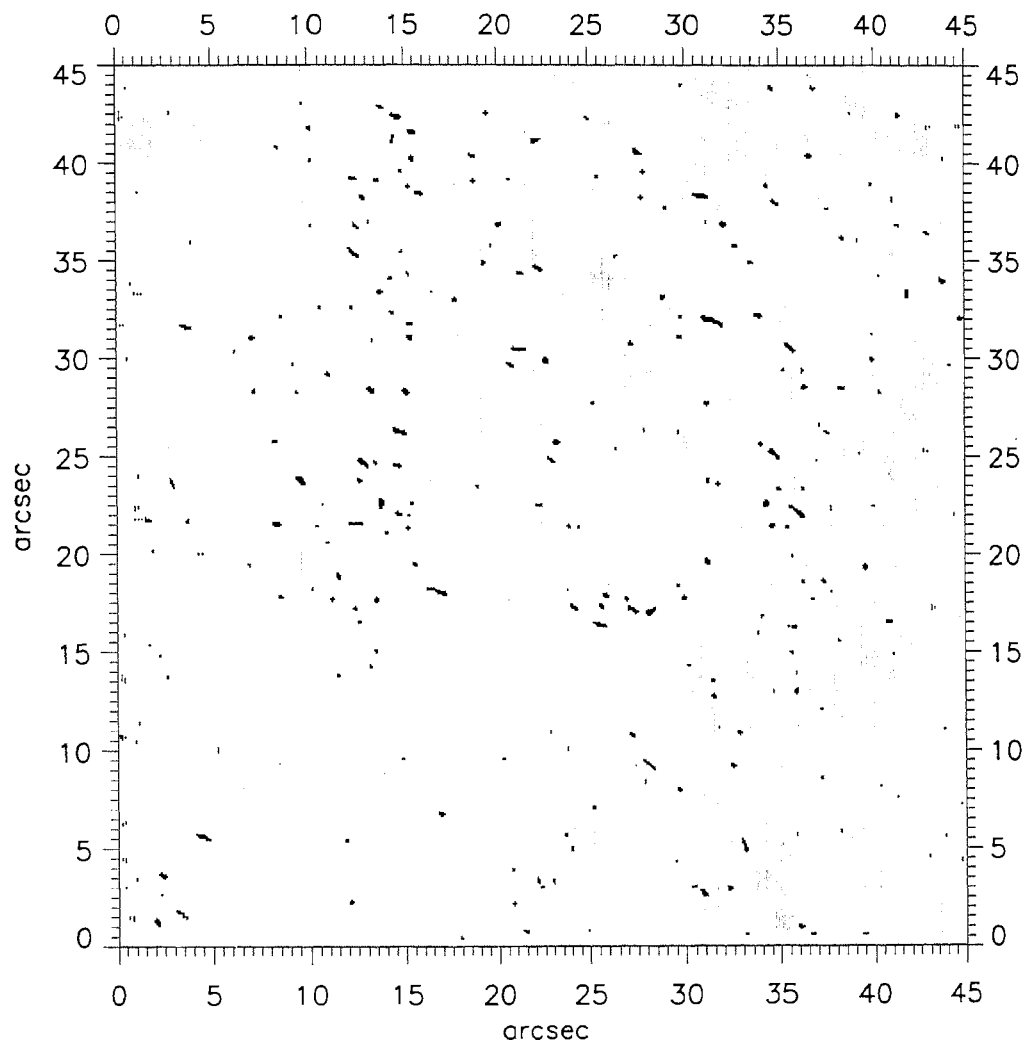


Figure 4.8: G-band binary map of a quiet Sun region overlaid on the corresponding reconstructed G-band image.

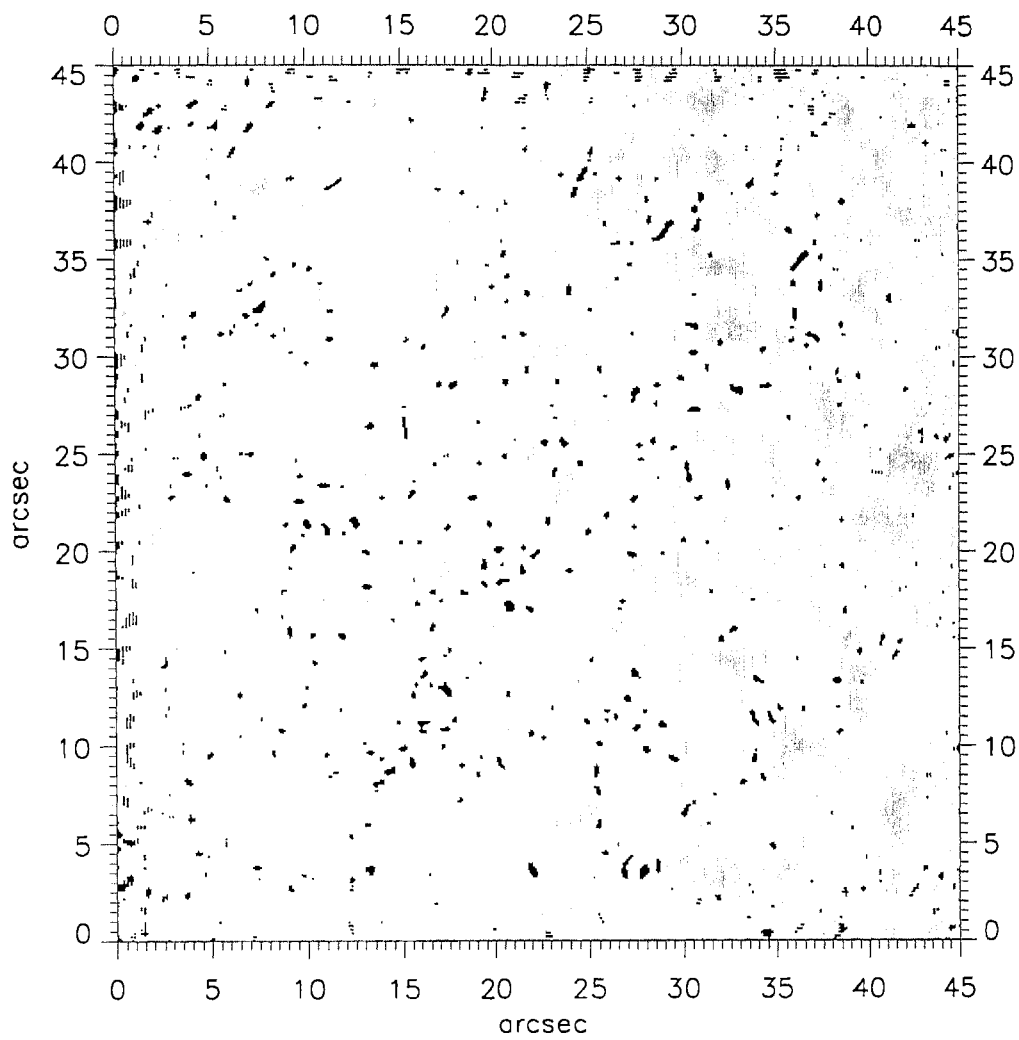


Figure 4.9: G-band binary map of the NOAA AR8923 overlaid on the corresponding reconstructed G-band image.

5. Relatively darker regions in Ca II K images have associated GBPs that are either co-spatial or offset by 3-6 pixels.

Quiet Sun Region (Figures 4.3 and 4.4):

1. The conspicuous network pattern in the Ca II K image ([7,16; 17.5,27]) has associated GBPs; but these GBPs are spread diffusely (unlike the dense clustering in plage region).

2. The brightening in the lower right corner of the Ca II K image ([41,3.5; 43,7]) does not have an associated GBP; The brightening at [43,32; 45,34] has got a tiny associated GBP at its edge; that is, at [45,32] in G-band image. In general, the brightenings on the right hand side edge of Ca II K image do not have associated GBPs.

3. Not all the brightenings in Ca II K image have associated GBPs.

4. Relatively darker regions of Ca II K image have associated bright points which are clearly evident; but in a few cases, this tendency is not clear.

AR8923 (Figures 4.5 and 4.6):

1. All the brightenings in Ca II K image have associated GBPs. The spatial density (the number of bright points per square cm) appears to be proportional to the degree of brightenings; that is, the higher the intensity in Ca II K image, the denser the distribution of bright points.

2. Here again, GBPs occur near the edges of Ca II K brightenings; at a few places GBPs are co-spatial with the Ca II K brightenings.

3. Relatively darker regions of Ca II image have got associated GBPs.

4. There is an isolated brightening in Ca II K image ([25.5,17.5]) for which there is no associated GBP.

In general, we find that the GBPs are densely clustered in the plage region than in quiet and the AR8923. However, since our exposure time was large, most of the GBPs could have been washed out and this could be one of the reasons for the absence of GBPs for some brightenings in Ca II K. This also implies that only those GBPs that are relatively larger in size and withstood the atmospheric blurring have been identified.

Our G-band binary map also contains bright points that are relatively bigger. These could be residuals of granulation. It should also be remembered that our bright point maps are vulnerable to the threshold value. The relatively higher density of GBPs at the locations of brightenings in Ca II K images implies that these GBPs must be of magnetic origin (as the Ca II network has been popularly known as poor man's magnetogram; Bray and Loughhead, 1974). Thus, there could be two varieties of GBPs: those closely associated with the photospheric magnetic field distribution and those present every where. Even these intra-network bright points could be associated with the intra-network Ca II K bright points (Sivaraman and Livingston, 1982), not resolved in the present data. The bright points which are present everywhere are swept by the horizontal motions in the supergranulation to the boundaries and hence there is clustering. At the same time, GBPs are continuously formed at all locations and hence at any given time we get to see the GBPs everywhere.

4.5 Summary

We performed speckle observations of a quiet Sun region, a plage region (remnant active region) and the NOAA AR8923 near-simultaneously at G-band and Ca II K with an exposure time of 50-70 ms and a frame rate of one frame per 2.7 seconds. We selected three consecutive best images from the sequences of images of the aforementioned regions using our frame selection scheme and obtained a reconstruction in each case. We obtained a binary map of the GBPs from the reconstructed G-band images using image segmentation techniques and then studied the morphology of the Ca II K and GBPs. We suggest that perhaps there could be two varieties of the GBPs: those present everywhere and those closely associated with the magnetic field distribution in the photosphere; the former are swept by supergranular horizontal motions to the boundaries and cause heating at the upper layers; continuous formation of GBPs at all locations is responsible for their uniform distribution at any given time. The intra-network GBPs are perhaps associated with the Ca II K_{2V} bright points, not resolved in the present data.

Chapter 5

Interferometric Imaging

5.1 Introduction

The formation of an image by an imaging system can be considered as an interferometric process. In Young's double slit experiment, a monochromatic light (light from a point source) falls on two closely spaced pinholes and the light passing through the pinholes forms a fringe pattern (interference pattern) at the region of superposition. Fringes get oriented in a direction perpendicular to the line joining the pinholes with a spatial frequency proportional to the separation between the pinholes. The fringes can be characterised by a quantity known as 'visibility' (Born and Wolf, 1980). As the size of the source increases (or when the source is observed with a wide bandwidth), the visibility decreases. In the case of astronomical imaging (quasi-monochromatic, incoherent imaging systems; see Born and Wolf, 1980; Goodman, 1996), the exit pupil of the telescope can be regarded as consisting of a large number of fictitious pinholes and the observed image intensity distribution can be considered as the resultant of a multitude of fringe patterns corresponding to all the possible separations and orientations of the pinholes. (Goodman, 1985; Roddier, 1988). In this case, the 'visibility' of a component fringe pattern is proportional to the complex degree of coherence $\mu_{ij}(\mathbf{d})$, where

the subscripts represent the corresponding pair of pinholes and $|\mathbf{d}|$ is the separation between them. For a quasi-monochromatic incoherent extended source, $\mu(\mathbf{d})$, which describes the correlation of vibrations between two points in space separated by the distance \mathbf{d} , is equal to the two dimensional Fourier transform of the intensity distribution across the source except for a phase factor and scaling constants. This is known as the Van Cittert-Zernike theorem and forms the basis of all high resolution interferometric imaging measurements (Born and Wolf, 1980). In Section 5.2, we briefly describe the method of extracting the information about the object from the recorded fringes. In Section 5.3, we describe the possibility of having two kinds of transfer functions for interferometric imaging systems. In Section 5.4, we describe the laboratory simulation of an interferometric imaging system. In Section 5.5, we describe the method of simulating a specklegram or interferogram. Finally, we simulate fringes that can be formed by small scale solar features and compare them with those obtained with real observations at KO.

5.2 Interferometric Imaging using Closure Phase Technique

In the simplest kind of interferometer, known as ‘Fizeau’s type’, the entrance pupil (or the re-image pupil plane) of a telescope is covered with a mask containing several holes (sub-apertures) and the fringes are recorded at the image plane. Small sub-aperture spacings provide information on the low spatial frequency components and large sub-aperture spacings provide information on the high-frequency components. When no two baselines (a vector connecting the centers of two sub-apertures) are identical, the mask is called Non-Redundant Mask (NRM). While the redundancy improves the signal to noise ratio of the system, it could be harmful in the presence of telescope aberrations or phase error introduced by the atmosphere as the position of the fringes is different for

identical baselines and thus there is reduction in the visibility of the fringes (Goodman, 1985).

At the image plane, one gets crossed set of fringes due to different baselines. The fringes bear the information about the object. The contrast of the fringe gives the fringe amplitude and the position of the fringe with respect to that of a point source along the axis of the telescope gives the fringe phase. The amplitudes and phases of the fringes are the amplitudes and phases of the complex mutual coherence function which in turn is the Fourier transform of the object intensity distribution (Born and Wolf, 1980). The amplitudes and phases of the fringes are corrupted by the atmosphere. The fringes keep moving across the detector and short exposures are necessary to “freeze” them. However, the fringe phase can be preserved using a closed set of three baselines.

If α_i is the phase error at the i^{th} element (sub-aperture) of an interferometric array, and ϕ_{ij} is the phase produced by the source structure corresponding to the baseline connecting the i^{th} and j^{th} elements, then the observed phase is given by

$$\phi'_{ij} = \phi_{ij} + \alpha_i - \alpha_j. \quad (5.1)$$

When the observed phases corresponding to the baselines joining three elements $i = 1, 2, 3$ are added, we get a conserved quantity called *closure phase* which is independent of the atmospheric and instrumental phase errors.

$$\phi_{closure} = \phi'_{12} + \phi'_{23} + \phi'_{31} = \phi_{12} + \phi_{23} + \phi_{31} \quad (5.2)$$

From the closure phases, component phases can be determined. Using the normalised amplitudes and the phases of the fringes the complex mutual coherence function can be obtained and then Fourier inverted to get the object intensity distribution. This reconstructed image is called “dirty map” of the object in radio astronomy. It is ‘CLEANed’ (deconvolved) using a “dirty beam” obtained by observing a point source (Högbom, 1974; Schwarz, 1978; Steer, Dewdney and Ito, 1984; Thompson, Moran, and Swenson, 1986; Dwarakanath, Deshpande and Udaya Shankar, 1990).

5.3 Interferometric Imaging Systems with Non-zero Transfer Functions

The maximum resolution obtained in a Fizeau's type interferometer is limited by the diameter of the telescope. In another kind of interferometer, known as 'Michelson's type interferometer', the light reflected by two movable mirrors mounted on a rigid arm falls on the primary mirror of a telescope and is combined at the image plane to form fringes. While the frequency of the fringes is a function of the separation between the light beams at the primary mirror of the telescope, the visibility of the fringes is a function of the separation between the two reflecting mirrors. By varying the separation between the mirrors, the Fourier components of the object can be measured one by one (assuming that the object intensity distribution does not change during the period of observation).

As the resolution of an imaging system is defined as an integral over the spatial frequencies of the ensemble averaged MTF of the system (Section 1.4), it is of interest to compare the MTF of an interferometer with an equivalent telescope. The relative sizes of the elements of an interferometer with respect to the separation between them is an important factor in deciding the performance of an interferometer. With proper choice of the size and the inter-element separation, one can arrive at an optimum array configuration such that the transfer function of the array does not contain zeros (to be distinguished from the zeros in the uv plane when the observed object is completely resolved at the corresponding spatial frequency) within the diffraction limit of an equivalent monolithic telescope. In such cases, one can extend the bispectrum technique to reconstruct images from the fringes (Reinheimer and Weigelt, 1987). The transfer function (equivalent of Korff's function of the monolithic case) can be obtained through simulations and deconvolution can be performed using linear deconvolution techniques (Gonzalez and Wintz, 1977). On the other hand, when the transfer function of the

array contains zeros within the diffraction limit of an equivalent monolithic telescope, one has to use non-linear deconvolution techniques like the Maximum Entropy Method (Nityananda and Narayan, 1982; Narayan and Nityananda, 1986). As the amount of information available is limited in such sparsely filled arrays (that have zeros in their transfer function), it can have significant effects on the reconstructed images. However, when the observed field-of-view contains an isolated bright feature (bursts), sparsely filled arrays may still lead to reliable reconstructions.

5.4 Laboratory Simulation of Interferometric Imaging

The Experiment: We performed a simple experiment in the laboratory. The basic aim of this experiment was to study some aspects of the interferometric imaging (or closure phase imaging) technique. Figure 5.1 shows the experimental setup. The

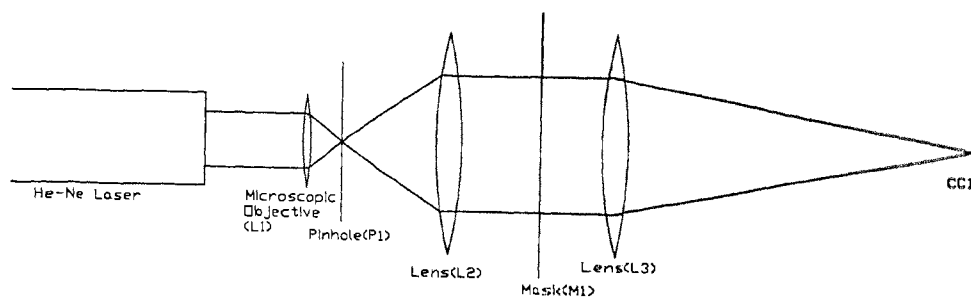


Figure 5.1: Experimental setup for interferometric imaging.

light from a He-Ne ($\lambda = 6328 \text{ \AA}$) laser was spatially filtered using a combination of a microscopic objective ($L1$, focal length 53 mm) and a 30 micron pinhole aperture $p1$. As the size of the central maximum of the diffraction pattern of the objective at the pinhole aperture was larger than the size of the pinhole, the illumination at the pinhole was spatially coherent. A lens $L2$ of focal length $f1 = 500 \text{ mm}$ collimated the beam.

An aperture of 15 mm diameter(not shown in Figure) was placed just before the lens L_2 . The diffraction at the pinhole p_1 produced an Airy pattern of size ~ 13 mm at the aperture plane of L_2 . A mask (similar to the one shown in Figure 2.2) containing seven identical holes of size 750 micron was kept in the collimated beam closer to a third lens L_3 of focal length $f_3=1000$ mm. The smallest separation between the holes was 2 mm. The third lens focused the interfering beams on to a charge coupled device detector (EEVTM, P46382) consisting of 385 by 576 pixels of size 22 by 22 micron. For the given pixel size, wavelength and f_3 , the largest possible separation between the holes b was 14 mm (that is, $b \leq 14$ mm). The Airy diffraction pattern of the lens L_2 was smaller than the size of the pinhole and hence the pinhole acted as an extended source. Each pair of holes produced fringes at the detector plane. These fringes were

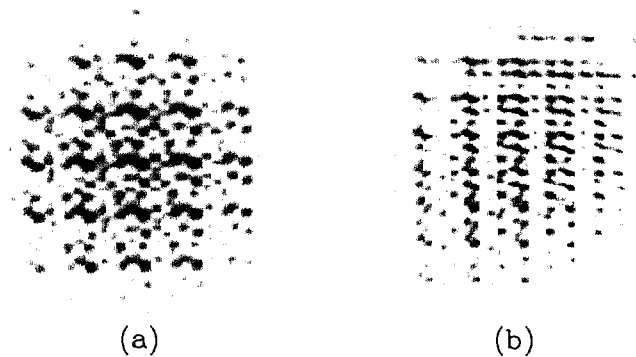


Figure 5.2: (a) Fringes formed at the image plane of an optical interferometric imaging system. Twenty one sets of fringes (due to seven holes in a mask) are superimposed on each other and are modulated by the diffraction pattern of a single hole in the mask. This figure shows the central maximum of the diffraction pattern in the absence of wave-front distortions. (b) Fringes formed at the image plane of an optical interferometric imaging system in the presence of wave-front distortions created by introducing a glass plate sprayed with silicon oil. Note the shift in the position of the fringes. Fringes keep moving across the image plane because of the distortions. The Figures show the negative fringes.

modulated by the diffraction pattern of the single hole. The fringes corresponding to all the pairs were superimposed and an example of the negative of the resulting pattern is shown in Figure 5.2 (a). It contains 21 (7C_2) distinct fringe patterns. The dark regions correspond to the coherent superposition of the fringes. First, a sequence of 16 frames were recorded using a DT2861 frame grabber card. Then a thin glass plate sprayed with silicon oil was kept rotated close to the lens $L3$ and another sequence of 16 distorted fringe patterns were recorded (One example is seen in Figure 5.2 (b)).

Image Reconstruction from the Fringes: We reconstructed the image from both the undistorted and distorted fringe patterns using the following procedure (similar to that used by Nakajima *et al.*, 1989).

- a:* We estimated the baselines as seen from the image plane in this way: If dx and dy are the separations between any two holes in x and y directions, then the discrete spatial frequency components of the corresponding fringe pattern is $(M sx dx/\lambda f_3, N sy dy/\lambda f_3)$, where M and N are the number of samples in the two directions and sx and sy are the pixel size in the two directions. If the image is shifted in either direction by half the size before and after computing the Fourier transform so as to make the zero frequency component appear at the pixel $(M/2, N/2)$, then the spatial frequency components are given by $(M sx dx/\lambda f_3 + M/2, N sy dy/\lambda f_3 + N/2)$. In the power spectrum peaks occur at the corresponding spatial frequencies. In practice, the positions of the peaks in the power spectrum will be slightly shifted on either side of the theoretical values. We identified the positions of the peaks through visual inspection of the average power spectrum of all the sixteen frames. Assuming $(x_i, y_i), i = 0, 1, 2, \dots, 6$ are the positions (co-ordinates) of the holes in the mask plane with respect to one of the holes and $p_{ij}, (i = 0, 1, 2, \dots, 6$ and for each $i, j = i + 1, i + 2, \dots, 6)$ are the positions (co-ordinates) of the peaks in the average power spectrum corresponding to the baselines joining the i^{th} and j^{th} hole

in the mask, we formed 21 equations of the form

$$dx_{ij} = x_i - x_j = (p_{ij} - (M/2)) \lambda f_3 / (M s x) \quad (5.3)$$

where $i = 0, 1, \dots, 5$ and for each $i, j = i + 1, i + 2, \dots, 6$, λ is the wavelength of observation and f_3 is the focal length of the lens L_3 . We solved these equations using Singular Value Decomposition method (SVD; see Antia, 1991). From the coordinates of the holes, we determined the baselines and by dividing them by wavelength, we obtained the spatial frequencies.

- b: Next, we estimated the average power spectrum at the estimated spatial frequencies using a 2-D discrete Fourier transform. We assumed that the power at the origin of the Fourier plane is approximately equal to the power at the smallest spatial frequencies. We normalised the power spectrum by dividing it by its value at the origin of the Fourier plane.
- c: We estimated the average closure phases using the following procedure: If a mask contains n holes, there will be $n(n-1)/2$ baselines and $(n-2)(n-1)/2$ independent closure phases (Thompson, Moran and Swenson, 1986). In the presence of additive noise, one can consider all the possible closure phases (Nakajima *et al.*, 1989). If ϕ'_{ij} is the phase of the Fourier transform of an interferogram corresponding to the baseline d_{ij} joining the holes i and j , then one can obtain the closure phases ϕ_{ijk} as

$$\phi'_{ij} + \phi'_{jk} - \phi'_{ik} = \phi_{ijk} \quad (5.4)$$

As the mask contained 7 holes in our case, we estimated 35 average closure phase values. Assuming the phase of the Fourier transform of the object corresponding to the shortest baselines in either directions as zero, we estimated the remaining Fourier phases from the closure phases using SVD (Antia, 1991) method.

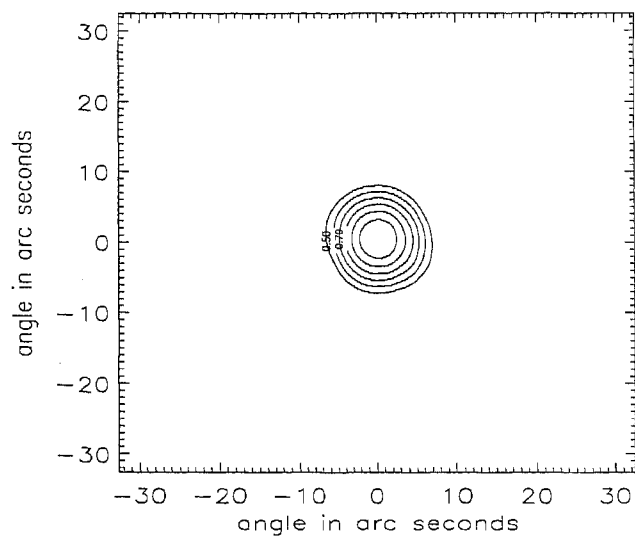
- d: We formed a complex array of numbers by multiplying the square root of the normalised average power spectrum and the corresponding estimated Fourier

phases and performed an inverse Fourier transform to obtain the reconstructed object.

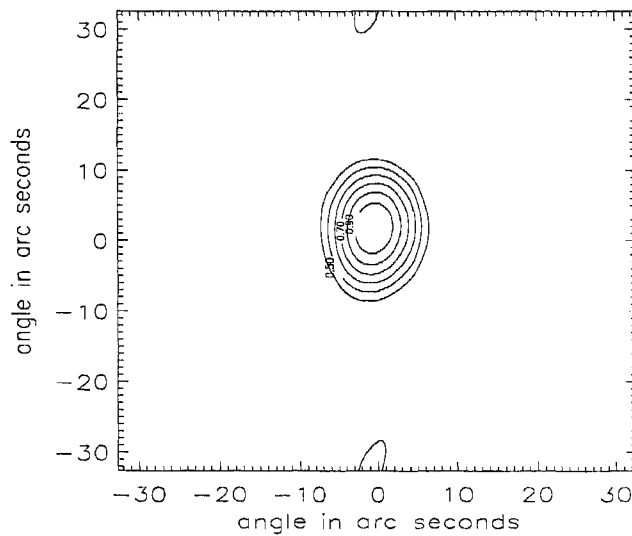
Figures 5.3 (a) and (b) represent the reconstructed images in the absence and presence of the wave-front distortions respectively.

5.5 Computer Simulations on Interferometric Imaging

We developed software for simulating specklegrams and interferograms. The aim is to simulate the fringes that can be obtained while observing small scale solar features that ride on a bright background. The procedure for simulating a time series of specklegrams or interferograms is as follows: First, a large ‘phase screen’ $\phi(x, y)$, that simulates the behaviour of a turbulent layer(s) is generated, either by the classical FFT based method (McGlamery, 1976) or by the ‘Zernike Polynomials’ method (Roddier, 1990). A stationary, atmospherically distorted wave-front $A(x, y)$ is then obtained using the expression $A(x, y) = \exp(j\phi(x, y))$. Assuming Taylor’s frozen turbulence hypothesis (that is, the turbulence pattern due to an atmospheric layer blows past the telescope aperture faster than any changes that occur in it), the large wave-front is divided into a series of small wave-fronts of appropriate size, the spatial separation between the consecutive wave-fronts being determined by the time interval between them and the wind speed. Then each wave-front of the series multiplied by a (complex) pupil function (in the case of interferogram, the pupil function resembles an interferometric array). The power spectrum of the series of wave-fronts produces a series of specklegrams or interferograms.



(a)



(b)

Figure 5.3: Contour maps of the images reconstructed from the interference fringes using the closure phase technique invented by radio astronomers. (a) Reconstruction in the absence of wave-front distortions. (b) Reconstruction in the presence of wave-front distortions. The width of the contour at the half the maximum value is ~ 30 micron (12 arc sec) used in the experiment.

5.5.1 Generation of Phase Screens

We followed the classical FFT based method to generate the phase screens. Under small perturbations- and near-field-approximations (Roddier, 1981), and assuming von Kármán spectrum for the fluctuations in the refractive index, an expression for the power spectrum (squared modulus of the average Fourier transform) of phase fluctuations (resulting from path-length fluctuations) can be obtained as (Noll, 1976; Roddier 1981)

$$W_{\phi_0}(\mathbf{f}) = 0.0227r_0^{-5/3}(f^2 + 1/L_0^2)^{-11/6} \quad (5.5)$$

where r_0 is the Fried's parameter, f is the absolute value of the spatial frequency \mathbf{f} (in units of 1/length) and L_0 is the outer scale of the turbulence. The exponential term containing the inner scale of the turbulence l_0 , present present in the von Kármán spectrum, has a value of the order of unity and hence has been neglected in arriving at Equation 5.5. Given the average power spectrum of the phase fluctuations, one of the realisations of the phase screen can be obtained by inverse Fourier transforming the product of square root of the power spectrum and an unit amplitude phasor $\exp(j\theta)$, where θ is a random number distributed uniformly between $-\pi$ and π . This can be proved as follows: If i^{th} realisation of the phase screen is given by,

$$\phi_i(x, y) = \int_{-\infty}^{+\infty} \sqrt{(W_{\phi_0}(\mathbf{f}))} \exp(j\theta_i) \exp(j2\pi(f_x x + f_y y)) df_x df_y \quad (5.6)$$

Adding the Fourier transform $\Phi_i(f_x, f_y)$, of a large number ($i = 1, 2, \dots, N$) of realisations of the phase screen, we get

$$\sum_{i=1}^N \Phi_i(f_x, f_y) = \sum_{i=1}^N \sqrt{(W_{\phi_0}(\mathbf{f}))} \exp(j\theta_i). \quad (5.7)$$

The average power spectrum is then given by

$$\frac{1}{N^2} \sum_{i=1}^N \Phi_i(f_x, f_y) \sum_{i=1}^N \Phi_i^*(f_x, f_y) = W_{\phi_0}(\mathbf{f}) \frac{1}{N^2} \left| \sum_{i=1}^N \exp(j\theta_i) \right|^2 = W_{\phi_0}(\mathbf{f}). \quad (5.8)$$

Thus, we obtain the power spectrum that we start with.

As any practically realisable phase-screen has to have a limited size (of length L or area L^2), an expression for its power spectrum $W_L(\mathbf{f})$ can be obtained using the following definition (<http://www.eso.org/~fdelplan/laos/node5.html>) of the phase power spectrum:

$$W_{\phi_0}(\mathbf{f}) = \lim_{L \rightarrow \infty} \left(\frac{\langle |W_L(\mathbf{f})|^2 \rangle}{L^2} \right). \quad (5.9)$$

This implies that the phase screens are generated in such a way that the mean squared power spectrum at any frequency of a large number of phase screens of limited size is equal to the theoretical power spectrum at the same frequency. $|W_L(\mathbf{f})|^2$ is the sum of the square of the powers in the real and imaginary parts. Assuming that the power in the real and imaginary parts are equal, the absolute value of $W_L(\mathbf{f})$, according to Equation 5.9, is $\sqrt{2}$ times the square root of the real part (theoretical power spectrum).

$$|W_L(\mathbf{f})| = L\sqrt{2 \times 0.0227} r_0^{-5/6} (f^2 + 1/L_0^2)^{-11/12}. \quad (5.10)$$

Thus, two phase screens of length L can be obtained in the discrete form from the real and imaginary parts of the following Equation:

$$\phi_0(i, j) = \sqrt{2 \times 0.0227} (L/r_0)^{5/6} F^{-1} \left[\left(k^2 + l^2 + (L/L_0)^2 \right)^{-11/12} \exp \left\{ j\theta(k, l) \right\} \right], \quad (5.11)$$

where i, j are indices in the direct space, k, l are the indices in the Fourier space and F^{-1} represents inverse Fourier transform. Note that the factor L^2 gets cancelled with the integrating variable in the Fourier domain having the dimension of $1/L^2$, leaving the phase screen dimensionless.

The behavior of the phase screen at low frequencies depends on the size of the outer scale of the turbulence L_0 (Jakobsson, 1996). Its value varies between 10 and 100 m (Buscher *et al.*, 1995). The size of the phase screen must be greater than or equal to the outer scale of the turbulence in order to include major fraction of turbulent power in the simulation (Sedmak, 1998). Thus, when outer scale lengths of 100 m are considered in the simulation, the generation of phase screens using FFT demands intense computations and huge memory resources. This can be reduced by adding phase screens corresponding to low frequencies, generated using Discrete Fourier

Transform, to the FFT based phase screen (Glindemann, Lane and Dainty, 1993; Lane, Glindemann and Dainty, 1992).

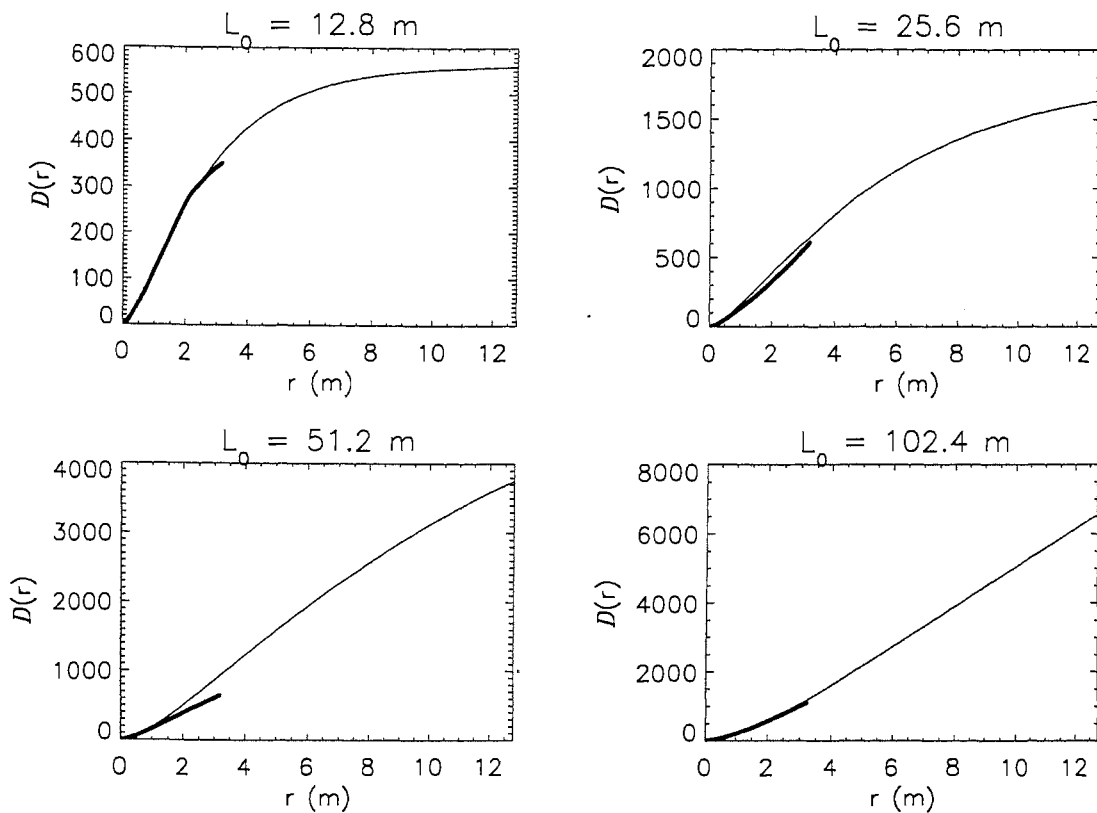


Figure 5.4: Structure functions estimated for different values of the outer scale of the turbulence L_0 ; The thin curve indicates the theoretical value (Herman and Strugala, 1990); The thick curve represents the simulated values.

5.5.2 Validation of the Simulated Phase Screens

We generated the phase screens using Equation 5.11. As we could generate phase screens of size 100 m with a sampling of 2.5 cm using powerful memory and computing resources, we did not have to add sub-harmonics. We generated phase screens of size equal to the outer scale of the turbulence for different values of L_0 and r_0 . We estimated the phase structure function from the simulated phase screens and compared

it with the theoretical phase structure function (Herman and Strugula, 1990). Figure 5.4 represents the simulated and theoretical structure functions. The theoretical structure functions were estimated using *Mathematica 4.0* software. We also estimated the variance of phase over different pupil sizes. Figure 5.5 indicates the normalised phase variance over pupils of different sizes. The discrepancy between the theory and the simulated curves at low values of d/r_0 is because of the less number of pixels in the corresponding pupils.

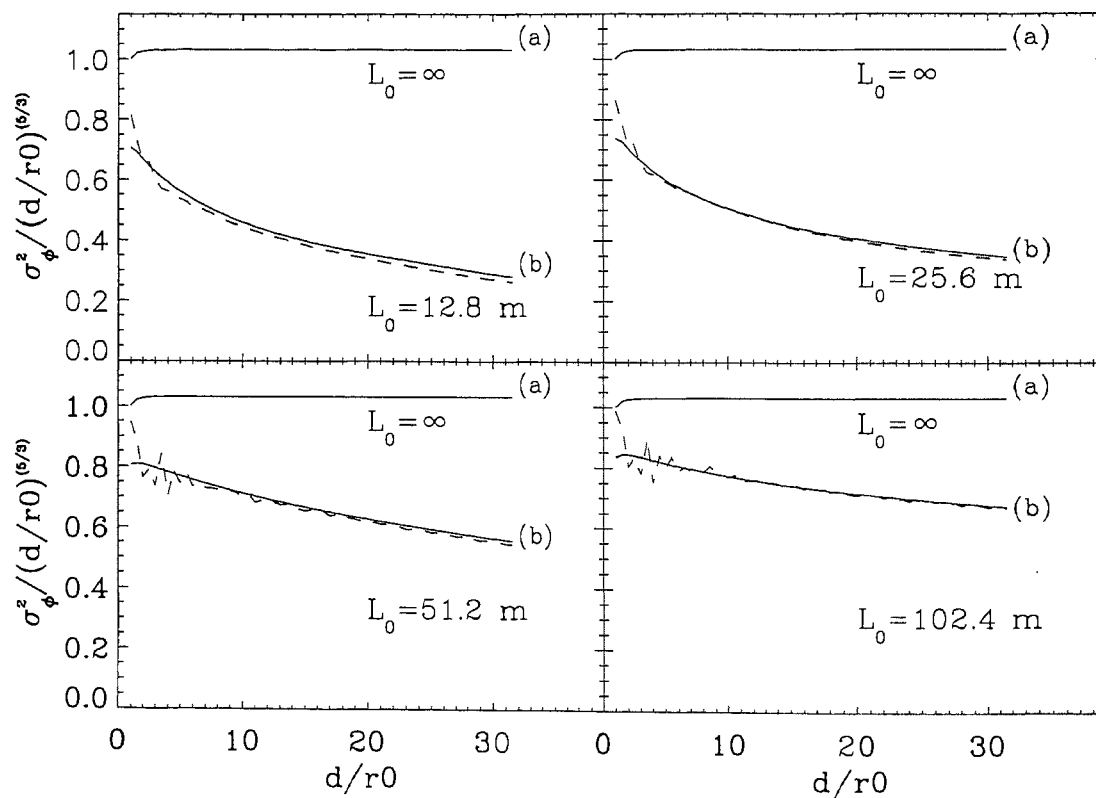


Figure 5.5: Normalised phase variance over the pupils of different diameters, expressed as a function of d/r_0 for different values of the outer scale of the turbulence L_0 ; (a) For Kolmogorov's spectrum (Infinite L_0); (b) For von Kármán spectrum. The continuous curve indicates the theoretical value (Fried, 1965); The dotted curve represents the simulated values.

5.6 Simulation of Interferometric Imaging of Small Scale Solar Features

In Section 2.2 (Page 24), we described the details of the interferometric imaging observations of small scale solar features using a NRM (Figure 2.2). We recorded fringes in the interferometric imaging mode and immediately (~ 17 s later) recorded speckle images of the same features (by removing the mask from the collimated beam; Figure 2.1).

Figure 5.6 represents two sequences of 16 images (interferograms) of a pore region. These images were recorded immediately (~ 17 s) before recording the speckle images of the same region (Figure 3.6). The speckle images were reconstructed using our speckle code (Section 3.2.1, Feature 3, Figure 3.7, Page 61).

The Sun as a whole being an extended source can not produce fringes. However, various small scale, bright and low contrast features riding on the bright background intensity of the Sun (or small scale bright features present in a locally depressed background such as sunspots and pores) may produce fringes.

In order to confirm the possibility of recording fringes due to small scale low contrast features, and study the nature of the fringes, we simulated interferograms following the procedure described in Section 5.5 for the parameters (r_0 , pupil configuration, spatial sampling) of our observations and compared them with those obtained in real observations. Our aim was to check whether features like the ones shown in Figure 3.7 (Page 61) can produce fringes with sufficient contrast. In this Section, we present the details of the simulation.

5.6.1 Effect of Finite Bandwidth on the Visibility of the Fringes

When an interferometer is used to record the fringes in a narrow bandwidth $\Delta\nu$, fringes due to each monochromatic component get displaced with respect to each other and the visibility of the fringes decreases. The fringes disappear completely when the path difference (due to the difference in the wavelengths) is sufficiently large. Assuming

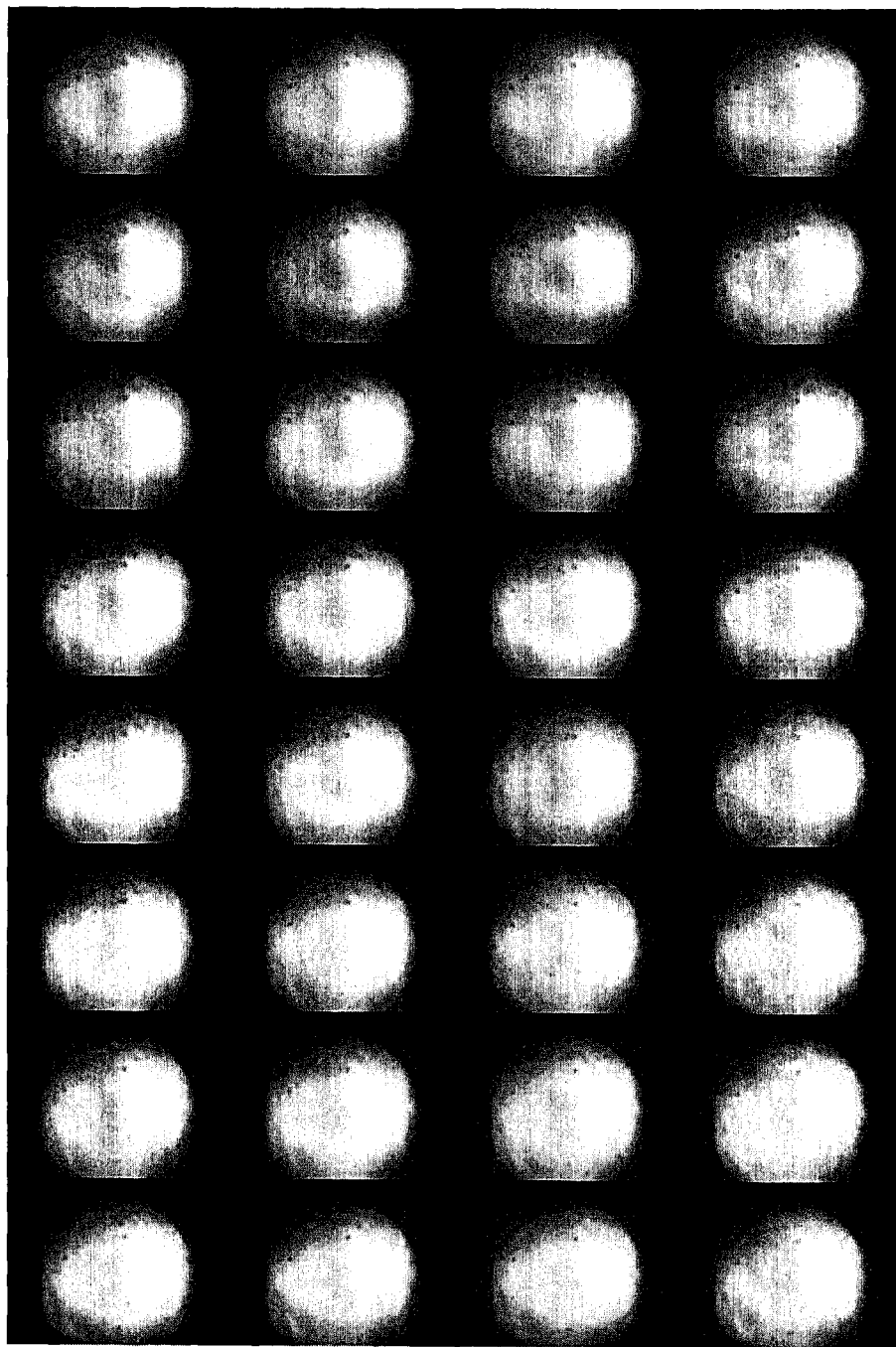


Figure 5.6: Fringes recorded with the NRM (Figure 2.2, Page 26) during the interferometric imaging observations at KO. Two sequences of 16 interferograms of a pore region ($2 \times 16 = 32$ interferograms).

that the spectral energy distribution of the source is constant within the bandwidth $\nu_0 - \Delta\nu/2 \leq \nu \leq \nu_0 + \Delta\nu/2$, it is found (Born and Wolf, 1980) that the visibility is attenuated by a factor $\text{sinc}(\pi(\nu - \nu_0)\Delta t)$, where Δt is the coherence time of the light. In other words, if $\bar{\lambda}_0$ is the mean wavelength, the visibility is attenuated by a factor $\text{sinc}(\pi\Delta P/\Delta l)$ where ΔP is the difference in the path length and $\Delta l = \lambda^2/\Delta\lambda$ the coherence length. In practice, the standard deviation of the optical path difference for a baseline length r is given by $\sigma_z = (2.62/2\pi)\bar{\lambda}_0(r/r_0)^{5/6}$ (Roddier, 1981). Assuming $r \sim 36$ cm, the longest baseline used in our observations, $r_0 = 8$ cm, the typical value estimated from our observations (Section 2.4.1, Page 29), $\bar{\lambda}_0 = 6520$ Å and $\delta\lambda = 160$ Å (Section 2.2, Page 24) we find that the visibility is attenuated by a factor $\text{sinc}(0.434537) \sim 0.9688$. Since the loss in visibility is only 3.2%, we assumed monochromatic light of wavelength $\bar{\lambda}_0$ in our simulations.

5.6.2 Simulation of Interferograms

Determination of the size of the phase screen needed for producing specklegrams: The size M of the phase screen (an array of M by M pixels) required for producing specklegrams for a given pupil configuration (either single aperture or a mask containing multiple sub apertures) can be determined as follows: If Δr is the sampling in the phase screen, then in the wave-front corresponding to this phase screen, the number of pixels for a telescope of diameter D is simply $D/\Delta r$. The specklegram of a point source is obtained as the modulus squared Fourier transform of the wave-front multiplied by the pupil function of the telescope. This is equivalent to the instantaneous PSF of the combination of the telescope and the atmosphere. Inverse Fourier transform of the PSF gives the complex autocorrelation of the pupil function. If sx is the sampling in the specklegram (in the image plane), $\bar{\lambda}_0$ is the wavelength of observation, R is the focal length of the imaging lens, then

$$Msx = (1.22\bar{\lambda}_0 R/\Delta r). \quad (5.12)$$

If η is the number of samples (in the image plane) per diffraction limit, then

$$sx = 1.22\bar{\lambda}_0 R/\eta D. \quad (5.13)$$

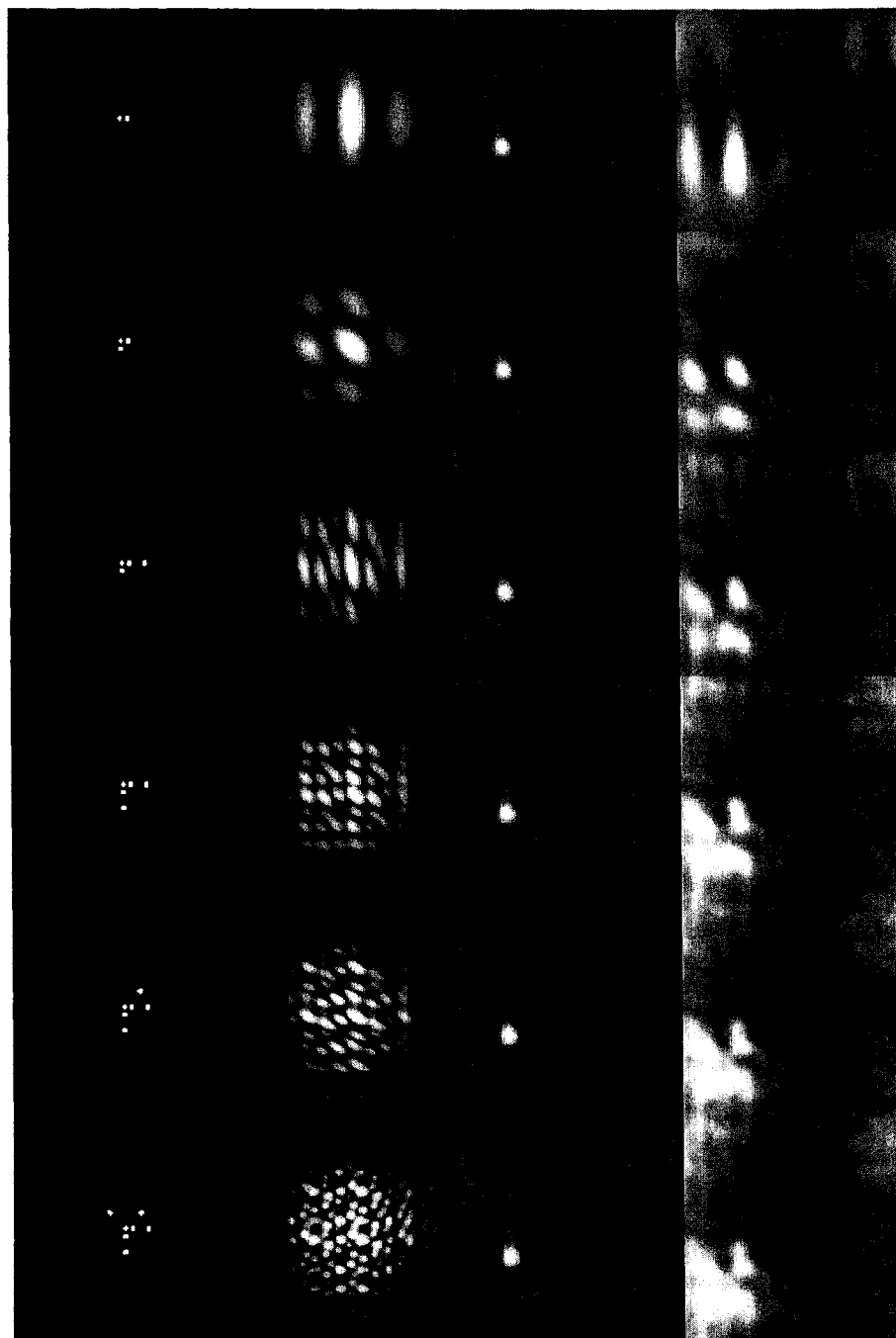


Figure 5.7: Simulated fringes: First column represents the mask configuration; Second column represents the corresponding PSF; Third column represents the object (reconstructed from first sequence speckle data); Fourth column represents the simulated fringes formed by the object

Substituting Equation 5.13 in Equation 5.12, we obtain $M\Delta r/\eta D = 1$. As the minimum value of η is 2, the relation implies that *for simulating the performance of a telescope of diameter D meters, the size of the wave-front (phase screen) must be at least twice size of the diameter*. Conversely, if $M\Delta r$ is the size of the phase screen and D is the size of the telescope, then the sampling would be $M\Delta r/D$.

Sampling in the Phase Screen: In general, one can generate phase screen with certain spacing Δr and select the size of the phase screen for a given telescope of effective diameter D using the relation mentioned earlier. The only constraint is that there should be at least two samples within the atmospheric coherence diameter r_0 . However, in the present case, our aim was to generate a phase screen with a sampling corresponding to the plate scale our image. We used the image of a pore region, reconstructed from a sequence 16 specklegrams (Section 3.2.1, Feature 3, Figure 3.7, Page 61) as the object intensity distribution. We re-sampled the reconstructed image consisting of 46 by 46 pixels with a field of view of 4.3 arc sec into 128 by 128 pixels (as it is convenient to have array sizes integral powers of 2, while performing Fourier transforms) using CONGRID routine of IDL software. We assumed that the resulting plate scale to be same at the initial plate scale (0.093 arc sec per pixel) the recorded images. This corresponded to $\eta = 4.8$ samples per diffraction limit. Having decided η , we estimated the required spatial sampling in the phase screen Δr from Equations 5.12 and 5.13 as $\Delta r = \eta D/M = 4.8 \times 0.36/128 = 1.32$ cm.

As the recorded image $i(\mathbf{x})$ of an extended object is the convolution of the PSF $p(\mathbf{x})$ and object intensity distribution $o(\mathbf{x})$, the interference fringes due to an extended object can be obtained by inverse Fourier transforming the product of the Fourier transform of the PSF ($P(\mathbf{f})$) and that of the object ($O(\mathbf{f})$), that is,

$$i(\mathbf{x}) = F^{-1}\{P(\mathbf{f}) \cdot O(\mathbf{f})\}. \quad (5.14)$$

Thus, we generated a phase screen of 4096 by 4096 pixels, with a sampling of 1.32 cm per pixel, an outer scale length of the turbulence of ~ 54 m (4096×0.013) and $r_0 = 10$ cm. We assumed a wind speed of 2 m/s and a frame rate of 20 frames per

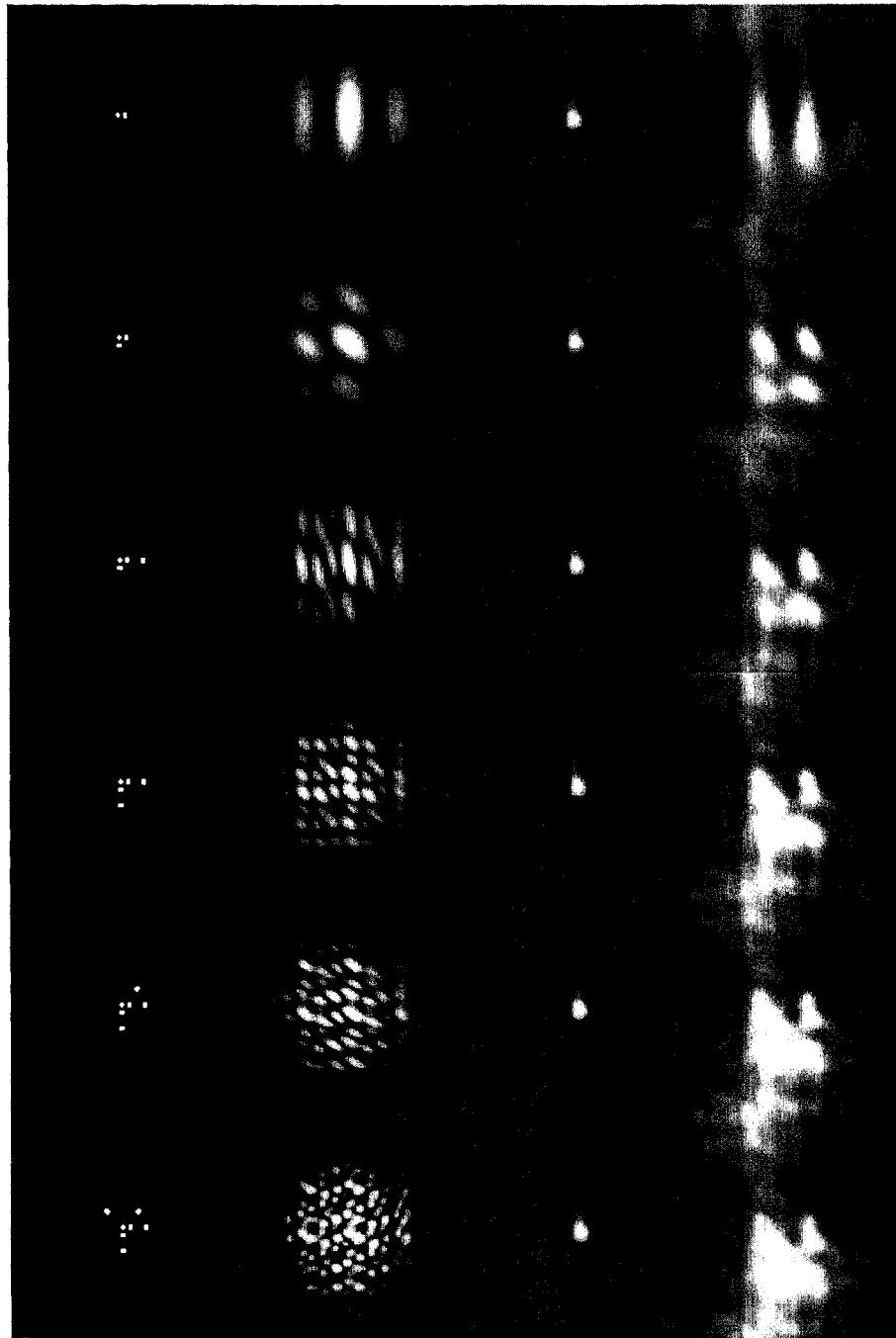


Figure 5.8: Simulated fringes: First column represents the mask configuration; Second column represents the corresponding PSF; Third column represents the object (reconstructed from first sequence speckle data shifted here, close to the center of the field-of-view.) Fourth column represents the simulated fringes formed by the object

second. We obtained a sequence of phase screens of size 128 by 128 pixels from the bigger screen, by shifting the origin by 4 pixels in each step. We then generated the corresponding wave-fronts, multiplied them by the NRM (Figure 2.2), and obtained fringes. Finally, we obtained the fringes due the solar features using Equation 5.14.

Discussion: Figures 5.7 - 5.9 represent the fringes simulated by the procedure described above. It should be remembered that the plate scale is not the same as used in the actual observations at KO. As we had extracted a portion of the observed specklegrams and reconstructed them using our speckle code, the effective field of view was reduced to half the original size (4.3 arc sec square as against the circular field of view of 8.25 arc sec used in the actual experiment). Nevertheless, the aim here is to see whether we can get some fringes due to such low contrast features riding on a bright background and we find that fringes could indeed be formed by such features. It implies that interferometry is still a viable tool for high resolution imaging of extended sources, at least when the observed field-of-view contains isolated bright features; that is, when there is minimum “source confusion” (Thompson, Moran and Swenson, 1986). In practice, regions of interest (for example, NPBs) can be identified using a relatively small telescope and then used for interferometric imaging in a sufficiently narrow bandwidth; the field of view can be restricted to about an arc sec centered at the isolated region to avoid the problem of “source confusion”. It should be noted that several authors (Harvey, 1972; Zirker, 1987, 1989; Damé, L., Matric, M., and Porteneuve, 1994; von der Lühe, 1989) have explored the possibility of imaging small scale solar features with interferometers through numerical simulations and real observations.

5.7 Summary

In this Chapter, we first briefly described the basic principle of interferometric imaging and the method of extracting the information about an object from its fringes. Then we described the possibility of having two kinds interferometric imaging systems, namely, the ones having non-zero transfer function up to the diffraction limit of an equivalent

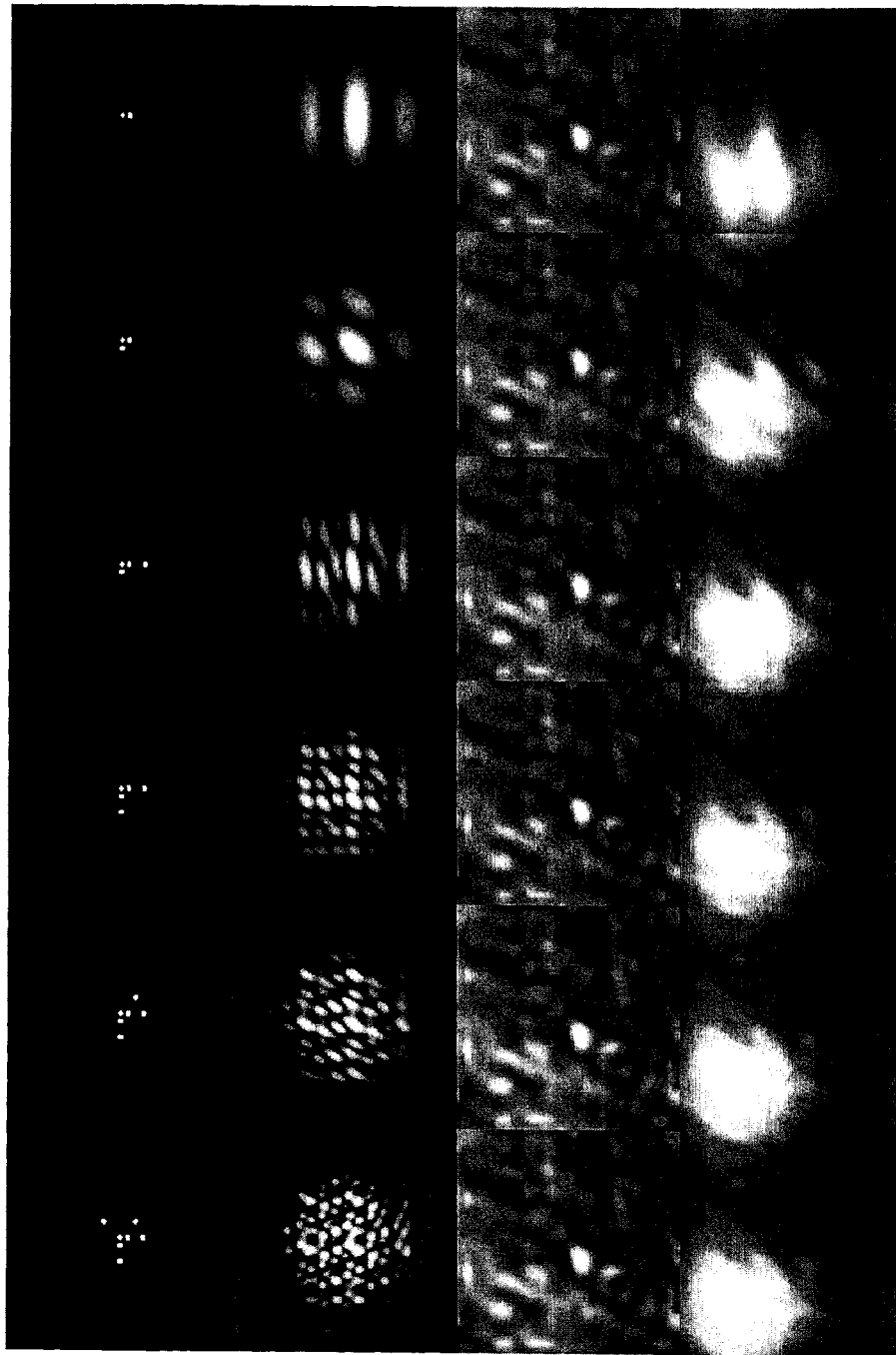


Figure 5.9: Simulated fringes: First column represents the mask configuration; Second column represents the corresponding PSF; Third column represents the object (reconstructed from second sequence of speckle data); Fourth column represents the simulated fringes formed by the object

monolithic telescope and the other having zeros in the transfer function. We presented the details of a simple laboratory experiment on the interferometric imaging. We recorded fringes due to an extended source with a NRM reconstructed the image from the distorted fringes using the 'closure phase' technique. We had used a similar mask in our interferometric imaging observations at KO and recorded the fringes. In order to confirm the possibility of recording fringes due to small scale features riding on a bright background or in a locally depressed background, we performed computer simulations. We described the procedure that we adopted for method of obtaining a sequence of phase screens, and validated it by (a) comparing the theoretical and simulated structure functions and (b) comparing the normalised phase variance over pupils of different sizes in the phase screen with that obtained theoretically by Fried (1965). Finally, we simulated interferograms using the speckle reconstructed image as object intensity distributions, for typical conditions that prevailed during our observations, and compared them with those recorded in our interferometric imaging observations at KO. We found that small scale solar features can indeed produce fringes of the nature that was actually observed. Thus we conclude that interferometric imaging can be probably used for finding the sub-structure/morphology of isolated bright point-like sources.

Chapter 6

Summary and Future Directions

In this Chapter, we first present the chapter-wise summary of the thesis work and highlight the main results. The major outcome of this thesis work has been the development of the software (speckle code) required for processing speckle images, that in principle can be extended to reconstruct images obtained from an array of telescopes. We critically assess the advantages of our speckle code, compare it with the other existing codes to the extent possible and comment on its limitations. Then we briefly describe our future plans.

6.1 Present Work

In the first Chapter, we highlighted the fact that *the phase of the Fourier transform of an object bears the information on the positional or structural details of the object* with an example. We also explained how the earth's turbulent atmosphere corrupts the phases of the Fourier transform of the object and thereby reduces the resolution of a ground based telescope to about an arc second.

In the second Chapter, we presented the details of the speckle imaging observations performed at KO, UPSO and USO. We also presented the methods of the pre-processing of the speckle data. We explored the possibility of estimating Fried's parameter using

three different methods, namely, from the fluctuations in the angle of arrival of the light, by the power spectrum equalisation method and by the spectral ratio method. While estimating r_0 from the angle of arrival fluctuations, we found that *high spatial frequency components of the image contribute more to the image motion than the low frequency components*. We enumerated the limitations of these and a few more methods of estimating r_0 . We identified the spectral ratio method as the best method for the speckle data analysis. The average value of r_0 at USO and UPSO was ~ 3 cm during our observations. A small variation of r_0 over a large field-of-view implied that most of the degradation was close to the ground. At KO, values of r_0 ranging from 6-10 cm were estimated during our observations.

In the third Chapter, we presented the details of our speckle code and validated it with an example. *We observed small scale brightenings inside pores in our observations at KO and achieved 0.43 arc sec resolution, which is the diffraction limit of the telescope at 6520 Å. This has been possible only because of the short exposure nature of the speckle observations.* We reconstructed two sub-flare regions of the NOAA AR8898 from the speckle data obtained at USO. We found the presence of chromospheric umbral dots inside a sunspot region. We also found the breaking-up of a filament. *We could observe such events even with moderate seeing conditions only because of the speckle technique. Regular use of the speckle technique will enable us to collect more details about such events.*

In the Fourth Chapter, we presented the details of our speckle data obtained from NSO/SP. We obtained near-simultaneous filtergrams of a quiet Sun region, a plage region and the NOAA AR8923 in the G-band and the K line of Ca II. As the seeing conditions were poor, we selected three best images from the sequences of images of the aforementioned regions and obtained a reconstruction in each case. In addition to the usual speckle technique, we also used image segmentation techniques to extract the GBPs. Our aim was to see whether this data can offer a clue on the mechanism that leads to the preferential heating at the chromospheric level (network boundaries) while the source, if assumed to be the GBPs, is distributed everywhere. We studied the morphology of the G-band and Ca II K bright points in the aforementioned regions.

We suggest that perhaps there could be two classes of the GBPs namely, those present everywhere and those closely associated with the magnetic field distribution. The GBPs that are present everywhere are swept by the supergranular horizontal motions to the network boundaries and cause heating at the chromospheric levels. At the same time, continuous formation of the GBPs at all locations makes them observable everywhere at any given time. The intra-network GBPs are perhaps associated with the K_{2V} bright points (Sivaraman and Livingston, 1982). However, the latter are not resolved in our data.

In the fifth Chapter, we presented the basic principle of interferometric imaging technique. We mentioned that with proper choice of the relative size and separation between the elements of an interferometer, an optimum array configuration with a non-zero transfer function can be achieved and the ‘bispectrum’ technique can be extended to reconstruct the images. Then we presented the details of a laboratory experiment, performed to understand the processing methods of the ‘closure phase imaging’ technique. *We performed interferometric imaging (closure phase imaging) observations at KO using a NRM at the re-imaged pupil plane and recorded fringes.* In order to confirm the possibility of recording fringes produced by small, bright, low contrast features that ride on a bright background or a locally depressed background, we performed computer simulations. *We developed a computer code for simulating phase screens and generated specklegrams and interferograms using them. We simulated interferograms using the image reconstructed from our speckle data as input object intensity distribution and found that fringes could indeed be formed by the low contrast small scale features.* While the ‘closure phase imaging’ (even with zeros in the corresponding transfer function) can be useful for resolving isolated bright features, the ‘bispectrum technique’ (with non-zero transfer function) can be extended for reconstructing images obtained by combining several telescopes.

6.2 Comments on the Speckle Code

In our speckle code, we estimate the Fourier amplitudes using Labeyrie's (1970) speckle interferometry technique and the Fourier phases using the 'bispectrum' or 'speckle masking' (Weigelt, 1977; Lohmann, Weigelt and Wirtitzer, 1983) technique. We have incorporated all relevant procedures developed by several others for enhancing the quality of the reconstructions. For example, we use noise filters developed by Pehlemann and von der Lühe (1989) and de Boer (1996) for phase estimation, the noise filter developed by Von der Lühe (1993) for the amplitude estimation. In the absence of suitable flat field-images for estimating noise filter, we use the optimum filter (Press *et al.*, 1993) or the Wiener filter (Gonzalez and Wintz, 1977). We use the 'optimum apodisation window' developed by Keller (1999) to apodise the sub-images to decrease the effect of the usual 'cosine bell function' on the phase of the estimated bispectrum. We use the real time frame selection scheme developed by Scharmer (2000) for selecting the best frames. When the field-of-view is larger than the typical size of the isoplanatic patch (~ 5 arc sec), we 'de-stretch' the images using the code developed by scientific staff of NSO/SP. We reconstruct the image as a mosaic of several sub-images following the procedure described by Von der Lühe (1993). Our speckle code takes about 10 minutes to reconstruct an image from a series of 90 images of size 128 by 128 pixels and requires a RAM size of ~ 100 MB.

Our speckle reconstructed images show enhancement in the contrast. We are able to obtain 'good' reconstructions even with a few selected best frames. This is partly because of the frame selection and also because of the the increase in the signal-to-noise of the reconstructions due to high redundancy in the Fourier phase estimation. (Pehlemann and von der Lühe, 1989). As the diameter of a telescope increases, the life time of the smaller scale features that can be theoretically resolved becomes shorter and only a few frames can be combined to get a reconstruction (von der Lühe and Zirker, 1988). Thus the ability to reconstruct an image from a few frames is essential while observing with large telescopes and our speckle code meets that requirement. It is known (Pehlemann and von der Lühe, 1989; Reinheimer and Weigelt, 1987) that the

'bispectrum' technique can be used to reconstruct speckle interferograms obtained with coherent, non-redundant or redundant optical arrays. Thus, *our speckle code can be used to reconstruct images obtained from an array of telescopes*. It is also known (von der Lühe and Pehlemann, 1988) that the bispectrum technique is less sensitive to the anisoplanatic effects. In all these aspects, *our speckle code is superior to those those which use Knox-Thompson algorithm* (Knox and Thompson, 1974) *or its extension* (Keller, 1999).

The major difference between our speckle code and that developed by Von der Lühe (1993) is the method of estimation of the Fourier phase of the object. He uses the Knox-Thompson algorithm for estimating the phase, whereas we use the 'bispectrum' technique. Pehlemann and von der Lühe (1989) have developed a speckle masking phase reconstruction algorithm called the 'Octagon Method' using the symmetry properties of the bispectrum. They sequentially access the elements of the 4-D array of bispectrum values. However, in our speckle code, we store the 4-D bispectrum values in a 1-D array and access the elements in a sequential from, keeping track of the component phases. Though the memory required is independent of the dimensionality of the array (1-D or 4-D), the time required to access an element in a 1-D array is much smaller than that in a 4-D array. In this aspect, our speckle code is expected to be faster than that developed by Pehlemann and von der Lühe (1989). We estimate all the possible bispectrum values and do not truncate it as mentioned by Pehlemann and von der Lühe (1989). While recovering the Fourier phases of the object from the bispectrum phases, we consider all possible paths to a given spatial frequency point from the origin and estimate a large number of Fourier phases (unit amplitude phasors) for that point and use the phase consistency filter to give less weight to those phasors that significantly differ from their counterparts (Pehlemann and von der Lühe, 1989; de Boer, 1996). We do not know the technical details of the speckle code developed by de Boer and used by Denker (1998) and hence can not compare with our code. However, we found that they also use the bispectrum technique.

Our speckle code enforces time and memory constraints when a large number of images of size 512 by 512 are analysed.

One of the major factors that delays our speckle reconstruction procedure is the determination of r_0 for all the segments (sub-images) of an image. We estimate r_0 using the spectral ratio method (von der Lühe, 1984). This method involves the estimation of the theoretical STF (Korff, 1973). Evaluation of this function becomes highly time consuming for large array sizes. von der Lühe estimates the theoretical STF for different values of D/r_0 , stores them in a separate library of and uses it (if required, does interpolation in the frequency domain) for further analysis. However, as of now we estimate the theoretical STF for every set of data (for various values of D/r_0 and the frequency sampling defined by the array size). Moreover, the estimation of r_0 often needs visual inspection of the observed and the theoretical spectral ratios, which again is highly time consuming.

6.3 Future Directions

The following is the brief description of our future plans.

- *Parallelising the Speckle Code:* The first improvement that we would like to achieve is the parallelisation of the speckle code. At present, we obtain the speckle reconstruction as a mosaic reconstructions of a large number of overlapping segments. These segments are processed independently in a sequential form. In order to increase the speed further, we plan to parallelise our code. This would be much useful when we acquire a large amount of data. We have identified a few areas in which our speckle code, where the algorithm presently used can be improved. We plan to implement these changes while parallelising the code.
- *Hardware Implementation of the Speckle code:* We plan to implement the speckle image reconstruction procedure through hardware. This will enable us to obtain a reconstruction very quickly. We plan to select a few best frames using the frame selection algorithm (Scharmer, 2000) and use Digital Signal Processing chips for performing real time Fourier transforms. We plan to implement the de-stretching and the speckle code through hardware. This would be our long term goal.

- *Speckle Imaging of With Existing Solar Telescopes:* Our speckle code has been optimised to reconstruct solar images. Several authors (Stachnik *et al.*, 1977; Stachnik, Nisenson and Noyes, 1983; de Boer and Kneer, 1992; de Boer, Kneer and Nesis, 1992; von der Lühe, 1994) have performed speckle imaging of small scale solar features with broad bandwidth. Keller and von der Lühe (1992) adopted a differential speckle imaging method to provide new insight into the small scale solar magnetic features. We would like to combine speckle and polarimetric observations (Sankarasubramanian, 2000) in sufficiently narrow band with the existing solar telescopes on a regular basis.
- *Extension of Bispectrum Technique:* We have developed a computer code to simulate phase screens and generate specklegrams or interferograms from them. We plan to perform more realistic simulation on the interferometric imaging technique. We plan simulate fringes (speckle interferograms) that could be formed by small scale solar features and reconstruct the images using our speckle code with suitable modifications (for amplitude calibration).

Appendix:A

Computer Programs in IDL and FORTRAN

In this appendix, we present a few sample programs written in IDL and FORTRAN 77. The IDL function (user defined) `f_ccorra.pro` is for registering two images. It estimates the required shift to align the images. The function `sushift.pro` is for shifting an image with an accuracy of fraction of a pixel by introducing the required shifts in the phase of the Fourier transform of the object. The program `ldbpm.pro` is just to demonstrate the phase reconstruction procedure for 1-D objects. This is followed by a FORTRAN program that estimates Korff's function for various values of D/r_0 . Finally, the speckle code is presented. The inputs files have to be in FITS format. To read/write FITS images, a software package called FITSIO was used. The latest version of the FITSIO source code, documentation and example programs are all available on the World-Wide Web at the following URL: <http://heasarc.gsfc.nasa.gov.fitsio>. The programs are presented in a two-column page style in the same order as they have been described above.

```

FUNCTION f_ccorra, img1, img2, PRINT=print
;NAME: f_ccorra
;PURPOSE: Perform a cross correlation match on two images using Fourier transform
;
;SAMPLE CALLING SEQUENCE:
; result = f_ccorra(img1, img2) intentionally spelt wrongly (shift)
; INPUTS: img1: 2-D image
;         img2: 2-D image
;
; OUTPUTS: mx : peak correlation coefficient
;
; RETURNS: shift: ftxarr(3), shift(0) = x-shift in pixels FROM img1 to img2.
;         shift(1) = y-shift in pixels FROM img1 to img2.
;         shift(2) = peak cross correlation co-efficient.
;
; HISTORY: Written by R. Sridharan ; modified to the present form on 25 Oct 2000.
;         Algorithm was already written in a program called
;         fct.pro, cross_check.pro, all for same purpose sometime in Jan 2000.

!except=2
k = systime(1)

sz1 = size(img1)
sz2 = size(img2)
if sz1(0) ne 2 or sz2(0) ne 2 then begin
    message, 'Images must be 2-D'
    RETURN, -1
end
if sz1(1) ne sz2(1) or sz1(2) ne sz2(2) then begin
    message, 'Images must be of identical dimension'
    RETURN, -1
end
mx = sz1(1)
ny = sz1(2)

img1 = img1
img2 = img2
img1 = img1/(total(img1)/n_elements(img1))
img2 = img2/(total(img2)/n_elements(img2))

s1 = sftc(img1, 1, kx = val)
img1 = (img1-s1)
s2 = sftc(img2, 1, kx = val)
img2 = (img2-s2)

; estimate power spectrum
fimg1 = shift(ftt(shift(img1, nx/2, ny/2), -1, double=3), nx/2, ny/2)
pimg1 = total(abs(fimg1)*abs(fimg1))
fimg2 = shift(ftt(shift(img2, nx/2, ny/2), -1, double=3), nx/2, ny/2)
pimg2 = total(abs(fimg2)*abs(fimg2))

cc1 = fimg1*conj(fimg2)/sqrt(pimg1*pimg2)
cc = shift(ftt(cc, nx/2, ny/2), 1, double=3), nx/2, ny/2)
cc = float(cc)
mx = max(cc, nval)
kc = nval mod mx
kr = nval/nx

shift = ftxarr(3)

if mx ne 1, then begin
    if (kr*kc ne 0) and (kr lt ny-1) and (kc lt nx-1) then begin
        dr = mx-2*cc(kc-1, kr)/cc(kc-1, kr)
        cr = (kc-0.5)+(mx-cc(kc-1, kr))/dr
        dx = mx-2*cc(kc, kr-1)-cc(kc, kr+1)
        rx = (kr-0.5)+(mx-cc(kc, kr-1))/dr
    endif else begin
        cr = kc
        rx = kr
    endif else
        shift(0) = cr-nx/2
        shift(1) = rx-ny/2
endif else begin
    cr = kc
    rx = kr

    shift(0) = cr-nx/2
    shift(1) = rx-ny/2
endif else
    shift(2) = mx

if keyword_set(print) then begin
    print, 'shifts (pixels): ', shift
    print, 'Runtime = ', systime(1)-k, ' seconds'
endif

RETURN, shift
END
;-----END of Cross Correlation Program-----

FUNCTION eushift, img, sifx, sify
;NAME: eushift
;PURPOSE: Shifting an image by fraction of a pixel
;
;SAMPLE CALLING SEQUENCE:
; result = eushift(img, sifx, sify) intentionally spelt wrongly (sifx, sify)
; INPUTS: img: 2-D image
;         sifx: desired shift in x direction
;         sify: desired shift in y direction
;
; OUTPUTS: img1: shifted image
;
; RETURNS: img1: 2-D image.
;
; HISTORY: Written by R. Sridharan ; got the idea from Dr. R. Srikanth, IIA.

!except=2

t = systime(1)

sz = size(img)
img = shift(ftt(shift(img, sz(1)/2, sz(2)/2), -1, double=3), sz(1)/2, sz(2)/2)
fimg1 = dcomplexarr(sz(1), sz(2))
for i = 0, sz(1)-1 do begin
    for j = 0, sz(2)-1 do begin
        fimg1(i, j) = img(i, j)*exp(complex(0, 1)*(2*pi*i*8
            ((i-(sz(1)/2.))-(sifx))/sz(1)+((j-(sz(2)/2.))-(sify))/sz(2)))
    endfor
endfor
img2 = float(shift(ftt(shift(fimg1, sz(1)/2, sz(2)/2), 1, double=3), sz(1)/2, sz(2)/2))
RETURN, img2
END
;-----END of Superhifter Program -----

;This program is a demonstration program
;It shows that triple correlation of a 1-D image is a 2-D function
;Fourier transform of this 2-D triple correlation produces 2-D bispectrum

on_error, 2
n = 128.0 ; initialise array size
m = 128.0

a1 = ftxarr(m) ; initialise array for 1-D object
tcn = ftxarr(m, m); initialise array for triple correlation

a1(62:66) = 100. ; object intensity distribution.
a1(46:50) = 70.
a1(28:30) = 50.
a1(78:80) = 50.

fa1 = shift(ftt(shift(a1, m/2), -1, double=3), m/2); Fourier transform
amp = abs(fa1)*abs(fa1); power spectrum

; following loop estimates the triple correlation.
for i = 0, m-1 do begin
    for j = 0, m-1 do begin
        a2 = shift(a1, i); shift the object by i pixels to the right.
        a3 = shift(a1, i+j); shift the object by i+j pixels to the right
        for k = 0, m-1 do begin
            tcn(i, j) = tcn(i, j)+a2(k)*a3(k); triple correlation
        endfor
    endfor
endfor

tcn1 = shift(tcn, 64, 64); shift it so that center becomes the origin.
; estimate bispectrum by Fourier transforming the triple correlation
bpm = shift(ftt(shift(tcn1, 64, 64), -1, double=3), 64, 64)

plot, a1, xstyle=1, yrange = [-10, 110], pos=[0.1, 0.55, 0.5, 0.8], ystyle=1, normal, $
title='16(a) Object', charsize=1.5; background=255
;vhist, (tcn1), 481-m/2, 383-m/2
twc1, (log10(tcen1)), 481-m/2, 383-m/2
xyouts, 370, 480-10, '15(b) Triple Correlation', /device, charsize=2
;xyouts, 100, 480-15, '16(c) Bispectrum', /device, charsize=1.5

;vhist, (abs(bpm)), 192-m/2+290, 141-m/2
twc1, (log10(abs(bpm))), 600, 192-m/2+290, 141-m/2
xyouts, 370, 180+50, '16(c) Bispectrum', /device, charsize=2

; Estimate the bispectrum from object Fourier transform, i.e from fa1.
biamp = dcomplexarr(1024)
biamp1 = dcomplexarr(m, m)

k = 0.0
for ci = m/2-2, 0, -1 do begin
    cnt = (ci-m/2*(ci-fix(ci/2)+2))/2+m/2
    for i1 = m/2, cnt, -1 do begin
        biamp1(i1, ci+m/2-i1) = biamp1(i1, ci-m/2-i1)+fa1(i1)*(ci+m/2-i1)*conj(fa1(ci))
        biamp(k) = biamp(k)+fa1(i1)*fa1(ci-m/2-i1)*conj(fa1(ci))
        k = long(k+1)
    endfor
endfor

; Estimate phase from the bispectrum
for i = 0, m-1 do begin
    for j = 0, m-1 do begin
        if biamp1(i, j) ne 0.0 then biamp1(i, j) = biamp1(i, j)/abs(biamp1(i, j))
    endfor
endfor
ephase = complexarr(m)
ephase(m/2) = complex(1, 0)
ephase(m/2-1) = complex(1, 0); fa1(m/2-1)/abs(fa1(m/2-1))
ephase(m/2+1) = complex(1, 0); fa1(m/2+1)/abs(fa1(m/2+1))

k = 0.0
for ci = m/2-2, 0, -1 do begin
    cnt = (ci-m/2*(ci-fix(ci/2)+2))/2+m/2
    for i1 = m/2, cnt, -1 do begin
        ephase(ci) = ephase(ci)+ephase(i1)+ephase(ci+m/2-i1)*conj(biamp1(i1, ci+m/2-i1))
        ephase(ci) = ephase(ci)+ephase(i1)+ephase(ci+m/2-i1)*conj(biamp(k))
        k = long(k+1)
    endfor
    if abs(ephase(ci)) ne 0.0 then ephase(ci) = ephase(ci)/abs(ephase(ci))
endfor
; use Hermitian symmetry to find phase in the upper half of the Fourier plane
for i = m/2+1, m-1 do ephase(i) = conj(ephase(m-i))

reim = ephase+sqrt(amp); reconstruct the object

img = shift(ftt(shift(reim, m/2), 1, double=3), m/2)
;plot, img, xstyle=1, pos=[0.55, 0.05, 0.95, 0.48], /normal, /noerase, ystyle=1
;plot, img, xstyle=1, yrange = [-10, 110], pos=[0.1, 0.08, 0.5, 0.43], /normal, /noerase, ystyle=1.5
linestyle=3, title='(d) Reconstructed object', charsize=1.5
;xyouts, 80, 225, '15(d) Reconstructed', /device, charsize=1.5
;xyouts, 115, 205, '15 Object', /device, charsize=1.5
;plot, e1, xstyle=1, pos=[0.1, 0.55, 0.5, 0.95]

end
;-----END of Phase reconstruction validation (1-D) program-----

```

```

C      The files in granules directory are for Nainital images.
C      Program to estimate theoretical mtf

integer n,m
parameter(n=16,n=16,pi = 3.1415926535897932400)
parameter(num=80)
real ttime(2),time1,alpha
double precision wf(m),vf(n),sf(m,n),sfn(m,n),w1,z,ax,ay,di
double precision theta(m,2),ctheta(m,n),stheta(m,n),dx,dy
double precision a(m,n),rtheta(m,n),yc(m,n),s(m,n)
double precision bal(m,n),bdl(m,n),dal(m,n),q(m,n)
double precision tau2(m,n),senn(m,n),tele(m,n),lenn(m,n)
double precision deltav(m,n),r00(num)
double precision deltavk(n),deltavy(n),y(m,n)
double precision s11,as,asa,qa,qpa,qpb,qpc,qpd,qy
double precision bdx1,bdy1,bax1,bay1
character tau2name(num)=80,sennname(num)=80
character lenname(num)=80

sx = 11e-6/100/128.
sy = 13e-6/82/128.
w1 = 6583e-10
z = 0.136
z = 5.04
dx = 1.22*w1*z/(n*sx)
dy = 1.22*w1*z/(n*sy)

wf(n/2+1) = 0.0
vf(n/2+1) = 0.0

do i = 1,n/2+1
  wf(i) = wf(i-1)*(dx/w1)
enddo

do j = 1,n/2+1
  vf(j) = vf(j-1)*(dy/w1)
enddo

do i = n/2+1,-1
  wf(i) = wf(i+1)*(dx/w1)
enddo

do j = n/2+1,-1
  vf(j) = vf(j+1)*(dy/w1)
enddo

do i = 1,n
  do j = 1,n
    sf(i,j) = dsqrt(wf(i)*vf(j)+vf(j)*vf(j))
    sfn(i,j) = sf(i,j)*w1/di
    deltav(i,j) = sf(i,j)*w1
    y(i,j) = deltav(i,j)/(di)
  enddo
enddo

do i = 1,n
  deltavr(i) = wf(i)*w1
enddo

do j = 1,n
  deltavy(j) = vf(j)*w1
enddo

open(22,file='tau2name')
read(22,22){tau2name(i),i = 1,num}
close(22)

open(24,file='sennname')
read(24,22){sennname(i),i = 1,num}
close(24)

open(25,file='lennname')
read(25,22){lennname(i),i = 1,num}
close(25)

do kk = 2,num
  r00(kk) = r00(kk-1)+0.1
enddo

32  format(a80)

do loop = 1,num
  do i = 1,m
    do j = 1,n
      tau2(i,j) = 0.
      senn(i,j) = 0.
      lenn(i,j) = 0.
    enddo
  enddo

  alpha = di*100/r00(loop)

  do i = 1,m
    do j = 1,n

      if (sfn(i,j) .lt. 1.0) then

        do k = 1,m
          do l = 1,n

            if (y(k,l) .lt. 1.0) then

              if (sfn(i,j) .eq. 0.0) a(k,l) = y(k,l)
              if (y(k,l) .eq. 0.0) a(k,l) = sfn(i,j)

              if ((y(k,l) .ne. 0.0) .and. (sfn(i,j) .ne. 0.0)) then

                ctheta(k,l) = (deltavr(k)+wf(l)+deltavy(l)+vf(j))/
                  (deltav(k)+sf(i,j))
                if (ctheta(k,l) .lt. -1.0) ctheta(k,l) = -1.0
                if (ctheta(k,l) .gt. 1.0) ctheta(k,l) = 1.0

                theta(k,l) = acos(ctheta(k,l))
                ctheta(k,l) = cos(theta(k,l))
                stheta(k,l) = sin(theta(k,l))
                a(k,l) = dsqrt(sfn(i,j)*sfn(i,j)+y(k,l)*y(k,l)+
                  2*sfn(i,j)*y(k,l)*ctheta(k,l))
                endif

                yc(k,l) = abs(dsqrt(1-szn(i,j)*sfn(i,j)+stheta(k,l)-
                  sfn(i,j)*ctheta(k,l)))
                thetaac(i,j) = asin(sfn(i,j))

                if (a(k,l) .gt. 1.0) a(k,l) = 1.0
            endif
          endif
        endif
      endif
    endif
  endif

  if ((theta(k,l) .lt. thetaac(i,j)) .or. ((theta(k,l) .gt.
    thetaac(i,j)) .and. (y(k,l) .gt. yc(k,l)))) then
    a(k,l) = 0.5*(acos(a(k,l))-a(k,l))+dsqrt(1-a(k,l)*a(k,l))
    endif

  if ((theta(k,l) .gt. thetaac(i,j)) .and.
    (y(k,l) .lt. yc(k,l))) then
    bax1 = (0.5*cos(theta(k,l)-acos(y(k,l))))-0.5*sfn(i,j)-
      y(k,l)*ctheta(k,l)*(2.0)
    bay1 = (0.5*sin(theta(k,l)-acos(y(k,l))) + 0.5*dsqrt(
      1-sfn(i,j)*sfn(i,j))-y(k,l)*stheta(k,l))*(2.0)
    bal(k,l) = dsqrt(bax1+bay1)
    bdx1 = (0.5*cos(theta(k,l)-acos(y(k,l))) - 0.5*sfn(i,j))
      *(2.0)
    bdy1 = (0.5*sin(theta(k,l)-acos(y(k,l))) - 0.5*dsqrt(
      1-sfn(i,j)*sfn(i,j)))*(2.0)
    bdl(k,l) = dsqrt(bdx1+bdy1)
    dal(k,l) = dsqrt(y(k,l)*y(k,l)+(1-sfn(i,j)*sfn(i,j))-2*
      y(k,l)*stheta(k,l)*dsqrt(1-sfn(i,j)*sfn(i,j)))
    s11 = 0.5*(bal(k,l)+bdl(k,l)+dal(k,l))
    as = 0.5*(asin(bal(k,l))+asin(bdl(k,l))-bal(k,l)+
      dsqrt(1-bal(k,l)*bal(k,l))-bdl(k,l)+dsqrt(1-bdl(k,l)*
      bdl(k,l)))
    ass = 2*dsqrt(s11*(s11-bal(k,l))+(s11-bdl(k,l))
      *(s11-dal(k,l)))
    if ((s11-dal(k,l)) .lt. 0.0) print='yes',k,l
    a(k,l) = as+ass
  endif

  qr = 6.88*(sfn(i,j)+alpha)**(6/3.)
  qya = (abs(y(k,l)*sfn(i,j)+alpha)**(6/3.))
  qyb = (abs(y(k,l)-sfn(i,j)+alpha)**(6/3.))
  qyc = (qya+qyb)*0.5
  qyd = (y(k,l)+alpha)**(6/3.)
  qy = 6.88*(qya-qyb)
  if ((abs(qy) .lt. 708.0) .and. (abs(qy) .lt. 708.))
    q(k,l) = exp(-qy)+exp(-qy)

    tau2(i,j) = tau2(i,j)+a(k,l)*q(k,l)+di*y(k,l)

  endif
enddo

tele(i,j) = 2*(acos(sfn(i,j))-sfn(i,j)+dsqrt(1-sfn(i,j)*
sfn(i,j)))/pi)

senn(i,j) = tele(i,j)*exp(-0.5*6.88*(alpha*
sfn(i,j))**(6/3.)*(1-sfn(i,j))**(1/3.))

lenn(i,j) = tele(i,j)*exp(-0.5*6.88*(alpha*
sfn(i,j))**(6/3.))

senn(i,j) = senn(i,j)+senn(i,j)
lenn(i,j) = lenn(i,j)+lenn(i,j)
if (lenn(i,j) .lt. 1e-20) lenn(i,j) = 0.0
if (senn(i,j) .lt. 1e-20) senn(i,j) = 0.0
endif

enddo

open(12,file=tau2name(loop))
write(12,*) tau2
close(12)

open(13,file=sennname(loop))
write(13,*) senn
close(13)

open(15,file=lennname(loop))
write(15,*) lenn
close(15)

enddo

time1 = ctime(ttime)
print='execution time in seconds',time1
end

C-----END of Korrif's function evaluation program-----

```

```

C   Speckle Code in F77
CXXXXXXXXXXXXXXXXXXXXXXXXXXXXXXXXXXXXXXXXXXXXXXXXXXXXXXXXXXXXXXXXXXXX
C   m, n - size of full image to be processed
C   m1, n1 - size of sub-images to be processed
C   nm(2), iflg, ier, nd - used in FFT routine
C   cnt - used in bispectrum estimation
C   nimages, nframes - total number of object and flat-field images
C   nframes - a variable to limit the number of frames processed
C   lenx - segment size in x, leny - segment size in y
C   nusegt - total number of segments = (2*lenx-1)*(2*leny-1)
C   datain, datamax - real numbers used in the subroutines to read fits image
C   r00 - Fried's parameter
C   d2image - full 2d image
C   nsf - normalised spatial frequency
C   ftime(2), time3 to find execution time
C   drdcube - deconvolved, registered datacube
C   fldcube - flat-field datacube
C   sffit, sffit - surface fit for images and their mean
C   asp - power spectrum of image; fourth moment
C   pspl - noise power spectrum
C   ncomp - noise corrected power spectrum
C   famp - Fourier amplitude of the object
C   corr(1000) - array used for correlation of phases of a particular frequency
C   count, cnt, cnt1, cnt2, csun, csun1 - temporary variable used in counting
C   contr - contains contrast of the images
C   simage - a sub-image, smoi - a sub-image of noise
C   phaerr - error in estimated phase values, phaer-azimuthal average of phaerr
C   libr - library of hanning functions used in mosaicking
C   recon - reconstruction before dividing by libr
C   simageid, smoid - id form of a sub-image of object and noise respectively
C   ax, ay, kx, ky, ut, utt - all used in surface fit routine
C   savg - average intensity of a sub-image
C   asavg - average of all savg's
C   pcm - perpendicular components of bispectrum
C   prcm - perpendicular component of unit amplitude phasors
C   avg, std, var - average, standard deviation and variance
C   tau - korff' function, tauaux - its maximum value
C   blspm - bispectrum values
C   smflt - smoothed noise filter
C   limage - long exposure image
C   blsper - error in bispectrum
C   sph - number of phasors for a particular spatial frequency
C   mbspm - mean bispectrum, nblspm - normalised mean bispectrum
C   cg - complex array use in FFT, filal - Fourier transform of long exposure image
C   ephase - unit amplitude phasors.
C   ftime - Fourier transform of reconstructed image
C   flatfilname - name of flat-field image
C   objfilname - name of the object file
C   reconfile - reconstructed filname
C   r0val - Fried's parameter for all the segments
CXXXXXXXXXXXXXXXXXXXXXXXXXXXXXXXXXXXXXXXXXXXXXXXXXXXXXXXXXXXXXXXXXXXX
integer m(2), n1, n2, nd, iflg, ier, m, n
integer k, kppa, lenx, leny, lc, lcount
integer nkk, nfra, num, nusegt, nimages, nframes
parameter (m=128, n=128, n1=16, n2=16, nfra=32)
parameter (nimages=32, nframes=16)
parameter (pi= 3.1415926535897932440)
integer ind(nimages)
real corr(1000), count, cnt, cnt1, cnt2, image(m,n), contr(nimages)
real datain, datamax, contrast, avm, nsf(n1,n2), simage(n1,n2)
real smoi(n1,n2), han(n1,n2), hanning(n1,n2), ftime(2), p(spl,n2)
real drdcube(m,n,nimages), fldcube(m,n,nimages), phaerr(n1,n2)
real sffit(n1,n2,images), qn(n1/2), phaer(n1/2-1), recon(m,n)
real sffit(n1,n2), simageid(n1,n2), kx(2,2), ax(n1,n2), ay(n1,n2)
real kx(4,n1,n2), ur(4,n1,n2), urt(n1,n2,4), libr(m,n), reim(n1,n2)
real smoid(n1,n2), asvg, asavg
double precision pcm(nfra), pccom(500), avg, std, var, tau(n1,n2)
double precision tauaux, sffit(n1,n2), asp(n1,n2)
double precision pspl(n1,n2), ncomp(n1,n2), smflt(n1,n2), prod
double precision famp(n1,n2), limage(n1,n2), blsper(22650)
complex*16 sph(1000), mbspm(22650), nblspm, blspm(22650, nfra)
complex*16 cg(n1,n2), filal(n1,n2), ephase(n1,n2), treis(n1,n2)
complex csun, csun1
character flatfilname*80, objfilname*80, reconfilname*80
character r0val(226)*10

nm(1) = n1
nm(2) = n2
nd = 2

C   Determine normalised spatial frequency; call subroutine nf
call nf(nsf,n1,n2)

C   Normalised spatial frequency used in plots (x axis)
do i = n1/2+1, n1
  qn(i-n1/2) = nsf(i,n2/2+1)
enddo

C   Use 100% hanning function as weighting function in re-assembling
the sub-images.
call hanning(hanning,n1,n2)

CXXXXXXXXXXXXXXXXXXXXXXXXXXXXXXXXXXXXXXXXXXXXXXXXXXXXXXXXXXXXXXXXXXXX
CXX Generate Optimised Apodisation Window (Keller, 1999) XX
CXXXXXXXXXXXXXXXXXXXXXXXXXXXXXXXXXXXXXXXXXXXXXXXXXXXXXXXXXXXXXXXXXXXX
C   Estimate 20% hanning function (Brault and White, A & A, 1971)
C   to apodise the sub-image
call hn(han,n1,n2)

C   Convert the image into complex array; FFT is for complex array.
do k2 = 1, n2
  do k1 = 1, n1
    cg(k1,k2) = cplx(han(k1,k2), 0)
  enddo
enddo

C   Fourier transform; includes shifting by half the size of the array
before and after doing transform. iflg=1 for inverse transform
iflg=-1
call hshift(cg,n1,n2)
call FFTW(nd, nm, cg, iflg, ier)
call hshift(cg,n1,n2)

C   Divide the result by total number of elements when iflg=-1
do k2 = 1, n2
  do k1 = 1, n1
    cg(k1,k2) = cg(k1,k2)/dbl(n1*n2)
  enddo
enddo

C   Force first Fourier components to zero; reduces the phase errors
introduced by apodisation (Keller, 1999)
cg(n1/2+1, n2/2+2) = 0.
cg(n1/2+1, n2/2) = 0.
cg(n1/2+2, n2/2+1) = 0.
cg(n1/2, n2/2+1) = 0.

C   Fourier transform; set iflg=1 for direct transform
iflg = +1
call hshift(cg,n1,n2)
call FFTW(nd, nm, cg, iflg, ier)
call hshift(cg,n1,n2)

C   Take out only the real part; imaginary part will be zero anyway.
This is the optimum apodisation window.
do k2 = 1, n2
  do k1 = 1, n1
    han(k1,k2) = real(cg(k1,k2))
  enddo
enddo

C   Estimate the number of sub-images
lenx = m/4
leny = n/4
nusegt = (2*lenx-1)*(2*leny-1)

CXXXXXXXXXXXXXXXXXXXXXXXXXXXXXXXXXXXXXXXXXXXXXXXXXXXXXXXXXXXXXXXXXXXX
CXX Generation of Optimised Apodisation Window ends here XX
CXX Get the input data 1: Object data cube 2: Flat-field data XX
CXX cube 3: Filenames of Korff's functions for all the segments. XX
CXXXXXXXXXXXXXXXXXXXXXXXXXXXXXXXXXXXXXXXXXXXXXXXXXXXXXXXXXXXXXXXXXXXX

C   Reading object files into a datacube; Use the input data file here.
objfilname = './drdcubobj1.fits'
call readheaderplusimage(objfilname, drdcube, datain, datamax)

C   Reading flat field files into a datacube; Use flat-field files here.
flatfilname = './fldcubeobj1.fits'
call readheaderplusimage(flatfilname, fldcube, datain, datamax)

C   Read the files containing names of Korff's functions to be
used for amplitude calibration of each subimage or segment.
open('11.fil', './fldcubeobj1')
read(12, '(r0val(i), i=1, nusegt)')
close(12)

CXXXXXXXXXXXXXXXXXXXXXXXXXXXXXXXXXXXXXXXXXXXXXXXXXXXXXXXXXXXXXXXXXXXX
CXX Reading the input data ends here XX
CXX Estimate contrast, select good/bad frames for reconstruction XX
CXXXXXXXXXXXXXXXXXXXXXXXXXXXXXXXXXXXXXXXXXXXXXXXXXXXXXXXXXXXXXXXXXXXX

C   Estimate contrast of the images to select good/bad frames
do i = 1, nimages
  do k2 = 1, m
    do k1 = 1, n
      image(k1,k2) = drdcube(k1,k2,i)
    enddo
  enddo
  call findsharp(image, m, n, contrast)
  contr(i) = contrast
enddo

C   Sort in ascending or descending order so that first 'nfra' bad or
good frames can be chosen; Use .gt. or .lt. in the subroutine sort
for selecting bad or good frames respectively.
call sort(contr, ind, nimages)

CXXXXXXXXXXXXXXXXXXXXXXXXXXXXXXXXXXXXXXXXXXXXXXXXXXXXXXXXXXXXXXXXXXXX
CXX Selection of best frames ends here XX
CXXXXXXXXXXXXXXXXXXXXXXXXXXXXXXXXXXXXXXXXXXXXXXXXXXXXXXXXXXXXXXXXXXXX

C   Segmentation starts here 1a:1a=15, 1b:1b=15 is segments
lc = 0
lcount = 0

C   For each segment repeat the following
do nuseg = 1, nusegt
  if (lcount .ge. 2*lenx-1) then
    lcount = lcount - (2*lenx-1)
  endif
  la = lcount + (n1/2) + 1
  lb = lc + (n2/2) + 1
  lcount = lcount + 1

C   Initialise all the arrays
do k2 = 1, n2
  do k1 = 1, n1
    limage(k1,k2) = 0
    asp(k1,k2) = 0
    pspl(k1,k2) = 0.
    pck(k1,k2) = 0.
    ephase(k1,k2) = 0
    phaerr(k1,k2) = 0
  enddo
enddo

```

```

enddo
do i = 1,22660
do j = 1,nfra
bispm(i,j) = 0
enddo
asavg=0.
C Repeat the following for all the frames.
do i = 1, nfra
C Read a sub-image from the databse drdcube.
do k2 = 1,n2
do k1 = 1,n1
simage(k1,k2) = drdcube(k1+1:n1-1,k2+1:n2-1,ind(i))
enddo
C Find the average value.
avg = 0.
do k2 = 1,n2
do k1 = 1,n1
savg = savg+simage(k1,k2)
enddo
savg = savg/float(n1*n2)
C Add the averages and preserve them. Use the average of averages
C to multiply the final reconstruction.
asavg = asavg+savg
C Divide by average value to account for sky brightness variations.
C Convert into a 1D array
nkk = 1
do k2 = 1,n2
do k1 = 1,n1
simage(k1,k2) = simage(k1,k2)/savg
simageid(nkk) = simage(k1,k2)
nkk = nkk+1
enddo
C Fit a bilinear fit of the form a0+a1*x+a2*y+a3*x*y
C kx contains co-efficients a0,a1,a2,a3; fitter surface is
C converted into 1D again; simageid is the fit in 1D
call sfit2d(simageid,n1,n2,ax,ay,ut,ut,kk,kx)
C Convert the fitted 1D array to 2D surface; subtract it from the subimage.
nkk = 1
do k2 = 1,n2
do k1 = 1,n1
sfit(k1,k2,i) = simageid(nkk)
simage(k1,k2) = simage(k1,k2)-sfit(k1,k2,i)
nkk = nkk+1
enddo
C Multiply by optimum apodization window; add the images to obtain
C an equivalent long exposure image; convert the array into complex
C as FFT works for complex array
do k2 = 1,n2
do k1 = 1,n1
simage(k1,k2)=simage(k1,k2)*aban(k1,k2)
limage(k1,k2) = limage(k1,k2)+simage(k1,k2)
cg(k1,k2) = cplx(simage(k1,k2),0)
enddo
C Do Fourier transform; use hshift before and after transform.
iflg = +1
call hshift(cg,n1,n2)
call FFTW(nd,nn,cg,iflg,ier)
call hshift(cg,n1,n2)
C Estimate power spectrum
do k2 = 1,n2
do k1 = 1,n1
prod = abs(cg(k1,k2))*abs(cg(k1,k2))
amp(k1,k2) = amp(k1,k2)+prod
enddo
enddo
C Bispectrum calculation starts here
C First along positive spatial frequency axis; i.e., f_x direction;
k = 1
do ri = n2/2-1,-1
cut = (ri-(n2/2+1))*((ri+1)-int((ri+1)/2))/2+(n2/2)+1
do j1 = n2/2,cnt,-1
bispm(k,1) = bispm(k,1)+
k cg(n1/2+1,j1)*cg(n1/2+1,ri+(n2/2+1)-j1)*conj(cg(n1/2+1,ri))
k = k+1
enddo
enddo
C Next along positive spatial frequency axis; i.e., f_y direction;
do ci = n1/2-1,-1
cut = (ci-(n1/2+1))*((ci+1)-int((ci+1)/2))/2+n1/2+1
do i1 = n1/2,cnt,-1
bispm(k,1) = bispm(k,1)+
k cg(i1,n2/2+1)*cg(ci+n1/2+1-i1,n2/2+1)*conj(cg(ci,n2/2+1))
k = k+1
enddo
enddo
C Now in lower left half of the Fourier plans
do ci = n1/2,1,-1
do i1 = n1/2+1,cnt,-1
cut = (ci-(n1/2+1))*((ci+1)-int((ci+1)/2))/2+n1/2+1
k cnt1 = ri+(i1-ne. ((ci-(n1/2+1))/2)+n1/2+1) +
((ri-(n2/2+1))*((ri+1)-int((ri+1)/2))/2+n2/2+1)*
(i1-ne. ((ci-(n1/2+1))/2)+n1/2+1)
do j1 = n2/2+1-(i1-ne. (n1/2+1)),cnt1,-1
bispm(k,1) = bispm(k,1)+cg(i1,j1)*
k cg(ci+n1/2+1-i1,ri+n2/2+1-j1)*
k conj(cg(ci,ri))
k = k+1
enddo
enddo
C Along first column in upper left half of the Fourier plans
ci = 1.
do ri = n2/2+2,n2
do i1 = n1/2+1,((ci-(n1/2+1))/2)+n1/2+1,-1
cut2 = ri+(i1-ne. ((ci-(n1/2+1))/2)+n1/2+1)*
((ri-(n2/2+1))*((ri+1)-int((ri+1)/2))/2+n2/2+1)+
k (i1-ne. ((ci-(n1/2+1))/2)+n1/2+1)
k do j1 = n2/2+1-(i1-ne. (n1/2+1)),cnt1,-1
bispm(k,1) = bispm(k,1)+cg(i1,j1)*
k cg(ci+n1/2+1-i1,ri+n2/2+1-j1)*
k conj(cg(ci,ri))
k = k+1
enddo
enddo
C Print k here to find total bispectrum values: print*,k
C Average over the frames ends here
enddo
CXXXXXXXXXXXXXXXXXXXXXXXXXXXXXXXXXXXXXXXXXXXXXXXXXXXXXXXXXXXXXXXXXXXXXXXXXXXX
CXX Estimation of the sum of Power Spectrum and bispectrum of XX
CXX a sub-image ends here. (do loop in the previous line). XX
CXXXXXXXXXXXXXXXXXXXXXXXXXXXXXXXXXXXXXXXXXXXXXXXXXXXXXXXXXXXXXXXXXXXXXXXXXXXX
C Estimate mean bispectrum and component of each bispectrum perpendicular
C to the direction of mean. Estimate error in bispectrum (Busher, 1988).
do i = 1,k-1
mbispm(i) = 0.
do j = 1,nfra
mbispm(i) = mbispm(i)+bispm(i,j)
enddo
mbispm(i) = mbispm(i)/real(nfra)
nmbispm = mbispm(i)/abs(mbispm(i))
do j = 1,nfra
pcn(j) = mag(bispm(i,j))+real(nmbispm) -
k real(bispm(i,j))+mag(nmbispm)
enddo
C Error in bispectrum is defined as variance of perpendicular component
C divided by absolute value of bispectrum times square root of number of
C frames ( For large number of frames; Busher, 1988).
call stdevrid(pcn,nfra,avg,std)
bisprer(i) = std*std/abs(mbispm(i))*sqrt(real(nfra) )
enddo
C Estimate the average of estimated bilinear surface fits of all the frames.
do k2 = 1,n2
do k1 = 1,n1
msffit(k1,k2) = 0
do i = 1,nfra
sffit(k1,k2) = sffit(k1,k2)+sfit(k1,k2,i)
enddo
msffit(k1,k2) = sffit(k1,k2)/real(nfra)
enddo
enddo
C Estimate the average power-spectrum of flat-field image following
C the similar procedure to that of the object.
C Repeat the following for all the flat-field images
CXXXXXXXXXXXXXXXXXXXXXXXXXXXXXXXXXXXXXXXXXXXXXXXXXXXXXXXXXXXXXXXXXXXXXXXXXXXX
CXX Estimation of sum Noise Power Spectrum from Flat-field XX
CXX images starts here. (do loop in following line) XX
CXXXXXXXXXXXXXXXXXXXXXXXXXXXXXXXXXXXXXXXXXXXXXXXXXXXXXXXXXXXXXXXXXXXXXXXXXXXX
do i = 1,nfimages
C Extract the sub-image from the flat-field image
do k2 = 1,n2
do k1 = 1,n1
anoi(k1,k2) = fldcube(k1+1:n1-1,k2+1:n2-1,i)
enddo
enddo
C Estimate the average
avg = 0.
do k2 = 1,n2
do k1 = 1,n1
avg = avg+anoi(k1,k2)
enddo

```

```

        enddo
        avg = avg/float(n1*n2)
C Divide the sub-image by the average; convert into 1D array
        nkk = 1
        do k2 = 1, n2
        do k1 = 1, n1
                snoi(k1,k2) = snoi(k1,k2)/avg
                snoid(nkk) = snoi(k1,k2)
                nkk = nkk+1
        enddo
        enddo
C Estimate and subtract bilinear fit
        call sfit2d(snoiid,n1,n2,ax,ay,ut,vt,kk,kk)
        nkk = 1
        do k2 = 1, n2
        do k1 = 1, n1
                snoi(k1,k2) = snoi(k1,k2)-snoid(nkk)
                nkk = nkk+1
        enddo
        enddo
C Multiply by optimum apodisation window; convert into complex array for FFT
        do k2 = 1, n2
        do k1 = 1, n1
                snoi(k1,k2) = snoi(k1,k2)*hau(cg(k1,k2))
                cg(k1,k2) = cmplx(snoi(k1,k2),0)
        enddo
        enddo
C Estimate Fourier transform (FFT)
        iflg = +1
        call hahift(cg,n1,n2)
        call FFTM(nd,nn,cg,iflg,ier)
        call hahift(cg,n1,n2)
C Estimate the power spectrum; it is equivalent to noise power spectrum
        do k2 = 1, n2
        do k1 = 1, n1
                pprod = abs(cg(k1,k2))*abs(cg(k1,k2))
                pnoi(k1,k2) = pnoi(k1,k2)+pprod
        enddo
        enddo
C Average over flat-field images ends here
        enddo
CXXXXXXXXXXXXXXXXXXXXXXXXXXXXXXXXXXXXXXXXXXXXXXXXXXXXXXXXXXXXXXXXXXXXXXXXXXXX
CXX Estimation of sum of Noise Power Spectrum from Flat-field XX
CXX images ends here. (do loop in previous lines) XX
CXXXXXXXXXXXXXXXXXXXXXXXXXXXXXXXXXXXXXXXXXXXXXXXXXXXXXXXXXXXXXXXXXXXXXXXXXXXX
CXX Estimation of Fourier amplitudes of the object from the XX
CXX average power spectrum of the images starts here; XX
CXXXXXXXXXXXXXXXXXXXXXXXXXXXXXXXXXXXXXXXXXXXXXXXXXXXXXXXXXXXXXXXXXXXXXXXXXXXX
        do k2 = 1, n2
        do k1 = 1, n1
                amp(k1,k2) = amp(k1,k2)/real(nfra)
                limage(k1,k2) = limage(k1,k2)/real(nfra)
                flml(k1,k2) = cmplx(limage(k1,k2),0)
                pnoi(k1,k2) = pnoi(k1,k2)/real(nfra)
                ncamp(k1,k2) = amp(k1,k2)-pnoi(k1,k2)
                if (ncamp(k1,k2) .lt. 0) ncamp(k1,k2) = 0.
        enddo
        enddo
C Read the Korff's function for the segment and normalise it
        open('f5,file=r0val(nuseg))
        read('f5,*) tau !!!((tau(k1,k2),k1=1,n1),k2=1,n2)
        close('f5)
        open('f5,file='junk')
        write('f5,*) tau
        close('f5)
C Select the maximum value and use it for normalisation
        taumax = tau(n1/2+1,n2/2+1)
C Normalise the Korff's function
C Estimate the noise filter (Brault and White, 1971)
        do k2 = 1, n2
        do k1 = 1, n1
                tau(k1,k2) = tau(k1,k2)/taumax
                if (nax(k1,k2) .lt. 1.) then
                        nfilt(k1,k2) = ncamp(k1,k2)/amp(k1,k2)
                else
                        nfilt(k1,k2) = 0.
                endif
        enddo
        enddo
C Smooth the noise filter by 3 pixels; i.e., each pixel is
C average of itself and surrounding 8 pixels; leave the edges.
        do k2 = 1, n2
        do k1 = 1, n1
                snfilt(k1,k2) = nfilt(k1,k2)
                snfilt(n1,k2) = nfilt(n1,k2)
        enddo
        do k1 = 2, n1-1
        do k2 = 2, n2-1
                snfilt(k1,k2) = (nfilt(k1-1,k2-1)+nfilt(k1,k2-1)
                +nfilt(k1+1,k2-1)+nfilt(k1-1,k2)+nfilt(k1,k2)+nfilt(k1+1,k2)+
                +nfilt(k1-1,k2+1)+nfilt(k1,k2+1)+nfilt(k1+1,k2+1))/9.
        enddo
        enddo
C Divide by Korff's function if its value is less than 1e-3.
C Take the square root and multiply it by the smoothed noise filter.

```

```

C The resulting array 'famp' is the Fourier amplitude of the object.
        do k2 = 1, n2
        do k1 = 1, n1
                if (nax(k1,k2) .lt. 1.) then
                        if (tau(k1,k2) .gt. 1e-3) then
                                famp(k1,k2) = sqrt(amp(k1,k2)/tau(k1,k2))*snfilt(k1,k2)
                        else
                                famp(k1,k2) = sqrt(amp(k1,k2))*snfilt(k1,k2)
                        endif
                else
                        famp(k1,k2) = 0.
                endif
        enddo
        enddo
CXXXXXXXXXXXXXXXXXXXXXXXXXXXXXXXXXXXXXXXXXXXXXXXXXXXXXXXXXXXXXXXXXXXXXXXXXXXX
CXX Estimation of Fourier amplitudes of the object from the XX
CXX average power spectrum of the images ends here. XX
CXXXXXXXXXXXXXXXXXXXXXXXXXXXXXXXXXXXXXXXXXXXXXXXXXXXXXXXXXXXXXXXXXXXXXXXXXXXX
CXX Phase estimation from the average bispectrum of the images XX
CXX using phase consistency filter starts here. XX
CXXXXXXXXXXXXXXXXXXXXXXXXXXXXXXXXXXXXXXXXXXXXXXXXXXXXXXXXXXXXXXXXXXXXXXXXXXXX
C Estimate the unit amplitude bispectrum values for phase estimation
        do i1 = 1, k
        if (abs(mbispp(i1)) .ne. 0)
                k = mbispp(i1) = abs(mbispp(i1))
        enddo
C Estimate the Fourier transform of average short exposure image
        iflg = +1
        call hahift(fiml,n1,n2)
        call FFTM(nd,nn,fiml,iflg,ier)
        call hahift(fiml,n1,n2)
C Phase at the origin is zero
        ephase(n1/2+1,n2/2+1) = cmplx(1,0)
C Use its phase for the smallest Fourier component. (initial condition)
        ephase(n1/2+1,n2/2) = fiml(n1/2+1,n2/2)
        k = /abs(fiml(n1/2+1,n2/2))
        ephase(n1/2+1,n2/2+1) = fiml(n1/2+1,n2/2+1)
        k = /abs(fiml(n1/2+1,n2/2+1))
        ephase(n1/2,n2/2+1) = fiml(n1/2,n2/2+1)
        k = /abs(fiml(n1/2,n2/2+1))
        ephase(n1/2+2,n2/2+1) = fiml(n1/2+2,n2/2+1)
        k = /abs(fiml(n1/2+2,n2/2+1))
C Initialise phase consistency filter
        pc(n1/2+1,n2/2+1) = 1
        pc(n1/2+2,n2/2+1) = 1
        pc(n1/2,n2/2+1) = 1
        pc(n1/2+1,n2/2+2) = 1
        pc(n1/2+1,n2/2) = 1
C Estimate unit amplitude phaseors along f_x axis
        k = 1
        do ri = n2/2-1,1,-1
                cnt = (ri-(n2/2+1))*(ri+1-int((ri+1)/2)*2)/(ri*(n2/2+1)
                kapps = k
C Include phase consistency filter in phase estimation
        do j1 = n2/2,cnt,-1
                k = k+1
                eph(k-kapps) = pc(n1/2+1,j1)*ephase(n1/2+1,j1)
                k = pc(n1/2+1,ri+(n2/2+1)-j1)*ephase(n1/2+1,ri+(n2/2+1)-j1)
                k = cobjg(mbispp(k-k))
        enddo
C Estimate correlation of each phaseor with its counterparts
        do k1 = 1,(n2/2+1)-cnt-1
                corr(k1) = 0.
                do k2 = 1,(n2/2+1)-cnt-1
                        corr(k1) = corr(k1)+abs(eph(k1)*eph(k2))/2.
                enddo
                corr(k1) = corr(k1)/real(n2/2.-cnt+1)
        enddo
C If the number of estimates for a given frequency component is
C more than one, remove those which are less than 0.75 times the
C average correlation co-efficient and find the average of the rest.
        if ((k-kapps) .gt. 1) then
                avg = 0
                do l1 = 1,k-kapps
                        avg = avg+corr(l1)
                enddo
                avg = avg/(k-kapps)
                csun = 0.
                count = 0
                do l1 = 1,k-kapps
                        if (corr(l1) .gt. 0.75*avg) then
                                count = count+1
                                csun = csun+eph(l1)
                        endif
                enddo
                csun = csun/count
                if (abs(csun) .ne. 0) then
                        csun1 = csun/abs(csun)
                else
                        csun1 = 0.
                endif
                ephase(n1/2+1,ri) = csun1
C Estimate the phase error following Buser (1989)
        count = 0
        do l1 = 1,k-kapps
                if (corr(l1) .gt. 0.75*avg) then
                        count = count+1
                        rcom(count) = imag(eph(l1))*real(csun1)-
                        real(eph(l1))*imag(csun1)

```

```

endif
enddo
C If number of estimates is unity then phase error is zero
C Actually there is no meaning in estimating it.
if (count .eq. 1) then
  pherr(n1/2+1,ri) = 0.
else
C If number of components is more than one, estimate phase
C error (Buser, 1989); Also estimate phase consistency filter.
  avg=0.
  var=0.
  do li = 1,int(count)
    avg = avg+prcom(li)
  enddo
  avg = avg/count
  var = 0.
  do li = 1,int(count)
    var = var+(prcom(li)-avg)*(prcom(li)-avg)
  enddo
  var = var/(int(count)-1.)
  if (abs(csun) .ne. 0)
    pherr(n1/2+1,ri) = var/(abs(csun)*sqrt(count))
  endif
else
  csun = eph(ri)
  ephase(n1/2+1,ri) = csun/abs(csun)
  pherr(n1/2+1,ri) = 0.
endif
C Estimate phase consistency as absolute value of the sum of all the
C phase estimates corresponding to a point in the Fourier domain; Those
C which are significantly different from their counterparts are neglected.
  pc(n1/2+1,ri) = abs(csun)
enddo
C Estimate the phasor in negative f_x axis and negative f_y
C axis using hermitial symmetry
do i = n2/2+2,n2
  ephase(n1/2+1,i) = conjg(ephase(n1/2+1,n2+2-i))
  pherr(n1/2+1,i) = pherr(n1/2+1,n2+2-i)
  pc(n1/2+1,i) = pc(n1/2+1,n2+2-i)
enddo
do i = n1/2+2,n1
  ephase(n1,n2/2+1) = conjg(ephase(n1+2-i,n2/2+1))
  pherr(n1,n2/2+1) = pherr(n1+2-i,n2/2+1)
  pc(n1,n2/2+1) = pc(n1+2-i,n2/2+1)
enddo
C Phase estimation in lower left half of Fourier plane
do ci = n1/2,1,-1
  do ri = n2/2,1,-1
    cnt = (ci - (n1/2+1) + ((ci+1)-int((ci+1)/2))*2)/(2*(n1/2+1))
    kappa = x
C Estimate the number of phase estimates at a given point.
    num = 0
    do li = n1/2+1,cnt,-1
      cnt1 = ri+(li .ne. ((ci-(n1/2+1))/2)+n1/2+1) +
        ((ri-(n2/2+1)-(ci+1)-int((ri+1)/2))*2)/(2*n2/2+1)
      k
      (li .eq. ((ci-(n1/2+1))/2)+n1/2+1)
      num = (n2/2+1-(li .eq. (n1/2+1))-cnt1+1)*num
    enddo
C Estimate the unit phasors using phase consistency filter
    do ii = n1/2+1,cnt,-1
      cnt1 = ri+(ii .ne. ((ci-(n1/2+1))/2)+n1/2+1) +
        ((ri-(n2/2+1)-(ci+1)-int((ri+1)/2))*2)/(2*n2/2+1)
      k
      (ii .eq. ((ci-(n1/2+1))/2)+n1/2+1)
      do ji = n2/2+1-(ii .eq. (n1/2+1)),cnt1,-1
        k = k+1
        eph(k-kappa) = pc(ii,ji)*ephase(ii,ji)+
          pc((ci+1)/2+1-ii,ri+n2/2+1-ji)*ephase((ci+1)/2+1-ii,
          k
          ri+n2/2+1-ji)+conjg(abispa(k-1))
      enddo
    enddo
C Estimate the correlation function for each phase estimate.
    do kl = 1,num
      corr(kl) = 0
      do km = 1,num
        corr(kl) = corr(kl)+abs(eph(kl)*eph(km))/2.
      enddo
      corr(kl) = corr(kl)/(real(n1)/2+1.-cnt)
    enddo
C If the number of estimates for a given frequency component is
C more than one, remove those which are less than 0.75 times the
C average correlation co-efficient and find the average of the rest.
    if ((k-kappa) .gt. 1) then
      avg = 0
      do li = 1,k-kappa
        avg = avg+corr(li)
      enddo
      avg = avg/(k-kappa)
      csun = 0.
      count = 0.
      do li = 1,k-kappa
        if (corr(li) .gt. 0.75*avg) then
          count = count+1.
          csun = csun+eph(li)
        endif
      enddo
      csun = csun/count
      if (abs(csun) .ne. 0) then
        csun1 = csun/abs(csun)
      else
        csun1 = 0.
      endif
      ephase(ci,n2/2+1) = csun1
C Estimate the phase error following Buser (1989)
      count = 0.
      do li = 1,k-kappa
        if (corr(li) .gt. 0.75*avg) then
          count = count+1.
          prcom(count) = imag(eph(li))*real(csun1)-
          k
          real(eph(li))*imag(csun1)
        endif
      enddo
      if (count .eq. 1) then
        pherr(ci,n2/2+1) = 0.
      else
        avg=0.
        var=0.
        do li = 1,int(count)
          avg = avg+prcom(li)
        enddo
        avg = avg/count
        var = 0.
        do li = 1,int(count)
          var = var+(prcom(li)-avg)*(prcom(li)-avg)
        enddo
        var = var/(int(count)-1.)
        if (abs(csun) .ne. 0)
          pherr(ci,n2/2+1) = var/(abs(csun)*sqrt(count))
        endif
      endif
    endif
  endif
endif

```

```

k      phaerr(ci,ri) = var/(abs(csuum)*sqrt(count))
      endif
      else
      csuum = sph(1)
      sphase(ci,ri) = csuum
      phaerr(ci,ri) = 0.
      endif
C      Estimate phase consistency as absolute value of the sum of all the
C      phase estimates corresponding to a point in the Fourier domain; Those
C      which are significantly different from their counterparts are neglected.
      pc(ci,ri) = abs(csuum)
      enddo
      enddo
C      Phase estimation in lower right half of Fourier plane
      do ci = n1/2+2,n1,1
      do ri = n2/2,1,-1
          cnt = (ci-(n1/2+1))-((ci+1)-int((ci+1)/2))*2)/2+n1/2+1
          kappa = k
C      Estimate the number of phase estimates at a given point.
          num = 0
          do ii = n1/2+1,cnt,1
          cnt1 = xi*(11 .ne. ((ci-(n1/2+1))/2)+n1/2+1) +
          ((ri-(n2/2+1))+((ri+1)-int((ri+1)/2))*2)/2+n2/2+1+
          (11 .eq. ((ci-(n1/2+1))/2)+n1/2+1)
          k
          num = (n2/2+1-(11 .eq. (n1/2+1))-cnt1)*num
          enddo
C      Estimate the unit phasors using phase consistency filter.
          do ii = n1/2+1,cnt,1
          cnt1 = ri*(11 .ne. ((ci-(n1/2+1))/2)+n1/2+1) +
          ((ri-(n2/2+1))+((ri+1)-int((ri+1)/2))*2)/2+n2/2+1+
          (11 .eq. ((ci-(n1/2+1))/2)+n1/2+1)
          k
          do j1 = n2/2+1-(11 .eq. n1/2+1),cnt1,-1
          k = k+1
          eph(k-kappa) = pc(ii,j1)*sphase(ii,j1)+
          pc(ii+1/2+1-ii,ri+n2/2+1-j1)*sphase(ci+n1/2+1-ii,
          ri+n2/2+1-j1)*conjg(sphase(k-k-1))
          enddo
          k
C      Estimate the correlation function for each phase estimate.
          do k1 = 1,num
          corr(k1) = 0.
          do k2 = 1,num
          corr(k1) = corr(k1)+abs(eph(k1)+eph(k2))/2.
          enddo
          corr(k1) = corr(k1)/real(num)
          enddo
C      If the number of estimates is more than one then omit those
C      which are less than 0.75 times the mean correlation coefficient.
          if ((k-kappa) .gt. 1) then
          avg = 0.
          do li = 1,k-kappa
          avg = avg+corr(li)
          enddo
          avg = avg/(k-kappa)
          csuum = 0.
          count = 0.
          do li = 1,k-kappa
          if (corr(li) .gt. 0.75*avg) then
          count = count+1.
          csuum = csuum+eph(li)
          endif
          enddo
          csuum = csuum/count
          if (abs(csuum) .ne. 0) then
          csuul = csuum/abs(csuum)
          else
          csuul = 0.
          endif
          sphase(ci,ri) = csuul
          k
C      Estimate phase error following Buscher(1986)
          count = 0.
          do li = 1,k-kappa
          if (corr(li) .gt. 0.75*avg) then
          count = count+1.
          prcom(count) = imag(eph(li))+real(csuul)-
          real(eph(li))*imag(csuul)
          k
          endif
          enddo
          if (count .eq. 1) then
          phaerr(ci,ri) = 0.
          else
          avg=0.
          var=0.
          do li = 1,int(count)
          avg = avg+prcom(li)
          enddo
          avg = avg/count
          var = 0.
          do li = 1,int(count)
          var = var+(prcom(li)-avg)*(prcom(li)-avg)
          enddo
          var = var/(int(count)-1.)
          if (abs(csuum) .ne. 0)
          k
          phaerr(ci,ri) = var/(abs(csuum)*sqrt(count))
          endif
          else
          csuum = sph(1)
          sphase(ci,ri) = csuum
          phaerr(ci,ri) = 0.
          endif
C      Estimate phase consistency as absolute value of the sum of all the
C      phase estimates corresponding to a point in the Fourier domain; Those
C      which are significantly different from their counterparts are neglected.
          pc(ci,ri) = abs(csuum)
          enddo
          enddo
C      Use hermitian symmetry to estimate phase at remaining points in
C      the Fourier plane
          do i = 2,n1
          do j = n2/2+2,n2
          sphase(i,j) = conjg(sphase(n1+2-i,n2+2-j))
          phaerr(i,j) = phaerr(n1+2-i,n2+2-j)
          pc(i,j) = pc(n1+2-i,n2+2-j)
          enddo
          enddo
C      Estimate phase consistency as absolute value of the sum of all the
C      phase estimates corresponding to a point in the Fourier domain; Those
C      which are significantly different from their counterparts are neglected.
          pc(ci,ri) = abs(csuum)
          enddo
          enddo

```

```

        enddo
CXXXXXXXXXXXXXXXXXXXXXXXXXXXXXXXXXXXXXXXXXXXXXXXXXXXXXXXXXXXXXXXXXXXXXXXXXXXX
CXX Phase estimation from the average bispectrum of the images XX
CXX using phase consistency filter ends here. XX
CXXXXXXXXXXXXXXXXXXXXXXXXXXXXXXXXXXXXXXXXXXXXXXXXXXXXXXXXXXXXXXXXXXXXXXXXXXXX
C Azimuthal average of phase errors.
do i = 1,n1/2-1
  if (qn(i) .lt. 1) then
    sum = 0.
    num = 0.
    do k = 1,n2
      do j = 1,n1
        if ((nsf(j,k) .gt. qn(i)) .and. (nsf(j,k) .le. qn(i+1))) then
          sum = sum+phaerr(j,k)
          num = num+1
        endif
      enddo
    enddo
    sum = sum/float(num)
    phaer(i-1) = sum
  endif
enddo
CXXXXXXXXXXXXXXXXXXXXXXXXXXXXXXXXXXXXXXXXXXXXXXXXXXXXXXXXXXXXXXXXXXXXXXXXXXXX
CXX Reconstruction of single sub-image, Reconstruction of complete XX
CXX image using weighted re-assembly starts here. XX
CXXXXXXXXXXXXXXXXXXXXXXXXXXXXXXXXXXXXXXXXXXXXXXXXXXXXXXXXXXXXXXXXXXXXXXXXXXXX
C Form complex array of numbers with Fourier amplitudes and phases.
do k2 = 1,n2
  do k1 = 1,n1
    frcm(k1,k2) = famp(k1,k2)*ephase(k1,k2)
  enddo
enddo
C Perform Inverse Fourier transform
ifig=-1
call hahift(frcm,n1,n2)
call FFTN(ad,an,frcm,ifig,ier)
call hahift(frcm,n1,n2)
C Since ifig = -1 divide the Fourier transform by number of elements
do k2 = 1,n2
  do k1 = 1,n1
    frcm(k1,k2) = frcm(k1,k2)/dble(n1*n2)
  enddo
enddo
C Reconstructed image; imaginary part is almost zero; so omit it.
do k2 = 1,n2
  do k1 = 1,n1
    rrcm(k1,k2) = real(frcm(k1,k2))
  enddo
enddo
C Find average intensities of all the frames
asavg = asavg/real(nfra)
C Divided by optimum apodisation window, add mean of all bilinear
C surface fits, and multiply by average (asavg)
do k2 = 1,n2
  do k1 = 1,n1
    if (nan(k1,k2) .gt. 0.2) then
      rrcm(k1,k2) = rrcm(k1,k2)/dble(nan(k1,k2))
    else
      rrcm(k1,k2) = (rrcm(k1,k2))*asavg
    endif
  enddo
enddo
C Weighted re-assembly for the overlapping sub-images. Use
C 100 % hanning window for weighting. Store the weighting
C function in a separate library 'libr'.
do k2 = 1,n2
  do k1 = 1,n1
    recon(k1+1a-1,k2+1b-1) = recon(k1+1a-1,k2+1b-1)+
      rrcm(k1,k2)*hanning(k1,k2)
    libr(k1+1a-1,k2+1b-1) = libr(k1+1a-1,k2+1b-1)+hanning(k1,k2)
  enddo
enddo
C Processing for one segment ends in the following line; start next segment
enddo
CXXXXXXXXXXXXXXXXXXXXXXXXXXXXXXXXXXXXXXXXXXXXXXXXXXXXXXXXXXXXXXXXXXXXXXXXXXXX
CXX Reconstruction of complete image using weighted re-assembly XX
CXX ends here. XX
CXXXXXXXXXXXXXXXXXXXXXXXXXXXXXXXXXXXXXXXXXXXXXXXXXXXXXXXXXXXXXXXXXXXXXXXXXXXX
C Divide the re-assembled image by the library 'libr'.
C Resulting image is the mosaiced final reconstruction.
do k2 = 2,n-1
  do k1 = 2,m-1
    recon(k1,k2) = recon(k1,k2)/libr(k1,k2)
  enddo
enddo
C Save the mosaiced image (final reconstruction) as fits file.
reconfilename = './reconobj10.fits'
print*, 'writing fits image'
call writeimage2d(reconfilename,recon,m,n)
10 format(a30)
c20 format(32(1x,e21.14))
time3 = etime(ftime)
print*, 'execution time is ', time3
end
XXXXXXXXXXXXXXXXXXXXXXXXXXXXXXXXXXXXXXXXXXXXXXXXXXXXXXXXXXXXXXXXXXXXXXXXXXXX
subroutine Readheaderplusimage(filename,image,detamin,detamax)
C Print out all the header keywords in all extensions of a FITS file
integer status,unit,readwrite,blocksize,nkeys,nspace,hdtype,i
integer naxes(3),nfound,maxis1,maxis2,maxis3
integer group,firstpix,nbuffer,npixels,dim1,dim2
real detamin,detamax,nullval,buffer(100)
real image(*)
logical anynull,anyf
character filename*80,record*80
unit=98
status=0
blocksize=1
C open the FITS file, with readonly or readwrite access
C readwrite=0 for readonly access, 1 for readwrite access
readwrite=1
3 call fopen(unit,filename,readwrite,blocksize,status)
100 continue
C Determine the number of keywords in the header
4 call fghsp(unit,nkeys,nspace,status)
C Read each 80-character keyword record, and print it out
do i = 1, nkeys
5 call fgrcc(unit,i,record,status)
enddo
C Print out and END record, and a blank line to mark the end of the header
if (status .eq. 0) then
  print *, 'END'
  print *, ' '
endif
C try moving to the next extension in the FITS file, if it exists
6 call fmrhd(unit,i,hdtype,status)
if (status .eq. 0) then
  success, so loop back and print out keywords in this extension
  go to 100
7
else if (status .eq. 107) then
  hit end of file, so quit
  print *, '***** END OF FILE *****'
  status=0
  call ftcmsg
  end if
C determine the size of the image
9 call fctgnj(unit,'MAXIS',1,3,naxes,nfound,status)
C check that it found both MAXIS1 and MAXIS2 keywords
10 if (nfound .ne. 3) then
  print *, 'READIMAGE failed to read the MAXISn keywords.'
  return
  end if
C initialize variables
npixels=naxes(1)*naxes(2)*naxes(3)
group=0
firstpix=1
nullval=0.0
detamin=1.0E30
detamax=-1.0E30
C dim1 is the number of columns, same as naxes(1)
dim1 = naxes(1)
dim2 = naxes(2)
maxis1 = naxes(1)
maxis2 = naxes(2)
maxis3 = naxes(3)
do while (cpixels .gt. 0)
  read up to 100 pixels at a time
  nbuffer=min(100,npixels)
11 call fgpvc(unit,group,firstpix,nbuffer,nullval,
  buffer,anynull,status)
C find the min and max values
do i=1,nbuffer
  detamin=min(detamin,buffer(i))
  detamax=max(detamax,buffer(i))
  enddo
C increment pointers and loop back to read the next group of pixels
firstpix=firstpix+nbuffer
enddo
C print out the min and max values
print *, 'Min and max values in the image are:',detamin,detamax
call ffgdc(unit,group,nullval,dim1,dim2,maxis1,maxis2,
  k maxis3,image,anyf,status)
C close the file, free the unit number, and exit
12 call fcclos(unit, status)
C check for any error, and if so print out error messages
13 if (status .gt. 0) call printerror(status)
end
XXXXXXXXXXXXXXXXXXXXXXXXXXXXXXXXXXXXXXXXXXXXXXXXXXXXXXXXXXXXXXXXXXXXXXXXXXXX
subroutine printerror(status)
C Print out the FITSIO error messages to the user
integer status
character errtext*30,errmessage*80
C check if status is OK (no error); if so, simply return
if (status .le. 0) return
C get the text string which describes the error
1 call fgperr(status,errtext)
print *, 'FITSIO Error Status =',status,', ',errtext
C read and print out all the error messages on the FITSIO stack
2 call ftagg(errmessage)

```

```

do while (errmsgage .ne. ' ')
  print *,errmsgage
  call ftgmsg(errmessage)
end do
end

CXXXXXXXXXXXXXXXXXXXXXXXXXXXXXXXXXXXXXXXXXXXXXXXXXXXXXXXXXXXXXXXXXXXX
subroutine deletefile(filename,status)
C A simple little routine to delete a FITS file
integer status,unit,blocksize
character(*) filename
C simply return if status is greater than zero
if (status .gt. 0) return
C Get an unused Logical Unit Number to use to open the FITS file
1 call ftglou(unit,status)
C try to open the file, to see if it exists
2 call ftopen(unit,filename,1,blocksize,status)
if (status .eq. 0) then
  file was opened; so now delete it
3 call ftdelete(unit,status)
else if (status .eq. 103) then
  file doesn't exist, so just reset status to zero and clear errors
4 status=0
  call ftmsg
else
  there was some other error opening the file; delete the file anyway
5 status=0
  call ftmsg
  call ftdelete(unit,status)
end if
C free the unit number for later reuse
6 call ftflou(unit, status)
end
CXXXXXXXXXXXXXXXXXXXXXXXXXXXXXXXXXXXXXXXXXXXXXXXXXXXXXXXXXXXXXXXXXXXX

subroutine stit2d(images,nx,ny,axs,
  & ays,uts,utts,kks,kxs)
integer nx,ny,indx(4),nkk
real axs(nx,ny),ays(nx,ny)
real sum,putt(4,4),putti(4,4)
real d,kxs(2,2),kxsid(4),kks(4,nx*ny)
real images(nx*ny)
real uts(4,nx*ny),utts(4,nx*ny,4)
do j = 1,ny
  do i = 1,nx
    kxs(i,j) = real(i)-i.
  enddo
  do i = 1,nx
    do j = 1,ny
      ays(i,j) = real(j)-i.
    enddo
  enddo
  do i = 1,4
    do j = 1,nx*ny
      uts(i,j) = i*1e-20
    enddo
  enddo
do i = 1,4
  nkk = 1
  do l = 1,ny
    do k = 1,nx
      if (l .eq. 1) then
        uts(i,nkk) = (axs(k,l)+*(0))*(ays(k,l)+*(0))
      elseif (l .eq. 2) then
        uts(i,nkk) = (axs(k,l)+*(0))*(ays(k,l)+*(1))
      elseif (l .eq. 3) then
        uts(i,nkk) = (axs(k,l)+*(1))*(ays(k,l)+*(0))
      else
        uts(i,nkk) = (axs(k,l)+*(1))*(ays(k,l)+*(1))
      endif
      nkk = nkk+1
    enddo
  enddo
  do i = 1,nx*ny
    do j = 1,4
      utts(i,j) = uts(j,i)
    enddo
  enddo
11 format(9(1x,f14.7))
10 format(4(1x,f21.14))

do i = 1,4
  do j = 1,4
    sum = 0.
    do k = 1,nx*ny
      sum = sum+uts(i,k)*utts(k,j)
    enddo
    putt(i,j) = sum
  enddo
enddo

do i = 1,4
  do j = 1,4
    putti(i,j) = 0.
  enddo
  puti(i,i) = 1.
enddo

call ludcomp(putt,4,4,indx,d)
do j = 1,4
  call lubkbb(putt,4,4,indx,putti(i,j))
enddo

do i = 1,4
  do j = 1,4
    sum = 0.
    do k = 1,4
      sum = sum+putti(i,k)*utts(k,j)
    enddo
    kks(i,j) = sum
  enddo
enddo

do i = 1,4
  do j = 1,1
    sum = 0.
    do l = 1,2
      do i = 1,nx*ny
        sum = sum+kks(i,l)*images(l)
      enddo
      kxsid(i) = sum
    enddo
  enddo
  it = 1
  do j = 1,2
    do i = 1,2
      kxs(i,j) = kxsid(it)
      it = it+1
    enddo
  enddo
  do i = 1,1
    do j = 1,nx*ny
      sum = 0.
      do k = 1,4
        sum = sum+ kksid(k)*uts(k,j)
      enddo
      images(j) = sum
    enddo
  enddo
  return
end
CXXXXXXXXXXXXXXXXXXXXXXXXXXXXXXXXXXXXXXXXXXXXXXXXXXXXXXXXXXXXXXXXXXXX

SUBROUTINE ludcomp(n,n,np,indx,d)
INTEGER n,np,indx(n),NMAX
REAL d,a(np,np),TINY
PARAMETER (NMAX=600,TINY=1.0e-20)
INTEGER i,imax,j,k
REAL aamax,dum,sum_vv(NMAX)
d=1.
do 12 i=1,n
  aamax=0.
  do 11 j=1,n
    if (abs(a(i,j)).gt..n*aamax) aamax=abs(a(i,j))
  11 continue
  if (aamax.eq.0.) pause 'singular matrix in ludcomp'
  vv(i)=1./aamax
  12 continue
  do 13 j=1,n
    do 14 i=1,j-1
      sum=a(i,j)
    13 continue
    sum=sum-a(i,k)*a(k,j)
    a(i,j)=sum
  14 continue
  aamax=0.
  do 16 i=j,n
    sum=a(i,j)
    do 15 k=i,j-1
      sum=sum-a(i,k)*a(k,j)
    15 continue
    a(i,j)=sum
    dum=vv(i)*abs(sum)
    if (dum.gt.aamax) then
      imax=i
      aamax=dum
    endif
  16 continue
  if (j.ne.imax) then
    do 17 k=i,n
      dum=a(imax,k)
      a(imax,k)=a(k,k)
      a(k,k)=dum
    17 continue
    de=d
    vv(imax)=vv(j)
  endif
  indx(j)=imax
  if (a(j,j).eq.0.) a(j,j)=TINY
  if (j.ne.n) then
    dum=1./a(j,j)
    do 18 i=j+1,n
      a(i,j)=a(i,j)*dum
    18 continue
  endif
  19 continue
  return
END
CXXXXXXXXXXXXXXXXXXXXXXXXXXXXXXXXXXXXXXXXXXXXXXXXXXXXXXXXXXXXXXXXXXXX

SUBROUTINE lubkbb(a,n,np,indx,b)
INTEGER n,np,indx(n)
REAL a(np,np),b(n)
INTEGER i,i1,j,11
REAL sum
i1=0
do 12 i=1,n
  11=indx(i)
  sum=b(11)
  b(11)=b(i)
  if (i.ne.0) then
    do 11 i=i+1,i-1
      sum=sum-a(i,j)*b(j)
    11 continue
  else if (sum.ne.0.) then
    i=i
  endif
  12 continue
  do 14 i=n,i-1
    sum=b(i)
    do 13 j=i+1,n

```

```

sum=sum-a(i,j)+b(j)
13 continue
b(i)=sum/a(i,i)
14 continue
return
END

C*****
C This is a subroutine to calculate the Discrete Fourier Transform (DFT)
C in 'n' dimensions using a FFT algorithm. ND is the number of dimensions.
C NN is an array of length ND. NN(i) is the number of data points along
C the i-th co-ordinate, which must be equal to a power of 2. CG is a complex
C array of length NN(1)*NN(2)*NN(3)*...*NN(ND), which should contain the data
C points when called in the subroutine. The data should be stored in the
C normal Fortran order with
C
C CG(i+j1+j2*NN(1)+j3*NN(1)*NN(2)+...+jn*NN(1)*...NN(n-1))=g.j1, j2, ... jn
C
C for C=j,r < NN(i)-1. In fact, in the calling program CG can be treated
C as a ND dimensional complex array with dimension CG(NN(1), NN(2), NN(ND))
C and CG(j1+1, j2+1, ... jn+1) = g.j1, j2, jn. It may be noted that the
C dimensions of this ND dimensional array must be exactly equal to the
C number of data points in the corresponding variables. After execution
C the DFT will be overwritten on the same array CG. Hence, if necessary,
C a copy of the original data should be preserved for later use, before
C calling the subroutine. IFLAG is a flag. IF IFLAG >= 0, DFT is
C calculated, while if the IFLAG < 0 the inverse DFT will be calculated.
C IER is the error parameter. IER = 111 implies that atleast one of the
C NN(i), (i = 1, 2, ... ND) is not a power of 2.

C REMARK: This program is taken from Numerical Methods for Scientists &
C Engineers by R. N. Anis

C*****
subroutine FFTN(nd,nm,cg,iflg,ier)
implicit complex(c)
C use higher precision for calculating w^j
complex*16,cuf,cvj,cg(*)
C to control roundoff error
real*8,pi,th
parameter(pi=3.1415926535897932440)
dimension nm(nd)

ntot=1
do 1000 i=1,nd
ntot=ntot*nm(i)
1000 continue

npr1=1
if (iflg .ge. 0) then
C for DFT
i=1
else
C for inverse DFT
i=-1
endif

do 5000 id=1,nd
n=nm(id)
npr=npr1
npr1=npr*n

j=1
loop for bit reversal
do 2000 i=1,npr1,npr
if (j .gt. i) then
do 1600 i1=i,ntot,npr1
do 1600 i2=i1,i1+npr-1
j2=i2+i-1
ct=cg(i2)
cg(i2)=cg(j2)
cg(j2)=ct
1600 continue
endif
n=npr1/2
if (n .ge. npr .and. j .gt. n) then
j=j-n
n=n/2
go to 1800
endif
j=j+n
2000 continue

ier=0
j0=1
k0=n/2
th=pi/k0
cuf=-1

C loop for FFT calculation
3000 cvj=1
do 3600 jr=1,j0
jr0=(jr-1)*npr+1
do 3400 ir=jr0,ntot,2*j0*npr
do 3400 i=ir,ir+npr-1
i1=i-j0*npr
ct=cg(i1)*cvj
cg(i1)=cg(i1)-ct
cg(i)=cg(i)+ct
3400 continue
cvj=cvj*cvf
3600 continue

j0=2*j0
k0=k0/2
if (j0 .eq. n) go to 5000
N is not a power of 2
if (j0 .gt. n .or. k0 .eq. 0) then
iter=iter+1
return
endif
cuf=cuf*(cos(k0*th),i0*sin(k0*th))
go to 3000
5000 continue
end

C*****
subroutine hshift(as,ns,bs)
integer ns,bs,cs
complex*16 as(ns,ns),bs
dimension ass(512,512)
bs=ns/2

```

```

cs=ns/2
do j=1,ns
do i=1,ns/2
ass(i,j)=as(i+bs,j)
enddo
do i=ns/2+1,ns
ass(i,j)=as(i-bs,j)
enddo
enddo

do i=1,ns
do j=1,ns/2
ass(i,j)=ass(i,j*cs)
enddo
do j=ns/2+1,ns
ass(i,j)=ass(i,j-cs)
enddo
enddo

return
end

C*****
subroutine nf(nsfz,ms,ns)
C To obtain the normalised spatial frequencies.
integer ms,ns
real nsfz(ms,ns)
real sx,sy,dia,dl,f,afmax
real dx,dy,ufz,vfs,afn
parameter(sx=1000,dy=8/128.,sy=92*13e-6/128.,dia=13.5e-2,
& vld=553e-10,f=5.04)
dimension ufz(512),vfs(512),afz(512,512)

dx=1./f*(ns*sx)
dy=1./f*(ns*sy)

ufz(ns/2+1)=0.
vfs(ns/2+1)=0.
do i=ns/2+2,ns
ufz(i)=ufz(i-1)+dx
enddo
do j=ns/2+2,ns
vfs(j)=vfs(j-1)+dy
enddo
do i=ns/2,1,-1
ufz(i)=ufz(i+1)-dx
enddo
do j=ns/2,1,-1
vfs(j)=vfs(j+1)-dy
enddo
do j=1,ns
do i=1,ns
sfs(i,j)=sqrt(ufz(i)*ufz(i)+vfs(j)*vfs(j))
enddo
enddo

sfnz=dia/(1.22*dl*f)
do j=1,ns
do i=1,ns
nsfs(i,j)=sfs(i,j)/sfnz
enddo
enddo

return
end

C*****
subroutine hn(hnfs,ms,ns)
real pm,ps,hnfs(ms,ns)
parameter(pi=3.1415926535897932440)

pm=0.2*ns
pn=0.2*ns
do j=1,ns
do i=1,ns
hnfs(i,j)=(0.5*(1-cos(pi*(i-1)/pm))*((i-1).le.pm)+
& ((i-1).gt.pm).and.(i-1).lt.ms-pm)*
& 0.5*(1-cos(pi*(ms-i+1)/pm))*((i-1).ge.ms-pm)+
& ((i-1).gt.ms-pm).and.(i-1).lt.ms-pm)*
& 0.5*(1-cos(pi*(ns-j+1)/pn))*((j-1).ge.pn)+
& 0.5*(1-cos(pi*(ns-j+1)/pn))*((j-1).ge.pn)
enddo
enddo

return
end

C*****
subroutine hanzg(hanzg,ms,ns)
integer ms,ns
real hanzg(ms,ns)
parameter(pi=3.1415926535897932440)

do k2=1,ns
do k1=1,ns
hanzg(k1,k2)=0.25*(1-cos(2*pi*float(k1-1)/float(ns-1)))
& *(1-cos(2*pi*real(k2-1)/real(ns-1)))
enddo
enddo

return
end

C*****
Subroutine findsharp(arrays,ms,ns,conts)
integer ms,ns
real arrays(ms,ns),sum,conts

sum=0.
conts=0.
do k2=1,ns-3
do k1=1,ns-3
conts=conts+(arrays(k1+3,k2)-arrays(k1,k2))+
& (arrays(k1+3,k2)-arrays(k1,k2))*(arrays(k1,k2+3)-
& arrays(k1,k2))+(arrays(k1,k2+3)-arrays(k1,k2))
enddo
enddo

do k2=1,ns
do k1=1,ns
sum=sum+arrays(k1,k2)
enddo
enddo

```

```

enddo
conts = conts*ms+msns/(sum*ms)
return
end

C/*****

Subroutine sort(conts, ind, numbers)
integer numbers, ind(numbers)
real conts(numbers), temp, temp(1000)

do i = 1, numbers
  temp(i) = conts(i)
enddo

do i = 1, numbers-1
  do j = i+1, numbers
    if (conts(i) .lt. conts(j)) then
      temp = conts(i)
      conts(i) = conts(j)
      conts(j) = temp
    endif
  enddo

do i = 1, numbers
  do j = 1, numbers
    if (conts(i) .eq. temp(j)) ind(i) = j
  enddo
enddo

return
end

C/*****

C for finding standard deviation, mean for real ID array

Subroutine stddev(arrs, ms, avgs, stds)
integer ms
double precision arrs(ms), avgs, stds

avg = 0.
do i = 1, ms
  avgs = avgs+arrs(i)
enddo
avgs = avgs/real(ms)
stds = 0.
do i = 1, ms
  stds = stds+(arrs(i)-avgs)*(arrs(i)-avgs)
enddo
stds = stds/real(ms)-1.
stds = sqrt(stds)
return
end

C/*****

Subroutine writeimg2d(filename, array, ms, ns)

C Create a FITS primary array containing a 2-D image

integer status, unit, blocksize, bitpix, naxis, naxes(2)
integer group, fpixel, nelements, dim1, ms, ns
real array(*)
character filename*80
logical simple, extend

1 status=0
C Name of the FITS file to be created:
C Delete the file if it already exists, so we can then recreate it
2 call deletefile(filename, status)

C Get an unused logical unit number to use to open the FITS file
3 call ftgou(unit, status)

C create the new empty FITS file
blocksize=1
4 call ftinit(unit, filename, blocksize, status)

C initialize parameters about the FITS image (300 x 200 16-bit integers)
simple=.true.
bitpix=32
naxis=2
naxes(1)=ms
naxes(2)=ns
extend=.true.

C write the required header keywords
5 call ftphpr(unit, simple, bitpix, naxis, naxes, 0, 1, extend, status)

C write the array to the FITS file
group=1
fpixel=1

C dim1 is the number of columns, same as naxes(1)
dim1 = naxes(1)
naxis1 = naxes(1)
naxis2 = naxes(2)

nelements=naxes(1)*naxes(2)
6 call ft2do(unit, group, dim1, naxis1, naxis2,
k array, status)

C close the file and free the unit number
7 call ftclos(unit, status)
call ftfou(unit, status)

C check for any error, and if so print out error messages
8 if (status .gt. 0) call printerror(status)
end

C/*****

subroutine readheaderplusimg2d(filename, image, datamin, datamax)

C Print out all the header keywords in all extensions of a FITS file

integer status, unit, readwrite, blocksize, nkeys, nspace, bdtype, l
integer naxes(2), nfound, naxis1, naxis2
integer group, firstpix, nbuffer, npixels, dim1
real datamin, datamax, nullval, buffer(100)
real image(*)

logical anynull, anyf
character filename*80, record*80

unit=99
1 status=0
blocksize=1

C open the FITS file, with readonly or readwrite access
C readwrite=0 for readonly access, 1 for readwrite access
readwrite=1
3 call ftopen(unit, filename, readwrite, blocksize, status)

100 continue

C Determine the number of keywords in the header
4 call ftgshp(unit, nkeys, nspace, status)

C Read each 80-character keyword record, and print it out
do i = 1, nkeys
5 call ftgrec(unit, i, record, status)
enddo

C Print out and END record, and a blank line to mark the end of the header
if (status .eq. 0) then
  print *, 'END'
  print *, ' '
endif

C try moving to the next extension in the FITS file, if it exists
6 call ftarhd(unit, i, hduType, status)

if (status .eq. 0) then
  success, so loop back and print out keywords in this extension
  go to 100
7

else if (status .eq. 107) then
  hit end of file, so quit
  print *, '**** END OF FILE ****'
  status=0
  call ftomsg
  end if

C determine the size of the image
9 call ftgkzj(unit, 'NAXIS', 1, 2, naxes, nfound, status)

C check that it found both NAXIS1 and NAXIS2 keywords
10 if (nfound .ne. 2) then
  print *, 'READIMAGE failed to read the NAXISn keywords.'
  return
endif

C initialize variables
npixels=naxes(1)*naxes(2)
group=0
firstpix=1
nullval=0.0
datamin=-1.0E30
datamax=-1.0E30
dim1 = naxes(1)
naxis1 = naxes(1)
naxis2 = naxes(2)

do while (npixels .gt. 0)
  read up to 100 pixels at a time
  nbuffer=min(100, npixels)
  11 call ftgprv(unit, group, firstpix, nbuffer, nullval,
k buffer, anynull, status)
  C find the min and max values
  do l=1, nbuffer
    datamin=min(datamin, buffer(l))
    datamax=max(datamax, buffer(l))
  enddo

  C increment pointers and loop back to read the next group of pixels
  npixels=npixels-nbuffer
  firstpix=firstpix+nbuffer
  enddo

  C print out the min and max values
  print *, 'Min and max values in the image are:', datamin, datamax
  call ft2de(unit, group, nullval, dim1, naxis1, naxis2,
k image, anyf, status)

  C close the file, free the unit number, and exit
  12 call ftclos(unit, status)

  C check for any error, and if so print out error messages
  13 if (status .gt. 0) call printerror(status)
  end
C----END of Speckle Code----

```

Appendix:B

Effect of Apodisation Window on Bispectrum Phases

In this appendix, we prove that the average bispectrum of a sequence of images is corrupted when they are apodized with a 20% cosine bell function. Keller(1999) had shown that using 20% hamming window affects the phases of the Knox-Thompson bispectrum. Here we follow a similar procedure and show that even the phases of bispectrum (Fourier transform of triple correlation) are affected by the window function.

A window function that has the form of a cosine bell function over the first and last 10 or 20 percent of its size is defined as

$$w(x) = \begin{cases} \frac{1}{2} - \frac{1}{2} \cos(\pi x/mL) & 0 \leq x \leq mL \\ 1 & mL \leq x \leq L(1-m) \\ \frac{1}{2} - \frac{1}{2} \cos(\pi(L-x)/mL) & L(1-m) \geq x < L \end{cases} \quad (\text{B.1})$$

where L is the size of the image and m is the fraction of the size over which the image is masked by the cosine bell (Brault and White, 1971).

Multiplying the image with an apodisation window will lead to the convolution of its Fourier transform with that of the apodisation window in the Fourier plane. In general, the Fourier transform of an image ($I(f)$) is the product of the Fourier transform of the object ($O(f)$) and that of the PSF ($P(f)$). In the presence of additive noise, the relation can be expressed mathematically as

$$I(f) = O(f) P(f) + N(f) = I_0(f) + N(f). \quad (\text{B.2})$$

where $N(f)$ is the Fourier transform of the noise. As the value of the window function is unity over majority of its size, it has a narrow peak at the origin ($f = 0$) of the Fourier plane and falls off rapidly on either side. If we assume that the Fourier components at

$f = 1$ is a^* , at $f = -1$ is a at $f = 0$ is b and the remaining components are zero, then the Fourier transform of the product of the image and the window function is given by

$$I'(f) = I(f) \odot W(f) = bI(f) + aI(f - 1) + a^*I(f + 1). \quad (\text{B.3})$$

Now,

$$I'(f_1) = bI(f_1) + aI(f_1 - 1) + a^*I(f_1 + 1) \quad (\text{B.4})$$

$$I'(f_2) = bI(f_2) + aI(f_2 - 1) + a^*I(f_2 + 1) \quad (\text{B.5})$$

$$(I')^*(f_1 + f_2) = bI^*(f_1 + f_2) + aI^*(f_1 + f_2 - 1) + a^*I^*(f_1 + f_2 + 1) \quad (\text{B.6})$$

The bispectrum $b(f_1, f_2)$ is given by the product of the equations, B.5, B.6 and B.6. Substituting for $I(f)$ from equation B.2, we get

$$\begin{aligned} b(f_1, f_2) &= I'(f_1) I'(f_2) (I')^*(f_1 + f_2) \\ &= A \cdot B \cdot C, \end{aligned} \quad (\text{B.7})$$

where

$$\begin{aligned} A &= bI_0(f_1) + bN(f_1) + aI_0(f_1 - 1) + \\ &\quad aN(f_1 - 1) + a^*I_0(f_1 + 1) + a^*N(f_1 + 1), \\ B &= bI_0(f_2) + bN(f_2) + aI_0(f_2 - 1) + \\ &\quad aN(f_2 - 1) + a^*I_0(f_2 + 1) + a^*N(f_2 + 1), \\ C &= bI_0^*(f_1 + f_2) + bN^*(f_1 + f_2) + aI_0^*(f_1 + f_2 - 1) + \\ &\quad aN^*(f_1 + f_2 - 1) + a^*I_0^*(f_1 + f_2 + 1) + a^*N^*(f_1 + f_2 + 1). \end{aligned}$$

Assuming that noise and signal are not correlated (and hence their product vanishes upon averaging) and the noise at different frequencies are not correlated with each other, and neglecting terms containing $|a|^2$ (as $\frac{|a|}{|b|} \ll 1$, when the hanning window is unity over 80 % of the image.) we get 16 non-vanishing (when averaged over an ensemble) terms in the product $A \cdot B \cdot C$. They are the ensemble average of the terms given in the following table.

1	$b^3 I_0(f1)I_0(f2)I_0^*(f1+f2)$	2	$a^*b^2 I_0(f1)I_0(f2)I_0^*(f1+f2-1)$
3	$ab^2 I_0(f1)I_0(f2)I_0^*(f1+f2+1)$	4	$ab^2 I_0(f1)I_0(f2-1)I_0^*(f1+f2)$
5	$a^2b I_0(f1)I_0(f2-1)I_0^*(f1+f2+1)$	6	$a^*b^2 I_0(f1)I_0(f2+1)I_0^*(f1+f2)$
7	$(a^*)^2b I_0(f1)I_0(f2+1)I_0^*(f1+f2-1)$	8	$ab^2 I_0(f1-1)I_0(f2)I_0^*(f1+f2)$
9	$a^2b I_0(f1-1)I_0(f2)I_0^*(f1+f2+1)$	10	$a^2b I_0(f1-1)I_0(f2-1)I_0^*(f1+f2)$
11	$a^2a^* I_0(f1-1)I_0(f2-1)I_0^*(f1+f2-1)$	12	$a^3 I_0(f1-1)I_0(f2-1)I_0^*(f1+f2+1)$
13	$a^*b^2 I_0(f1+1)I_0(f2)I_0^*(f1+f2)$	14	$(a^*)^2b I_0(f1+1)I_0(f2)I_0^*(f1+f2-1)$
15	$(a^*)^2b I_0(f1+1)I_0(f2+1)I_0^*(f1+f2)$	16	$(a^*)^3 I_0(f1+1)I_0(f2+1)I_0^*(f1+f2-1)$

The ensemble average of the first term is proportional to the ‘true’ bispectrum ($I_0 = OP$). Since b is a real number, phase of the bispectrum remains unaffected. The ensemble average of the remaining terms is non-zero and thus the bispectrum is affected by their presence. The contribution of the last 15 terms is zero when a is forced to zero. (Keller, 1999). To achieve this, the window function is first Fourier transformed, its Fourier components at $f = \pm 1$ are replaced by zeros and then inverse Fourier transformed. The resulting function is used as an optimum apodisation window. It has a ‘trough’ at the middle and extended ‘ears’ near the edges. As the reconstructed image is divided by this function, there is no side effect apart from data loss near the edges.

Bibliography

- [1] Ables, J. G.:1974, "Maximum entropy spectral analysis", *Astron. Astrophys. Suppl. Ser.* **15**, 383.
- [2] Aime, C., Ricort, G., Roddier, C., and Lago, G.:1978, "Changes in the atmospheric-lens modulation transfer function used for calibration in solar speckle interferometry", *J. Opt. Soc. Am.* **68**, 1063.
- [3] Ambasta, A.:1999, in M. S. Narayanan, Hari Om Vats, B. Manikiam, Harish Chandra and S. P. Gupta (eds.), *Space Research in India: Accomplishments and Prospects, Solar Optical Astronomy at Udaipur Solar Observatory August*, PRL Alumni Association, Ahmedabad.
- [4] Andrews, H. C. and Hunt, B. R.:1977, *Digital image restoration*, Printice-Hall, Inc., Englewood cliffs, New Jersey.
- [5] Antia, H. M.:1991, *Numerical Methods for Scientists and Engineers*, Tata McGraw-Hill Publishing Company Limited, New Delhi.
- [6] Armstrong, J. T., Hutter, D. J., Johnson, K. J., and Mozurkewich, D.:1995, "Stellar optical interferometry in the 1990s", *Physics Today* **May**, 42.
- [7] Babcock, H. W.:1953, "The possibility of compensating astronomical seeing", *Publ. Astron. Soc. Pac.* **65**, 229.
- [8] Baldwin, J. E., Haniff, C. A., Mackay, C. D., and Warner, P. J.:1986, "Closure phase in high resolution optical imaging", *Nature* **320**, 595.

-
- [9] Bappu, M. K. V.:1967, "Solar physics at Kodaikanal (Report from solar institute)", *Solar Phys.* **1**, 151.
- [10] Bates, R. H. T.:1982, "Astronomical speckle imaging", *Physics Reports (Review section of Physics Letters)* **90**, 203.
- [11] Beckers, J. M.:1989, "Detailed compensation of atmospheric seeing using multi-conjugate adaptive optics", *SPIE* **1114**, 215.
- [12] Berger, T. E., Schrijver, C. J., Shine, R. A., Tarbell, T. D., Title, A. M., and Scharmer, G.:1995, "New observations of subarcsecond photospheric bright points", *Astrophys. J.* **454**, 531.
- [13] Berger, T. E. and Title, A. M.:1996, "On the dynamics of small-scale solar magnetic elements", *Astrophys. J.* **463**, 365.
- [14] Berger, T. E. and Title, A. M.:2001, "On the relation of G-band bright points to the photospheric magnetic field", *Astrophys. J.* **553**, 449.
- [15] Bevington, P. R. and Robinson, D. K.:1992, *Data reduction and error analysis for the physical sciences*, McGraw-Hill, Inc., New Delhi.
- [16] Born, M. and Wolf, E.:1980, *Principles of Optics*, Chapter10, Pergamon, Oxford.
- [17] Bracewell, R. M.:1986, *Fourier transform and its applications*, McGraw-Hill International Editions, Second Edition, Revised, New Delhi.
- [18] Brandt, P. N.:1969, "Frequency spectra of solar image motion", *Solar Phys.* **7**, 187.
- [19] Brandt, P. N.:1970, "Measurement of solar image motion and blurring", *Solar Phys.* **13**, 243.
- [20] Brault, J. W. and White, O. R.:1971, "The analysis and restoration of astronomical data via the fast Fourier transform", *Astron. Astrophys.* **13**, 169.

- [21] Bray, R. J. and Loughhead, R. E.:1974, *The solar chromosphere*, Chapman and Hall, London.
- [22] Breckinridge, J. B. and McAllister, H. A.:1976, "Measurement of atmospheric speckle isoplanicity, *J. Opt. Soc. Am.* **66**, 1077(A).
- [23] Brown, Jr., W. P.:1966, "Validity of the Rytov Approximation in optical propagation calculation", *J. Opt. Soc. Am.* **56**, 1045.
- [24] Brown, Jr., W. P.:1967, "Validity of the Rytov Approximation", *J. Opt. Soc. Am.* **57**, 1539.
- [25] Buscher, D.:1988, "Optimizing a ground-based optical interferometer for sensitivity at low light levels", *Monthly Notices Royal Astron. Soc.* **235**, 1203.
- [26] Buscher, D. F., Armstrong, J. T., Hummel, C. A., Quirrenbach, A., Mozurkewich, D., Johnston, K. J., Denison, C. S., Colavita, M. M., and Shao, M.:1995, "Interferometric seeing measurements at Mt. Wilson: power spectra and outer scales", *Appl. Opt.* **34**, 1081.
- [27] Castleman, K. R.:1979, *Digital image processing*, Printice-Hall, Inc., Englewood cliffs, New Jersey.
- [28] Chapman, G. A. and Sheeley, Jr., N. R.:1968, "The photospheric network", *Solar Phys.* **5**, 442.
- [29] Chapman, G. A.:1970, "An interference filter for observing the photospheric network", *Solar Phys.* **13**, 78.
- [30] Damé, L., Matric, M., and Porteneuve, J.:1994, "Solar interferometric imaging from the moon", *Adv. Space Res.* **14**, 49.
- [31] de Boer, C. R. and Kneer, F.:1992, "Speckle observations of abnormal solar granulation", *Astron. Astrophys.* **264**, L24.
- [32] de Boer, C. R., Kneer, F., and Nesis, A.:1992, "Speckle observations of solar granulation", *Astron. Astrophys.* **257**, L4.

-
- [33] de Boer, C. R.:1996, "Noise filtering in solar speckle masking reconstructions", *Astron. Astrophys. Suppl. Ser.* **120**, 195.
- [34] Denker, C.:1998, "Speckle masking of sunspots and pores", *Solar Phys.* **180**, 81.
- [35] Dwarkanath, K. S., Despande, A. A., and Udaya Shankar, N.:1990, "A modified algorithm for CLEANing wide-field maps with extended structures", *J. Astrophys. Astron.* **11**, 311.
- [36] Ellerbroek, B. and Rigaut, F.:2000, "Optics adapt to the whole sky", *Nature* **403**, 25.
- [37] Evans, J. W.:1967, "Sacramento Peak Observatory (Report from solar institute)", *Solar phys.* **1**, 157.
- [38] Fleck, B., Domingo, V., and Poland, A.:1995, *The SOHO mission*, Kluwer Academic Publishers, London; Reprinted from *Solar Phys.* **162**, Nos. 1-2.
- [39] Foukal, P.:1990, *Solar Astrophysics*, John Wiley and Sons, Inc., New York.
- [40] Fried, D. L.:1965, "Statistics of a geometric representation of wave-front distortion", *J. Opt. Soc. Am.* **55**, 1427.
- [41] Fried, D. L.:1966, "Optical resolution through a randomly inhomogeneous medium for very long and very short exposures", *J. Opt. Soc. Am.* **56**, 1372.
- [42] Fried, D. L.:1967, "Test of Rytov approximation", *J. Opt. Soc. Am.* **57**, 268.
- [43] Fried, D. L.:1975, "Differential angle of arrival: Theory, evaluation, and measurement feasibility", *Radio Science* **10**, 71.
- [44] Fried, D. L.:1977, "Resolution, signal-to-noise ratio, and measurement precision", *J. Opt. Soc. Am.* **69**, 399.
- [45] Fried, D. L.:1979, "Angular dependence of the atmospheric turbulence effect in speckle interferometry", *Optica Acta* **26**, 597.

- [46] Frieden, B. R.:1972, "Restoring with Maximum Likelihood and Maximum Entropy", *J. Opt. Soc. Am.* **62**, 511.
- [47] Glindemann, A., Lane, R. G., and Dainty, J. C.:1993, "Simulation of time-evolving speckle patterns using Kolmogorov statistics", *J. Mod. Opt.* **40**, 2381.
- [48] Gonsalves, R. A. and Childlaw, R.:1979, "Wavefront Sensing by Phase Retrieval", in A. G. Teschev, (ed.), *Applications of Digital Image Processing III*, *SPIE* **207**, 32.
- [49] Gonsalves, R. A.:1982, "Phase Retrieval and Diversity in Adaptive Optics", *Opt. Eng.* **21**, 829.
- [50] Gonzalez, R. C. and Wintz, P.:1977, *Digital Image Processing*, Addison-Wesley Publishing Company, London.
- [51] Goodman, J. W.:1985, *Statistical Optics*, John Wiley and Sons, New York.
- [52] Goodman, J. W.:1996, *Introduction to Fourier Optics*, McGraw-Hill Book Company, New York.
- [53] Hanbury Brown, R. and Twiss, R. Q.:1954, "A New Type of Interferometer for Use in Radio Astronomy", *Philos. Mag. series 7* **45**, 663.
- [54] Hanbury Brown, R. and Twiss, R. Q.:1957, "Interferometry of the intensity fluctuations in light. I. Basic theory: the correlation between photons in coherent beams of radiation", *Proc. Roy. Soc. London* **242**, 300.
- [55] Haniff, C. A., Mackay, C. D., Titterton, D. J., Sivia, D., Baldwin, J. E., and Warner, P. J.:1987, "The first images from optical aperture synthesis", *Nature* **328**, 694.
- [56] Haralick, R. M., Sternberg, S. R., and Zhuang, X.:1987, "Image analysis using mathematical morphology", *IEEE Trans. PAMI* **9**, 532.
- [57] Harris, J. L.:1964, "Resolving power and decision theory", *J. Opt. Soc. Am.* **54**, 606.

- [58] Harvey, J. W.:1972, "Interferometry applied to visible solar features", *Nature Physical Science* **235**, 90.
- [59] Harvey, J. W. and Breckinridge, J. B.:1973, "Solar speckle interferometry", *Astrophys. J.* **182**, L137.
- [60] Herman, B. J. and Strugula, L. A.:1990, "Method for inclusion of low frequency contributions in numerical representation of atmospheric turbulence", in P. B. Ulrich and E. Wilson (eds.), *Propagation of High-Energy Laser Beams through the Earth's Atmosphere*, *SPIE* **1221**, 183.
- [61] Högbom, J.:1974, "Aperture synthesis with a non-regular distribution of interferometer baselines", *Astron. Astrophys. Suppl. Ser.* **15**, 417.
- [62] Huang, T. S., Schreiber, W. F., and Tretiak, O. J.:1971, *Image Processing*, *IEEE* **59**, 1586.
- [63] Ishimaru, A.:1978, *Wave propagation and scattering in random media* **2**, Academic Press, Inc., New York.
- [64] Jakobsson, H.:1996, "Simulations of time series of atmospherically distorted wavefronts", *Appl. Opt.* **35**, 1561.
- [65] Jennison, R. C.:1958, "A phase sensitive interferometer technique for the measurement of the Fourier transforms of spatial brightness distributions of small angular extent", *Monthly Notices Royal Astron. Soc.* **118**, 276.
- [66] Jennison, R. C. and Das Gupta, M. K.:1953, "Fine Structure in the Extra-terrestrial Radio Source Cygnus 1", *Nature* **172**, 996.
- [67] Jennison, R. C. and Das Gupta, M. K.:1956, "The Measurement of the Angular Diameter of Two Intense Radio Sources", *Philos. Mag. series 8* **1**, 55.
- [68] Karbelkar, S.:1989, "Statistical methods of phase reconstruction in speckle interferometry", *Ph.D. thesis*, Department of Physics, Indian Institute of Science, Bangalore, India.

- [69] Keil, S.:2000, *Private communication*.
- [70] Keller, C. U.:1992, "Resolution of magnetic flux tubes on the Sun", *Nature* **359**, 307.
- [71] Keller, C. U. and Von der Lühe, O.:1992, "Solar speckle polarimetry", *Astron. Astrophys.* **261**, 321.
- [72] Keller, C. U.:1999, "Optimum apodisation for speckle imaging of extended sources", *ASP Conf. Series*, **183**, 342.
- [73] Keller, J. B.:1969, "Accuracy and validity of the Born and Rytov approximation", *J. Opt. Soc. Am.* **59**, 1003.
- [74] Kitai, R.:1986, "Photospheric and chromospheric umbral dots in a decaying sunspot", *Solar Phys.* **104**, 287.
- [75] Kitai, R. and Muller, R.:1984, "On the relation between chromospheric and photospheric fine structures in active region", *Solar Phys.* **90**, 303.
- [76] Knölker, M., Schüssler, M.:1988, "Model calculations of magnetic flux tubes. IV Convective energy transport & the nature of intermediate size flux concentrations", *Astron. Astrophys.* **202**, 275.
- [77] Knox, K. T. and Thompson, B. J.:1974, "Recovery of images from atmospherically degraded short exposure images", *Astrophys. J. Lett.* **193**, L45.
- [78] Kolmogorov, A. N.:1941, *Dan. S. S. S. R* **30**, 229.
- [79] Korff, D.:1973, "Analysis of a method for obtaining near-diffraction limited information in the presence of atmospheric turbulence", *J. Opt. Soc. Am.* **63**, 971.
- [80] Krishnakumar, V.:1998, "High angular resolution imaging of Sun", *Ph.D. Thesis*, Indian Institute of Astrophysics, Bangalore University, Bangalore, India.
- [81] Krishnakumar, V. and Venkatakrishnan, P.:1997, *Astron. Astrophys. Suppl. Ser.* **126**, 177.

- [82] Labeyrie, A.:1970, "Attainment of diffraction limited resolution in large telescopes by Fourier analysing speckle patterns in star images", *Astron. Astrophys.* **6**, 85.
- [83] Labeyrie, A.:1976, "High-resolution techniques in optical astronomy", in E. Wolf (ed.), *Progress in Optics XIV*, 47, North-Holland, Amsterdam.
- [84] Lane, R. G., Glindemann, A.:1992, and Dainty, J. C., "Simulation of a Kolmogorov phase screen", *Waves in random media* **2**, 202.
- [85] Löfdahl, M. G. and Scharmer, G. B.:1994, "Wavefront sensing and image restoration from focused and defocused solar images", *Astron. Astrophys. Suppl. Ser.* **107**, 243.
- [86] Lohmann, A. W., Weigelt, G., and Wirtitzer, B.:1983, "Speckle masking in astronomy: triple correlation theory and applications", *Appl. Opt.* **22**, 4028.
- [87] McGlamery, B. L.:1976, "Computer simulation studies of compensation of turbulence degraded images", in J. C. Urbach (ed.), *Image Processing, SPIE 74*, 225.
- [88] McLean, I. S.:1989, *Electronic and Computer-aided astronomy: From eyes to electronic sensors*, Chapter 8, Ellis Horwood Ltd., John Wiley and Sons, New York.
- [89] Michelson, A. A.:1891, "Measurement of Jupiter's satellites by interference", *Nature* **45**, 160.
- [90] Michelson, A. A. and Pease, F. G.:1921, "Measurement of the diameter of α orionis with the interferometer", *Astrophys. J.* **53**, 249. **LI**, 257.
- [91] Muller, R. and Roudier, Th.:1984, "Variability of the quiet photospheric network", *Solar Phys.* **94**, 33.
- [92] Muller, R.:1985, "The fine structure of the quiet Sun", *Solar Phys.* **100**, 237.

- [93] Muller, R., Dollfus, A., Montagne, M, Moity, J., and Vigneau, J.:2000, "Spatial and temporal relations between magnetic elements and bright points in the photospheric network", *Astron. Astrophys.* **359**, 373.
- [94] Nakajima, T., Kulkarni, S. R., Gorham, P. W., Ghez, A. M., Neugebauer, G., Oke, J. B., Prince, T. A., and Readhead, A. C. S.:1989, "Diffraction limited imaging. II. Optical aperture synthesis imaging of two binary stars", *Astron. J.* **97**, 1510.
- [95] Narayan, R. and Nityananda, R.:1986, "Maximum entropy image restoration in astronomy", *Ann. Rev. Astron. Astrophys.* **24**, 127.
- [96] Niblack, W.:1986, *An Introduction to Digital Image Processing*, Printice Hall International, New Jersey, p. 139.
- [97] Nisenson, P. and Stachnik, R. V.:1978, "Measurements of atmospheric isoplanatism using speckle interferometry", *J. Opt. Soc. Am.* **68**, 169.
- [98] Nityananda, R. and Narayan, R.:1982, "Maximum entropy image reconstruction – A practical non-information-theoretic approach", *J. Astrophys. Astron.* **3**, 419.
- [99] Noll, R. J.:1976, "Zernike polynomials and atmospheric turbulence", *J. Opt. Soc. Am.* **66**, 207.
- [100] November, L. J.:1986, "Measurement of geometric distortion in a turbulent atmosphere", *Appl. Opt.* **25**, 392.
- [101] Oppenheim, A. V. and Lim, J. S.:1981, "The importance of phase in signals", *Proc. of the IEEE* **69**, 529.
- [102] Paxman, R. G. and Fienup, J. R.:1988, "Optical Mis-alignment Sensing and Image Reconstruction Using Phase-Diversity", *J. Opt. Soc. Am. A* **5**, 914.
- [103] Paxman, R. G., Seldin, J., Löfdhal, M., Scharmer, G. B., and Keller, C. U.:1996, "Evaluation of Phase-Diversity techniques for solar-image restoration", *Astrophys. J.* **466**, 1087.

-
- [104] Paxman, R. G., Seldin, J., and Keller, C. U.:1999, "Phase-Diversity Data Sets and Processing Strategies", *ASP Conf. Series* **183**, 311.
- [105] Pehlemann, E. and Von der Lühe, O.:1989, "Technical aspects of speckle masking phase reconstruction algorithm", *Astron. Astrophys.* **216**, 337.
- [106] Peterson, C. C. and Brandt, J. C.:1995, *Hubble vision-astronomy with the Hubble Space Telescope*, Cambridge University Press, Cambridge.
- [107] Pollaine, S., Buffington, A., and Crawford, F. S.:1979, "Measurement of the size of the isoplanatic patch using phase-correcting telescope", *J. Opt. Soc. Am.* **69**, 84.
- [108] Ponsonby, J. E. B.:1973, "An Entropy Measure for Partially Polarized Radiation and its application to Estimating Radio Sky Polarization Distributions from Incomplete 'Aperture Synthesis' Data by the Maximum Entropy Method", *Monthly Notices Royal Astron. Soc.* **163**, 369.
- [109] Press, H. W., Teukolsky, S. A., Vetterling, W. T., and Flannery, B. P.:1993, *Numerical recipes in FORTRAN; The art of scientific computing*, Second edition, Cambridge University Press, New Delhi.
- [110] Ragazzoni, R., Marchetti, E, and Valente, G.:2000, "Adaptive-optics corrections available for the whole sky", *Nature* **403**, 54.
- [111] Reinheimer, T. and Weigelt, G.:1987, "Optical long-baseline interferometry and aperture synthesis by speckle masking", *Astron. Astrophys.* **176**, L17.
- [112] Ricort, G. and Aime, C.:1979, "Solar seeing and the statistical properties of the photospheric solar granulation, III Solar speckle interferometry", *Astron. Astrophys.* **76**, 324.
- [113] Roddier, F.:1981, "The effects of atmospheric turbulence in optical astronomy", in E. Wolf (ed.), *Progress in Optics* **XIX**, 281, North-Holland, Amsterdam.

- [114] Roddier, F., Gilli, J. M., and J. Vernin.:1982, "On the isoplanatic patch size in stellar speckle interferometry", *J. Optics* **13**, 63.
- [115] Roddier, F.:1988, "Interferometric imaging in Optical Astronomy", *Physics Reports* **170**, 2.
- [116] Roddier, N.:1990, "Atmospheric wave-front simulation using Zernike polynomials", *Optical Engineering* **29**, 1174.
- [117] Roudier, Th., Espagnet, O., Muller, R., and Vigneau, J.:1994, "Peculiar interactions between granules and network bright points in the solar photosphere", *Astron. Astrophys.* **287**, 982.
- [118] Ryle, M. and Vonberg, D. D.:1946, "Solar Radiation at 175 Mc/s", *Nature* **158**, 339.
- [119] Sánchez Almeida, J., Landi Degl'Innocenti, E., Martínez Pillet, V., and Lites, B. W.:1996, *Astrophys. J.* **466**, 537.
- [120] Sánchez Almeida, J.:1998, "Current status of the MISMA hypothesis", in K. N. Nagendra and Stenflo, J. O. (eds.), *Proc. of the second international workshop on solar polarisation*, Kluwer Academic Publishers, p. 251.
- [121] Sankarasubramanian, K.:2000, "Solar polarimetry: Techniques and applications", *Ph.D. Thesis*, Indian Institute of Astrophysics, Bangalore University, Bangalore, India.
- [122] Sarazin, M. and Roddier, F.:1990, "The ESO differential image motion monitor", *Astron. Astrophys.* **227**, 294.
- [123] Scharmer, G. B.:2000, *Private communication*.
- [124] Schrijver, C. J., Title, A. M., Harvey, K. L., Sheeley, Jr., N. R., Wang, Y. M., van den Oord, G. H. J., Shine, R. A., Tarbell, T. D., and Hurlburt, N. E.:1998, "Large-scale coronal heating by small-scale magnetic field of the Sun", *Nature* **394**, 152.

- [125] Schwarz, U. J.:1978, "Mathematical-statistical description of the iterative beam removing technique (method CLEAN)", *Astron. Astrophys.* **65**, 345.
- [126] Sedmak, G.:1998, "Performance analysis of and compensation for aspect-ratio effects of fast-Fourier-transform-based simulations of large atmospheric wavefronts", *Appl. Opt.* **37**, 4605.
- [127] Seldin, J. H. and Paxman, R. G.:1994, "Phase-Diverse Speckle Reconstruction of Solar Data", *SPIE* **2302**, 268.
- [128] Seykora, E. J.:1993, "Solar scintillation and the monitoring of solar seeing", *Solar Phys.* **145**, 389.
- [129] Sivaraman, K. R. and Livingston, W. C.:1982, "Ca II K_{2V} spectral features and their relation to small-scale photospheric magnetic fields", *Solar Phys.* **80**, 227.
- [130] Smithson, R. and Tarbell, T. D.:1977, "Correlation tracking study for meter-class solar telescope on space shuttle", Lockheed Palo Alto Research Lab.
- [131] Solanki, S. K., Zufferey, D., Lin, H., Rüedi, I., and Kuhn, J. R.:1996, "Infrared lines as probes of solar magnetic features XII. Magnetic flux tubes: evidence of convective collapse?", *Astron. Astrophys.* **310**, L33.
- [132] Spruit, H. C.:1976, "Pressure equilibrium and energy balance of small photospheric flux tubes", *Solar. Phys.* **50**, 269.
- [133] Stachnik, R. V., Nisenson, P., Ehn, D. C., Hudgin, R. H., and Schirf, V. E.:1977, "Speckle image reconstruction of solar features", *Nature* **266**, 149.
- [134] Stachnik, R. V., Nisenson, P., and Noyes, R.W.:1983, "Speckle image reconstruction of solar features", *Astrophys. J.* **271**, L37.
- [135] Steer, D. G., Dewdney, P. E., and Ito, M.R.:1984, "Enhancements to the deconvolution algorithm 'CLEAN'", *Astron. Astrophys.* **137**, 159.

- [136] Steiner, O., Hauschildt, P. H., and Bruls, J.:2001, "Radiative properties of magnetic elements I. Why are G-band bright points bright", *Astron. Astrophys.* **372**, L13.
- [137] Stenflo, J. O.:1973, "Magnetic-field structure of the photospheric network", *Solar Phys.* **32**, 41.
- [138] Stenflo, J. O. and Harvey, J. W.:1985, "Dependence of the properties of magnetic flux tubes on area factor or amount of flux", *Solar Phys.* **95**, 99.
- [139] Stein, R. F. and Nordlund, Å.:1998, "Simulations of solar granulations: I, General properties", *Astrophys. J.* **499**, 914.
- [140] Stockham, T. G., Cannon, T. M., and Ingebretsen, R. B.:1975, "Blind deconvolution through digital signal processing", *Proc. of the IEEE* **63**, 678.
- [141] Sylvester, B. and Sylvester, J.:2000, "Evolution of YOHKOH observed white light flares", *Solar Phys.* **194**, 305.
- [142] Tatarski, V. I.:1961, *Wave Propagation in a Turbulent Medium* McGraw-Hill Book Company, Inc., New York.
- [143] Tatarski, V. I.:1968, *The effects of the turbulent atmosphere on wave propagation*, National Science Foundation Report TT-68-50464.
- [144] Thompson, A. R., Moran, J. M., and Swenson, G. W.:1986, *Interferometry and Synthesis in Radio Astronomy*, John Wiley & Sons, Inc., New York.
- [145] Title, A.:1966, *Selected Spectroheliograms*, Calif. Inst. Tech., Pasadena.
- [146] Title, A. M., Topka, K. P., Tarbell, T. D., Schmidt, W., Balke, C., and Scharmer, G. B.:1992. "On the differences between plage and quiet Sun in the solar photosphere", *Astrophys. J.* **393**, 782.
- [147] Title, A. M. and Berger, T. E.:1996, "Double-Gaussian models of bright points or why bright points are usually dark", *Astrophys. J.* **463**, 797.

- [148] Tomita, F.:1990, *Computer Analysis of Visual Textures*, Kluwer Academic Publishers, Boston.
- [149] Topka, K. P., Tarbell, T. D., and Title, A. M.:1986, "High resolution observations of changing magnetic features on the Sun" *Astrophys. J.* **306**, 304.
- [150] Venkatakrisnan, P.:1986, "Inhibition of convective collapse of solar magnetic flux tubes by radiative diffusion", *Nature* **322**, 156.
- [151] Verma, V. K.:1999, "Development of an instrument for the observations of solar H α flares with time resolution of 25 ms", *High Resolution Solar Physics: Theory, Observations, and Techniques, ASP Conf. Series* **183**, 1999.
- [152] von der Lühe, O.:1983, "A study of a correlation tracking method to improve imaging quality of a ground based solar telescope", *Astron. Astrophys* **119**, 85.
- [153] von der Lühe, O.:1984a, "Estimating Fried's parameter from a time series of an arbitrary resolved object imaged through atmospheric turbulence", *J. Opt. Soc. Am. A* **1**, 510.
- [154] von der Lühe, O.:1984b, "High resolution speckle imaging of small-scale structure: the influence of anisoplanatism", in R. Muller(ed.), *High Resolution in Solar Physics, Lecture Notes in Physics* **233**, 96.
- [155] von der Lühe, O. and Pehlemann, E.:1988, "Speckle masking imaging of extended sources", in F. Merkle (ed.), *NOAO-ESO Conference on High-Resolution Imaging by Interferometry*, Garching bei München, Part I, p. 159.
- [156] von der Lühe, O.:1989, "Imaging of the solar surface with interferometric arrays", *private communication*.
- [157] von der Lühe, O. and Zirker, J. B.:1988, "Scientific goals for solar interferometry", in F. Merkle (ed.), *NOAO-ESO Conference on High-Resolution Imaging By Interferometry* 15-18 March, Garching bei München, F.R.G., Part I, p. 77.

- [158] von der Lühe, O.:1993, "Speckle imaging of solar small scale structure: I methods", *Astron. Astrophys.* **268**, 374.
- [159] von der Lühe, O.:1994, "Speckle imaging of solar small scale structure: II study of small scale structure in active regions", *Astron. Astrophys.* **281**, 889.
- [160] Wang, C. P.:1975, "Isoplanacity for imaging through turbulent media", *Opt. Commun.* **14**, 200.
- [161] Weigelt, G.:1977, "Modified speckle interferometry: speckle masking", *Opt. Commun.* **21**, 55.
- [162] Xuan, J. Y., Gu, X. M, Lin, J., Jiang, Y. C., Zhong, S. H., and Li, Y. S.:1998 "Time evolution and morphological characteristics of white light flare on 18 January 1989", *Astron. Astrophys. Suppl. Ser.* **129**, 553.
- [163] Yi, Z. and Engvold, O.:1993, "Filigree, magnetic fields and flows in the photosphere", *Solar Phys.* **144**, 1.
- [164] Young, A. T.:1971, "Seeing and scintillation", *Sky and Telescope* **September**, 139.
- [165] Zirin, H.:1989, *Astrophysics of the Sun*, Cambridge university press, Cambridge.
- [166] Zirker, J. B.:1987, "Interferometric imaging: A numerical simulation", *Solar Phys.* **111**, 235.
- [167] Zirker, J. B.:1989. "Interferometric imaging II: Two dimensional non-redundant arrays", *Solar Phys.* **120**, 253.